وزارة التعليم العالي و البحث العلمي

MINISTERE DE L'ENSEIGNEMENT SUPERIEUR ET DE LA RECHERCHE SCIENTIFIQUE

جامعة فرحات عباس سطيف 1

UNIVERSITE FERHAT ABBAS – SETIF

THESE

Présentée à la

FACULTE DE TECHNOLOGIE

DEPARTEMENT D'ELECTROTECHNIQUE

Pour l'Obtention du Diplôme de

Doctorat en Sciences

Option : Machines Electriques et leurs Commandes

Par

BABES BADREDDINE

Thème

Commande Prédictive de la Machine Synchrone à Aimant Permanent Utilisée dans un Système éolien

Soutenue le **15/02/2018** devant la commission d'examen composée de

Pr. Hammoud RADJEAI	Président	Université de Sétif
Pr. Lazhar RAHMANI	Directeur de thèse	Université de Sétif
HDr. Abdelmadjid CHAOUI	Co-directeur de thèse	Université de Sétif
Pr. Toufik REKIOUA	Examinateur	Université de Bejaia
Pr. Achour BETKA	Examinateur	Université de Biskra
Pr. Nasreddine BOUDJERDA	Examinateur	Université de Jijel

PREDICTIVE CONTROL OF PERMANENT MAGNET SYNCHRONOUS MACHINE USED IN A WIND SYSTEM

By

BABES BADREDDINE

A dissertation
presented to FERHAT Abbas – Sétif 1 University
in partial fulfillment of the
requirements for the degree of Doctor of science
in the Program of Electrical Machinery and their Controls

University of Sétif 1, Algeria, 2018

Acknowledgements

At the outset, I would like to express my deepest and sincerest gratitude to the God Almighty, the most compassionate and merciful who guides me in the most appropriate way towards the completion of my research.

I would like to express my sincere gratitude and appreciation goes to my primary supervisor **Prof. Lazhar RAHMANI,** University Ferhat ABBAS-Sétif 1, Algeria for his suggesting the topic, valuable advice, continuous guidance and help over the duration of this work. Also, I would like to thank **HDr. Abdelmadjid CHAOUI,** University of Ferhat ABBAS-Sétif 1, Algeria for his advice and help.

I would also like to express my gratitude to **Prof Hammoud RADJEAI** University of Ferhat ABBAS-Sétif 1, Algeria, **Prof Toufik REKIOUA** University of Abderrahmane MIRA-Bejaia, Algeria, **Prof Achour BETKA** University of Mohamed KHIDER-Biskra, Algeria, and **Pr Nasreddine BOUDJERDA** University of Mohammed Seddik BENYAHIA-Jijel, Algeria for sparing their time to be my examiners.

Thanks to the LAS group, especially**, Dr. Amar BOUAFASSA**, and future doctors **Antar BEDDAR, Noureddine HAMOUDA, Idris AZIZI, Mohamed FERHAT, Oussama GHEROUAT, Mohamed NASRI** and **Amine OUCHEN** for their great friendship, help and support. Thanks also to **Dr. Oualid AISSA, Hicham ZERGUINE, Khaled BELHAOUCHET** and **Farid BELOUAHCHI** for their precious friendship and help over all these years.

Thanks to everyone who helped me to complete this thesis. Appreciations also go to all academic staff at the Electrical Engineering Department.

Finally, I would like to express many thanks to my parents and my family for their constant encouragement and support over all this time far away from home. I'm asking God to save them and give them care and health.

Baderddine BABES

Thank you.

Abstract

This research project presents various advanced predictive control strategies for different power electronic converters employed in permanent magnet synchronous generator (PMSG) wind energy systems. The proposed systems combine the advantages of proven wind turbine technologies, such as low-cost machine-side converters, and efficient grid-side converters. The classical control techniques, based on linear PI regulators and low band-width modulation, present several technical issues during system operation, to overcome these issues, a high performance predictive control strategies are proposed in this thesis to control the power converters. The main feature of these control techniques are that a particular attention is paid to increase the efficiency and sustainability, reduce the torque and DC-link ripples, operating at considerably constant switching frequency and help higher penetration of renewable fluctuating power into the grid. Detailed technical work is supported by MATLAB/SIMULINK model based simulations and validated by experimental work on a laboratory prototype consisting in a PMSG and power converters, considering the fluctuation of the wind speed.

Key words: Permanent magnet synchronous generator (PMSG), Wind energy systems, Predictive control strategies, Experimental work.

Résumé

Ce projet de recherche présente diverses stratégies avancées de contrôle prédictif pour différents convertisseurs statiques utilisés dans les systèmes d'énergie éolienne à générateur synchrone à aimant permanent (GSAP). Les systèmes proposés combinent les avantages des technologies de turbines éoliennes éprouvées, telles que des convertisseurs côté machine à faible coût et des convertisseurs statiques efficaces côté réseaux électrique. Les techniques de contrôle classiques, basées sur des régulateurs PI linéaires présentent plusieurs problèmes techniques lors de l'opération du système. Afin de surmonter ces problèmes, une stratégie de contrôle prédictive de haute performance est proposée dans cette thèse pour contrôler les convertisseurs statiques. La principale caractéristique de ces techniques de contrôle est qu'une particulière attention est accordée pour améliorer l'efficacité de la conversion électromécanique et la qualité de l'énergie fournie au réseau, fonctionner à une fréquence de commutation considérablement fixe et aider à une plus grande pénétration de la puissance de renouvellement renouvelable dans le réseaux électrique. Le travail technique détaillé est supporté par des simulations basées sur des modèles MATLAB/SIMULINK et validé par des travaux expérimentaux sur un prototype de laboratoire composé d'une GSAP et de convertisseurs statiques, compte tenu de la fluctuation de la vitesse du vent.

Mots clés : Générateur synchrone à aimant permanent (GSAP), Systèmes d'énergie éolienne, Stratégies de commande prédictive, Travaux expérimentaux.

ملخص:

هذا المشروع البحثي يقدم العديد من استراتيجيات التحكم التنبؤية المتطورة لمختلف المحولات الإلكترونية الساكنة المستخدمة في أنظمة طاقة الرياح للمولد المتزامن ذو المغناطيس الدائم. إن الأنظمة المقترحة تجمع بين مزايا تكنولوجيا توربينات الرياح المعروفة مثل التكلفة المنخفضة للمحولات الإلكترونية الساكنة من جانب الماكينة، والمحولات الإلكترونية الفعالة من جانب الشبكة الكهربائية. وبما أن تقنيات التحكم التقليدية القائمة على وحدات تحكم PI الخطية تتعرض للعديد من المشاكل التقنية أثناء تشغيل النظام. وللتغلب على هذه المشاكل نقترح في هذه الأطروحة وضع استراتيجيات رقابة تنبؤية عالية الأداء للتحكم في محولات القدرة الإلكترونية. وتتمثل السمة الرئيسية لتقنيات التحكم التنبؤية المقترحة في منح اهتمام خاص لتحسين كفاءة التحويل الكهربائية ونوعية الطاقة التي تزود بها الشبكة، الحد من تموجات عزم الدوران، العمل إلى حد كبير على تردد تحويل ثابت والمساعدة على ادماج أمثل للطاقة المتجددة المتغيرة في شبكة الكهرباء. ويدعم العمل الفني التفصيلي من خلال المحاكاة على أساس نماذج MATLAB / SIMULINKوالتحقق من صحتها من خلال العمل التطبيقي على النموذج المخبري المتكون من مولد متزامن ذو مغناطيس دائم، ومحولات إلكترونية ساكنة مع الاخذ بعين الاعتبار التذبذب في سرعة الرياح.

الكلمات المفتاحية: مولد متزامن ذو مغناطيس دائم، أنظمة طاقة الرياح، استراتيجيات الرقابة تنبؤية، عمل تطبيقي.

Table of Contents

List of Figures

List of Tables

List of Abbreviations

PMSG Permanent Magnet Synchronous Generator.
AWEA American Wind Energy Association.
ANFIS Adaptive network-based Fuzzy-inference system.
FRT Fault Ride Through.
AC Alternating Current.
APF Active Power Filter.
BIBO Bounded-Input Bounded-Output.
2L Two-Level.
WT Wind Turbine.
DTC Direct Torque Control.
FS-MPC Finite-Set Model Predictive Control.
FLC Fuzzy Logic Controller.
FMMPC Fuzzy Model-based Multivariable Predictive Controller.
EMF Electro-Motive Force.
ESS Energy Storage System.
FOC Field Oriented Control.
SCIG Squirrel Cage Induction Generator.
FSWT Fixed-Speed Wind Turbine.
VSWT Variable Speed Wind Turbine.
DFIG Doubly Fed Induction Generator.
SG Synchronous Generator.
STATCOM Static Var Compensator.
PCC Predictive Current Control.
PI Proportional-Integral.
PLL Phase Locked Loop.
PWM Pulse Width Modulation.
THD Total Harmonic Distortion.
TSR Tip-Speed Ratio.
VOC Voltage Oriented Control.
VSI Voltage Source Inverter.
LMI Linear Matrix Inequalities.
LAS Laboratoire d’Automatique Sétif.

LPF Low Pass Filter.
LRPC Long Range Predictive Control.
CRHPC Constrained Receding Horizon Predictive Control.
MPC Model Predictive Control.
MOSFET Metal Oxide Semiconductor Field Effect Transistor.
MPP Maximum Power Point.
MPPT Wind Maximum Power Point Tracking.
SPMG Surface Permanent Magnet Generator.
IPMG Interior Permanent Magnet Generator.
WRSG Wound Rotor Synchronous Generator.
WRIG Wound Rotor Induction Generator.
MSC Machine-Side Converter.
MIMO Multi-Input/Multi-Output.
SISO Single- Input/Single- Output.
GSC Grid-Side Converter.
CSC Current Source Converter.
VSC Voltage Source Converter.
DC Direct Current.
DMC Dynamic Matrix Control.
DSP Digital Signal Processor.
DPC Direct Power Control.
IGBT Insulated Gate Bipolar Transistor.
IPCC Improved Predictive Current Controller.
IPMG Interior Permanent Magnet Generator.
WRSG Wound Rotor Synchronous Generator.
WRIG Wound Rotor Induction Generators.
EEM Electro-Magnetic Interference.
EMF Electro-Motive Force.
FC Flying Capacitor.
FPGA Field-Programmable Gate Array.
GPC Generalized Predictive Control.
NPC Neutral Point Clamped.
CHB Cascaded H-bridge.
3L-NPC Three Level Neutral Point Clamped.
9L-ANPC Nine Level Active Neutral Point Clamped.
VF Variable Frequency.
CF Constant Frequency.
COA Centroid of Area.
UDE Uncertainty and Disturbance Estimator.
ZSI Z Source Inverter.
ZOH Zero Order Hold.
RMS Root Mean Square.
ST Switching Table.

SS Steady State.
TPCC Traditional Predictive Current Controller.
SIBC Switched Inductor Boost Converter.
3PH-VSI Three-Phase Voltage Source Inverter.
2L-3PH-VSI Two- Level Three-Phase Voltage Source Converter.
SVM Space Vector Modulation.
ORC Optimum Relationship-Based Control.
OTC Optimal Torque Control.
P&O Perturb and Observe.
PF Power Factor.
PCS Power Conditioning System.
PR Proportional Resonant.
HCS Hill Climb Search.

General Introduction

Wind power is one of the renewable energy sources which have been widely developed in recent years. Wind energy has many advantages such as no pollution, relatively low capital cost involved and the short gestation period. The American Wind Energy Association (AWEA) has suggested that if a 20% of total energy is generated by wind energy by 2030, it would reduce CO2 emissions by 825 million metric tons. This is a real benefit to reducing greenhouse gasses that are directly linked to increasing global warming. Considering the wind turbines installed worldwide, they are typically classified into two types: one is with a geared generator concept, such as those equipped with doubly-fed induction generators (DFIGs) and the other is based on a direct drive mechanism such as those using permanent magnet synchronous generators (PMSGs).

The doubly-fed induction generator (DFIG) has been traditionally preferred to implement the wind energy systems, because it provides good performance and variable speed operation with a converter designed for about the 30% of the machine nominal power. However, current trend points to an implementation based on a permanent magnet synchronous generator (PMSG) with a full power converter. Although this configuration has higher converter losses than DFIG, it presents some interesting properties: gearbox can be avoided in direct drive PMSG, no slip rings are required, provides extended speed operating range, provides full decoupling between the machine-side and the grid-side, which results in higher power capture at different wind speeds, and enhanced capability to meet the grid connection requirements enforced by the transmission and distribution system operators, and allows DC voltage power transmission. These properties can make it preferable than DFIG, because reliability and power ratings are increased, which are key issues, particularly with larger power and size off-shore wind turbines. However, the problems associated with their controllability, higher installation cost, and interconnection with grid are the major issues yet to be solved, as this kind of wind energy system requires full rating AC/DC/AC conversion stages and control of various parameters like voltage, frequency, active/reactive power, harmonics etc. There are several control approaches in the literature for the PMSG based wind energy systems connected to the grid, most of them based on the conventional control theory and symmetrical components. In the recent years, the predictive control techniques are emerging as a promising control solution for power AC machine drives. For that reason, this project adopts the predictive control theory, to develop several new and competitive control methods for the PMSG based wind energy systems.

Motivation for Dissertation Research

The motivation for this thesis is to investigate the next generation predictive control schemes and power converter configurations for PMSG wind energy systems, and to propose new technologies to: (1) decrease cost associated with the power converters, (2) improve wind energy conversion efficiency, and (3) achieve high-performance operation. In this thesis, both the power converters and predictive control schemes are studied in detail.

Thesis Objectives

The main focus of this thesis is the design and implementation of a high performance predictive control for the improvement of stability and fast response of PMSG based wind energy system .Taking into account the hybrid nature of the power electronic converters, the predictive control is a powerful tool for describing the behavior of the wind energy systems. The thesis deals with the modeling and predictive control strategy of five types of power electronic converters for wind energy applications, namely finite-set model predictive control (FS-MPC) of two level three-phase voltage source inverter (3PH-VSI), fixed frequency model predictive control of switched inductor boost converter (SIBC) and single-phase full bride inverter, fuzzy model based-multivariable predictive control (FMMPC) of the DC/DC boost converter, and generalized predictive control (GPC) of the three-phase two level back-to-back power converter. Predictive control is chosen from the different control possibilities because it is easy and coherent, with a comparable simple controller implementation. It is supposed to improve the dynamic performance compared with the classical control schemes. Other goals pursued in this thesis are to mitigate the computation delay and study the predictive controller's sensitivity to parameter uncertainties. Different predictive control schemes could fulfill these goals. Taking into account the simplicity of the implementation and the flexibility for including the different constraints and model predictive control (MPC) are the focus of investigation.

Thesis Limitations

One of the characteristics of predictive control strategy is the large computation time required. The lack of DSPs able to carry on all the required calculations fast enough for power electronics and drives applications, impede the development of the predictive techniques in this area. Computation time is still a limitation. The code should be optimized taking into account that the computation time for practical implementation is limited by the given dSpace DS1104 platform micro-controller. It should be noticed that the results obtained are very dependent of the given system, these are, the blade pitch angle is not regulable, the PMSG has a low inductance which benefits the high current ripples and the built inverter imposes a maximum switching frequency. For this project the converters components are considered ideal, no voltage drop in IGBT's or diodes are considered in simulations. Predictive control comprises a broad class of controllers. Because of time constraint, it is not possible to perform an extensive investigation and complete implementation of all the aspects that could improve the performance of the different control methods. A parallel study of the proposed predictive controllers starting from the simpler implementation and control delay compensation. .

Thesis Organization

The research presented in this thesis is organized into five main chapters. The work carried out in each chapter is summarized as follows:

Chapter 1: provides a general overview of the wind power technology, where the classification of wind turbines based on generators, power electronic converters, methods for maximum energy extraction and grid connection is described in detail. The chapter also presents a brief review of the grid interconnection issues related to output power smoothing, and active and reactive power control in addition to fault ride through (FRT), and grid support capabilities of PMSG based wind energy systems.

Chapter 2: proposes two new predictive control algorithms based on the finite control set strategy. The basic components of a two new finite-set model predictive control (FS-MPC) algorithms are described, such as the cost functions, weighting factors and prediction equations. As the main part of a predictive control with finite control set algorithm, the switching model of a power converters is also described, and the issues related to the control delay compensation, prediction of variables over two samples with reduced computational burden, and stability analysis, are also addressed in this chapter. Simulation and experimental results are presented to verify the performance of the proposed FS-MPC algorithms.

Chapter 3: describes the structure and main characteristics of a fixed frequency model predictive control (MPC) strategy for variable-speed PMSG wind energy systems. Two converter topologies are considered in this chapter, the DC/DC switched inductor boost converter (SIBC) which is the topology utilized in this research, and the single-phase full bridge inverter which was used in previous work. Details of their circuit configurations, analytical models and equations, operation principles and component design are presented. This is followed by the development of a fixed frequency model predictive control (MPC) of the SIBC. Then the predictive current controller with the traditional (TPCC) and improved control (IPCC) and the stability for the single-phase full bridge inverter is discussed. Simulation results are presented to verify the performance of the TPCC and IPCC. Finally the experimental results of the proposed control methodologies are also presented to validate the simulation results.

Chapter 4: presents new encoderless control method for variable-speed PMSG wind energy conversion system and his combination to the fuzzy model based-multivariable predictive control (FMMPC) algorithm in order to design a global optimal controller, overcome the issues related to using a shaft mounted encoder, improve the overall wind energy conversion efficiency and to deal with the time-varying operation points and nonlinear characteristic of the wind turbine generator. It is also presented a significant contribution of the practical implementation of the wind turbine emulator using real time dSPACE DS1104 controller board, in which the dSPACE DS1104 controller board is used to control the energy output of the wind turbine by controlling a DC motor torque. Simulation studies and experimental analysis have been used to verify the effectiveness of the proposed control strategy compared with the traditional PI controller.

Chapter 5: proposes a generalized predictive control based on the conventional vector control strategies for both machine-side and grid-side converters of full scale back-back converters with PMSG wind energy conversion system. It also presents a detailed description and development of the reliable DC-link voltage regulation control and its incorporation into the Uncertainty and Disturbance Estimator (UDE) control scheme, which can provide better robustness performance against the parameter uncertainties, such as power losses, equivalent series resistance, equivalent series inductance and here active power on the capacitor, and external disturbances with varying wind speed conditions. Experimental studies for demonstrating the performance of the proposed control methods are carried out based on dSpace DS1104 platform micro-controller.

Chapter 1 Literature Review of Power Converters and Control Techniques for Grid Integrated PMSG Based Wind Energy Systems

Abstract

The growing trends in wind energy technology are motivating the researchers to work in this area with the aim towards the optimization of the energy extraction from the wind and the injection of the quality power into the grid. Over the last few years, wind generators based on permanent magnet synchronous generators (PMSGs) are becoming the most popular solution for the modern wind energy systems. This chapter presents literature review on the technologies and control methods used in grid integrated wind energy systems employing PMSGs. It reviews the trends in power converter topologies, control methodologies, and methods for maximum energy extraction in PMSG based wind energy systems, which have been reported in various research literatures during last few years. It also presents an overview to the grid interconnection issues related to output power smoothing, and active and reactive power control in addition to fault ride through (FRT), and grid support capabilities of PMSG based wind energy systems.

1.1. Introduction

Recently, the clean energy sources such as solar, tidal and wind energy sources are gaining importance due to their less damaging environmental influences. The wind energy technology is one of the most emerging renewable energy technologies. Over the past few decades, the capacities of wind turbine (WT) units have increased from a few tens of kW power capacity to today's multi-MW level. In view to the steady growth in the power level of the WTs and its increased penetration into the power grid; more advanced generators, power converter systems and control solutions have to be developed so as to make the WT units more suitable to be integrated into the power grid. Any WT generator may operate either at a fixed or variable speed. For instance, the squirrel cage induction generators (SCIGs) can be employed both in fixed-speed wind turbines (FSWTs) and in variable speed wind turbines (VSWTs), while doubly fed induction generators (DFIGs), and synchronous generators (SGs) usually find their applications in

VSWTs [1]. An overview of possible wind generator systems along with their comparisons is presented in [2].

A fixed speed SCIG based wind energy system, even though is simple, reliable and less costly; strictly suffers from the short comings of high mechanical stress, reactive power burden on power grid, large power fluctuations and very limited fault-ride-through (FRT) ability [3].

When compared with FSWT, the VSWT can extract maximum power from the wind at different wind speeds and therefore, reduces the mechanical stress on WT by absorbing the wind power fluctuations [4]. This way, the variable speed operation of WT yields more power than the fixed speed operation of the same, resulting in the maximization of aerodynamic efficiency of the WT.

A mechanical gear box, which is generally employed in VSWT in order to match the low speed operation of the WT with the relatively high speed operation of the generator, not only increases the manufacturing cost and maintenance requirements but also reduces the aero-dynamic efficiency of the WT. The efficiency of VSWT may increase further if the mechanical gear box could be eliminated.

Therefore, several WT manufacturers have adopted the direct-drive PMSG concept so as to eliminate the gear box [5], and a list of such manufacturers is made available in [1]. A comparison of direct-drive and geared generator concepts for WTs is presented in [6] and a review of generator systems for direct-drive WT applications is presented in [7].

Modern VSWT systems, usually based on DFIGs with partial scale power electronic interfaces or PMSGs with full scale power electronics interfaces, are popular among others. The DFIG based VSWT system requires a multi-stage gearbox and also needs for excitation current.

Different from the DFIG based wind energy systems, those based on PMSGs with full scale power electronic interfaces are becoming more popular due to the number of advantages such as high energy density, simple control methodology, low maintenance cost, self excitation system and possibility to direct coupling to a WT with elimination of the gearbox; except initial installation costs [4].

Furthermore, other features such as complete decoupling from the grid, full controllability of the system for maximum wind power extraction, high performance, high efficiency, high precision, high reliability, wide operating range, and improved FRT capability make wind energy systems based on PMSGs even more attractive; though power converter losses increase [1,7]. The advantages and disadvantages of different VSWT generators are outlined in [1].

1.2. Variable speed wind turbines based on PMSGs

It has been recognized that the PMSG based wind energy system is an important trend in the development of wind generation systems [8]. The PMSG allows a small WT blade diameter and, therefore, is preferred in small scale turbine designs also. Besides, the direct-drive PMSG concept has nowadays been adopted by many WT manufacturers. A general model, that can be used to represent all types of VSWT in power system dynamics simulations, is presented in [9] to facilitate the analysis of the impact of large penetration of WTs on the behavior of an electric power system.

The modeling of WT systems based on PMSGs has widely been discussed in [9, 10] which can be used in computer simulations and analyses.

1.2.1. Wind turbine

A wind turbine basically consists of rotor blades and generator. The rotor blades transform the linear kinetic wind energy into rotational kinetic energy in a first step and finally the rotational kinetic energy is converted into electrical energy with the help of generator.

A schematic of wind turbine showing its basic components is given in Figure 1.1.

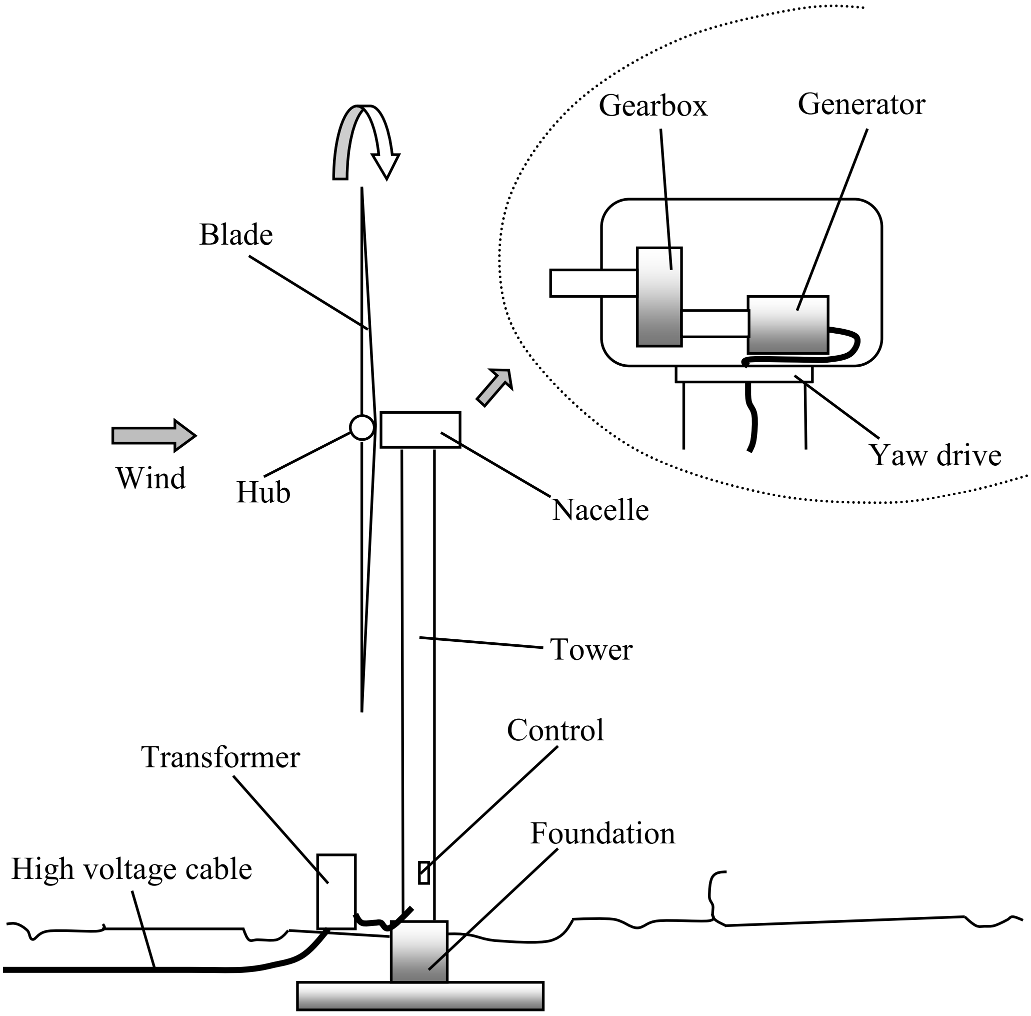

Figure 1.1. Major turbine components.

The output mechanical power available from a wind turbine is function of wind velocity cubed. It can be described mathematically as:

$$P_t = \frac{1}{2}\pi\rho\, C_p(\lambda,\beta) R^2 V_w^3 \tag{1.1}$$

Where ρ is the air density (kg/m^3), R is the wind turbine blade radius (m), λ is the Tip-Speed Ratio (TSR) of the wind turbine, β is the rotor blade pitch angle (d*eg*), C_p (λ,β) expresses the turbine power coefficient which is a non-linear function and depends on the blades aerodynamic design and wind turbine operating conditions, V_w is the effective wind velocity (m/s).

The power conversion coefficient of a wind turbine (C_p) is influenced by the pitch angle (β) and the TSR, which is given by the following equation:

$$TSR = \lambda = \frac{\omega_r R}{V_w} \tag{1.2}$$

Where ω_r is wind turbine angular shaft speed (*rad/s*). When the pitch angle is fixed to zero, λ approaches the maximum value.

Hence, the characteristics of the C_p mainly depend on only the TSR λ and thus can be expressed by an approximate polynomial as follows:

$$C_p(\lambda,\beta) = 0.22\left(\frac{116}{\lambda_i} - 0.4\beta - 5\right)e^{\frac{-12.5}{\lambda_i}} \tag{1.3}$$

Where:

$$\frac{1}{\lambda_i} = \frac{1}{\lambda + 0.08\beta} - \frac{0.035}{\beta^3 + 1} \tag{1.4}$$

Figure 1.2 shows the power coefficient surface for a typical WT. In the condition of certain pitch angle, there is only one TSR λ corresponding to maximum power coefficient C_{p_max}, which is the TSR is called the optimum λ_{opt}.

Hence, the turbine speed should be adjusted in such a way that λ corresponds to maximum power point (MPP).

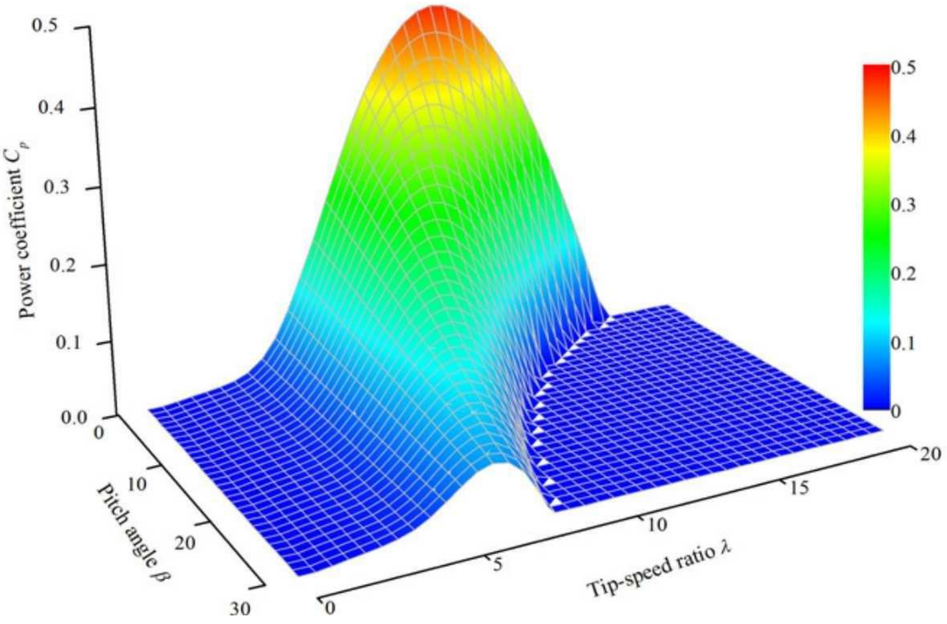

Figure 1.2. Power coefficient C_p as a function of λ and pitch angle of a typical wind turbine.

1.2.2. Permanent magnet synchronous generator (PMSG)

The permanent magnet synchronous generators (PMSGs) are synchronous AC machines. The PMSG consist of three-phase stator winding similar to (SCIG), while the rotor winding is replaced by the permanent magnets.

On the basis of rotor design, the PMSG can be divided in to two parts. Depending on the magnet placement on the rotor they are called either surface permanent magnet generators (SPMGs) or interior permanent magnet generators (IPMGs) as shown in Figure 1.3.

In SPMGs, the permanent magnets are glued on the rotor surface as shown in Figure 1.3(a). The rotor has an iron core which may be solid or made of punched laminations with skewed poles to minimize the cogging torque.

The simple rotor design makes it easy to build. However, the magnets are subject to centrifugal forces that can cause their detachment from the rotor and, therefore, the SPMGs are mainly used in low speed applications.

In the IPMGs, the permanent magnets are inset into the rotor surface as shown in Figure 1.3(b). This configuration also reduces rotational stress associated with centrifugal forces in comparison to the SPMGs and, therefore, this type of generator can operate at higher rotor speeds.

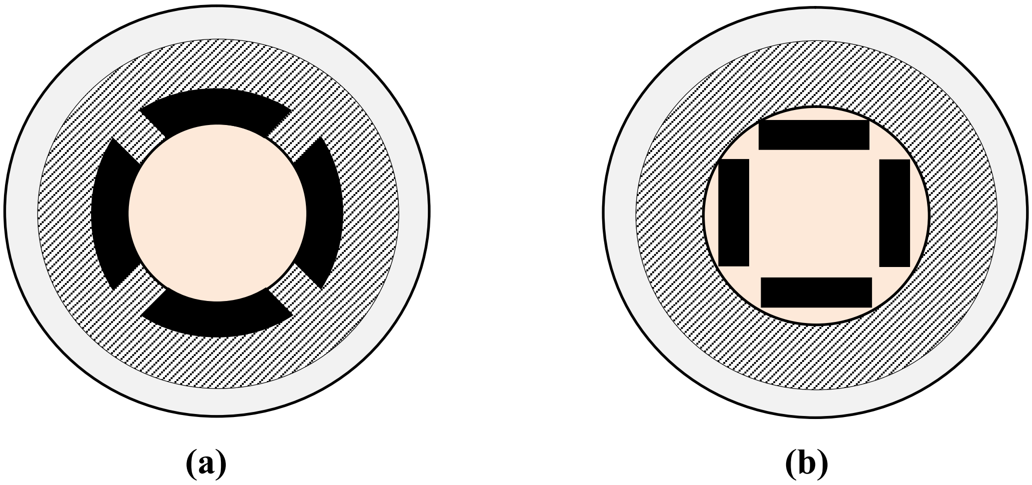

(a) **(b)**

Figure 1.3. Design of PMSG (a) SPMG, (b) IPMG.

Figure 1.4 shows the simplified cross section view of three-phase, two-pole PMSG with symmetrical stator windings, displaced by 120° electrical angle from each other. The relative motion in between rotor and stator induces sinusoidal MMF waves centered on the magnetic axes of the respective phases. The phase difference between rotor magnetic flux (*d*-axis) and the magnetic axis of stator phase-a winding is known as rotor position angle (θ_r). The rate of change of rotor position angle further calculates the angular rotor speed (ω_r).

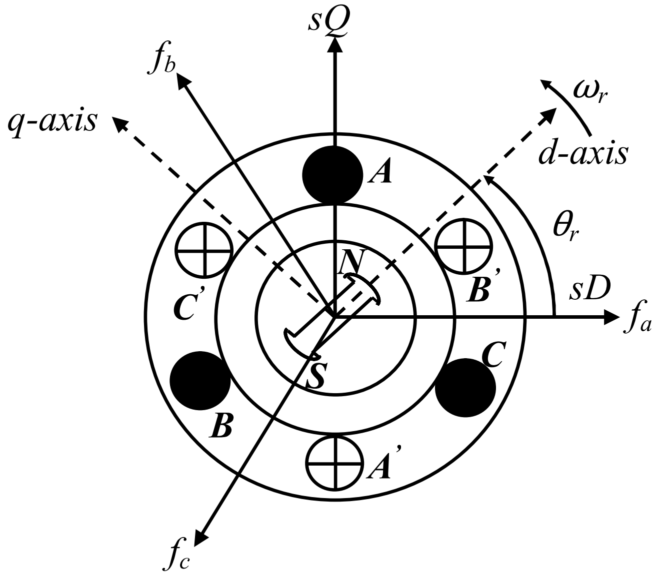

Figure 1.4. Cross section view of PMSM.

The mathematical model of PMSG is similar to that of wound rotor synchronous generator (WRSG). The PMSG stator voltage equations in *d*-*q* reference frame can be expressed in terms of instantaneous currents and stator flux linkages as:

$$V_{ds} = R_s I_{ds} + L_d \frac{d}{dt} I_{ds} - \omega_e L_q I_{qs} \tag{1.5}$$

$$V_{qs} = R_s I_{qs} + L_q \frac{d}{dt} I_{qs} + \omega_e L_d I_{ds} + \omega_e \Phi_m \tag{1.6}$$

where V_{ds}, V_{qs} are the *d-q* axes stator voltages; I_{ds}, I_{qs} are the *d-q* axes stator currents; R_s is the stator resistance; L_d and L_q are the *d-q* axes stator inductances; Φ_m is the rotor flux and, ω_e is the electrical speed, and $\omega_e = (P/2) * \omega r$. where *P* is the number of PMSG poles. The *d*-axis and *q*-axis equivalent diagram of PMSG are shown in Figure 1.5.

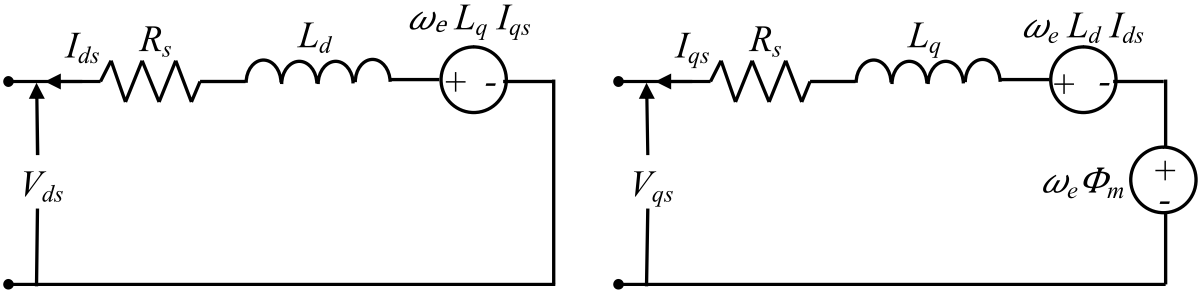

(a) **(b)**

Figure 1.5. Equivalent model of a PMSG. (a) d-axis. (b) q-axis.

The electromagnetic torque developed inside PMSG can be expressed as:

$$T_e = \left(\frac{3}{2}\right) \cdot \left(\frac{P}{2}\right) \cdot \left[\phi_m . I_{qs} + (L_d - L_q) . I_{ds} . I_{qs}\right] \tag{1.7}$$

The surface mounted permanent magnet generator (SPMG) is considered in this thesis. In SPMGs the rotor design is almost smooth and thus offers equal reluctance in both d-axis and q-axis, which results in to equal *d*- and *q*-axis inductances ($L_d = L_q$).

On substituting the equal value of *d*- and *q*-axis inductances ($L_d = L_q$), the electromagnetic torque equation in (1.7) can be further modified as:

$$T_e = \left(\frac{3}{2}\right) \cdot \left(\frac{P}{2}\right) . \phi_m . I_{qs} \tag{1.8}$$

Being the rotor magnetic flux linkage constant in PMSG, the electromagnetic torque is directly proportional to quadrature-axis stator current, as evident from equation (1.8). In other words, the electromagnetic torque in PMSG can be controlled by controlling its quadrature-axis current components.

1.3. Power electronic interface

The power semiconductor devices are the backbone of different power converter topologies used for interfacing renewable resources, and provide greater flexibility in their operation and control both during steady-state and transient system operating conditions. In the 1980s, the soft-starters were used to interconnect the SCIGs with the power grid [11]. In the1990s, the diode bridges with the chopper circuits were used for rotor resistance control of wound rotor induction generators (WRIGs) [12]. Since 2000, advanced AC/DC/AC converters were introduced; initially in the partial-scale power capacity to regulate the generated power from the DFIG based wind energy systems [13], and afterwards in the full scale power capacity to regulate the generated power from the SCIG or PMSG based wind energy systems [14].

The AC/DC/AC converter is one of the best topologies for wind energy systems in realization of two major objectives; firstly, maximum power extraction from the wind, and secondly, feeding the grid with high quality electricity. In DFIG based wind energy system, the stator is directly connected to the power grid; while the partial scale power converter on the rotor circuit controls the rotor speed, performs the reactive power compensation and can achieve the decoupled control of the generator's active and reactive powers. Nevertheless, the use of slip-rings and the protection issues in the event of grid-faults are the major drawbacks of DFIG based wind energy systems [15]. The PMSG based wind energy systems with full scale converters are much preferred since the power converters fully decouple the WT from the grid disturbances and can be caring in some sort of grid support. The full scale power converter offers the merits of high reliability and good power quality [1]. A full scale power converter configuration may avoid the bulky grid-side transformer, thereby, reduces the weight and volume of the nacelle [15]. The high installation cost is the only drawback of full scale converter though full converter rating is rarely utilized for the reason that the wind is intermittent in nature [16].

Several types of power electronic interfaces are presented in the literatures for direct-driven variable speed PMSG based wind energy systems [17, 18]. A typical configuration of PMSG based wind energy system with AC–DC–AC converter must consist a machine (generator)-side converter (MSC) and a grid-side converter (GSC) interconnected through a common DC-link element, which can either be an inductor in case of current source converter (CSC) or a capacitor in case of voltage source converter (VSC) based configuration [19], as shown in Figure 1.6 Among different high power and medium voltage power converter topologies the CSC based AC–DC–AC converter configuration appears to be a promising solution owing to its natural advantages such as simple topology, low device number, compact size, high power capability, low dV/dt, simple control scheme, reliable short-circuit current protection, flexible power flow control, and inherent four quadrant operation ability. On the other hand, in variable speed PMSG based wind energy systems, the diode rectifier based unidirectional converters and the back-to-back IGBT based two-level VSCs are the most popular topologies among others and are increasingly favored by the wind power industries [20]. The back-to-back VSCs used in the PMSG based wind energy system minimize the electromagnetic torque ripples for the generator, improves the power controllability, enhances the power quality by reducing the current harmonics and also aids to the FRT capability of the wind energy system [3]. The technology trends of power electronics used for WT applications and the potential converter topologies are addressed in [14, 21].

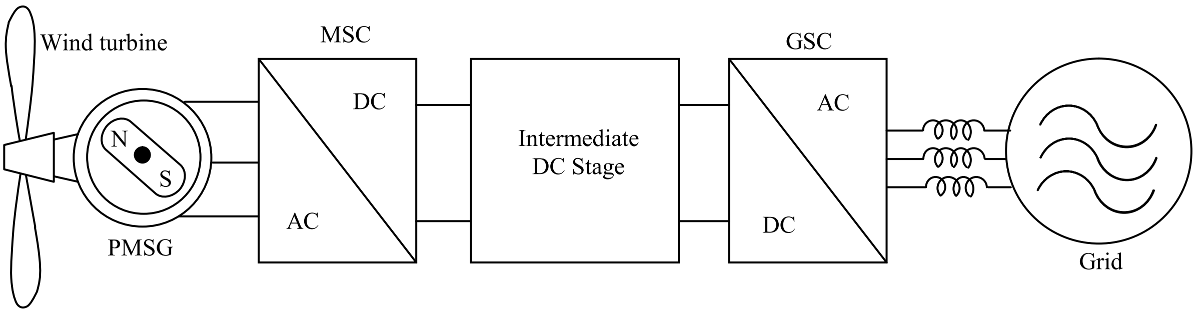

Figure 1.6. A typical configuration of PMSG based wind energy system.

1.3.1. Diode rectifier based topology

A small scale wind energy system scheme usually consists of a PMSG, a diode bridge rectifier based topology employing six diodes, a DC/DC boost converter (typically a DC chopper) and a grid-side inverter as shown in Figure 1.7 An uncontrolled diode rectifier cascaded by DC/DC boost converter is used as MSC to save cost. The variable–magnitude, variable–frequency AC power from the WT generator is firstly converted to a DC power by means of a diode rectifier circuit, and then is converted back to an AC power at desired frequency and voltage level by means of a grid-side controlled inverter.

The DC/DC boost converter utilized on the DC-side has two advantages; firstly, the ease in maximum power point tracking (MPPT), and secondly, the improved flexibility in GSC control. The control of a variable speed PMSG by a diode rectifier cascaded by a DC/DC boost converter is proposed in [22]. Though, this system is of low cost and simple in construction, it lacks control capability over the generator power factor thereby, reduction in the generator efficiency. Serious stator harmonic current distortions in the generator windings further degrade the efficiency; reduce the life span and lead to the significant electromagnetic torque ripple. Theoretical analysis in [23] suggests that the DC-link capacitor (which is normally used to smooth the rectified voltage between the rectifier and the DC/DC boost converter), should be removed to increase circuit impedance and suppress harmonic current for smoothing DC-side current, thereby reducing torque ripple. A variable structure controller is designed in [24] eliminating the

DC/DC boost converter. On occurrence of the grid fault, such a controller varies the generator-side power control from the maximum power point tracking (MPPT) to the reduced power output.

A novel rectifier topology with two three-phase diode bridges and three thyristors are proposed in [19] which provide a cost effective solution for MSC in high power variable speed PMSG based wind energy systems. Several power semiconductor manufacturers such as ABB, Mitsubishi Electric and Semikron produce components in a module form suitable for diode rectifier based converter topology [21].

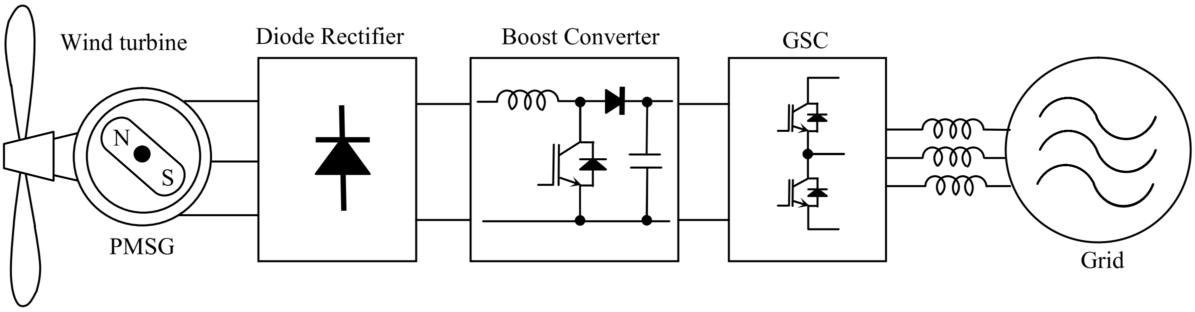

Figure 1.7. Diode rectifier based topology for PMSG based wind energy system.

1.3.2. Two-level back-to-back PWM converter topology

This topology differs from the diode rectifier based topology for the rectification stage, where the diode rectifier cascaded by DC/DC boost converter is replaced by a pulse width modulated (PWM) converter.

As shown in Figure 1.8, a full scale back-to-back converter consisting of a PWM rectifier, an intermediate DC-link capacitor and a PWM inverter is used to connect PMSG to the power grid. The PWM converter (used at the machine-side to control current) reduces the input current harmonics and results in a ripple free electromagnetic torque. Such a configuration allows the MSC to completely regulate the generator in terms of speed, power factor, and electromagnetic torque whilst the GSC to regulate the power flow to the grid in order to keep the DC-link capacitor voltage constant and to improve the output power quality by reducing the total harmonic distortion (THD).

Besides affording some protection, a technical advantage of two-level back-to-back converter topology is the simpler configuration, robust and reliable performance and capacitor decoupling between the MSC and GSC which allows the compensation of asymmetry both on the machine-side and on the grid-side through independent control of the two converters.

Since back-to-back PWM converter topology consists of two converters, the switching losses in such topology might be even more pronounced and may also require extra electromagnetic interference (EMI)-filters.

Further, this configuration requires more fully controlled switches; consequently, the system may not only suffer from larger switching losses and lower efficiency but also becomes more expensive, particularly for MW level applications. Several power semiconductor manufacturers such as ABB, Hitachi, Mitsubishi Electric, Semikron and Siemens produce components in a module form suitable for two-level back-to-back converter topology [21].

Gamesa adopted a multi-cell solution for 4.5MW WTs, which has several two-level back-to-back converters paralleled both on the machine and grid sides [25].

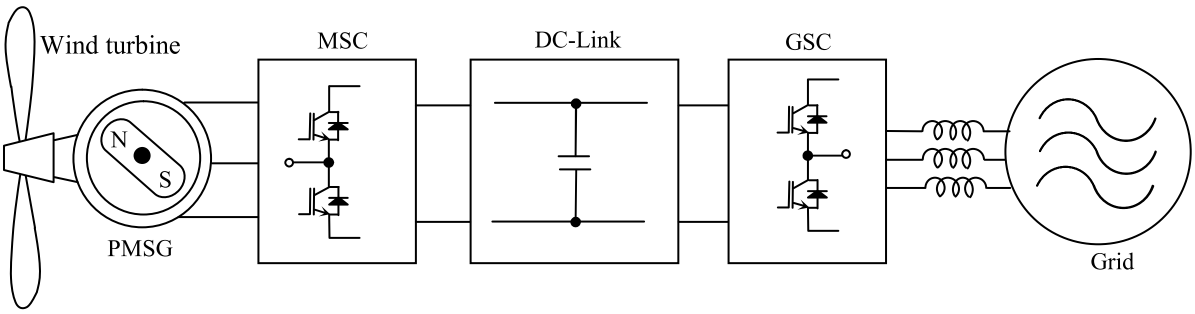

Figure 1.8. Two-level back-to-back VSC based topology for PMSG based wind energy system.

1.3.3. Z-source inverter based topology

The Z-source inverters, facilitating voltage boost capability with the turning “ON” of both switches in the same inverter phase-leg (i.e. shoot-through state); have recently been reported as a competitive alternative to existing inverter topologies [26].

The Z-source inverter overcomes the limitations of the traditional voltage source and current source inverters [21]. Recently, the application of Z-source inverter in wind energy systems is addressed by several researchers [27, 28].

A PMSG based wind energy system with Z-source inverter is proposed in [29] where characteristics of Z-source inverter are utilized for maximum power point tracking (MPPT) and power delivery to the grid.

A robust and reliable grid connected wind energy system, employing a combination of a generator-side three-switch buck-type rectifier and a grid-side Z-source inverter as a bridge between the PMSG and the power-grid, is proposed in [30]. The system operation reliability is improved as a result of no shoot-through risk in both MSC and GSC.

To overcome the drawbacks of the Z-source inverter, an improvement in the same is proposed in [31]. It is worth noticeable that the Z-source inverter based topology offers lower efficiency and requires two capacitors and two inductors [32]. A typical configuration of such topology is illustrated in Figure 1.9.

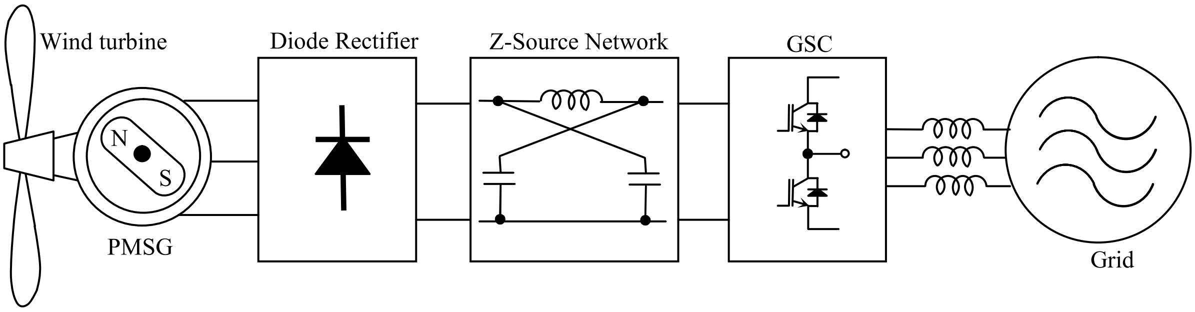

Figure 1.9. Z-source inverter based topology for PMSG based wind energy system.

1.3.4. Multi-level converter topology

For large WT applications, the multi-level converters are also becoming very attractive. The basic idea behind the multi-level converter topology is to produce a sinusoidal voltage waveform from several levels of voltages so as to achieve higher voltage capability of the converter topology. A typical configuration of such topology is shown in Figure 1.10. The neutral-point-clamped (NPC), flying capacitor (FC), and cascaded H-bridge (CHB) converters are the most well known topologies among various multi-level converters commonly practiced in high power and medium / high voltage applications [21,33]. Based on the performance, complexity and cost, the overall comparison among these multi-level converter topologies can be found in [15.34]. When compared with the two-level VSCs, the multi-level converters can handle higher voltages by enabling the use of a series of lower-voltage rating solid-state switching devices and provide better waveform quality of the converter output voltage and current [35]. The features of multi-level converters include lower harmonic distortion of output voltage, lower switching losses and reduced EMI; though the conduction losses are higher since the number of semiconductor devices in the conducting path is higher than that of the other converter topology. The voltage imbalance across the capacitors, and control complexity are another disadvantages of multi-level converter topology.

The three-level neutral-point-clamped (3L-NPC) topology, usually configured as a back-to-back structure, is one of the most commercialized multi-level converter topologies for the WT applications [36]. To improve the operation of back-to-back NPC converter during steady-state and transient system operating conditions, an advanced control scheme is proposed in [37]. The problem of mid-point DC-link voltage fluctuation in three-level back-to-back NPC is researched in [38] and it is considered to be improved by the controlling of redundant switching states. However, the problem of unequal loss distribution between the outer and inner switching devices in a switching arm might lead to a de-rated power capacity during practical use of the converter [36]. With the aim to improve the waveform quality of the converter output voltage and current, a new nine-level active neutral-point-clamped (9L-ANPC) converter is proposed in [33] as a grid interface of large WTs. A recently investigated topology considers a three-level unidirectional Vienna rectifier (an alternative to be used as MSC of a PMSG based wind energy system), which has several advantages compared to the conventional two-level VSCs, such as low manufacturing cost due to use of only three active switches, high frequency operation, improved voltage and current THDs and high efficiency [32,39].

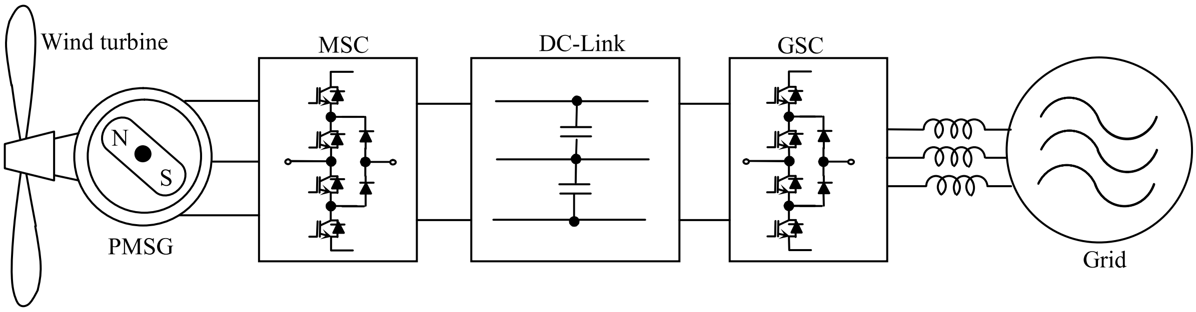

Figure 1.10. Multi-level converter based topology for PMSG based wind energy system.

1.3.5. Matrix converter topology

Unlike conventional two-level back-to-back converter which requires 12 active switches and a DC-link capacitor so as to make the control of the MSC and GSC completely independent; a matrix converter includes 6 additional active switches, requires no bulky and costly energy storage element and controls the generator-and grid-side quantities simultaneously. The output of the matrix converter is synthesized by selective closings and openings of the bidirectional switches positioned at the intersection points of the input and output phases. A matrix converter based topology for PMSG based wind energy system is illustrated in Figure 1.11 The superior benefits of matrix converter such as direct single-stage AC/AC operation, controllable input power factor and high reliability make it a good alternative to the back-to-back converter. Compared to the other converter topologies with constant DC-link capacitor voltage, the output harmonic content and switching losses of the matrix converter are lower [40]. On the other hand, complicated modulation, buck operation of matrix converter (maximum output voltage of the matrix converter is 0.866 times the input voltage without entering the over-modulation range), four step switching process of bidirectional switches, requirement of large number of switches, high manufacturing cost and no decoupling between the input and output are some of the drawbacks of matrix converter. Further, the output current of the matrix converter is required to be 1.15 times higher so as to achieve the same output power as of the back-to-back PWM voltage source converter topology, which results in higher conduction losses as well [40]. Recently, matrix converter has attracted considerable interest for wind power applications [41, 42]. The application of matrix converter in wind power system is presented in many literatures [43, 44]. For instance, a matrix converter is implemented in [45] to control the reactive power of permanent magnet synchronous wind generator. Optimum control of matrix converter based wind energy system is proposed in [44] for performance enhancement and efficiency optimization. It is worth noticeable that the hybrid operation of the renewable energy sources becomes complicated due to the lack of DC-link in matrix converter topology.

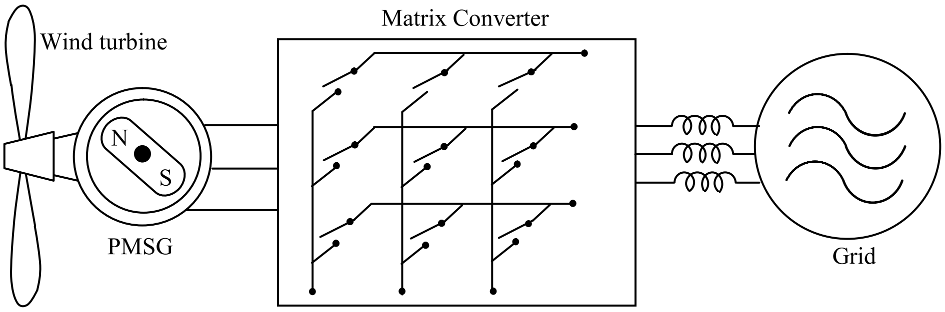

Figure 1.11. Matrix converter based topology for PMSG based WECS.

1.3.6. Nine-switch AC/AC converter topology

This converter topology was used in [46] as an AC/AC converter to deliver the power generated by the PMSG to the power grid. With this converter topology, three active switches and three diodes in a two-level back-to-back converter are omitted without any change in the objective of the wind energy system as shown in Figure 1.12 This new topology, features sinusoidal inputs and outputs, unity input power factor, and offers cost advantage compared to the conventional back-to-back converter topology. The constant frequency (CF) mode of nine-switch AC/AC converter operation (where only magnitude of the inverter output voltage is adjustable but output frequency remains the same as supply frequency) can be applied to UPS applications, whereas the variable frequency (VF) mode of converter operation (where both magnitude and frequency of the inverter output voltage are adjustable) can be applied to variable speed drive applications [47]. However, the semiconductor loss analysis performed in [47] reveals that the nine-switch AC/AC converter while working in CF mode has an overall higher efficiency than the two-level back-to-back converter at the cost of uneven loss distribution. On the other hand, the VF mode of operation requires higher ratings IGBT devices which results in considerably higher losses [47], and therefore, is not preferred. The comparison of mainstream power converter topologies used for

PMSG based wind energy Systems are presented in Table 1.1 with a clear focus to their features and limitations.

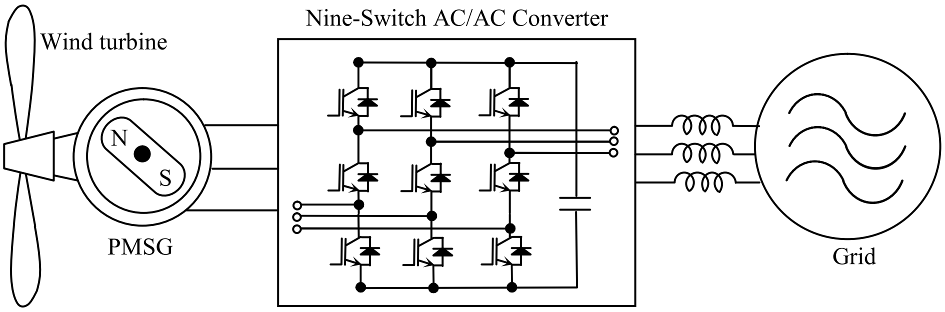

Figure 1.12. Nine-switch AC/AC converter based topology for PMSG based wind energy system.

Table 1.1

Comparison of mainstream power converter topologies.

Sr	Converter topology Features	Diode rectifier	2L-B2B VSC	ZSI	Multi-level converter	Matrix Converter	Nine-switch ac/ac converte
1.	Requirement of fully controlled switches	None	Less	Less	Large	Large	Least
2.	Circuit configuration	Simple	Simple	Simple	More complex	Complex	Simple
3.	Cost	Very low	Moderate	High	Very high	High	Low
4.	Requirement of dc link capacitor	Yes	Yes	Yes	Yes	No	Yes
5.	Control complexity	Easy	Moderate	Moderate	Most complex	More complex	Complex
6.	Operational stages	Two	Two	Two	Two	One	One
7.	Waveform quality	Good	Better	Better	Best	Better	Depends
8.	Harmonic distortion	High	Moderate	Low	Least	Low	Depends
9.	Switching losses	None	High	High	Low	Low	High
10.	Conduction losses	Low	Low	Low	Highest	High	Low
11.	Reliability	High	Low	High	Low	High	Low
12.	Bi-directional power flow	No	Yes	Yes	Yes	Yes	Yes
13.	Hybrid operation of renewable sources	Possible	Possible	Possible	Possible	Not Possible	Possible

1.4. Control Strategies Used in PMSG Based Wind Energy Systems

The incorporation of advanced control systems into wind energy system is one of the major technological advances together with improvements in materials, power electronics and blade designs [48]. In many studies, the researchers have attempted to develop a variety of control strategies for PMSG based wind energy system so as to come up with such a system which is simple, reliable, robust, and has the ability to handle intolerable disturbances those might occur during its operation. Different control issues in small PMSG based wind energy system were surveyed in [49].

1.4.1. Pitch angle control

The pitch angle control is a mechanical way of controlling the rotor blade angle of the WT so as to regulate the output power of the same. Most of the major WT manufacturers are now developing new MW scale VSWTs based on PMSGs with pitch angle control so as to protect the WT from over power and over torque conditions due to sudden wind gusts at higher wind speeds. The pitch angle is usually fixed at lower wind speeds. On the contrary, at high wind speeds, the pitch angle control is activated to shed off the aerodynamic power by turning the rotor blades through some angle from the direction of striking wind [50]. In accordance with the variation of wind speed, strategies for turbine pitch angle control and rotational velocity control are developed in [51]. Neural network and fuzzy logic control are employed in [52] to improve the performance. Pitch angle control may become complicated due to the nonlinear aerodynamic characteristics of the WT [53]. In view to that, a simple and robust pitch control technique, which can tolerate turbine parameter uncertainties and non-parametric perturbations, is reported in [53, 54].

1.4.2. Control of machine (generator)-side (MSC)/grid-side (GSC) converters

Two most dominant strategies classified under vector control. Field oriented control (FOC), and direct torque control (DTC) are used at the machine-side and have almost similar dynamic responses. The FOC is one of the most established strategies for generator speed control which involves dual loop control structure - an outer speed control loop and an inner current control loop usually based either on hysteresis control in natural reference frame or on PI control in synchronous reference frame. In FOC, the electromagnetic torque is controlled through q-axis component of the stator current and the d-axis stator current is forced to be zero so as to get the maximum electromagnetic torque with minimum stator current. Since, the current is controlled directly; the line currents of the machine contain low harmonics which in turn leads to high efficiency. An FOC strategy with hysteresis current control applied to the MSC is illustrated in Figure 1.13.

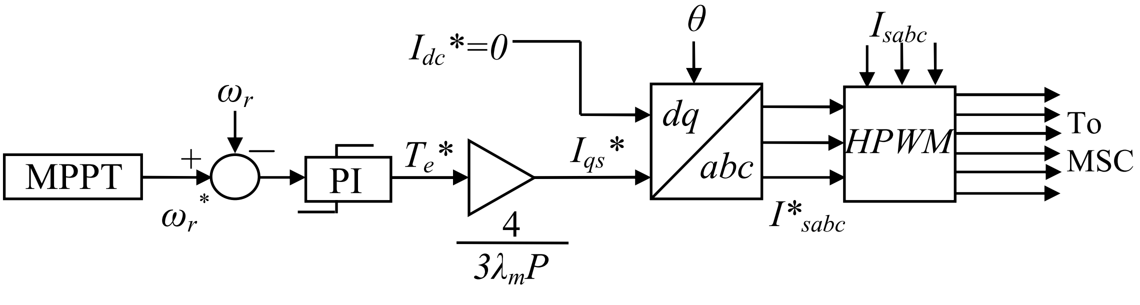

Figure 1.13. MSC control strategies – FOC.

On the contrary, the core of the DTC scheme comprises two hysteresis comparators and a switching table (ST) as shown in Figure 1.14, and this strategy is of interest, particularly for low power WT generator control [32, 55].

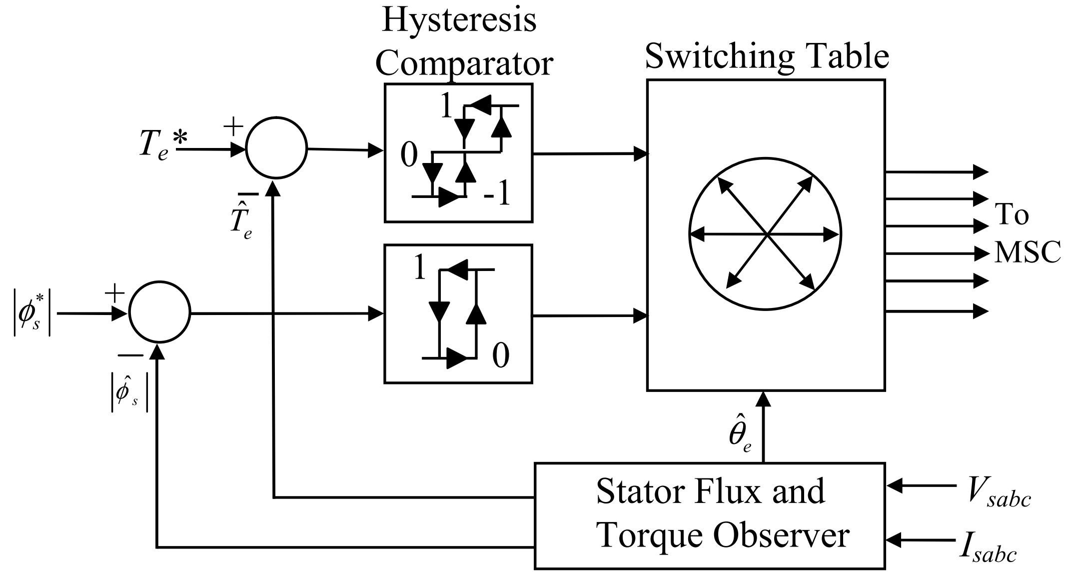

Figure 1.14. MSC control strategies – DTC.

In a DTC strategy, the stator flux and the electromagnetic torque are controlled directly and independently. Both methods have their own advantages and drawbacks. For instance, insensitivity to machine parameter variation, elimination of rotor position sensor, no current regulation loop, faster torque response, and reduced computation time are the various advantages; whereas high ripples in torque, flux and current; the variation in switching frequency with load torque and rotor speed; and two hysteresis comparators' bandwidth are some of the disadvantages of DTC compared to FOC [55]. However, both of these strategies allow torque and flux to be decoupled for independent control of the active and reactive powers handled by the generator. The irregular torque, flux and current ripples in a ST-DTC cause overstress on the turbine shaft, reduce the turbine life span and produce much acoustic noise. To solve the problems associated with ST-DTC, an effective approach is to integrate space vector modulation (SVM) into the DTC [56]. On the other hand, the GSC typically controls the DC-link voltage to balance the input and output powers and enables the grid to always absorb/supply a balanced set of fundamental current at unity power factor by providing parts of reactive power to the nonlinear loads connected at the point of common coupling (PCC) [57, 58]. Following the idea similar to that of the FOC, a voltage oriented control (VOC) strategy for the GSC involves dual-loop control structure -an outer DC-link voltage control loop and an inner current control loop based either on hysteresis control in natural reference frame or on PI control in synchronous reference frame and decouples instantaneously the d-and q-axes components of the injected current [59]. In VOC, a unity power factor operation can be achieved when q-axis current reference is set to zero. The VOC strategy guarantees fast transient response, high steady-state performance, good power quality and the minimum power ripple by means of internal current control loop [60, 61]. However, the cross-couplings between active and reactive components and requirement of reference frame transformation are some of the disadvantages of VOC [61]. A VOC strategy with PI based current control applied to the GSC is illustrated in Figure 1.15.

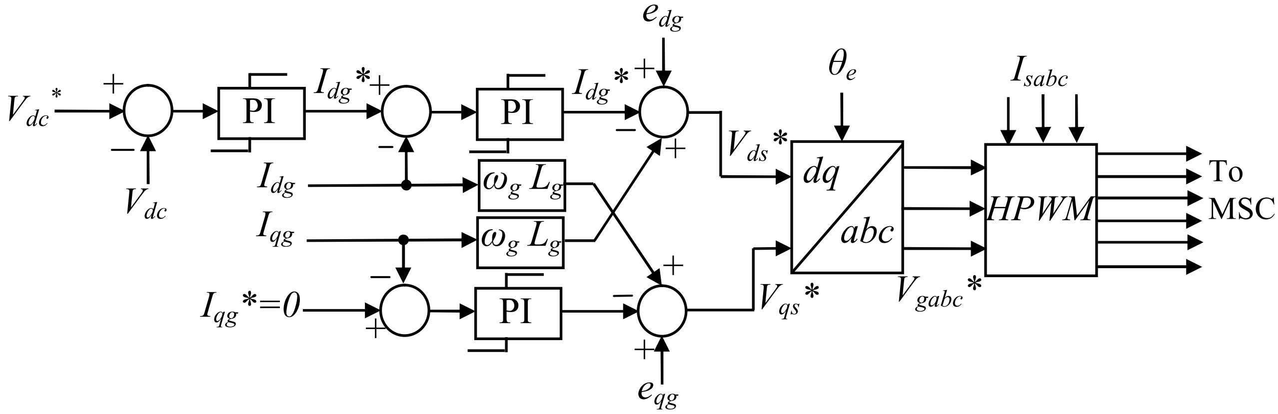

Figure 1.15. GSC control strategies - VOC.

In contrast, as shown in Figure 1.16, instantaneous active and reactive powers are two control variables in the direct power control (DPC) strategy for GSC which follows the idea similar to that of the DTC. There are no inner current control loop and no PWM modulator block.

A switching table (ST) is used to determine the switching states instead.

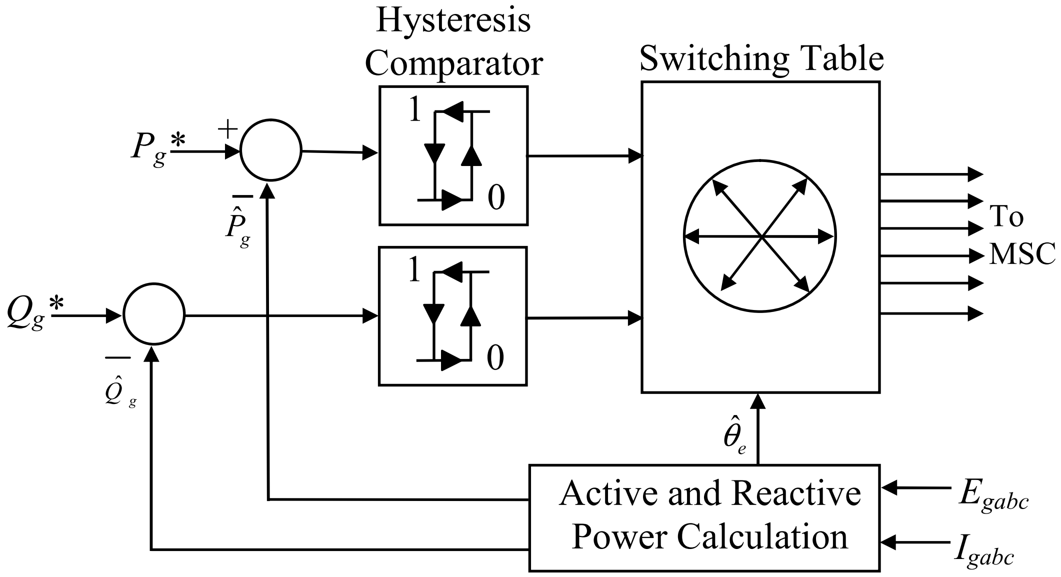

Figure 1.16. GSC control strategies - DPC.

In DPC, a unity power factor operation can be achieved when reactive power reference is set to zero. The DPC owns the advantages such as simple implementation, no coordinate transformation, no cross-coupling effect between the active and reactive powers, fast dynamic response, reduced computation time and high robustness to parameter variations; whereas, large THD with high power and current ripples are the major shortcomings of the DPC [60, 62].

Further, the DPC needs not only high sampling frequency due to fast changing estimated values of active and reactive powers but also high filter inductance because of the variable switching frequency [61]. The problem arising due to power and current ripples in a ST-DPC can be overcome by integrating a space vector modulation (SVM) into the DPC which leads to constant switching frequency and low THD [60]. The dynamics of SVM-DPC still depends on the merit of design of involved PI controller [63].

Nevertheless, the studies on DPC strategy for control of GSC of PMSG based wind energy system reported in the literature are a few. To establish an optimized control scheme for the machine-side three-switch buck-type rectifier; two PMSG control strategies, namely unity power factor control and rotor flux orientation control, are considered in [30].

The flux and torque ripple are reduced in the DTC scheme proposed in [64] using a fixed and low switching frequency. Further, for DC-link voltage control of a PMSG based wind energy system, a feedback linearization technique is reported in [65]. The work presented in [65] was extended in [66] which comprise experimental results as well. Ref. [60] present comparative analyses of a PMSG based wind energy system employing FOC and DTC control strategies for the MSC together with VOC and DPC control strategies for the GSC. A novel direct current vector control technology has recently been developed for control of the synchronous generator only in a variable speed wind energy system [67].

Using the conventional and direct current vector control configuration, the MSC and GSC control structures for a PMSG based wind energy system are designed in [68] so as to realize the MPPT, DC-link voltage regulation, reactive power control, and grid voltage support. While comparing, the direct current vector control has demonstrated many advantages over conventional vector control strategies such as enhanced system stability, reliability and efficiency, minimal DC-link voltage fluctuations and strong fault ride-through capability [68].

Conventionally, the MSC controls the flow of power produced by the generator while the GSC controls the DC-link voltage to balance the input and output powers in PMSG based wind energy Systems. However, in preference to the GSC, a few research works presented the MSC for DC-link voltage control [66, 69]. When control roles of the MSC and GSC are exchanged with each other, the DC-link voltage can be controlled to be constant particularly in the event of grid voltage sags by increasing the generator speed [66].

A scheme using the MSC for DC-link voltage control is investigated in [70] during normal and fault conditions. However, the control scheme is subject to certain limitations implied by the power–speed characteristic of the WT and requires to be further investigated in full range of turbine's operation. For the MW class PMSG based wind energy system operating under different grid conditions, a unified power control strategy necessitating no system parameters is proposed in [71] in which the MSC and GSC are responsible for the DC-link voltage control and the power flow control to the grid, respectively. The comparison of various control strategies used for MSC and GSC of PMSG based wind energy systems are presented in Tables 1.2 and 1.3, respectively emphasizing the major considerable aspects.

Table. 1.2

Comparison of MSC control strategies of PMSG.

Sr	Control strategy features	FOC	DTC	DCVC
1.	Rotor position sensor requirement	Yes	No	Yes
2.	Implementation	Complex	Simple	More complex
3.	Control at very low speed	Easy	Difficult	Easy
4.	Internal current control loop	Yes	No	Yes
5.	Requirement of coordinate transformation	Yes	No	Yes
6.	Computation time	More	Less	More
7.	Switching table requirement	No	Yes	No
8.	Modulation technique	PWM/hysteresis	Hysteresis	PWM
9.	Switching frequency	Fixed/variable	Variable	Fixed
10.	Cross-coupling effect	Yes	No	Yes
11.	Parameter sensitivity	Yes	Insensitive	Sensitive
12.	Dynamic response			
	Rise time	High	Low	Moderate
	Overshoot	Large	Small	Moderate
	Settling time	High	Low	Moderate
13.	Tracking error	Low	High	Low
14.	Torque ripple	Low	High	Very low
15.	Power/current ripple	Low	High	Very low
16.	Current THD	Low	High	Very low
17.	Power quality	Better	Poor	Best

Table. 1.3

Comparison of GSC control strategies of PMSG.

Sr	Control strategy features	FOC	DTC	DCVC
1.	Implementation	Complex	Simple	More complex
2.	Internal current control loop	Yes	No	Yes
3.	Requirement of coordinate transformation	Yes	No	Yes
4.	Computation time	More	Less	More
5.	Switching table requirement	No	Yes	No
6.	Modulation technique	PWM/hysteresis	Hysteresis	PWM
7.	Switching frequency	Fixed/variable	Variable	Fixed
8.	Cross-coupling effect	Yes	No	Yes
9.	Parameter sensitivity	Sensitive	Insensitive	Sensitive
10.	Dynamic response			
	Rise time	High	Low	Moderate
	Overshoot	Large	Small	Moderate
	Settling time	High	Low	Moderate
11.	Tracking error	Low	High	Low
12.	Voltage ripple in dc Link	Low	High	Very low
13.	Power/current ripple	Low	High	Very low
14.	Current THD	Low	High	Very low
15.	Power quality	Better	Poor	Best

1.5. Maximum power point tracking (MPPT)

Corresponding to each wind speed, there is a specific generator peed which yields the maximum possible wind power. Beyond this specific generator speed, the power extracted from the wind subsequently reduces [71]. Operating WT in variable speed mode, optimum energy extraction from the wind can be achieved. For the reason, many different MPPT control strategies such as optimum relationship-based (ORB) control, tip-speed ratio (TSR) control, optimal torque control (OTC), and perturb and observe (P&O)/ hill-climb search (HCS) control have been developed during the last few decades [72, 73, 74, 75]. Comparative studies of several MPPT methods are performed in [76]. A brief description of several MPPT methods used for PMSG based wind energy systems are presented in the following sub-sections, and their comparison is presented in Table 1.4.

Table. 1.4
Comparison of MPPT methods of PMSG.

Sr	MPPT algorithm features	ORB	TSR	OTC	HCS	Sensorless
1.	Requirement of wind speed sensor	No	Yes	No	No	No
2.	Requirement of shaft speed sensor	Depends	No	Yes	No	No
3.	Look-up table requirement	Yes	No	Depends	No	No
4.	Requirement of system pre-knowledge	Yes	Yes	Yes	No	No
5.	Memory requirement	Yes	No	Depends	No	Yes
6.	Complexity	Less	Least	Less	Moderate	High
7.	Cost	High	Very high	Moderate	Low	Low
8.	Convergence speed	Fast	Very fast	Fast	Moderate	Moderate
9.	Oscillation at MPP	No	No	No	Yes	Depends
10.	MPPT efficiency	High	Highest	High	Low	Moderate
11.	Reprogramming with variation in pitch angle	Yes	No	Yes	No	Yes
12.	Performance under rapid wind condition	Good	Very good	Very good Yes	Poor	Good
13.	Parameter sensitivity	Yes	No	No	No	No
14.	Online updating	No	No		Yes	Depends

1.5.1. Optimum relationship-based (ORB) control

The ORB control is a mature MPPT strategy in which wind speed measurement is not required and the response to wind speed change is fast. ORB control ensures MPPT using a pre-calculated look-up table which is structured with the aid of knowledge of optimum relationships among various system parameters; for instance, the power versus shaft speed [77], the power versus torque [78], the power versus rectified DC-link voltage [74] and the DC-link voltage and DC-side current [58]. The ORB control is simple to implement, has good dynamic response, requires no wind speed sensor, can produce smoother output power when compared with the other strategies and is widely used in commercial wind energy systems. The main drawback of ORB control is that system pre-knowledge is a requisite, which varies from one system to the other and may even change with the system aging. Furthermore, ORB control may require lots of memory space.

A schematic of ORB control exploiting the optimal power versus shaft speed curve for MPPT is illustrated in Figure 1.17.

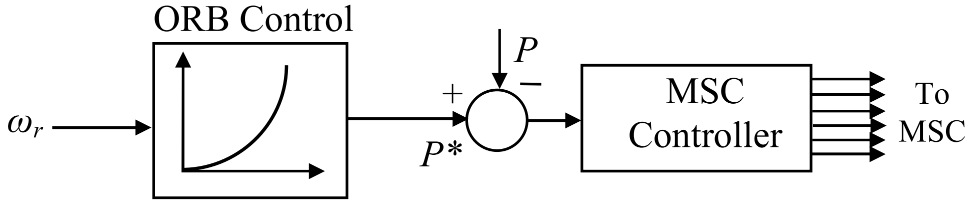

Figure 1.17. MPPT control algorithms - ORB.

1.5.2. Tip-speed ratio (TSR) control

Power efficiency maximization is one of the prime control objectives of the variable speed wind energy systems. At a given wind speed, the efficiency is drastically affected by the TSR, which is defined as the ratio of the rotor speed of the tip of a blade to the actual wind speed. By maintaining the turbine's TSR at its optimum value despite wind variations, the maximum energy conversion efficiency is achieved.

The wind speed is estimated/measured using an anemometer and a reference rotor speed corresponding to the MPP is generated using (1.9) as shown in Figure 1.18.

$$\omega_r^* = \frac{\lambda_{opt} . V_w}{R} \tag{1.9}$$

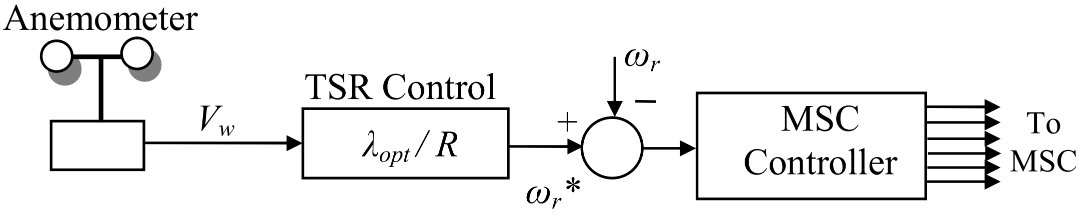

Figure 1.18. - MPPT control algorithms TSR.

It is obvious that the TSR control is a simple MPPT strategy but extremely reliant on the accuracy of the wind speed estimation or measurement using an anemometer which adds to the system cost. The simulation results presented in [79] show that the TSR control might cause severe power fluctuations in the generator power which can be mitigated using a modified TSR control algorithm with filter strategy. The TSR strategy is rarely used in real applications due to the dependence on the wind speed sensor and the fluctuations in the output power. Moreover, optimal value of TSR differs from one system to another and can be determined theoretically of experimentally.

1.5.2. Optimal torque control (OTC)

Without wind speed measurements, the objective of maximum conversion efficiency can be achieved by producing an optimum torque reference using (1.10) that relies only on few turbine parameters and on a simple measurement of the angular shaft speed as illustrated in Figure 1.19.

$$T_e^* = \left[\frac{0.5.\rho.C_{p\_\max}.\pi.R^5}{\lambda_{opt}^3} \right] \times \omega_r^2 \tag{1.10}$$

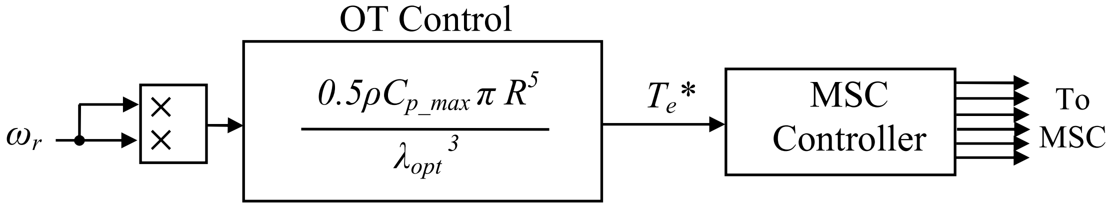

Figure 1.19. MPPT control algorithms - OTC.

The underlying principle is to adjust the electromagnetic torque of the PMSG in accordance with an experimentally obtained optimal reference torque curve or look-up table. OTC is an indirect strategy, in which the active power is regulated through the closed-loop control of the generator torque. However, this indirect strategy can hardly be extended to the situations with other output power requirements as a consequence of the nonlinear relationship in between the extracted wind power and the generator torque. It is interesting to examine the simulation results of [79] which verify that the OTC has a similar generator power fluctuations reduction performance as the modified TSR control with filter strategy has. Although OTC is extensively employed in wind energy systems owing to its simplicity, quick response and efficiency, it entails the information about air density and WT parameters which differ from system to system. Further, the experimentally obtained optimal reference torque curve might deviate with the system aging which, in turn, affects the MPPT efficiency. In addition, the efficiency of OTC is lower compared to that of the TSR control in view of the fact that wind speed changes are not reflected instantaneously on the reference signal [80].

1.5.2. Perturb & observe (P&O)/Hill-climb search (HCS) control

The conventional P&O/HCS control eliminates the necessity of speed sensors or estimators, and is a simple control concept based on perturbing a control variable in small step-size and observing the resulting changes in the target variable until the MPP is reached. Prior information of the WT parameters as well as wind speed measurements are also not required for the P&O algorithm to work, making this MPPT method less complex, flexible, less costly and more reliable.The schematic of P&O control is illustrated in Figure 1.20.

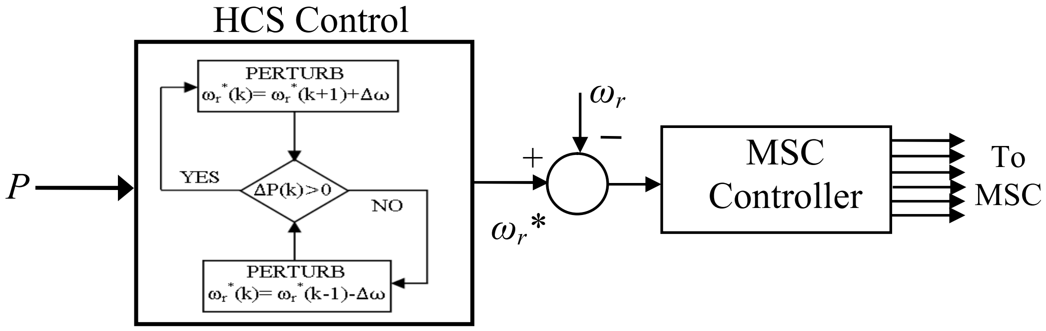

Figure 1.20. MPPT control algorithms - HCS.

The P&O algorithm monitors the output electrical power variations of generator and in relation to the result of comparison between successive generator output power measurements; it adjusts the generator speed towards MPP. The concept of P&O control is demonstrated in Figure 1.21.

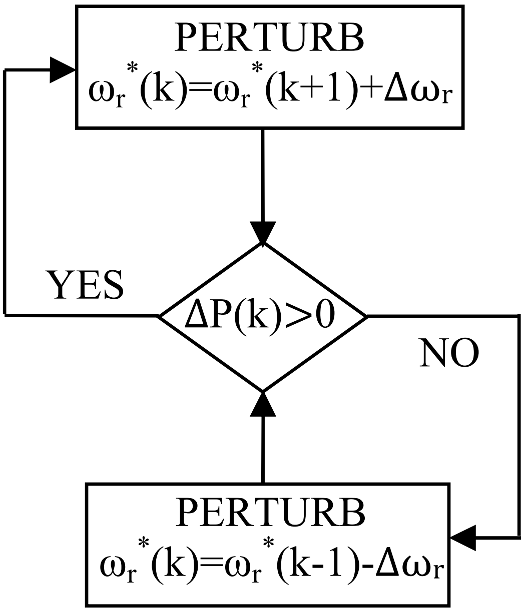

Figure. 1.21. Concept of P&O/HCS control.

In P&O control, a large step size results in a rapid tracking of MPP but inevitable oscillations occur around the MPP; whereas, a small step size results in the improvement in the MPP accuracy but reduces the speed of convergence. Further, a highly fluctuating wind speed condition always results in the MPP search in a wrong direction. Thus, there are two serious problems associated with P&O control namely, speed efficiency tradeoffs, and the wrong directionality, which significantly deteriorate its performance under rapid change in wind speed. In view to the speed efficiency trade-off problem, a variable-step HCS governed by the magnitude of the derivative of power with respect to the duty ratio of the MPPT converter is proposed in [81]. However, such variable-step scheme is impractical under fluctuating environmental conditions. A formula for the optimal perturbation step-size is proposed in [82] focusing on the solution to the issue of wrong directionality. However, the solution requires the knowledge of various system parameters and becomes rather complicated. A novel solution to these problems is also proposed in [83] which not only solves the tracking speed versus control efficiency trade-off but also ensures the MPP search in the correct direction during fluctuating wind speeds. Mostly, the power-speed relation of the WT is used as control input for P&O MPPT. However, to reduce the system cost, and to increase reliability by eliminating the need for shaft speed sensing, the use of other wind energy system parameters as control inputs has also been explored recently; for instance, the DC-link voltage and the duty cycle [84]. Based on the P&O technique, an online training method for MPPT has been proposed in [72]. After the training process, a look-up table containing reference currents of different wind speeds is populated and is directly applied to the MPPT control. However, it is time-consuming to train the system over the entire wind speed working range. For the reason that the response to wind speed change is extremely slow, especially for large inertia WTs, mostly P&O control is realized in small scale wind energy systems [72]. An advanced P&O control has been proposed in [72] for wind energy systems with different turbine inertia. A new MPPT technique combining perturb & observe (P&O) and ORB control for PMSG wind energy system is proposed in [85] in which the system's pre-knowledge is not a requisite.

1.6. Sensorless control

Accurate wind speed measurement is not so easy especially in case of large sized WTs. The anemometer, usually installed on top of nacelle of large sized WTs, offers wind speed measurement only at the hub height; therefore, the wind speed measured by the anemometer may not be the one intercepted by the WT. Thus, large numbers of researches are made to develop wind speed sensorless MPPT control algorithms. On the other hand, the PMSG based wind energy systems implement MPPT control algorithms with an instantaneous speed or torque control reference for different wind speed conditions using a generator-speed sensor. The problems associated with the use of mechanical speed sensors such as extra hardware cost, hardware complexity and increased failure rate can be resolved by adopting optimal position/speed sensorless control strategies; a variety of which have been reported for wind energy systems with different power electronic converters [86]. Because of the intermittent nature of wind power, the operating conditions of a wind energy system always vary from time to time. The requirement of sensorless control design for the direct-drive PMSG based wind energy systems in an attempt to achieve satisfactory steady-state and dynamic speed estimation/rotor position precision over the entire speed range, in most cases, cannot be met by a single sensorless control method and, therefore, for different operating conditions the sensorless control methods may be different. Several speed-estimating algorithms based on motional electro-motive force (EMF), flux-linkage variation, and Kalman filter have also been introduced in the past so as to alleviate the need of mechanical sensors [4]. However, most of these algorithms involve simplified computations based on several assumptions and ignorance of parameter variations. In addition, inaccuracy may arise with low-voltage signal measurement at lower speed, especially in case of directly-driven PMSGs. Consequently, the precise estimation of rotor position and speed is very difficult. Further, without pre-knowledge of the WT characteristics and wind speed, a universal MPPT control algorithm based on fuzzy-logic has been proved to be very effective [87]. For optimum rotor speed control, a fuzzy logic controller (FLC) is used in [88] which does not involve detailed mathematical model or linearization about an operating point, and is insensitive to system parameters' variation. An ANFIS based speed and position estimation of PMSG is presented in [4] which are essentially required to operate the system at MPP. Nevertheless, the performance of a sensorless control design for a grid connected wind energy system should also be investigated under abnormal or grid fault conditions [5]. A detailed study on position/speed sensorless control for PMSG based wind energy system has been performed in [5].

1.7. Grid interconnection requirements

Wind is a free and abundant source of energy and hence, is attractive in terms of the cost, and energy security. However, wind is intermittent in nature and due to wind speed variations, the output power of WT fluctuates which may cause grid-frequency deviations. This is one of the major technical problems of wind energy systems. Further, the increased penetration of WTs into the power system has a large impact on power-grid stability and has, therefore, led to serious concern about its influence. Here, the attention in the grid interconnection requirements is drawn mainly to the output power smoothing and reactive power control in addition to fault-ride-through (FRT) and grid support capabilities in PMSG based wind energy systems as follows:

1.7.1. Output power smoothing and reactive power control

In a grid integrated wind energy system, the power fluctuations lead to large ratings of installed electrical components, poor power quality and high losses. The primary control objective of the variable speed WTs is not only the maximization of power efficiency but also enhanced dynamic characteristics so as to reduce output power fluctuations. The blade pitch angle control, which can be viewed as a method for output power smoothing, not only suffers from the short comings of high mechanical stress on the WT system but also the power captured by the WT is not optimal.

Energy storage systems (ESSs) might be another good solution to the power smoothing problems [89]. The variable speed WT inertia is used in a method presented in [90] for output power smoothing of a PMSG based wind energy system. However, the large variations in wind speed may lead the system into unstable operating regions. For a PMSG based wind energy system with Z-source inverter; two active power control methods; firstly, the capacitor voltage control and secondly, the DC-link voltage control, are reported in [29] to address the problem of power fluctuation. When compared to the DC-link voltage control; the capacitor voltage control method results in less power fluctuations.

A simple coordinated control of pitch angle, and the DC-link voltage is reported in [10] for stable output power smoothing of a wind energy system based on PMSG. A high-order sliding-mode controller is designed in [91] for power control of the PMSG based wind energy system. Even though active power, in general, is supposed to be very important; reactive power is equally important and is responsible for system's voltage stability.

For voltage stability at the point of common coupling (PCC), the conventional wind energy systems usually employ custom power devices like active power filters (APFs), static compensators (STATCOMs), and static VAR compensators [92]. The additional hardware cost for these custom power devices can be saved if the GSC, in addition to its normal task, is utilized for solving power quality problems at PCC [4]. The GSC of a PMSG based wind energy system e.g. in [4] is optimally utilized as harmonic as well as reactive power compensator for nonlinear load at PCC, enabling the grid to always absorb/supply a balanced set of fundamental currents at unity power factor.

1.7.2. Fault-ride-through and grid-support capability

The wind energy systems are not only required to supply power but also support the grid under system faults and voltage unbalances. Such ability of wind energy systems is termed as fault-ride-through (FRT) capability. The FRT capability of a wind energy system is of particular concern in view of the fact that the disconnection of a large wind generator caused by grid disturbances may lead to system instability.

Dedicated grid codes have recently been issued in some countries for interconnection of WT system to the power grid. An overview of recent grid codes prepared specially for large wind farms are presented in [93].

These grid codes essentially demand the FRT capability necessitating the wind energy system to remain connected with the power grid in the event of voltage dip so that the network voltage and frequency could be maintained stable by delivering active and reactive powers to the grid with a specific profile depending on the depth of grid voltage dip. Under a grid voltage dip, the maximum active power that can be delivered to the grid is constrained so as to meet FRT requirements, which in turn, may result in active power mismatch between the generated power and the power delivered to the grid [94, 95]. It, therefore, is very challenging to design the control scheme for the wind energy system to meet the FRT requirements. Since the full-scale power converter decouples the generator system from the grid, it is easier to realize the FRT and grid support capabilities in PMSG based wind energy systems. The FRT capability of a 2-MW PMSG based wind energy system has been investigated in [94].

A unified DC-link current control scheme has been proposed in [96] so as to assist the CSC based wind energy system for fault-ride-through. Compliant with the grid codes, additional measure such as the braking chopper is applied to support the system operation during grid disturbances [94]. In the event of grid fault, the DC/DC boost converter dissipates the unbalanced power between the generator and the grid with no more control effort.

However, such a strategy can hardly satisfy the needs of some grid codes as reported in [71].The ESS added to wind energy system cannot only be viewed as a method for output power smoothing but also as an effective but costly solution to FRT problems [97].

The FRT requirements in a wind energy system can also be met by storing the surplus active power in the generator-turbine inertia system [37]. Similar approaches are reported for the wind energy systems with two-level back-to-back VSC in [98], and with CSC based topology in [99].

In other way, the STATCOM has been applied to keep the wind energy system connected to the grid during grid faults [100]. With this method, the voltage regulation is much improved not only in the transient-state but also in the steady-state.

1.8. Technology trends and status of research

Recent trends in and the status of researches on power converter topologies, control methodologies, MPPT control algorithms and grid interconnection issues concerning PMSG based wind energy systems are shown in Figure 1.22 and the relevant statistics are presented in Table 1.5.

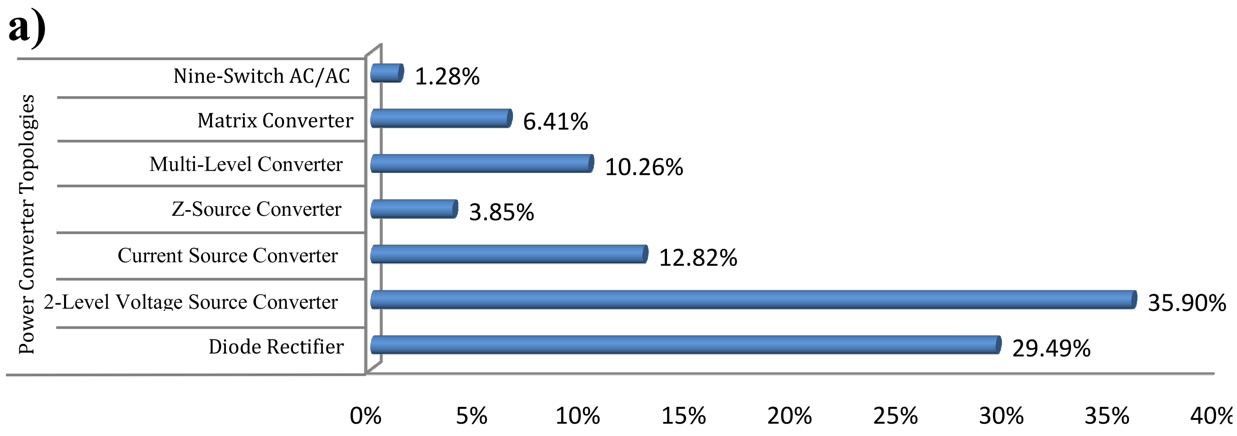

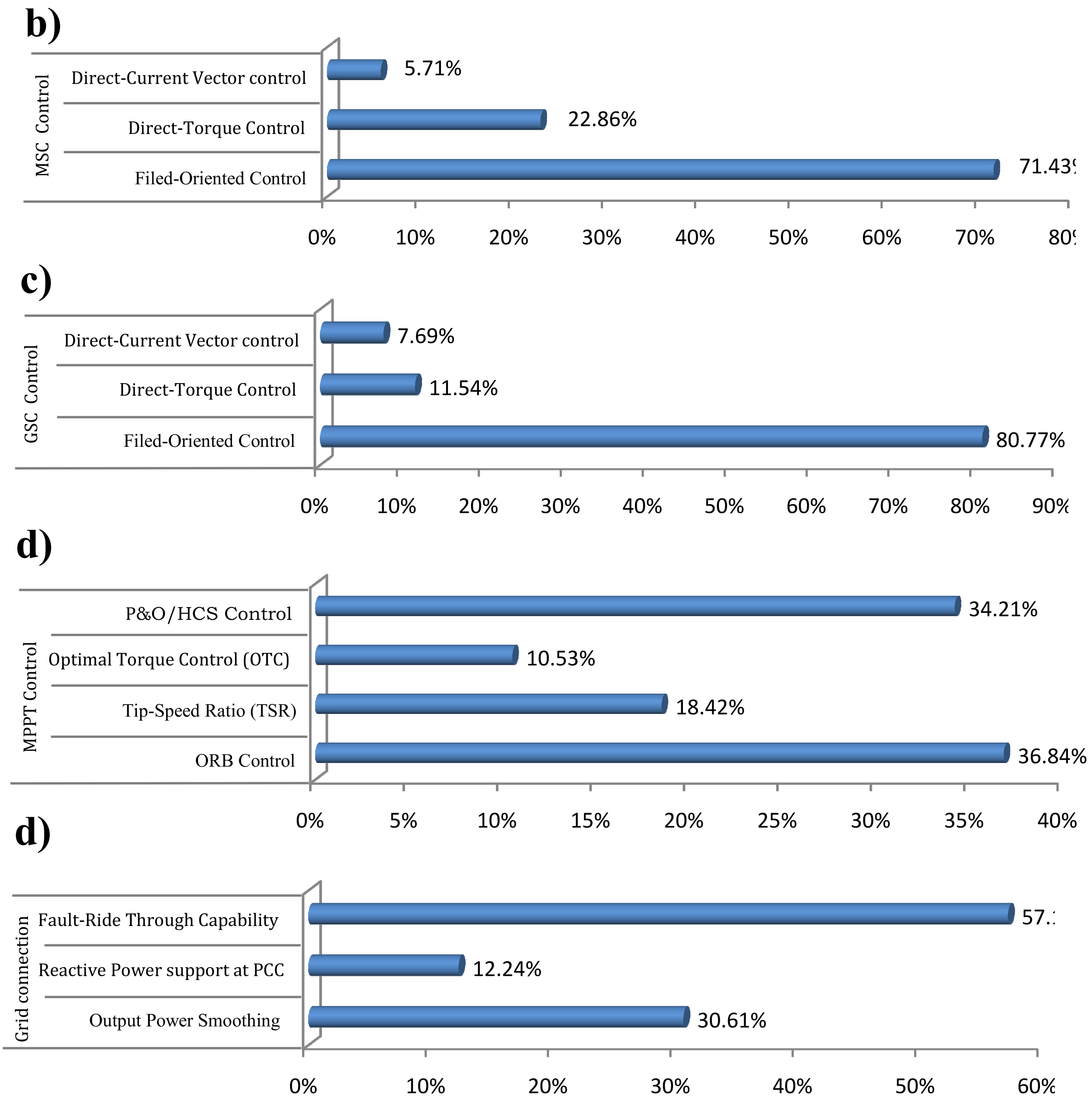

Figure 1.22. Recent trends in and status of researches concerning PMSG based wind energy systems - **(a)** power converter topologies **(b)** control methodologies employed at MSC **(c)** control methodologies employed at GSC **(d)** MPPT control algorithms, and **(e)** grid-interconnection issues.

Table 1.5

Trends in the technological development of permanent-magnet-synchronous-generator (PMSG)-based wind energy systems.

Power converter topologies								**Control methodologies**						**MPPT control algorithms**					**Grid-interconnection requirements**		
								MSC control			**GSC control**										
Diode Rectifier	2-Level VSC	CSC	ZSI	Multi-level	MC	9-Switch ac/ac	**Pitch Control**	FOC	DTC	DCVC	VOC	DPC	DCVC	ORB	TSR	OTC	P&O / HCS	**Sensorless Control**	Output Pow Smoothing	Reactive Powe Support at PCC	FRT Capability
29.49%	35.90%	12.82 %	3.85%	10.26%	6.41%	1.28%		71.43 %	22.86%	5.71%	80.77%	11.54%	7.69%	36.84%	18.42%	10.53%	34.21%		30.61%	12.24%	57.14%
29.52%							**3.66%**	**22.93%**						**14.29%**				**11.18%**	**18.42%**		

The trends in converter topologies point out that the 2-level back-to-back VSCs are the dominant power converter topologies used in PMSG based wind energy systems owing to the advantage of capacitor decoupling between the MSC and GSC which allows independent control of the two converters.

A low cost topology comprising diode rectifier cascaded by DC/DC boost converter has also been given large emphasis by the researchers for small scale PMSG based wind energy systems.

Multi-level converters are drawing attention of researchers for large WT applications. In many literatures, the FOC has been found as the most established strategy for PMSG speed control. On the other hand, the DTC scheme is also being considered by the researchers particularly for low power PMSG control. In a similar fashion, the VOC strategy for the GSC has been given maximum attention in many of the research studies; whereas, the DPC strategy for GSC has been given a moderate attention by the researchers. Further, the trends in MPPT control strategies signify that the ORB control has been established as a mature and the most investigated strategy.

The P&O/HCS control has also been given large consideration by many researchers and has been recognized as a simple MPPT control concept in which preknowledge of the WT parameters is not a requisite.

As far as the grid interconnection requirements are concerned, the enhancement of FRT capability of PMSG based wind energy systems has been established as a major issue in many of the research studies. Further, output power smoothing and reactive power support at PCC are other major challenges those have also been investigated in several research literatures. Altogether, the trends in technological developments in PMSG based wind energy systems are shown in Figure 1.23.

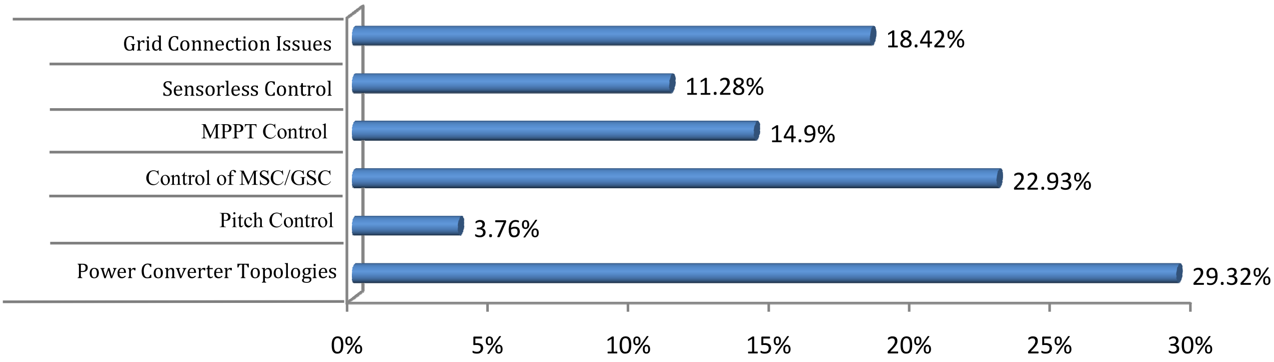

Figure 1.23. Trends on the whole in technological developments in PMSG based wind energy systems.

1.9. Conclusions

Efficient utilization of wind energy has been an important issue. As a result, VSWT systems with the power electronics interfaces have increasingly drawn the interest of WT manufacturers.

It is possible to increase the controllability of the WTs with the use of power electronics, which is a major concern for their integration into the power grid. Among the most popular concepts in the current VSWTs, the PMSG is the one which provides a realistic opportunity to realize the gearless operation, and is considered as a potential candidate for new designs in power WT applications. Recently, the cost reduction and advancements in the permanent magnet materials have made them even more attractive than before.

In this review, the mainstream power converter topologies used for PMSG based WTs were systematically reviewed with a clear focus to their features and limitations.

The back-to-back converter topology, which nowadays is state of the art among power converter topologies used in wind energy systems, can be used as a reference so as to set a benchmark to the implementation of other converter topologies keeping in view the requirement of active switches and auxiliary components along with their ratings, the harmonic performance and the converter efficiency.

As the power capacity of WTs is increasing, a trend towards the use of multilevel converter topologies in wind energy systems can also be observed. The trends in MSC and GSC control strategies used in PMSG based wind energy systems were also reviewed.

While comparing the MSC and GSC control strategies, it can be concluded that the FOC and VOC control strategies are better as adapted; whereas, the DTC and DPC control strategies might be preferred so as to achieve high dynamic performance.

Moreover, the advantages and limitations of several MPPT methods used for PMSG based wind energy systems were critically examined which could possibly be useful in the selection of an appropriate MPPT method for a particular application.

Brief opinions in relation to the grid interconnection issues for PMSG WT systems were also made focusing on the power controllability for better power quality, fault-ride-through and grid support capabilities during grid disturbances.

Looking at a glance towards the technology trends, and status of research, it was visualized that the two-level back-to-back converter and the diode rectifier based topologies; FOC and VOC methodologies; ORB and HCS based MPPT algorithms being the most researched concepts for PMSG based VSWTs.

It was also recognized that the FRT capability of PMSG based wind energy systems being the most investigated grid interconnection issue. With a goal toward more optimized wind energy systems, the future research studies expect more technological improvements in current WT design concepts.

Moreover, the existing control strategies can further be improved so as to obtain fast, and optimum control performance of PMSG based wind energy systems. Certain modifications in or hybrid combinations of MPPT algorithms in future research might lead to increased wind energy extraction efficiency of the WTs.

The advanced artificial intelligence (AI) based techniques can offer another new interesting perspective for future research. However, the most economic and reliable solution will only be recognized and preferred.

After all, this review is expected to be useful for not only the researchers working in the area of grid integrated PMSG based wind energy systems but also the commercial manufactures and designers of the same.

References

[1] **Zhu ZQ, Hu J:** “Electrical machines and power-electronic systems for high-power wind energy generation applications: Part I – market penetration, current technology and advanced machine systems”, *Int J Comput Math Electr Electron Eng 2013; 32(1):pp.7–33.*

[2] **Li H, Chen Z:** “Overview of different wind generator systems and their comparisons”, *IET Renew Power Gener 2008; 2(2):pp.123–138.*

[3] **Wang Zheng, Yuwen Bo, and Lang Y, Cheng Ming:** “Improvement of operating performance for the wind farm with a novel CSC-type wind turbine-SMES hybrid system”, *IEEE Trans Power Deliv 2013; 28(2):pp.693–703.*

[4] **Singh M, Chandra A:** “Application of adaptive network-based fuzzy inference system for sensorless control of PMSG-based wind turbine with nonlinear-load compensation capabilities” *IEEE Trans Power Electron 2011; 26(1):pp.165–175.*

[5] **Zhao Y, Wei C, Zhang Z, Qiao Wei:** “A review on position/speed sensorless control for permanent-magnet synchronous machine-based wind energy conversion systems”, *IEEE J Emerg Sel Top Power Electron 2013; 1(4):pp.203–216.*

[6] **Polinder H, van der Pijl FFA, de Vilder GJ, Tavner PJ:** “Comparison of direct-drive and geared generator concepts for wind turbines”, *IEEE Trans Energy Convers 2006; 21(3):pp.725–733.*

[7] **Bang D, Polinder H, Shrestha G, Ferreira J:** “Review of generator systems for direct-drive wind turbines”, *In: Proceedings of European Wind Energy Conference Exhibition; March/April 2008. pp. 1–11.*

[8] **Nishikata S, Tatsuta F:** “A new interconnecting method for wind turbine/generators in a wind farm and basic performances of the integrated system”, *IEEE Trans Ind Electron 2010; 57(2):pp.468–475.*

[9] **Slootweg JG, de Haan SWH, Polinder H, Kling WL:** “General model for representing variable speed wind turbines in power system dynamics simulations”, *IEEE Trans Power Syst 2003; 18(1):pp.144–151.*

[10] **Uehara Akie, Pratap Alok, Goya Tomonori, Senjyu Tomonobu, Yona Atsushi, Urasaki Naomitsu, et al: “**A coordinated control method to smooth wind power fluctuations of a PMSG-based WECS”, *IEEE Trans Energy Convers 2011; 26(2):pp.550–8.*

[11] **Chen Z, Guerrero JM, Blaabjerg F: “**A review of the state of the art of power electronics for wind turbines”, *IEEE Trans Power Electron 2009; 24 (8):pp.1859–1875.*

[12] **Hansen AD, Iov F, Blaabjerg F, Hansen LH: “**Review of contemporary wind turbine concepts and their market penetration”, *J Wind Eng* 2004*; 28 (3):pp.247–263.*

[13] **Muller S, Deicke M, Doncker RWDe:** “Doubly fed induction generator systems for wind turbines”, *IEEE Ind Appl Mag 2002; 8(3):pp.26–33.*

[14] **Blaabjerg F, Liserre M, Ma K:** “Power electronics converters for wind turbine systems”, *IEEE Trans Ind Appl 2012; 48(2):pp.708–719.*

[15] **Md., Rabiul Islam Y, Guo, Zhu J:** “A review of offshore wind turbine nacelle: technical challenges, and research and developmental trends”, *Renew Sustain Energy Rev 2014; 33:pp.161–176.*

[16] **Singh M, Khadkikar V, Chandra A:** "Grid synchronisation with harmonics and reactive power compensation capability of a permanent magnet synchronous generator-based variable speed wind energy conversion system", *IET Power Electron 2011; 4(1):pp.122–130.*

[17] **Chen Z, Spooner E:** "Grid power quality with variable speed wind turbines", *IEEE Trans Energy Convers 2001; 16(2):pp.148–154.*

[18] **Yazdani A, Iravani R:** "A neutral-point clamped converter system for direct-drive variable-speed wind power unit", *IEEE Trans Energy Convers 2006; 21(2):pp.596–607.*

[19] **Wang Jiacheng, Xu Dewei (David), Wu Bin, Luo Zhenhan:** "A low-cost rectifier topology for variable-speed high-power PMSG wind turbines", *IEEE Trans Power Electron 2011;26(8):pp.2192–2200.*

[20] **Baroudi, JA, Dinavahi, V, Knight, AM:** "A review of power converter topologies for wind generators", *In: Proceedings of Electric Machines and Drives, San Antonio, USA; May 2005: pp.458–465.*

[21] **Md., Rabiul Islam Y, Guo, Zhu J:** "Power converters for wind turbines: current and future development". *FORMATEX 2013:pp.559–571.*

[22] **Amei K, Takayasu Y, Ohji T, Sakui M:** "A maximum power control of wind generator system using a permanent magnet synchronous generator and a boost chopper circuit", *Proc PCC, Osaka, Japan 2002; 3:pp.1447–1452.*

[23] **Xia YY, Fletcher JE, Finney SJ, Ahmed KH, Williams BW:** "Torque ripples analysis and reduction for wind energy conversion systems using uncontrolled rectifier and boost converter", *IET Renew Power Gener 2011; 5 (5):pp.377–386.*

[24] **Muyeen S, Takahashi R, Murata T, Tamura J:** "A variable speed wind turbine control strategy to meet wind farm grid code requirements", *IEEE Trans Power Syst 2010; 25(1):pp.331–340.*

[25] **Andresen B, Birk J:** "A high power density converter system for the Gamesa G10x 4.5MW wind turbine" *Proc EPE 2007:pp.1–7.*

[26] **Peng FZ.** "Z-source inverter", *IEEE Trans Ind Appl* 2003*;39(2):pp.504–510.*

[27] **Vilathgamuwa DM, Wang X, Gajanayake CJ:** "Z-source converter based grid-interface for variable-speed permanent magnet wind turbine generators", *IEEE Power Electron Spec Conf (PESC) 2008:pp.4545–4550.*

[28] **Supatti U, Peng FZ:** "Z-source inverter with grid connected for wind power system", *Energy Convers Congr Expos IEEE 2009:pp.398–403.*

[29] **Dehghan Seyed Mohammad, Mohamadian Mustafa, Varjani Ali Yazdian:** "A new variable-speed wind energy conversion system using permanent magnet synchronous generator and Z-source inverter", *IEEE Trans Energy Convers 2009; 24(3):pp.714–724.*

[30] **Zhang Shao, Tseng King-Jet, Mahinda Vilathgamuwa D, Nguyen Trong Duy, Wang Xiao-Yu:** "Design of a robust grid interface system for PMSG-based wind turbine generators", *IEEE Trans Ind Electron 2011; 58(1):pp.316–328.*

[31] **Tang Y, Xie S, Zhang C:** "An improved Z-source inverter", *IEEE Trans Power Electron 2011; 26:pp.3865–8.*

[32] **Rajaei A, Mohamadian M, Varjani AY:** “Vienna-rectifier-based direct torque control of PMSG for wind energy application”, *IEEE Trans Ind Electron 2013; 60(7):pp.2919–2929.*

[33] **Li Jun, Bhattacharya Subhashish, Huang Alex Q:** “A new nine-Level Active NPC (ANPC) converter for grid connection of large wind turbines for distributed generation”, *IEEE Trans Power Electron 2011; 26(3):pp.961–972.*

[34] **Islam Md. R, Guo Y, Zhu J, Dorrell D:** “Design and comparison of 11 kV multilevel voltage source converters for local grid based renewable energy systems”, *In: Proceedings of 37th Annual Conference of the IEEE Industrial Electronic Society; 2011.pp.3596–3601.*

[35] **Rodriguez J, Franquelo LG, Kouro S, Leon JI, Portillo RC, Prats MAM, et al :** “Multilevel converters: an enabling technology for high-power applications”, *Proc IEEE 2009; 97(11):pp.1786–817.*

[36] **Frede Blaabjerg, Ma Ke:** “Future on power electronics for wind turbine systems”, *IEEE J Emerg Sel Top Power Electron 2013; 1(3):pp.139–152.*

[37] **Alepuz S, Calle A, Monge SB, Kouro S, Wu Bin:** “Use of stored energy in PMSG rotor inertia for low-voltage ride-through in back-to-back NPC converter-based wind power systems”, *IEEE Trans Ind Electron 2013; 60(5):pp.1787–1795.*

[38] **Zaragoza J, Pou J, Ceballos S, Robles E, Jaen C, Corbalan M:** “Voltage-balance compensator for a carrier-based modulation in the neutral-point-clamped converter”, *IEEE Trans Ind Electron 2009; 56(2):pp.305–314.*

[39] **Rajaei AH, Mohamadian M, Dehghan SM, Yazdian A:** “PMSG-based variable speed wind energy conversion system using Vienna rectifier”, *Euro Trans Elect Power 2011; 21(1):pp.954–72.*

[40] **Hansen LH, Helle L, Blaabjerg F, Ritchie E, Munk-Nielsen S, Bindner H, et al:** “Conceptual survey of generators and power electronics for wind turbines”, *Roskilde, Denmark: Risø National Laboratory; 2001.*

[41] **Kolar JW, Schafmeister F, Round SD, Ertl H:** “Novel three-phase AC–AC sparse matrix converters”, *IEEE Trans Power Electron 2007; 22:pp.1649–1661.*

[42] **Yamamoto Y, Hara H, Uchino T, Kawaji M, Kume TJ, Kang JK, et al:** “Development of MCs and its applications in industry”, *IEEE Ind Electron Mag 2011; 5:pp.4–12.*

[43] **Kang J, Takada N, Yamamoto E, Watanabe E:** “High power matrix converter for wind power generation applications”, *In: Proceedings of the IEEE 8th International Conference on Power Electronics (ECCE Asia);2011: pp.1331–1336.*

[44] **Kumar V, Joshi RR, Bansal RC:** “Optimal control of matrix-converter-based WECS for performance enhancement and efficiency optimization”, *IEEE Trans Energy Convers 2009: pp.24264–24673.*

[45] **Hojabri H, Mokhtari H, Chang L:** “Reactive power control of permanent magnet synchronous wind generator with matrix converter”, *IEEE Trans Power Deliv 2013; 28(2):pp.575–584.*

[46] **Heydari M, Varjani AY, Mohamadian M, Zahedi H:** “A novel variable-speed wind energy system using permanent-magnet synchronous generator and nine-switch AC/AC converter”, *In: Proceedings of the 2nd Power Electronics, Drive Systems and Technologies Conference; 2011.pp.5-9.*

[47] **Liu Congwei, Wu Bin, Zargari Navid R, Xu Dewei (David), Wang Jia-cheng:** "A novel three-phase three-leg AC/AC converter using nine IGBTs", *IEEE Trans Power Electron 2009; 24(5):pp.1151–1160.*

[48] **Swisher R, deAzua CR, Clendenin J:** "Strong winds on the horizon: wind power comes of age", *Proc IEEE 2001; 89(12):pp.1757–1764.*

[49] **Orlando NA, Liserre M, Mastromauro RA, Dell'Aquila A:** "A survey of control issues in PMSG-based small wind-turbine systems", *IEEE Trans Ind Inf 2013; 9 (3):pp.1211–1221.*

[50] **Mohamed AZ, Eskander MN, Ghali FA:** "Fuzzy logic control based maximum power tracking of wind energy system", *Renew Energy 2001; 23:pp.235–245.*

[51] **Yin M, Li GY, Zhang JC:** "Modeling and control strategies of directly driven wind turbine with permanent magnet synchronous generator", Power Syst Technol *2007;31(15):pp.60–5.*

[52] **Chedid R, Mrad F, Basma M:** "Intelligent control of class of wind energy conversion systems", *IEEE Trans Energy Convers 1999; 14:pp.1597–1604.*

[53] **Geng H, Yang G:** "Output power control for variable-speed variable pitch wind generation systems", *IEEE Trans Energy Convers 2010; 25(2):pp.494–503.*

[54] **Geng H, Yang G:** "Robust pitch controller for output power leveling of variable-speed variable-pitch wind turbine generator systems", *IET Renew Power Gener 2009; 3(2):pp.168–79.*

[55] **Zhang Zhe, Zhao Yue, Qiao Wei, Liyan Qu:** "A Space-vector modulated sensorless direct-torque control for direct-drive PMSG wind turbines", *IEEE Trans Ind Appl 2014; 50(4):pp.2331–2341.*

[56] **Zhang Z, Zhao Y, Qiao W, Qu L:** "A space-vector modulated sensorless direct torque control for direct-drive PMSG wind turbines", I*n: Proceedings of IEEE Industry Appications Society Annual Meeting*; *October 2012. pp .1-7.*

[57] **Hua Geng Dewei Xu, BinWu, Yang Geng:** "Active damping for PMSG-based WECS with DC-link current estimation", *IEEE Trans Ind Electron 2011; 58(4):pp.110–119.*

[58] **Zhang H-B, Fletcher J, Greeves N, Finney SJ, Williams BW:** One-power-point operation for variable speed wind/tidal stream turbines with synchronous generators. *IET Renew Power Gener 2011; 5(1):pp.99–108.*

[59] **Pucci Marcello, Cirrincione Maurizio:** "Neural MPPT control of wind generators with induction machines without speed sensors", *IEEE Trans Ind Electron 2011; 58(1):pp.37–47.*

[60] **Allagui Mehdi, Hasnaoui Othman Bk, Belhadj Jamel:** "A 2MW direct-drive wind turbine; vector control and direct torque control techniques comparison", *J Energy South Afr 2014; 25(2):pp.117–126.*

[61] **Sanjuan SL: "**Voltage oriented control of three-phase boost PWM converters: design, simulation and implementation of a 3-phase boost battery charger", *Master of Science Thesis in Electric Power Engineering. Göteborg, Sweden: Chalmers University of Technology*; *2010*.

[62] **Noguchi T, Tomiki H, Kondo S, Takahashi I:** "Direct power control of PWM converter without power source voltage sensors", *IEEE Trans Ind Appl 1998; 34(3):pp.473–9.*

[63] **Antoniewicz P:** Predictive control of three-phase AC/DC converters. *Ph.D. Thesis. Warsaw: Warsaw University of Technology*; *2009.*

[64] **Zhang Zhe, Zhao Yue, Qiao Wei, Liyan Qu:** "A Space-vector modulated sensorless direct-torque control for direct-drive PMSG wind turbines", *IEEE Trans Ind Appl 2014; 50(4):pp.2331–2341.*

[65] **Kim K-H, Jeung Y-C, Lee D-C, Kim H-G:** "Robust control of PMSG wind turbine systems with back-to-back PWM converters", *In: Proceedings of IEEE International Symposium on Power Electronics for Distributed Generation*; *2010. pp. 433–437.*

[66] **Kim Ki-Hong, Jeung Yoon-Cheul, Lee Dong-Choon, Kim Heung-Geun:** "LVRT scheme of PMSG wind power systems based on feedback linearization", *IEEE Trans Power Electron 2012; 27(5):pp.2376–2384.*

[67] **Li S, Haskew TA, Hong Y:** "PMSG maximum wind power extraction control using adaptive virtual lookup table approach in direct-current vector control structure", *Int J Energy Res 2011; 35(11):pp.929–1022.*

[68] **Li Shuhui, Haskew Timothy A, Swatloski Richard P, Gathings William:** "Optimal and direct-current vector control of direct-driven PMSG wind turbines", *IEEE Trans Power Electron 2012; 27(5):pp.2325–2337.*

[69] **Hansen AD, Michalke G:** "Multi-pole permanent magnet synchronous generator wind turbines, grid support capability in uninterrupted operation during grid faults", *IET Renew Power Gener 2009; 3(3):pp.333–348.*

[70] **Deng F, Chen Z: "**Low-voltage ride-through of variable speed wind turbines with permanent magnet synchronous generator", *In: Proceedings of 35th Annual Conference IEEE Industry and Electronics (IECON)*; *2009. pp. 621–626.*

[71] **Geng Hua, Yang Geng, Xu Dewei (David), Wu Bin: "**Unified power control for PMSG-based WECS operating under different grid conditions", *IEEE Trans Energy Convers 2011; 26(3):pp.822–830.*

[72] **Wang Q, Chang LC:** "An intelligent maximum power extraction algorithm for inverter based variable speed wind turbine systems", *IEEE Trans Power Electron 2004*; *19(5):pp.1242–9.*

[73] **Chinchilla M, Arnaltes S, Burgos J:** "Control of permanent-magnet generators applied to variable-speed wind-energy systems connected to the grid", *IEEE Trans Energy Convers 2006; 21(1):pp.130–5.*

[74] **Tan Kelvin, Islam Syed:** "Optimum control strategies in energy conversion of PMSG wind turbine system without mechanical sensors", *IEEE Trans Energy Convers 2004; 19(2):pp.392–409.*

[75] **Nishida Katsumi, Ahmed Tarek, Nakaoka Mutsuo:** "A cost-effective high efficiency power conditioner with simple MPPT control algorithm for wind-power grid integration", *IEEE Trans Ind Appl 2011; 47(2):pp.893–900.*

[76] **Shirazi M, Viki AH, Babayi O:** "A comparative study of maximum power extraction strategies in PMSG wind turbine system", *In: Proceedings of IEEE Electrical Power and Energy Conference*; *2009. pp. 1–6.*

[77] **Mirecki A, Roboam X, Richardeau F:** "Comparative study of maximum power strategy in wind turbines", *In: Proceedings of IEEE International Symposium on Industrial Electronics*; *May 2004. pp. 993-998.*

[78] **Yu Z, Elbuluk M, Sozer Y:** “Stability analysis on Maximum Power Points Tracking (MPPT) method in wind power system”, *In: Proceedings of IEEE Industry Applications Society Annual Meeting*; *October 2011. pp. 1-8.*

[79] **Zhou Z, Scuiller F, Charpentier JF, Benbouzid MEH, Tang T:** “Power smoothing control in a grid-connected marine current turbine system for compensating swell effect”, *IEEE Trans Sustain Energy 2013; 4(3):pp.816–826.*

[80] **Abdullah MA, Yatim AHM, Tan CW, Saidur R:** “A review of maximum power point tracking algorithms for wind energy systems”,. *Renew Sustain Energy Rev 2012(16):pp.3220–7.*

[81] **Yaoqin J, Zhongqing Y, Binggang C:** “A new maximum power point tracking control scheme for wind generation”, *In: Proceedings of Power Con; 2002. pp. 144–148.*

[82] **Femia N, Petrone G, Spagnuolo G, Vitelli M:** “Optimization of perturb and observe maximum power point tracking method”, *IEEE Trans Power Electron 2005; 20(4):pp.963–973.*

[83] **Kazmi SMR, Goto H, Guo H-J, Ichinokura O:** “A novel algorithm for fast and efficient speed-sensorless maximum power point tracking in wind energy conversion systems”, *IEEE Trans Ind Electron 2011; 58(1):pp.29–36.*

[84] **Koutroulis E, Kalaitzakis K:** “Design of a maximum power tracking system for wind-energy-conversion applications”, *IEEE Trans Ind Electron 2006; 53(2):pp.486–494.*

[85] **Xia Yuanye, Ahmed Khaled H, Williams Barry W:** “A New maximum power point tracking technique for permanent magnet synchronous generator based wind energy conversion system”, *IEEE Trans Power Electron 2011; 26 (12):pp.3609–3620.*

[86] **Wu B, Lang Y, Zargar N, Kouro S:** “Power conversion and control of wind energy Systems”, *New York, USA: Wiley*; *2011.*

[87] **Hui J, Bakhshai A, Jain PK:** “An adaptive approximation Method for Maximum Power Point Tracking (MPPT) in wind energy systems”, *In: Proceedings of the Energy Conversion Congress and Exposition*; *July 2011. pp. 2664-2669.*

[88] **Hilloowala RM, Sharaf AM:** “A rule-based fuzzy logic controller for a PWM inverter in a standalone wind energy conversion scheme”, *IEEE Trans Ind Appl 1996; 31(1):pp.57–65.*

[89] **Nguyen TH, Lee DC:** “Ride-through technique for PMSG wind turbine using energy storage systems”, *J Power Electron 2010; 10(6):pp.733–8.*

[90] **Rawn BG, Lehn PW, Maggiore M:** “Control methodology to mitigate the grid impact of wind turbines”, *IEEE Trans Energy Convers 2007; 22(2):pp.431–8.*

[91] **Valenciaga F, Puleston PF:** “High-order sliding control for a wind energy conversion system based on a permanent magnet synchronous generator”, *IEEE Trans Energy Convers 2008; 23(3):pp.860–7.*

[92] **Senjyu T, Kinjo T, Fujita H, Aichi :** “Analysis of terminal voltage and output power control of wind turbine generator by series and parallel compensation using SMES”, *In: Proceedings of the IEEE 35th Annual Power Electronics Specialists Conference, vol. 6; June 2004, pp. 4278–4284.*

[93] **Müfit Altın, Ömer Göksu, Remus Teodorescu, Pedro Rodriguez, Birgitte-Bak Jensen, Lars Helle:** “Overview of recent grid codes for wind power in-

tegration", *In: Proceedings of the 12th International Conference on Optimization of Electrical and Electronic Equipment (OPTIM); 2010, pp. 1152-1160.*

[94] **Conroy JF, Watson R:** "Low-voltage ride-through of a full converter wind turbine with permanent magnet generator", *IET Renew Power Gener 2007; 1(3):pp.182–9.*

[95] **Alepuj S, Busquets-Monge S, Bordonau J, Velasco JM, Silva C, Pontt J, et al:** "Control strategies based on symmetrical components for grid-connected converters under voltage dips", *IEEE Trans Ind Electron 2009; 56(6):pp.2162–2173.*

[96] **Dai Jingya, Xu Dewei (David), Wu Bin, Zargari Navid R:** "Unified DC-link current control for low-voltage ride-through in current source converter based wind energy conversion systems", *IEEE Trans Power Electron 2011; 26 (1):pp.288–297.*

[97] **Abbey C, Joos G.** "Supercapacitor energy storage for wind energy applications", *IEEE Trans Ind Appl 2007; 43(3):769–776.*

[98] **Fatu M, Lascu C, Andreescu GD, Teodorescu R, Blaabjerg F, Boldea I:** "Voltage sags ride-through of motion sensorless controlled PMSG for wind turbines", *In: Conference Record of IEEE IAS Annual Meeting,* vol. 1; *September 23-27, 2007: pp. 171-178.*

[99] **Dai J, Xu D, Wu B, Zargari NR:** "A unified DC link current control scheme for grid fault-ride through in current source converter based wind energy conversion systems", *In: Proceedings of IEEE ECCE. San Jose: CA*; *September 2009: pp. 1383-1390.*

[100] **Singh B, Saha R, Chandra A, Al-Haddad K:** "Static synchronous compensators (STATCOM): a review", *IET Power Electron 2009; 2(4):pp.297–324.*

Chapter 2

Finite-Set Model Predictive Decoupled Active and Reactive Power Control for Grid Connected Wind Energy Systems

Abstract

This Chapter introduces a novel approach for power control of three-phase voltage source inverter (3PH-VSI) in grid connected distribution wind energy system. In this approach, the control of active and reactive power is based on finite set model predictive control (FS-MPC) strategy. The proposed strategy has the simplicity of the direct power control technique and doesn't require any current control loops. To meet the future generation of PMSG wind turbines, a DC-DC boost converter is proposed at the machine-side to simplify the control and potentially reduce the cost of the wind energy system. In this chapter, the continuous- and discrete-time modeling of DC/DC boost convert and 3PH-VSI is analyzed. To achieve an optimal control performance, a modified two-step model predictive strategy is proposed. The wind generation system requirements, such as maximum energy harvesting and regulation of grid active and reactive power are expressed as cost functions. Best switching states are chosen and applied to the power converters during each sampling interval based on the minimization of cost functions. The feasibility of the proposed configuration and control scheme are verified through MATLAB/Simulink tests system and dSPACE 1104 experiments on a low power prototype.

2.1. Introduction

In efficient wind energy generation system, three main research areas play a crucial role: (i) semi-conductor devices, (ii) arrangement of these devices (called power converter configuration), and (iii) proper turn on/off of these devices (called the control scheme). The power converters' control is a very active research topic and is constantly evolving according to the technological developments in semiconductor devices and control platforms, control requirements, power quality standards, and grid code requirements, etc. [1-3]. To design an efficient controller, one needs to know about the true nature/behavior of the plant to be controlled. A power electronic converter exhibits the following properties, constraints and requirements [4, 5]:

- Nonlinear nature.
- Contains finite number of switching states, for example 8 switching states are available for two level three-phase voltage source converter.
- Imposes restrictions on the maximum current, switching frequency, efficiency and THD, etc., to achieve safe and reliable operation.
- Demands faster response for the electric control variables.
- Favors discrete-time implementation using the industry standard digital control plat-forms.

Different predictive strategies have been used in power electronics and drives [4, 6], namely deadbeat control, hysteresis-based predictive control, trajectory-based predictive control and finite set model predictive control. The finite set model predictive control (FS-MPC) strategy has proved one of the best methods for treating all the above properties and conditions. Recent academic works demonstrated that FS-MPC can easily be applied to a wide range of power converters, drives, power quality applications and wind energy systems [7].

Compared to the classical control techniques, this scheme eliminates the need for linear PI regulators and the modulation stage, and offers a conceptually different approach to control the power converters. This is truly a model-based optimization control strategy, and involves a large number of calculations [4, 6]. However, the computational issue is not prominent due to the advanced digital control platforms (DSPs and FPGAs) available in the market.

It is anticipated that this will be one of the next generation control tools, and thus is considered in this Chapter as a subject to control the wind energy systems. This Chapter presents the design, simulation and reel-time implementation of the converters and associated FS-MPC strategy for the grid connected wind energy system. Using the discrete-time model of the system, two individual control loops are developed, and they generate the gating signals to the DC/DC boost converter and 3PH-VSI based on minimization of cost functions. The use of linear controllers and modulation stage are eliminated with the proposed FS-MPC strategy, and as a result, good dynamic response has been obtained. The MPPT is effectively controlled by the DC/DC boost converter, while net DC-link voltage and active and reactive power are regulated by the 3PH-VSI.

Because of the control freedom for the inverter, a significant improvement in the grid power quality has been achieved. Through the simulation and experimental results, it has been demonstrated that the FS-MPC strategy performs very well in achieving the control goals for the complete wind energy system.

This Chapter will proceed as follows: In section 2, an overview for the FS-MPC is introduced. In sections 3 and 4, the converters modeling and the implementation of the FS-MPC control loops are described, respectively. In section 5, the simulation results and comparisons to the results of wind turbine using the conventional PI controller are illustrated. In section 6, the real-time validation of the different studied and developed FC-MPC algorithms with a scientific interpretation of the practical results are explained. . In section 7, some conclusions are drawn.

2.2. Overview of Finite-Set Model Predictive Control

2.2.1. FS-MPC applied to power converters

This section is focused on model predictive control with finite control set (FCS) or also called finite set model predictive control (FS-MPC), which is based on the switching model of a power converter and considers the control signal of every power switch as a control variable. FS-MPC does not need a modulator since the switching signals are the output of the controller and these are directly applied to the power converter. Therefore, this strategy produces a variable switching frequency. For this approach, the optimization is carried out online at every sampling period, and generally a prediction and a control horizon equal to one are used [8, 9]. Figures 2.1 and 2.2 shows an example of an FS-MPC scheme when implemented on a power electronic system and the concept of this control strategy, respectively.

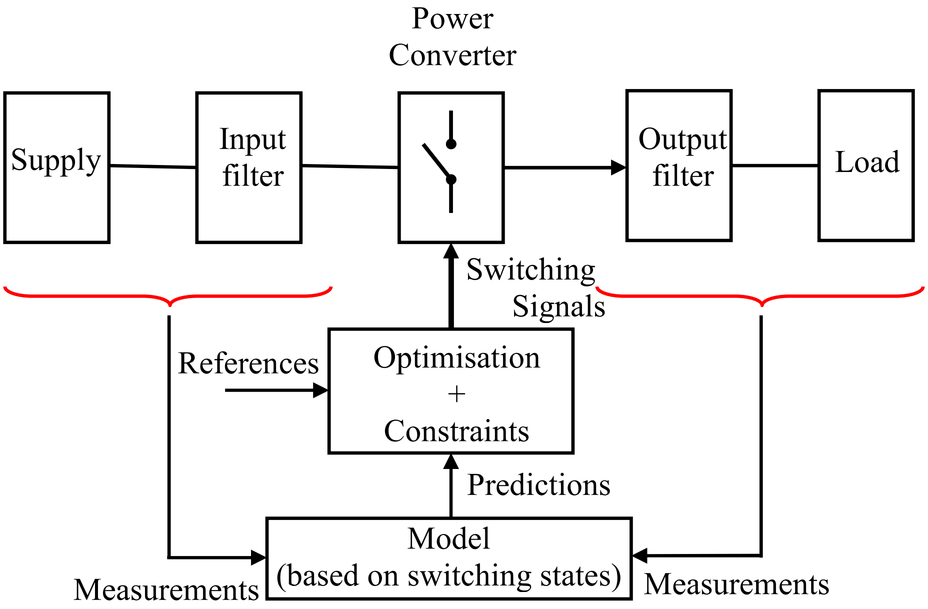

Figure 2.1. Scheme of FCS-MPC for a power electronic system.

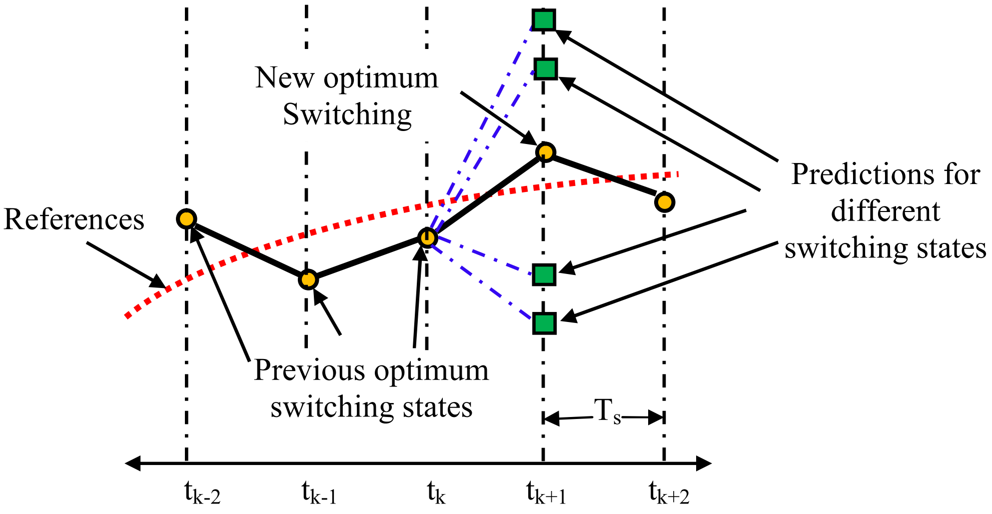

Figure 2.2. Concept of FCS-MPC.

2.2.2. Advantages and disadvantages of FS-MPC

FS-MPC has a lot of advantages over PID controllers in power electronics. Some of the advantages of FS-MPC are [10-12]:

1. FS-MPC concepts are very intuitive, and are easy to understand and implement.
2. A variety of processes can be controlled at once: anything from processes with simple dynamics to complex systems with long delay times.
3. Multiple variables can be controlled at once, without the need for complex loops. This is in contrast to traditional PID controllers which require superposition of variables where there is more than one variable to control.
4. Non-linearities, such as dead times, are included in the predictions.
5. Additional constraints can easily be included.
6. The effects of the present actions on happenings in the future are taken into account in the control system.

Some of the disadvantages of FS-MPC are:

1. The derivation of an FS-MPC control law is more complex than it would be for the PID controller.
2. Dynamic systems require that all computations be done at each sampling time.
3. Requires a lot of computing if there are several constraints to be considered.
4. Requires an appropriate model of the plant.

2.2.3. Switching model of a power converter

A power converter can be considered as a set of power switches, which correspond to power semiconductor devices such as IGBT, MOSFET, diodes, etc.

For a switched mode converter, these semiconductor devices operate in two states, namely “saturation” and “cut-off”, which function as “on” and “off” states, respectively.

To analyze the behavior of a power converter, a power switch is considered to be ideal, appearing as a short circuit (zero impedance) when “on” and as an open circuit (infinite impedance) when “off” [13, 14].

In addition, every change between states, from “on” to “off” and vice versa, is considered to be instantaneous, incurring zero loss during the transition.

Although an ideal switch operation is considered when analyzing a power converter, in reality, when a switch is “on”, there is a small voltage drop across the terminals whose value depends on the semiconductor device employed and the operational state of the circuit. Similarly, during an “off” state, there is a small leakage current [13, 14].

Furthermore, the process of turning a device "on" and "off" does not occur instantaneously, thus, the current through the device increases or decreases gradually.

The switching model of a power converter is based on the on-off operation of a power switch, which is defined by a switching function. An example of a switching function is given in equation (2.1).

Therefore, using this function, voltages and currents of the power converter may be obtained. Generally, the switching functions are result of a modulation strategy, such as pulse width modulation (PWM).

$$S(\mathrm{t}) = \begin{cases} 1, \ when\ power\ switch\ is\ "on" \\ 0, when\ power\ switch\ is\ "off" \end{cases} \tag{2.1}$$

Some strategies to control power converters, such as space vector modulation (SVM), are based on all possible allowed combinations of switching elements.

Each combination [9, 15], called a switching state, produces different input and output voltages/currents, hence, the behavior of a power converter can be determined by these states.

In order to determine the switching states of a power converter, it is necessary to consider some restrictions related to the converter operation.

Thus, depending on whether the power converter has a voltage or current source, the switching states for a similar power converter structure, considering ideal switches, are different in order to ensure that Kirchhoff's voltage and current laws are maintained.

Figure 2.3 shows a three-phase current source inverter (CSI), using IGBTs. In addition, Table 2.1 presents the switching states for three-phase CSI.

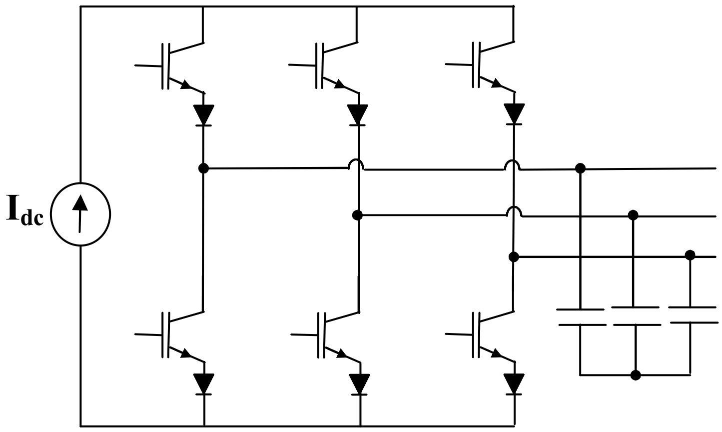

Figure 2.3 Switching states for three-phase current source inverter (CSI).

Table 2.1
Switching states for three-phase current source inverter (CSI).

Three-Phase Current Source Inverter (CSI)				
	Switching state	I_c	I_b	I_c
Active switching states	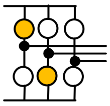	I_{dc}	$- I_{dc}$	0
	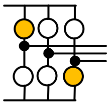	I_{dc}	0	$- I_{dc}$
	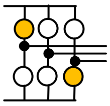	0	I_{dc}	$- I_{dc}$
	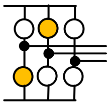	$- I_{dc}$	I_{dc}	0
	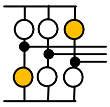	$- I_{dc}$	0	I_{dc}
	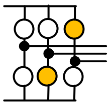	0	$- I_{dc}$	I_{dc}
Zero switching states	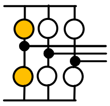	0	0	0
	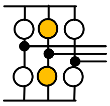	0	0	0
	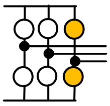	0	0	0

● Power Switch ON ○ Power Switch OFF

Consequently, a switching model may be represented mathematically, such as equations (2.2), (2.3) and (2.4) for three-phase CSI topology [13, 15].

$$I_a(t) = [S_1(t) - S_2(t)]\,I_{dc} \tag{2.2}$$

$$I_b(t) = [S_3(t) - S_4(t)]\,I_{dc} \tag{2.3}$$

$$I_c(t) = \left[S_2(t) - S_6(t)\right] I_{dc} \tag{2.4}$$

2.2.4. Prediction equations

For the FS-MPC strategy, prediction equations of every variable to be controlled are needed, hence, to control a power electronic system, a model including power converter, load, filters, etc. must be defined. From the previous section, a power converter may be represented by a switching model, thus, in order to obtain the prediction equations, the model of every component of the system (load, filter, etc.) must be combined with the switching model, which provides output and input voltages/currents of the power converter. Prediction equations are usually derived using a first order approximation of the derivative, as given in equation (2.5), or a discrete-time state-space representation, as in equation (2.6) [6, 8].

$$\frac{d}{dt}x(t) = \frac{x(k+1) - x(k)}{T_s} \tag{2.5}$$

$$\begin{aligned} \underline{x}(\mathrm{k}+1) &= A\underline{x}(k) + B\underline{u}(k) \\ \underline{y}(k+1) &= C\underline{x}(k+1) \end{aligned} \tag{2.6}$$

2.2.5. Cost function and optimization

The controller output (switching state) is determined by minimizing the error between the reference and the prediction of the variable to be controlled. The expression to be optimized is denominated cost function (J) and it may include several variables (multivariable control). Normally, this is implemented via the absolute value or the square of the error [8, 9], as given by equations (2.7) and (2.8), where $X^*$is a reference value and X_p is the corresponding prediction.

$$J = \left| x^* - x^p \right| \tag{2.7}$$

$$J = \left(x^* - x^p \right) \tag{2.8}$$

Optimization of the cost function is carried out by evaluating the cost function using every switching state and selecting the one which achieves the minimum value. Since this procedure depends on the number of switching states, it may demand a significant number of calculations. A flowchart of the optimization process is shown in Figure 2.4, where is the number of switching states, X_i *(1+k)*is the prediction at the next sampling interval (t_k+1) for the i-th switching state ($1 \leq i \leq N$), $X(k)$ is the value of X at sampling time (t_k), k*)*Siis the i-th switching state, and $S_{opt}(k)$ is the switching state to be applied at sampling time (t_k) .As previously mentioned, the cost function can contain different terms, such as another variable to be controlled, some additional terms related to the control effort or some constraints, for example, minimization of switching frequency, reduction of the switching losses and voltage/current limitations [8, 9].

When the cost function is composed of several terms, in order to consider the significance of each term, coefficients known as weighting factors are employed [8, 9], which allow tuning of the cost function.

Equation (2.9) gives an example of a cost function with two variables to be controlled and an additional term (F), where λ_1, λ_2 and λ_3 are weighting factors.

$$J = \lambda_1 \left| x_1^* - x_1^p \right| + \lambda_2 \left| x_2^* - x_2^p \right| + \lambda_3 F \tag{2.9}$$

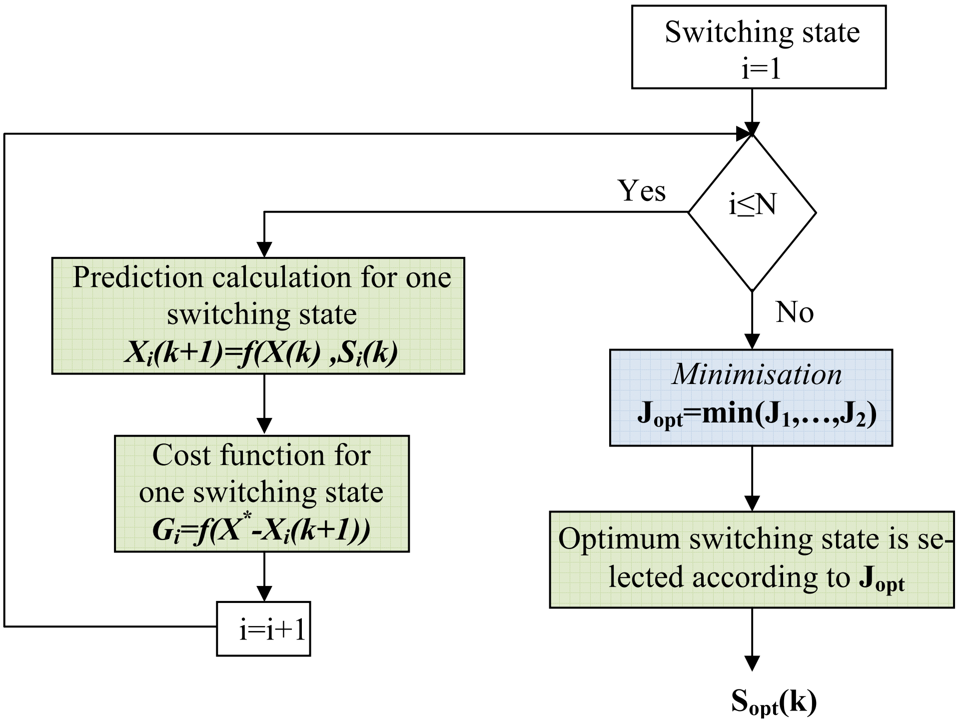

Figure 2.4. Optimization process.

Furthermore, when two or more variables have to be regulated, the error of each variable can be normalized [8, 9], resulting in per-unit values, which leads to a homogeneous cost function. An example is given by equation (2.10), where X_1, X_2 and X_3 are the corresponding nominal values.

$$J = \lambda_1 \frac{\left| x_1^* - x_1^p \right|}{x_1^n} + \lambda_2 \frac{\left| x_2^* - x_2^p \right|}{x_2^n} + \lambda_3 \frac{\left| x_3^* - x_3^p \right|}{x_3^n} \tag{2.10}$$

2.2.6. Delay compensation

Ideally, a predictive control strategy can minimize the error at (tk+1) by applying a new switching state (Sopt) at (tk), as shown in Figure 2.5.

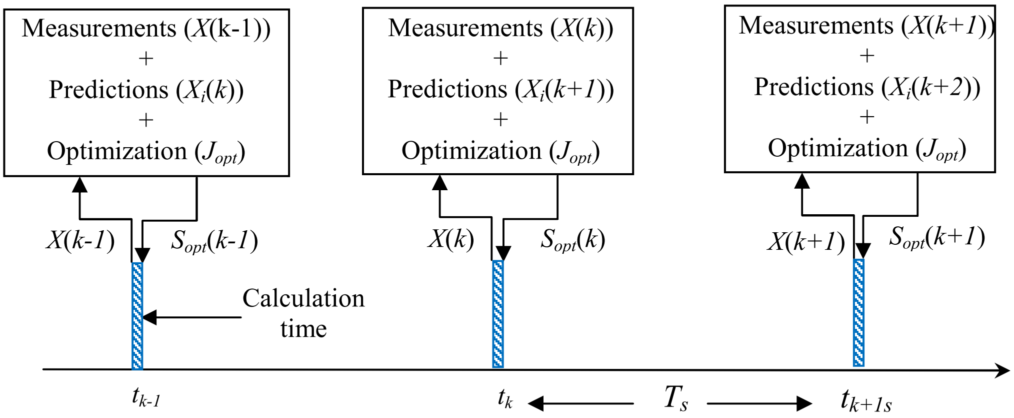

Figure 2.5. Ideal implementation of FS-MPC.

Since FS-MPC is digitally implemented, every calculation consumes time, as a consequence, this generates a predictable delay which must be compensated. One compensation approach is based on optimizing the cost function at (tk+2) and applying the optimum switching state at (tk+1)]6, 8]. In order to implement this approach, it is necessary to obtain every variable at (tk+1) instead of measurements at (tk), therefore, a simple option is to estimate the values at (tk+1) using the optimum switching state applied at (tk))previous result of optimization), measurements and the model of the system. In Figures 2.6 and 2.7, a flowchart of the optimization process taking into account the calculation delay and a diagram of FS-MPC implemented in a digital control platform are depicted, respectively.

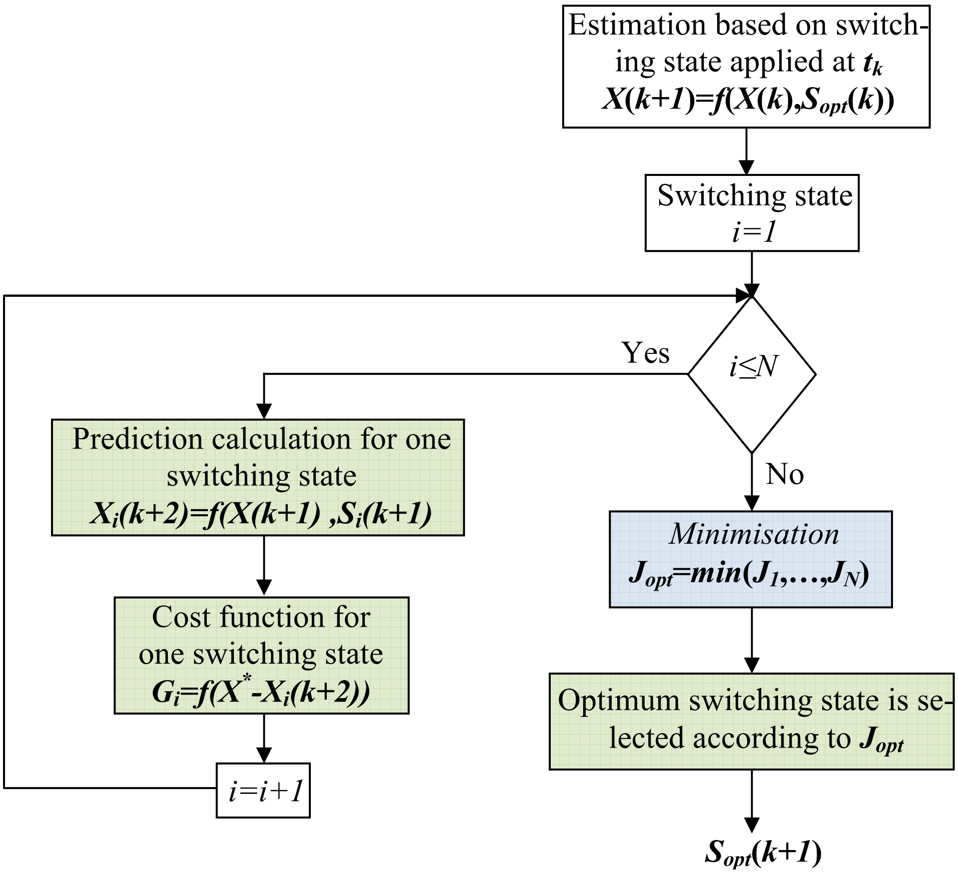

Figure 2.6. Optimization process with calculation delay.

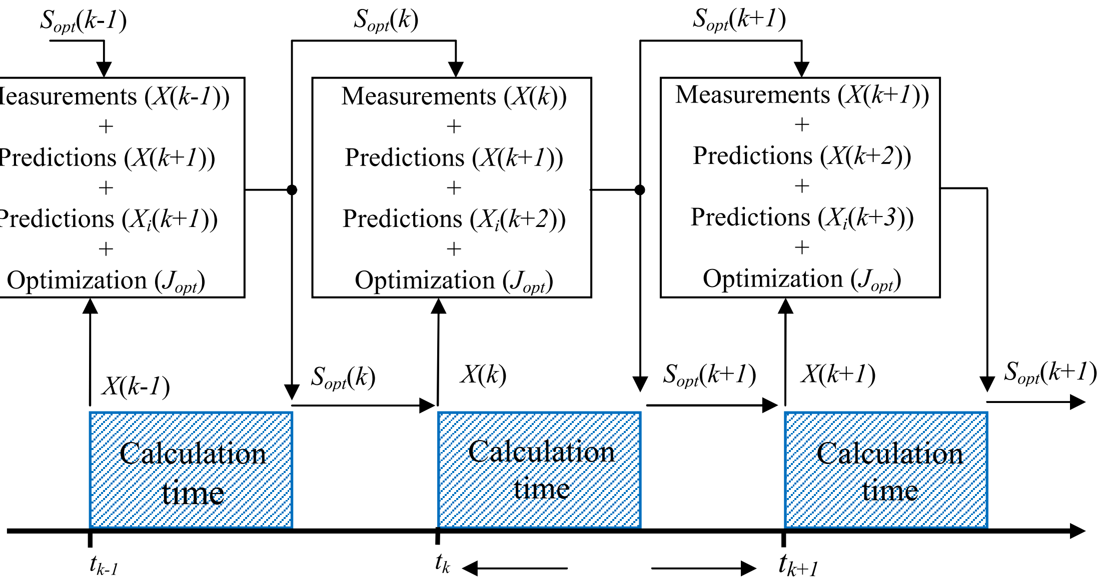

Figure 2.7 Actual implementation of FS-MPC.

2.2.7. FS-MPC Stability

Determining stability of an FS-MPC system has been a difficult subject. The results have not been valid due to constraints that are active as they are based on linear analysis. To ensure existence of stability, however, a system must have the following characteristics:

1. An accurate plant model: An accurate plant model will ensure an accurate prediction and hence the instability of the plant can be detected early. Prediction mismatch can cause instability.
2. Short sampling steps and longer prediction horizon. A shorter sampling step will detect any deviation from the prediction before the plant goes out of control. Duration of the sampling step will depend on the boundary of performance set by the designer through cost functions and inputs. A longer prediction horizon will also be better able to predict any issues of possibility of future instabilities.
3. Tighter cost function on performance and constraints. The tighter the cost function and constraints the better effect on stability. The plant will be forced to operate within safe operating areas and very close to the control objectives most of the time and hence prevent instances of instability.

2.2.8. Predictive control implementation

There are four basic stages in the implementation of an FS-MPC algorithm: measurements, estimations, predictions and optimization. Each of these stages is explained as follows:

- **Measurements:** In this stage, all of the variables needed are measured, either variables to be controlled or any state variable. If it is not possible to measure some variable, an observer may be utilized in order to estimate its value.
- **Estimations:** Owing to the calculation delay generated (actual digital implementation), it is not feasible to minimize the error at (t_k+1) and apply the optimal switching state at (t_k), therefore, the entire process is shifted from (t_k) to (t_k+1), and, as a result, the model is employed to estimate the variables at (t_k+1) as well as to predict the variables at (t_k+2). In order to calculate the estimations at (t_k+1), the previous optimum switching state calculated at (t_k+1) but applied at $(\mathrm{t_k})$, $S_{opt}(k)$, is used.
- **Predictions:** The predictions at (t_k+2) are calculated by using the estimated values of every variable at (t_k+1) and every switching state. These predicted values are used to obtain the errors at (t_k+2) which are included in the cost function (J).
- **Optimization:** After calculating the predicted values for every switching state at (t_k+2), a cost function is defined (one value for each switching state), mainly, based on each error at (t_k+2). Then, the optimization (minimization) is performed online, i.e. it is carried out during every sampling period, and, according to the minimum value of the cost function, the optimal switching state to be applied at (t_k+1) is determined.

In Figures 2.8 and 2.9, flowcharts of FS-MPC implementation with and without delay compensation are depicted. In these, a general system is considered, hence, a multi-input/multi-output (MIMO) state-space model is used.

Outputs and inputs are measured, and the output predictions are calculated based on the state vector predictions, which depend on the converter switching states.

The cost function (J_i) is also given in a general form, where Λ is a diagonal matrix, given in equation (2.11), that contains the weighting factors, and F is an additional term which represents some constraint or other variable to be taken into account during optimization.

The optimization process compares every value of the cost function in order to determine the switching state that minimizes it. Finally, the optimal switching state is applied to the power converter. The MIMO system considered is given by (2.12), where $\underline{x}$ is the state vector, $\underline{v}$ is an input vector (related to the power converter), S is a matrix of switching functions, which is different for each switching state, $\underline{y}$ is the output vector and N is the number of switching states.

In equations (2.11) and (2.13), *n*, *m*, *q* and *r* are used to indicate the dimension of every element.

$$[\Lambda]_{r\times r}=\begin{bmatrix}\lambda_1 & \cdots & 0\\ \vdots & \ddots & \vdots\\ 0 & \dots & \lambda_r\end{bmatrix} \tag{2.11}$$

$$\begin{aligned}\left[\underline{x}(k+1)\right]_{n\times 1}&=[A]_{n\times n}[\underline{x}(k+1)]_{n\times 1}+[B]_{n\times m}\left\{[S(k)]_{m\times q}[\underline{v}(k)]_{q\times 1}\right\}\\ \left[\underline{\mathrm{y}}(k+1)\right]_{r\times 1}&=[\mathrm{C}]_{r\times n}[\underline{x}(k+1)]_{n\times 1}\end{aligned} \tag{2.12}$$

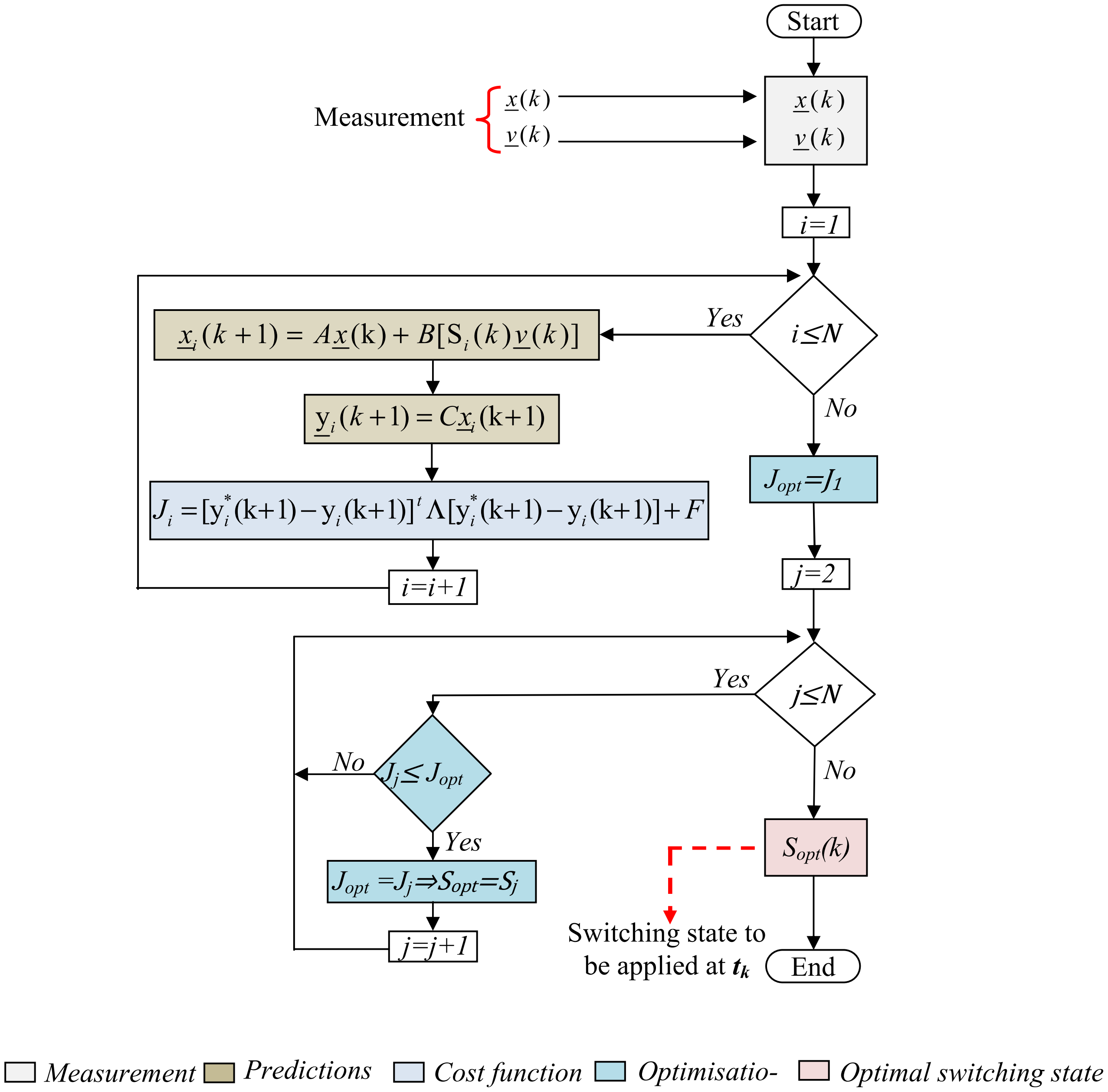

Figure 2.8. Flowchart of FCS-MPC without delay compensation.

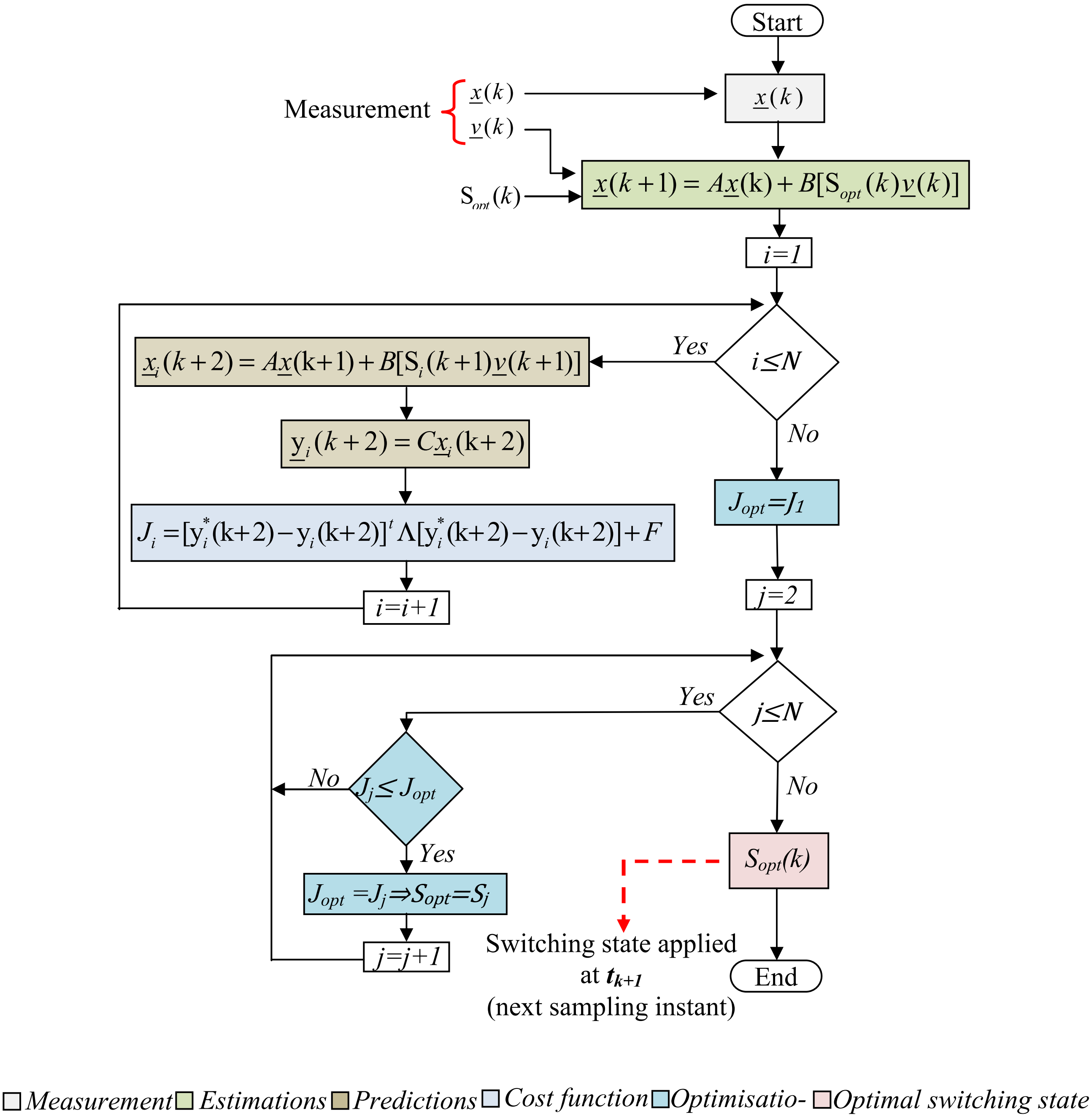

Figure 2.9. Flowchart of FCS-MPC with delay compensation.

2.3. System Configuration and Modeling

The power conversion system for direct-driven PMSG in grid connected distribution generation system is shown in Figure 2.10. The system consists of three stages: AC/DC, DC/DC and DC/AC, and these are implemented using a passive diode rectifier, a DC/DC boost converter and three-phase two-level inverter, respectively. The diode rectifier limits the direction of power flow, and only the generating mode is possible which the typical requirement is in a wind generation systems. The output voltage of the diode rectifier remains unregulated but is limited by the rated speed of the turbine, which defines the voltage rating of the capacitor (800V). The DC/DC boost converter enables MPPT operation for the wind generation system. The system can be operated efficiently in the complete wind speed range by controlling the gating signals for the DC/DC boost converter. The output of DC/DC boost converter directly fits the DC-link capacitor of the grid-tied inverter. This second DC-link provides decoupling for the machine- and grid-side converters and thus individual control loops can be developed. The inverter is used to transfer power from distributed generation system to the utility grid through an Lg filter. In the proposed system, the following four variables need to be regulated:

- Maximum power point tracking (MPPT) during all wind speed conditions to improve wind energy conversion efficiency.
- Net DC-link voltage control to ensure proper operation for the grid-tied inverter.
- Active and reactive power control to meet the grid codes.

The first variable is regulated by the DC/DC boost converter, and the last two variables are handled by the three-phase voltage source inverter. In this section, the modeling is presented to demonstrate that the proposed power converters accomplish the above-mentioned control requirements.

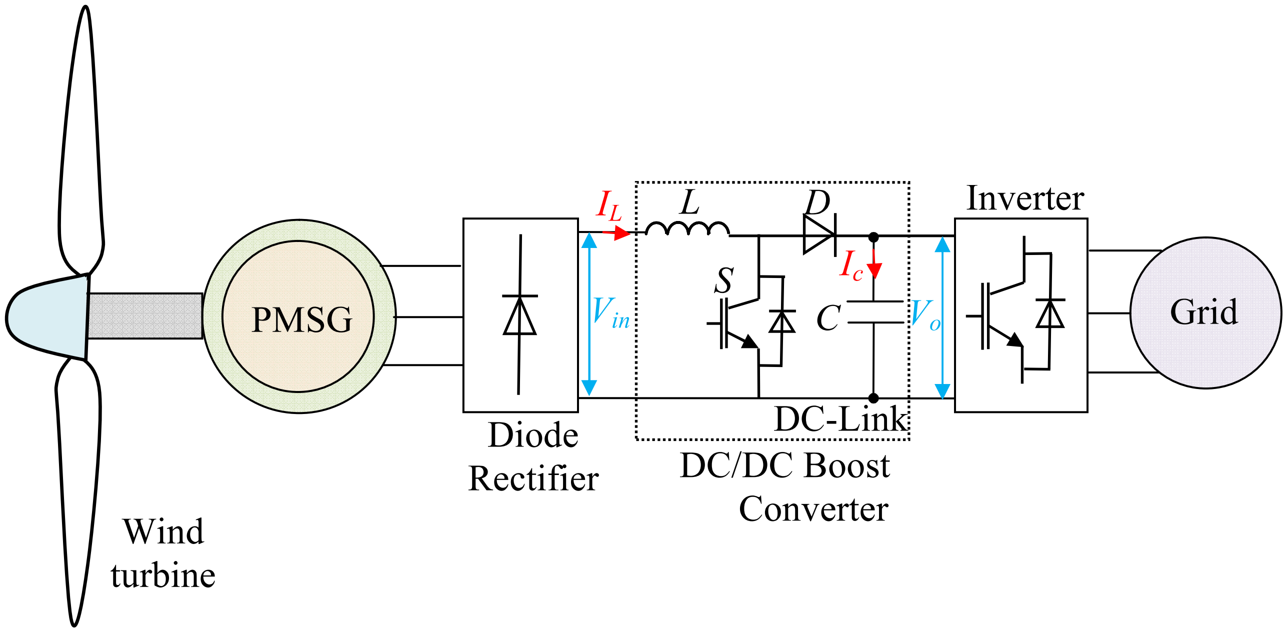

Figure 2.10. Considered wind energy system.

2.3.1. DC-DC Boost Converter Model

A DC/DC boost converter is a power converter with an output DC voltage (V_o) greater than its input DC voltage (V_{in}). A typical circuit diagram for a standard DC/DC boost converter is shown in Figure 2.11. it is composed of a switch *S*, a diode *D*, a DC inductor *L*, and a filter capacitor *C*.

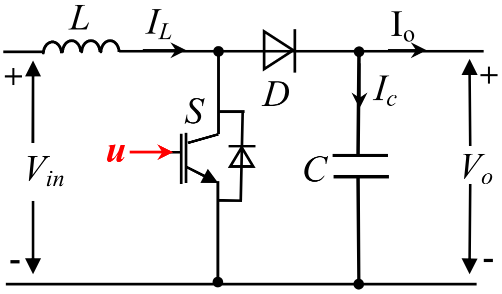

Figure 2.11. A simplified circuit for DC/DC boost converter.

The modeling and control of a DC/DC boost converter was analyzed in [16]. In this Chapter, a similar approach is used for the modeling of the DC/DC boost converter. The switching model for DC/DC boost converter is derived by finding expressions for the inductor current in the "on" and "off" states. A simplified circuit as shown in Figure 2.12 is derived to facilitate the modeling of the DC/DC boost converter.

2.3.2. OFF state

As shown in Fig. 2.12(a), the switch S is in off state ($s(t)$=0), and the load is connected to the voltage source (V_{in}). So, the DC/DC boost converter reacts as indicated by the following equation:

$$\frac{di_L}{dt} = -\frac{1}{L}v_o + \frac{1}{L}v_{in} \tag{2.13}$$

2.3.3. ON state

In this state, the switch S is in on state ($s(t)$ =1), and the load is disconnected from the voltage source (V_{in}). The equivalent circuit is shown in Figure 2.12 below.

On the other hand, the first order terms of equation (2.13) disappear and the former equation system is given as:

$$\frac{di_L}{dt} = \frac{1}{L}v_{in} \tag{2.14}$$

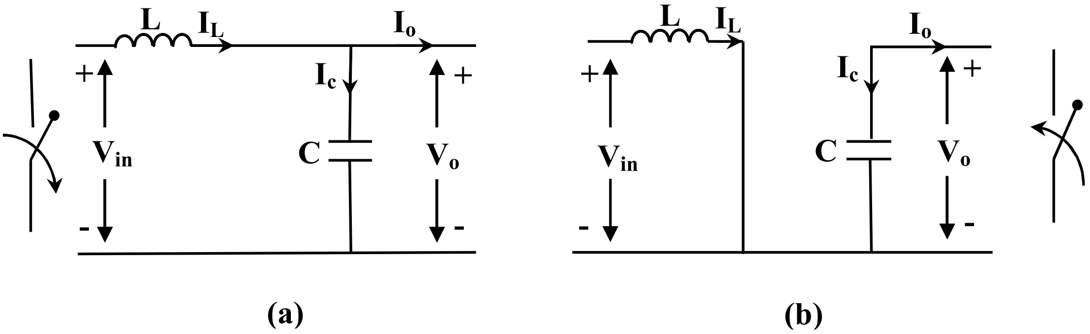

(a) **(b)**

Figure 2.12. Two operating modes of the DC/DC boost converter circuit, (a) Open switch, $S(t)$=0, (b) Closed switch, $S(t)$=1.

2.3.4. Three-phase voltage source inverter (VSI) model

The power circuit of the three-phase two level inverter converts electrical power from DC to AC form using the electrical scheme shown in Figure 2.13.

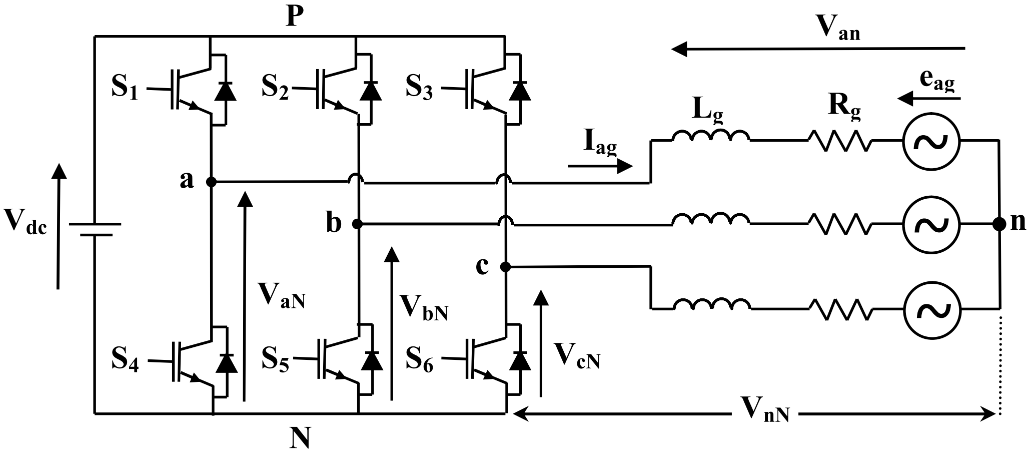

Figure 2.13. Voltage source inverter power circuit.

Considering that the two switches in each inverter phase operate in a complementary mode in order to avoid short-circuiting the DC-link voltage, the switching state of the power switches S_n, with n = 1,..., 6, can be represented by the switching signals S_a, S_b, and S_c defined as follows:

$$S_a = \begin{cases} 1 & if\ \ S_1\ on\ and\ \ S_4\ off \\ 0 & if\ \ S_1\ off\ and\ \ S_4\ on \end{cases} \tag{2.15}$$

$$S_b = \begin{cases} 1 & if\ \ S_2\ on\ and\ \ S_5\ off \\ 0 & if\ \ S_2\ off\ and\ \ S_5\ on \end{cases} \tag{2.16}$$

$$S_{ca} = \begin{cases} 1 & if\ \ S_3\ on\ and\ \ S_6\ off \\ 0 & if\ \ S_3\ off\ and\ \ S_6\ on \end{cases} \tag{2.17}$$

These switching signals define the value of the output voltages:

$$V_{aN} = S_a V_{dc} \tag{2.18}$$

$$V_{bN} = S_b V_{dc} \tag{2.19}$$

$$V_{cN} = S_c V_{dc} \tag{2.20}$$

where V_{dc} is the DC-link voltage capacitor.

Considering the unitary vector $a = e^{j2\pi/3} = -\frac{1}{2} + j\sqrt{3/2},$ which represents the 120° phase displacement between the phases, the output voltage vector can be defined as:

$$V = \frac{2}{3}\left(V_{aN} + aV_{bN} + a^2 V_{cN}\right) \tag{2.21}$$

Where V_{aN}, V_{bN}, and V_{cN} are the phase-to-neutral (N) voltages of the inverter.

In this way, switching state (S_a, S_b, S_c) = (0, 0, 0) generates voltage vector V_0 defined as:

$$V_0 = \frac{2}{3}\left(0 + a0 + a^2 0\right) = 0 \tag{2.22}$$

And corresponds to the circuit shown in Figure 2.14(a).

Switching state (1, 0, 0) generates voltage vector V_1 defined as:

$$V_1 = \frac{2}{3}\left(V_{dc} + a0 + a^2 0\right) = \frac{2}{3}V_{dc} \tag{2.23}$$

And corresponds to the circuit shown in Figure 2.14(b).

Voltage vector V_2 is generated by switching state (1, 1, 0) and is defined as:

$$V_1 = \frac{2}{3}\left(V_{dc} + aV_{dc} + a^2 0\right) \tag{2.24}$$

$$V_1 = \frac{2}{3}\left(V_{dc} + \left(-\frac{1}{2} + j\frac{\sqrt{3}}{2}\right)V_{dc}\right) = \frac{V_{dc}}{3} + j\frac{\sqrt{3}}{3}V_{dc} \tag{2.25}$$

And corresponds to the circuit shown in Figure 2.14(c).

Switching state (1, 1, 1) generates voltage vector V_7 that is calculated as:

$$V_1 = \frac{2}{3}\left(V_{dc} + aV_{dc} + a^2 V_{dc}\right) = \frac{2}{3}V_{dc}\left(1 + a + a^2\right) = 0 \tag{2.26}$$

And corresponds to the circuit shown in Figure 2.14(d).

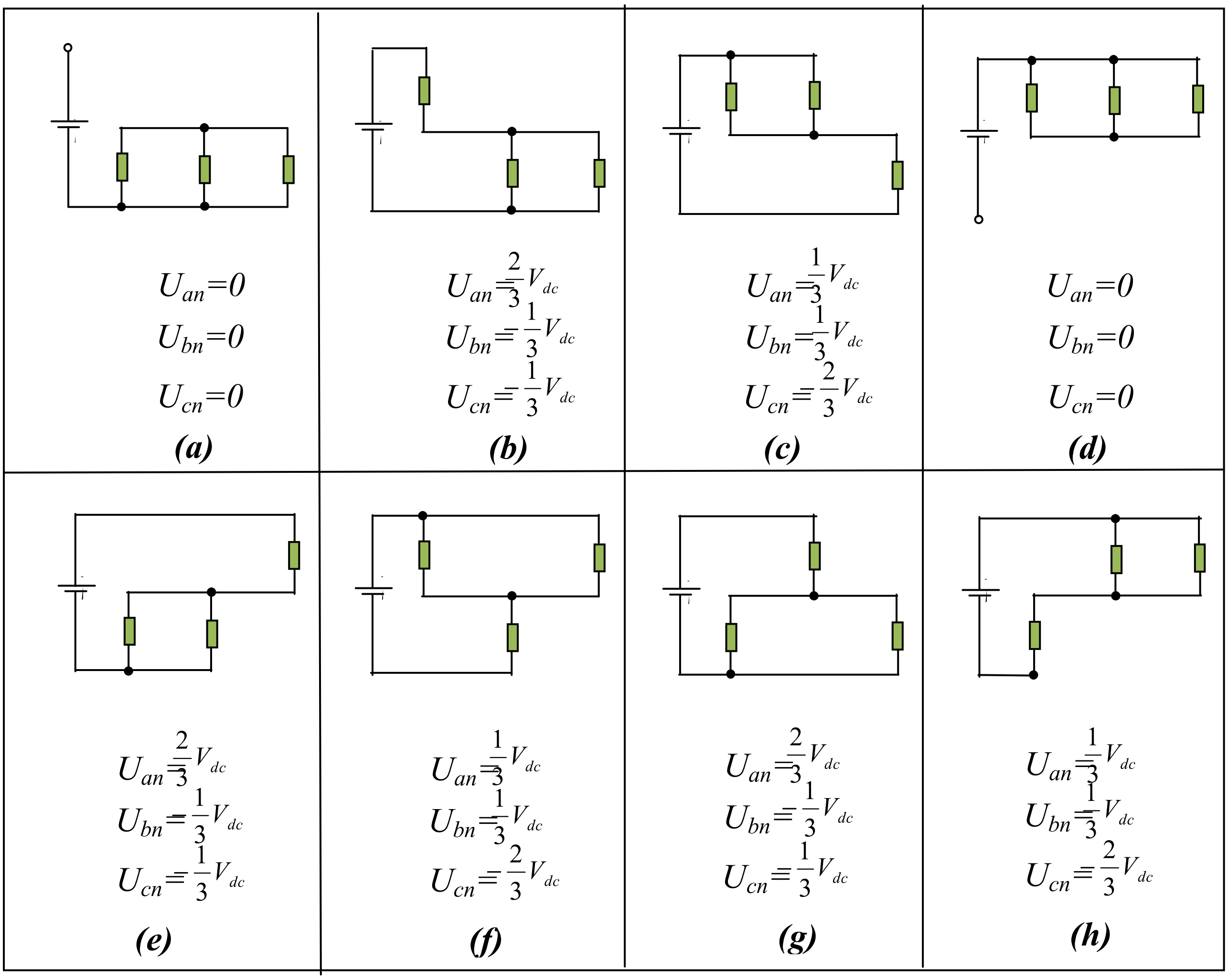

Figure 2.14. Equivalent configurations for different switching states.

By considering equations (2.18), (2.19), (2.20) and (2.21) eight switching states, six active states and two zero states, can be defined and consequently eight voltage vectors are obtained ($V_0 \ldots V_7$) as shown in Figure 2.15.

In These figure note that $V_0 = V_7$, resulting in a finite set of only seven different voltage vectors in the complex plane. Moreover, the corresponding output voltage is given in table 2.2.

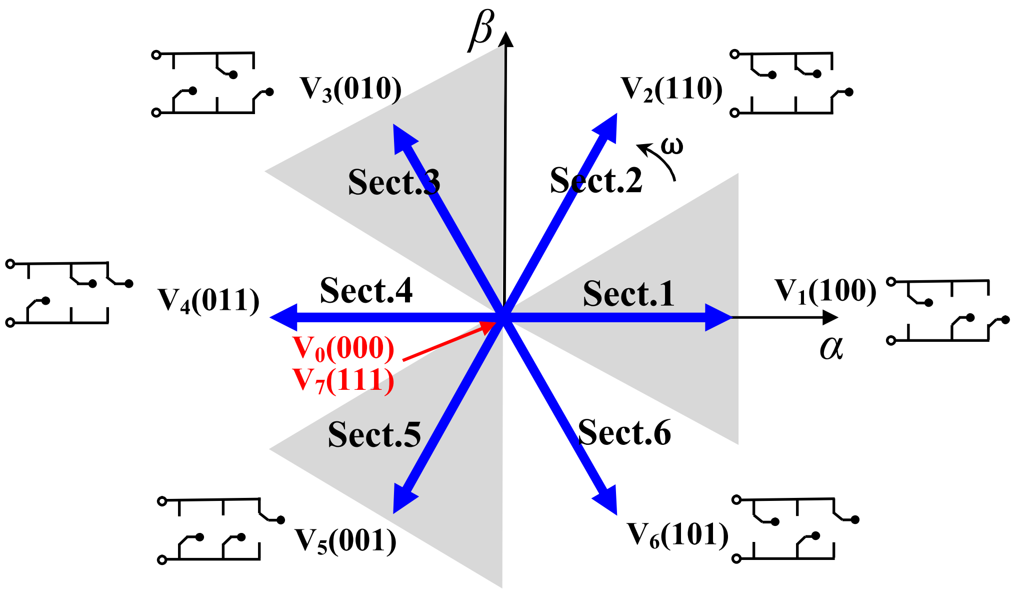

Figure 2.15. Inverter possible output voltage vectors in the αβ plane.

Table 2.2
Switching states and voltage vectors of VSI.

S_a	S_a	S_a	Voltage vector V
0	0	0	$V_0 = 0$
1	0	0	$V_1 = \frac{2}{3}V_{dc}$
1	1	0	$V_2 = \frac{1}{3}V_{dc} + j\frac{\sqrt{3}}{3}V_{dc}$
0	1	0	$V_3 = -\frac{1}{3}V_{dc} + j\frac{\sqrt{3}}{3}V$
0	1	1	$V_4 = -\frac{2}{3}V_{dc}$
0	0	1	$V_5 = -\frac{1}{3}V_{dc} - j\frac{\sqrt{3}}{3}V$
1	0	1	$V_6 = \frac{1}{3}V_{dc} - j\frac{\sqrt{3}}{3}V_{dc}$
1	1	1	$V_7 = 0$

Once the 3PH-VSI model has been presented, the rest of the grid-side system components are analyzed next: the inductive filter and the grid voltage model.

2.3.5. Grid Model

The grid voltage is modeled as an ideal three-phase balanced voltage. The three-phase system can be modeled as three independent, but equivalent, single-phase systems as depicted in Figure 2.16.

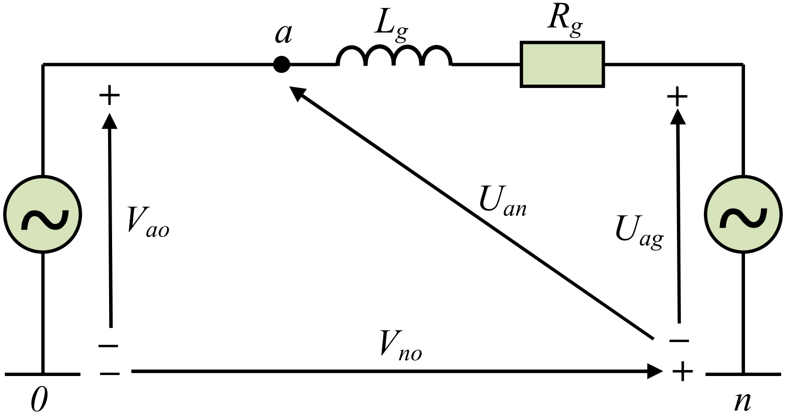

Figure 2.16. Simplified equivalent single-phase grid circuit (a phase).

Taking into account the definitions of variables from the circuit shown in Figure 2.16, the equations for grid current dynamics can be rewritten in the stationary *α-β* reference frame as the following vector equation [17]:

$$U_{\alpha\beta} = L_g \frac{dI_{\alpha\beta}}{dt} + R_g I_{\alpha\beta} + V_{\alpha\beta} \tag{2.27}$$

Where R_g and L_g are the equivalent series resistance and inductance of grid-side filter, respectively. $V_{\alpha\beta}$ is the voltage vector generated by the inverter, $I_{\alpha\beta}$ is the grid current vector, and $U_{\alpha\beta}$ is the grid voltage vector. Note that for simulation and experimental results, the grid voltage is assumed to be sinusoidal with constant amplitude and constant frequency.

For wind energy applications, the power is normally delivered from the inverter to the grid. The instantaneous active power exchanged with the grid (P_g) is a scalar product between the line grid voltages and currents instantaneous space vectors, whereas the instantaneous reactive power (Q_g) is a vector product between them, and they can be expressed in complex form as:

$$P_g = \frac{3}{2}\mathrm{Re}\{U_g I_g^*\} \tag{2.28}$$

$$Q_g = \frac{3}{2}\mathrm{Im}\{U_g I_g^*\} \tag{2.29}$$

where * denotes conjugate of the vector.

After calculation in stationary *αβ* coordinates, instantaneous active and reactive power can be calculated as [18]:

$$P_g = \frac{3}{2}\left(U_\alpha I_\alpha + U_\beta I_\beta\right) \tag{2.30}$$

$$Q_g = \frac{3}{2}\left(U_\beta I_\alpha - U_\alpha I_\beta\right) \tag{2.31}$$

On the other hand, the instantaneous change of active and reactive power can be derived from equations (2.32) and (2.33) as:

$$\frac{dP_g}{dt} = \frac{3}{2}\left(\frac{dU_\alpha}{dt} I_\alpha + U_\alpha \frac{dI_\alpha}{dt} + \frac{dU_\beta}{dt} I_\beta + U_\beta \frac{dI_\beta}{dt}\right) \tag{2.32}$$

$$\frac{dQ_g}{dt} = \frac{3}{2}\left(\frac{dU_\beta}{dt} I_\alpha + \frac{dI_\alpha}{dt} U_\beta - \frac{dU_\alpha}{dt} I_\beta - U_\alpha \frac{dI_\beta}{dt}\right) \tag{2.33}$$

Knowing that the mains voltage is sinusoidal and balanced, the components can be given by the following expression:

$$\overline{U} = U_\alpha + jU_\beta = \left|\overline{U}\right| e^{j\omega t} = \left|\overline{U}\right| \cos \omega t + j\left|\overline{U}\right| \sin \omega\, t \tag{2.34}$$

where ω is the angular frequency of the grid voltage in *rad/s* given by:

$$\omega = 2\pi f \tag{2.35}$$

And *f* is the frequency of the grid voltage in *Hz*.
Therefore, the following equation can be deduced form equation (2.34) as:

$$\frac{dU_\alpha}{dt} = \frac{d\left(\left|\overline{U}\right| \cos \omega t\right)}{dt} = -\omega\left|\overline{U}\right| \sin \omega t \tag{2.36}$$

$$\frac{dU_\beta}{dt} = \frac{d\left(\left|\overline{U}\right| \sin \omega t\right)}{dt} = \omega\left|\overline{U}\right| \cos \omega t \tag{2.37}$$

To simplify, equations (2.36) and (2.37) become as:

$$\frac{dU_\alpha}{dt} = -\omega\, U_\beta \tag{2.38}$$

$$\frac{dU_\beta}{dt} = \omega\, U_\alpha \qquad (2.39$$

Substituting equations (2.27), (2.38), and (2.39) into equations (2.32) and (2.33), the power variations can thus be obtained as:

$$\frac{dP_g}{dt} = \frac{3}{2}\left[-\omega U_\beta I_\alpha + \frac{U_\alpha}{L_g}\left(V_\alpha - U_\alpha - I_\alpha R_g\right) + \omega\, U_\alpha I_\beta + U_\beta\left(V_\beta - U_\beta - I_\beta R_g\right) \right] \qquad (2.40)$$

$$\frac{dQ_g}{dt} = \frac{3}{2}\left[\omega U_\alpha I_\alpha + \frac{U_\beta}{L_g}\left(V_\alpha - U_\alpha - I_\alpha R_g\right) + \omega U_\beta I_\beta - U_\alpha\left(V_\beta - U_\beta - I_\beta R_g\right) \right] \qquad (2.41)$$

By considering equations (2.30) and (2.31), $\overline{U}\overline{V}^* = \left(U_\alpha V_\alpha + U_\beta V_\beta\right) + j\left(U_\beta V_\alpha - U_\alpha V_\beta\right)$, and $\left|\overline{U}\right|^2 = U_\alpha^2 + U_\beta^2$, equation (2.40) and (2.41) can be rewritten as:

$$\frac{dP_g}{dt} = -\frac{R_g}{L_g} P_g - \omega\, Q_g + \frac{3}{2L_g}\left(\mathrm{Re}\left(\overline{U}\,\overline{V}^*\right) - \left|\overline{U}\right|^2\right) \qquad (2.42)$$

$$\frac{dQ_g}{dt} = \omega\, P_g - \frac{R_g}{L_g} Q_g + \frac{3}{2L_g}\mathrm{Im}\left(\overline{U}\,\overline{V}^*\right) \qquad (2.43)$$

2.4. Control System Development

This section presents a control development for a DC/DC boost converter and a three-phase voltage source inverter (3PH-VSI) using FS-MPC strategy. Two individual FS-MPC control loops are developed due to the decoupled nature of the DC/DC boost converter and 3PH-VSI. The control strategy minimizes cost functions, which represent the desired behavior of the converters. At the machine-side, the rectified (inductor) current error is minimized, while at the grid-side, the active power and reactive power are directly controlled.

2.4.1. FS-MPC of DC/DC boost converter with Maximum Power Extraction

2.4.2. Proposed MPPT control

A block diagram of the developed FS-MPC strategy for DC-DC boost converter is depicted in Figure 2.17. Owing to the control of switch S, the maximum power of the variable speed wind turbine is extracted and energy is transferred to the utility grid via three-phase voltage source inverter (3PH-VSI). The steps necessary for the control algorithm are as follows:

1. The wind speed V_w is measured.

2. The desired generator speed ($\omega^* = \omega_{r\_opt}$) is calculated with the following equation:

$$\omega^* = \frac{\lambda_{opt}}{R} V_w \tag{2.44}$$

3. The error between reference and actual speed is fed into the PI controller to set the reference torque generator (T_e*). The reference torque generator can be expressed as:

$$T_e^* = \left(K_{p\omega} + \frac{K_{i\omega}}{S}\right)(\omega^* - \omega_r) \tag{2.45}$$

Where $K_{p\omega}$ and $K_{i\omega}$ are the proportional and integral gains for generator speed control.

4. The reference torque (T_e*) participates to calculate the reference rectified (inductor) current (I_L*) by measuring the rectified output voltage (V_{in}), as indicated in the following equation:

$$I_L^* = \frac{T_e^* \, \omega_r}{V_{in}} \tag{2.46}$$

5. The I_L* obtained from equation (2.46), the actual rectified (inductor) current I_L, and the converter voltages V_{in} and V_o are defined as inputs of the digital FS-MPC to obtain considerable information in one sampling period (T_s) and to generate control pulses for the insulated gate bipolar transistor-based DC/DC boost converter for operating the wind generator at the optimum speed.

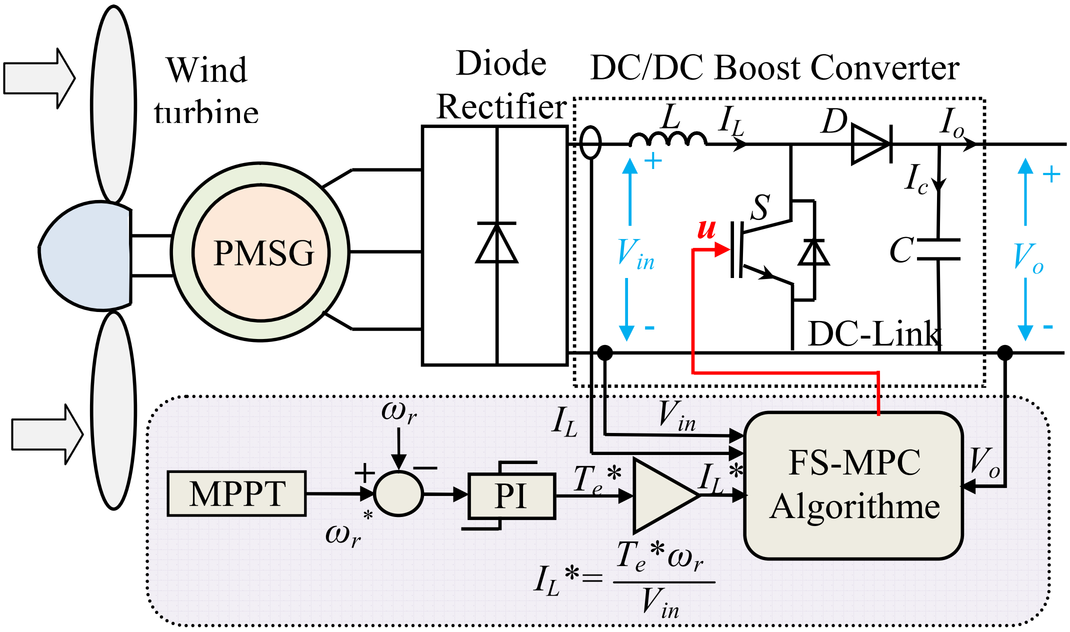

Figure 2.17. DC/DC boost converter control for Maximum Power Point Tracking.

2.4.3. Design of the FS-MPC algorithm for DC/DC boost converter

The main characteristic of FS-MPC strategy of converters is the use of the converter model to predict the behavior of the controlled variables in the following sampling instants. To predict the future behavior of the system variables, the discrete-time model of the DC/DC boost converter should be developed. For simplicity, the forward Euler method is used here.

The discrete-time model of the DC/DC boost converter is used to derive equation (2.13) and (2.14), considering the sampling period T_s, when the switch is turned "off" or "on" the predicted control variables is given by equation (2.47) and (2.48), respectively.

$$i_L(k+1)=i_L(k)+\frac{T_s}{L}\left(v_{in}(k)-v_o(k)\right) \tag{2.47}$$

$$i_L(k+1)=i_L(k)+\frac{T_s}{L}v_{in}(k) \tag{2.48}$$

The prediction of the controlled variable I_L can be realized for the next sampling interval ($t_k + 1$) with the aim to have control schemes simultaneously in the present and in the future. Measured values of I_L, V_{in}, and V_o are considered as inputs for the FS-MPC algorithm. The estimation of the future behavior of the controlled variables is performed on the basis of the evaluation of a cost function.

The determination of cost function type is a very important factor in FS-MPC algorithm because it represents the optimized difference between the controlled and the desired values of the variables.

In our studied case the cost function for the DC/DC boost converter is given by the following equation:

$$J=\left| i_L(k+1)-i_L^* \right| \tag{2.49}$$

The cost function assures the tracking of the rectified (inductor) current I_L from the reference current I_L* provided by the MPPT algorithm. For each sampling step the cost function is evaluated twice for each switching state.

Evaluation of cost function for different switching states determines the control actions for the next time instant. Figure 2.18 illustrates the FS-MPC process for the MPPT control of DC/DC boost converter.

The dotted line corresponds to the MPPT output, which defines the desired current I_L*. At the sampling time t_k the FS-MPC algorithm must decide between S_0 and S_1 on the basis of having a minimized error thanks to the used cost function J.

The control actions taken by this technique are shown in black line while the other choices are inactive. All steps of the proposed FS-MPC algorithm are presented in Figure 2.19.

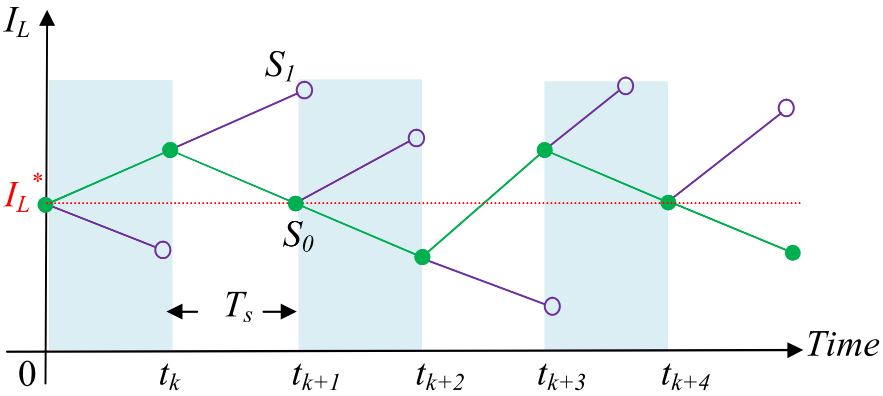

Figure 2.18. Finite state MPC process.

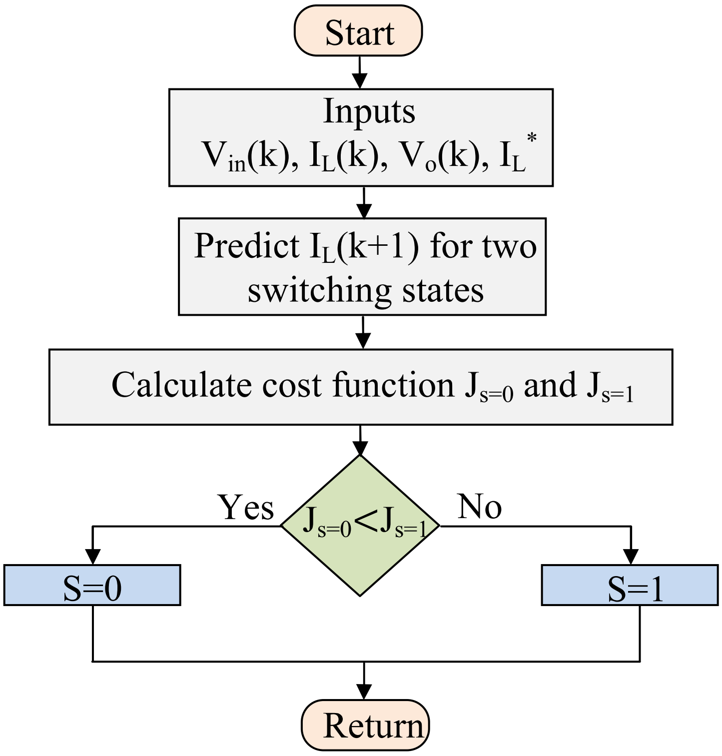

Figure 2.19. Flow chart of FS-MPC.

2.4.4. FS-MPC for direct Power Control of 3PH-VSI

The grid power factor can be unity, leading, or lagging, as shown in Figure 2.20. It is often required by the grid operator that a wind energy system provide a controllable reactive power to the grid support the grid voltage in addition to the active power production. Therefore, a wind energy system can operate with the power factor angle in the range of $\pi/2 \leq \varphi \leq 3\pi/2$.

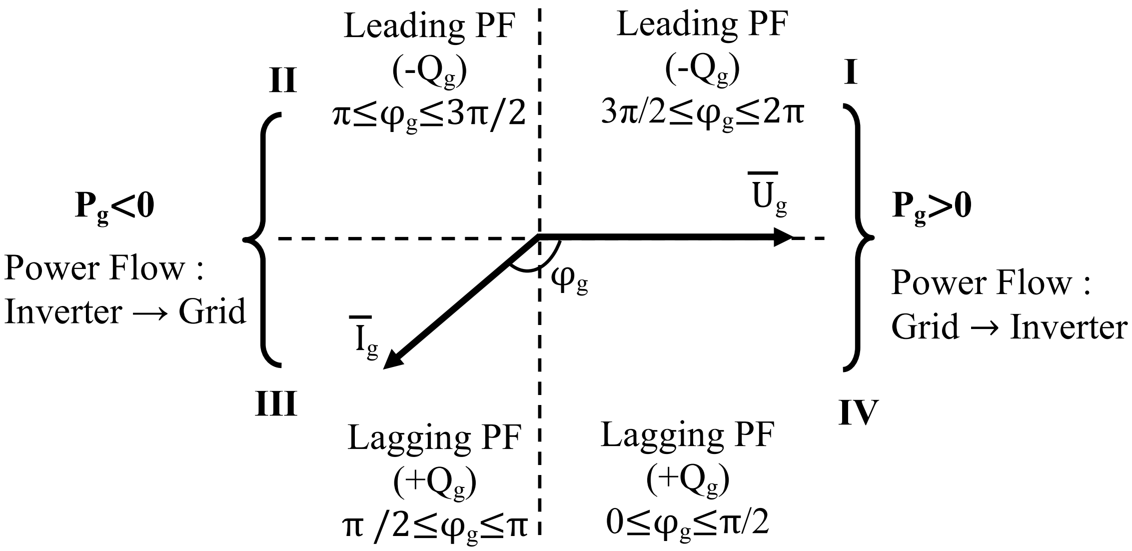

Figure 2.20. Phasor diagram and of power factor (PF).

Various schemes of control systems for the grid-tied inverter were proposed [19, 20]. Presented stable systems are based on independent control of the grid active and reactive power. Here, to design the structure of the control system a simpler FS-MPC scheme is developed.

Such strategy makes it possible to directly control the active and reactive power of the whole system without inner control loops. In order to independently control the grid power components (P_g and Q_g), the behavior of the grid active and reactive power should be predicted.

By using the utility grid model, and considering the instantaneous power theory, it is possible to predict the behavior of the grid active and reactive power at the output of the 3PH-VSI. So, prediction equations for the both powers can be defined by discretising equations (2.42) and (2.43). Hence, the discrete-time model of the grid power components is as follows:

$$P_g(k+1) = T_s\left[-\frac{R_g}{L_g}P(k) - \omega Q(k) + \frac{3}{2L_g}\left(\mathrm{Re}\left(\overline{U}\overline{V}^*\right) - \left|\overline{U}\right|^2\right)\right] + P_g(k) \tag{2.50}$$

$$Q_g(k+1) = T_s\left[\omega P(k) - \frac{R_g}{L_g}Q(k) + \frac{3}{2L_g}\mathrm{Im}\left(\overline{U}\overline{V}^*\right)\right] + Q_g(k) \tag{2.51}$$

where Ts is the time length of sampling period.

However, it can be seen that the prediction based on power derivatives using equations (2.50) and (2.51) are very complicated, making it not easy to implementation. Here, a simpler prediction scheme is developed.

The discrete-time model of equation (2.27) can be expressed as:

$$I_{\alpha\beta}(k+1) = T_s\left(U_{\alpha\beta}(k) - V_{\alpha\beta}(k) - I_{\alpha\beta}(k)R_g\right)/\,L_g + I_{\alpha\beta}(k) \tag{2.52}$$

Assuming the constant grid voltage during the sampling period, $P_g(k+1)$ and $Q_g(k+1)$ can then be calculated by substituting equation (2.52) into equations (2.30) and (2.31).

This prediction scheme is more straightforward than equations (2.50) and (2.51) where power derivatives are used, thus reducing the computational burden.

This is quite useful because calculating the cost function can be very time consuming for a hardware processor, especially if several constraints are included in the cost function while high sampling frequency is required.

After the power is predicted, the next step is to evaluate the effects of each voltage vector on the active and reactive powers and to select the one which produces the least power ripple according to a specific cost function.

For this command, the control objectives are chosen as the DC-link voltage and the power factor of the AC grid, which can be regulated by controlling the active power P_g and reactive power Q_g, respectively.

Therefore, the cost function for three-phase voltage source inverter (3PH-VSI) can be defined as follows:

$$J = \sqrt{\left(\left(P_g * - P_g(k+1)\right)^2 - \left(Q_g * - Q_g(k+1)\right)^2\right)} \tag{2.53}$$

The block diagram of grid-side inverter control system that's the FS-MPC approach performs a direct control of the active and the reactive power for the possible switching combinations is depicted in Figure 2.21.

The powers are controlled directly without any inner loops. The DC-link voltage V_o is regulated by means of a proportional-integral (PI) controller whose output is the active power delivered to the grid.

The grid reference power can be computed from Equation. (2.54) as:

$$P_g * = (V_o * - V_o)\left(K_p^p + \frac{K_i^p}{s}\right) \tag{2.54}$$

Where:

K_{pp} is the DC-link voltage controller proportional gain [*W/V*];

K_{ip} is the DC-link voltage controller integral gain [*W/Vs*];

There are additional blocks in the control system: the variables transformations, calculations, and powers estimation. As a result, stable, fast, and decoupled control of both powers.

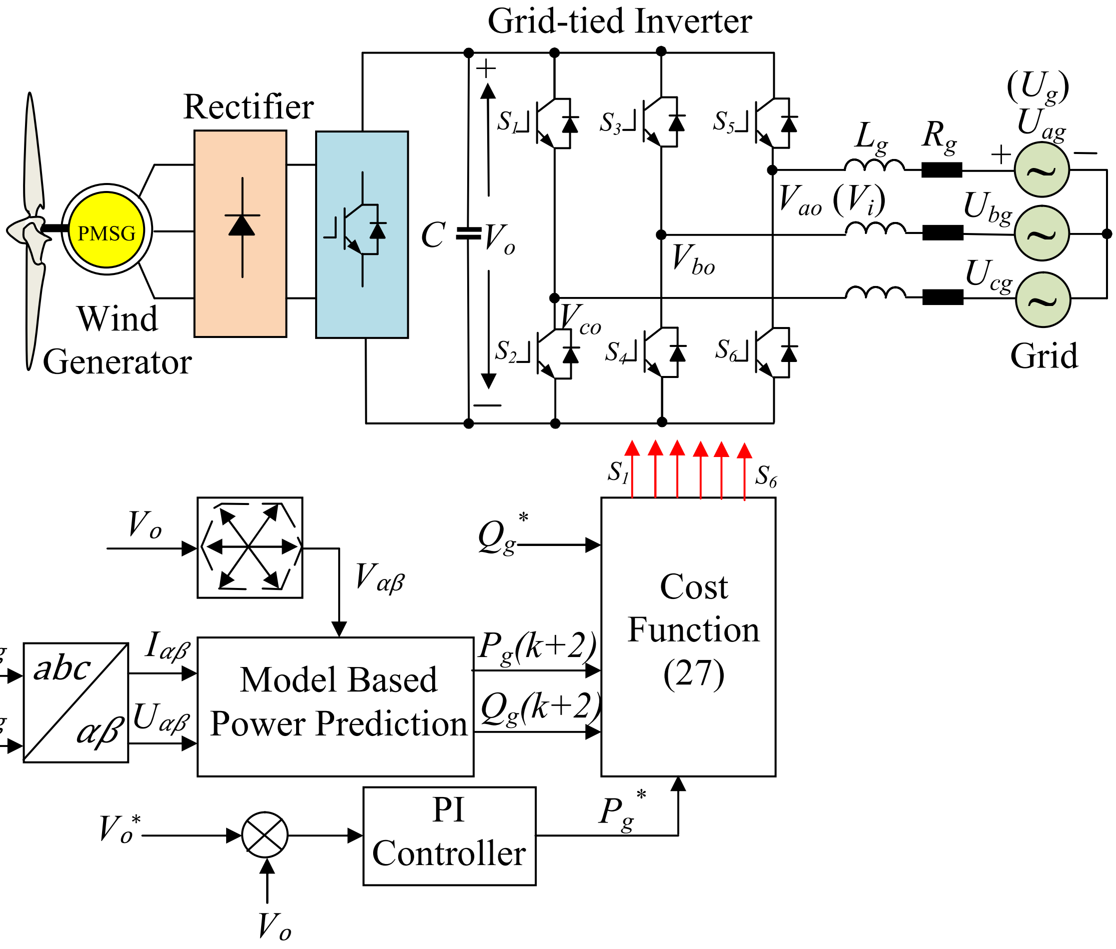

Figure 2.21. Basic principle of the proposed FS-MPC direct power control strategy for delivered power to the grid.

Once again, as explained previously, one-step delay influence needs to be eliminated. Here, a two-step prediction is employed to eliminate the influence of one-step delay.

2.4.5. Delay compensation

To compensate the delay associated with the digital implementation, the error between the reference and the predicted value at (t_k+2) is considered, as discussed in section 2.7. Thus, the predictive algorithms minimize the error at (t_k+2) and apply the optimum switching state at (t_k+2) .

However, it can be seen that the power prediction using equation (2.50) and (2.51) are very complicated, which makes difficult implementation.

To overcome this issue a simple prediction scheme using linear extrapolations is used [21, 22]. To visualize this prediction theory, Figure 2.22 depicts an example of the active power trajectory and the switching position with 2-step prediction.

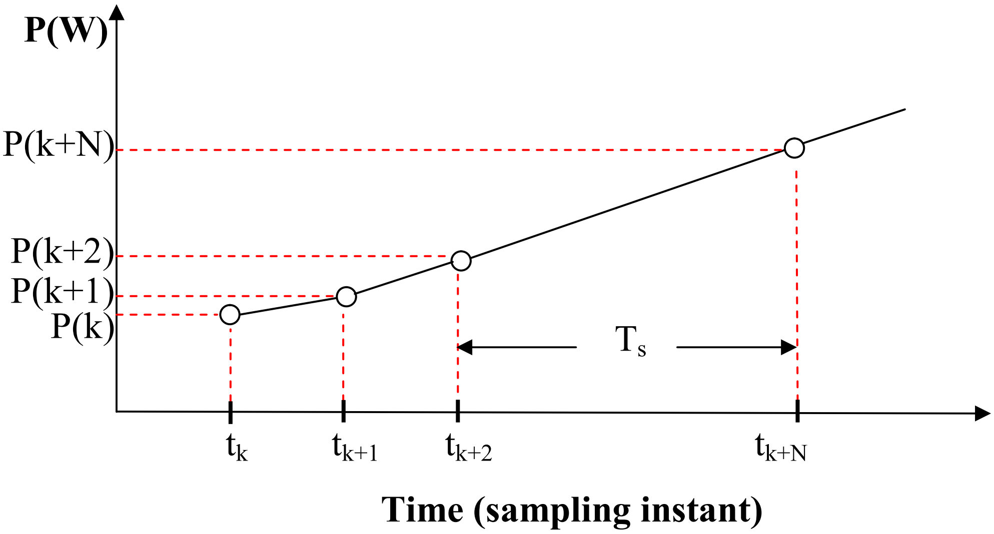

Figure 2.22. Active power trajectories and switching position with *N*-step prediction.

Since the predicted active and reactive power $P_g(K+1)$ and $Q_g(k+1)$ they can be simply extrapolated to the (t_k+2) state as follows:

$$P_g(k+2) = 2P_g(k+1) - P_g(k) \tag{2.55}$$

$$Q_g(k+2) = 2Q_g(k+1) - Q_g(k) \tag{2.56}$$

Hence, the cost function in equation (2.53) should be modified and presented in the new form as follows:

$$J = \sqrt{\left(\left(P_g * - P_g(k+2)\right)^2 - \left(Q_g * - Q_g(k+2)\right)^2\right)} \tag{2.55}$$

2.5. Simulation Results and Discussion

Simulations are conducted with MATLAB 7.1 software to confirm the effectiveness of the proposed FS-MPC strategy. The particular parameters of the system are given in the Table 2.3.

Table 2.3

Wind Energy System Parameters.

Parameter	Value	Units
Rated output power of PMSG (P_N)	5	*Kw*
Rated torque (T_N)	22.5	*Nm*
PMSG stator resistance (R_s)	0.65	Ω
PMSG stator inductance (L_s)	8	*mH*
Permanent magnet flux (Ψ)	0.39	*Wb*
Pole pairs (P)	4	-
Torque constant (k_T)	2.39	*Nm/A*
Wind turbine blade length (R)	1.02	*m*
Air density (ρ)	1.225	kg/m^3
Optimal tip speed ratio (λ_{opt})	8.08	-
Maximum power coefficient ($C_{p\,max}$)	0.48	-

The simulation of the wind speed profile corresponding to the used turbine is shown in Figure 2.23(a). Figure 2.23(b) show that the power coefficient C_p is adjusted to its reference, which indicate that the captured power is maximal.

Figure 2.23(c) shows the control performance of the rectified current. As depicted, the control performance of the FS-MPC algorithm is good under wind fluctuations. Figure 2.23(d) shows a good following of the rotor speed to the reference speed which controlled by the generator torque shown in Figure 2.23(e).

Figure 2.23(f) shows the DC-link voltage, which is kept constant at approximately 300V. It is observed that the grid current is almost sinusoidal that improves the performances of the grid-side converter (Figures 2.23(g)).

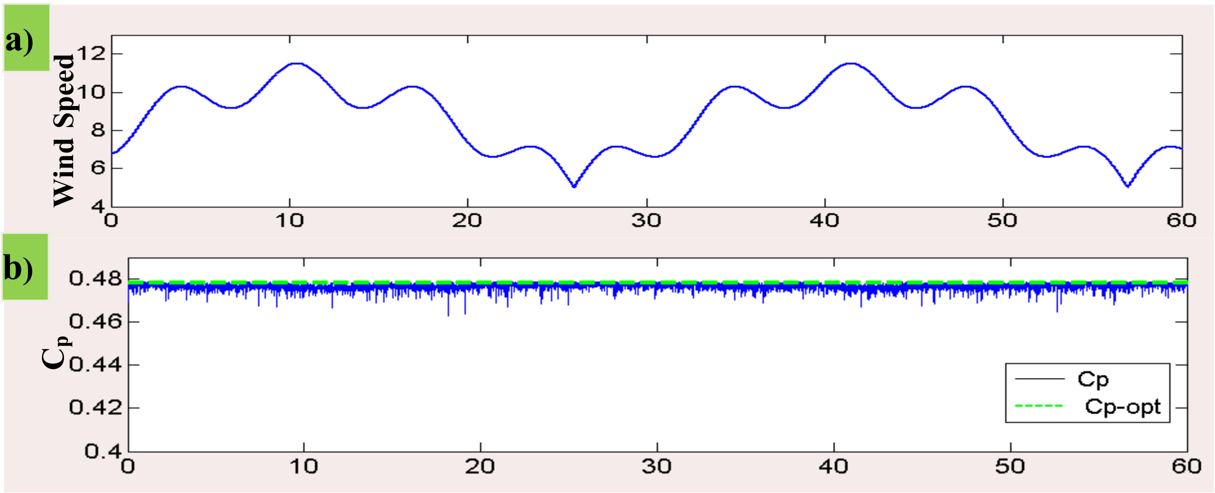

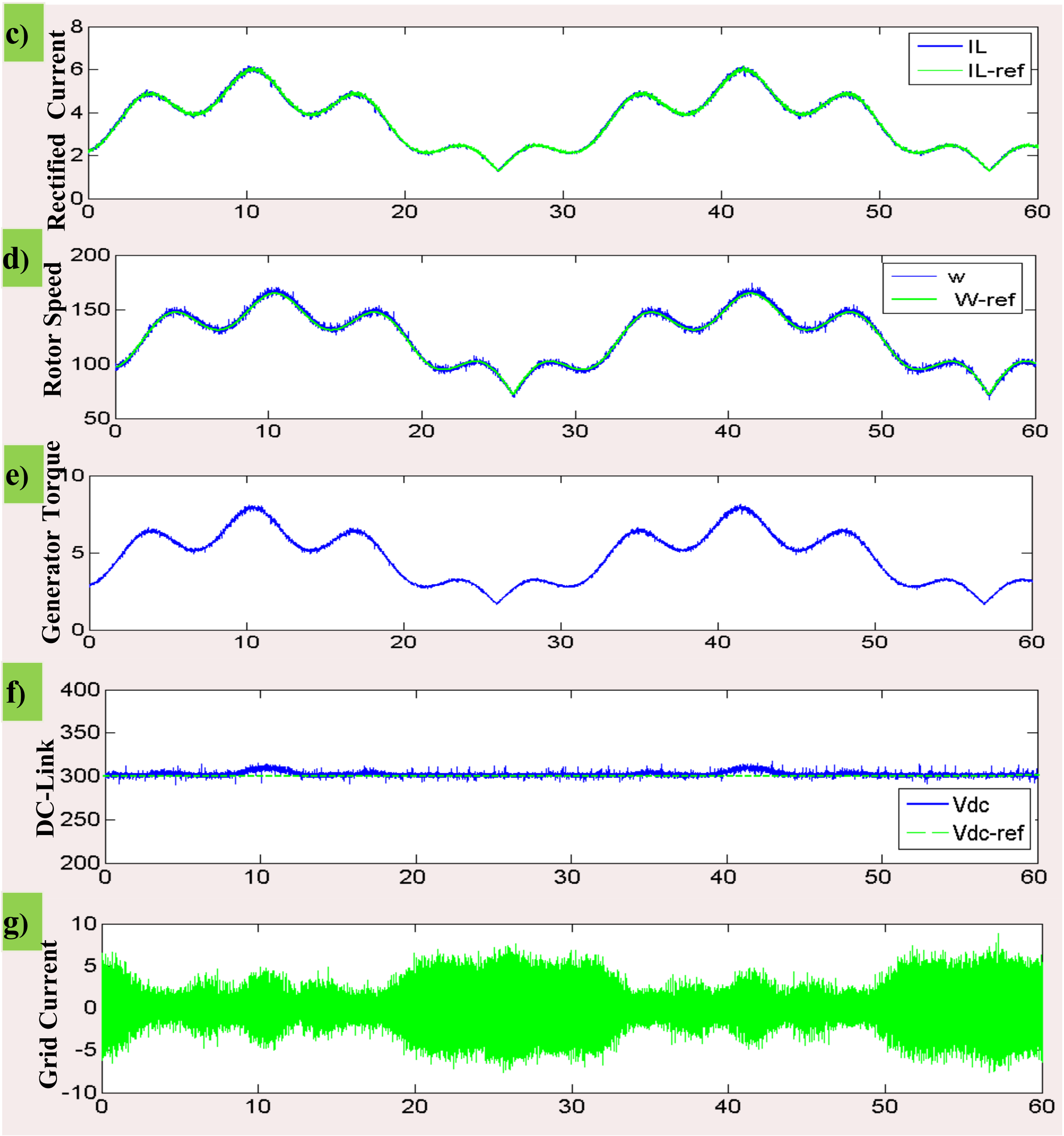

Figure 2.23. Simulation results of system for wind speed variation.

2.5.1. Simulation Results and Discussion

This section compares the simulation results of the PMSG wind turbine using the proposed FS-MPC control scheme with that of the same wind turbine using the traditional PI controller.The wind speed profile shown in Figure 2.24(a) is used to test the proposed FS-MPC strategy and conventional PI controller. We compare power coefficient C_p in Figure 2.24(b). Figure 2.24(b) depicts that with the proposed FS-MPC method, C_p only varies in a narrow range, $0.40 < Cp < 0.48$. By contrast, with the traditional PI controller, C_p varies in a wide range. As shown in Figure 2.24(c), the optimum generator power tracking error can be maintained within 5% by using the proposed FS-MPC strategy, whereas this tracking error commonly exceeds 15% when the conventional PI controller is used, and thus is completely unacceptable. Generally because the power coefficient C_p, with the conventional PI controller, is reduced significantly during sudden variations in wind speed.

These comparative simulation results demonstrate that the proposed FS-MPC strategy is superior to the conventional PI control method in terms of optimum generator power tracking control and maximum power extraction. As shown in Figure 2.24(d), rotor speed can be accurately controlled to adapt to the wind speed variations, and the speed tracking error can be kept within 5% by using the proposed FS-MPC strategy. On the contrary, the speed tracking error exceeds 10% when the conventional PI controller is used. Thus, the proposed FS-MPC strategy achieves better optimum rotor speed tracking control than the conventional PI controller. Figure 2.24(e) indicates that a higher mechanical energy part is stored in its mechanical system to accelerate the rotor speed by the proposed FS-MPC strategy than that by the traditional PI controller. This result affirms the improved efficiency of the proposed FS-MPC strategy.

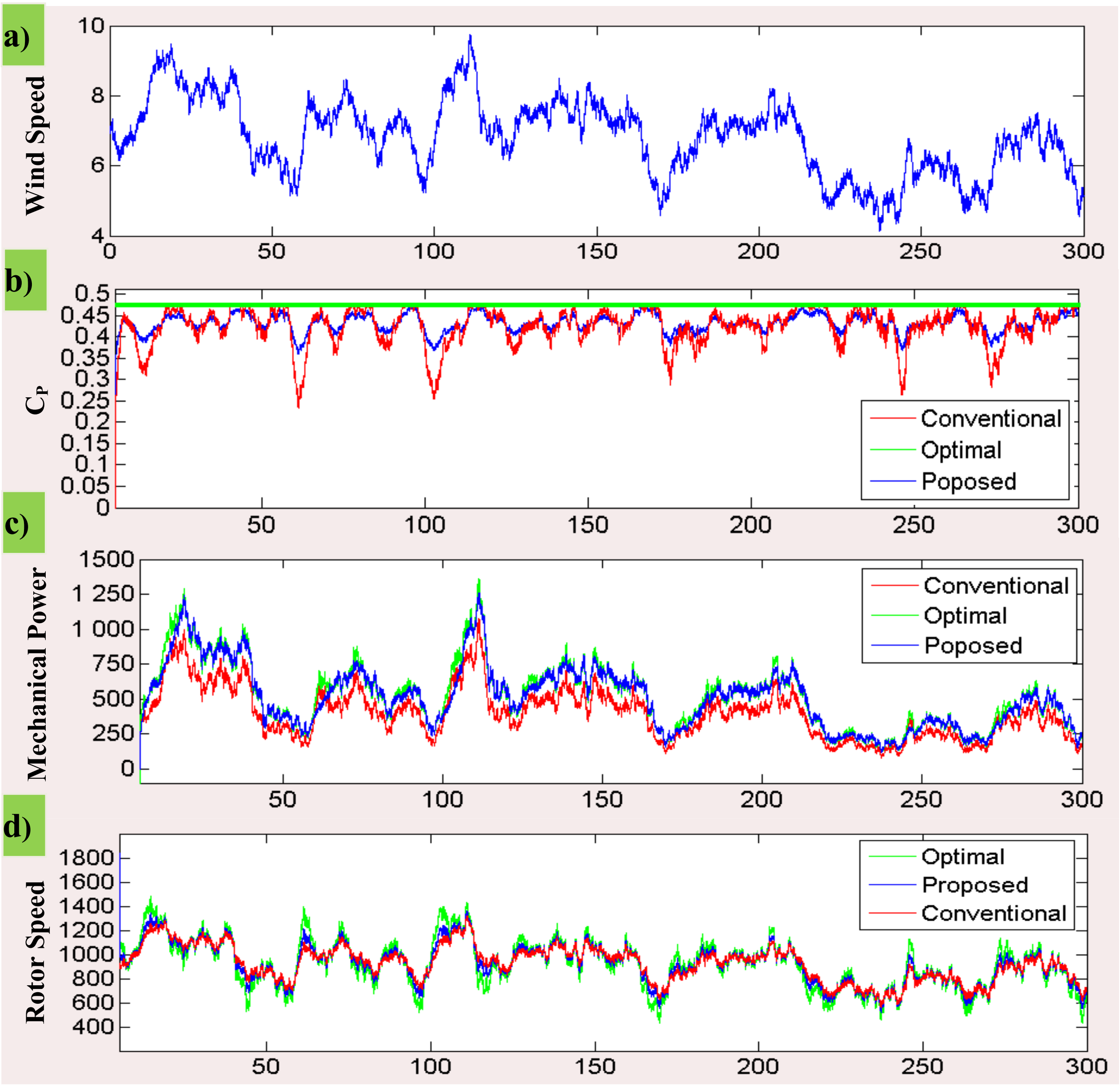

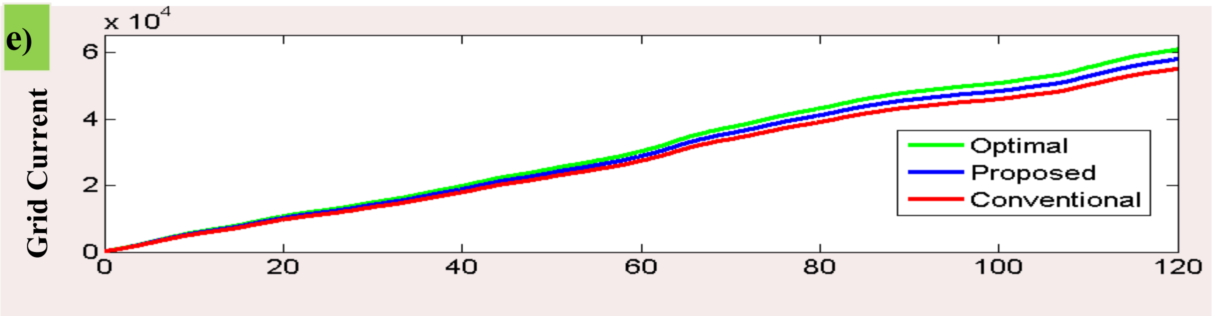

Figure 2.24. Comparison of the proposed FS-MPC method and traditional PI control method.

2.6. Experimental Results and Discussion

An experimental platform of wind energy system connected to the grid is developed in the LAS laboratory as shown in Figure 2.25 to verify the performance of the developed FS-MPC technique. The first machine is a DC-motor controlled in torque producing mode, in which the torque reference changes along with the rotor speed. A preset table is created between the reference torque and speed depending on the power characteristic of the wind turbine, in which the mechanical torque is changed by wind velocity and generator speed.

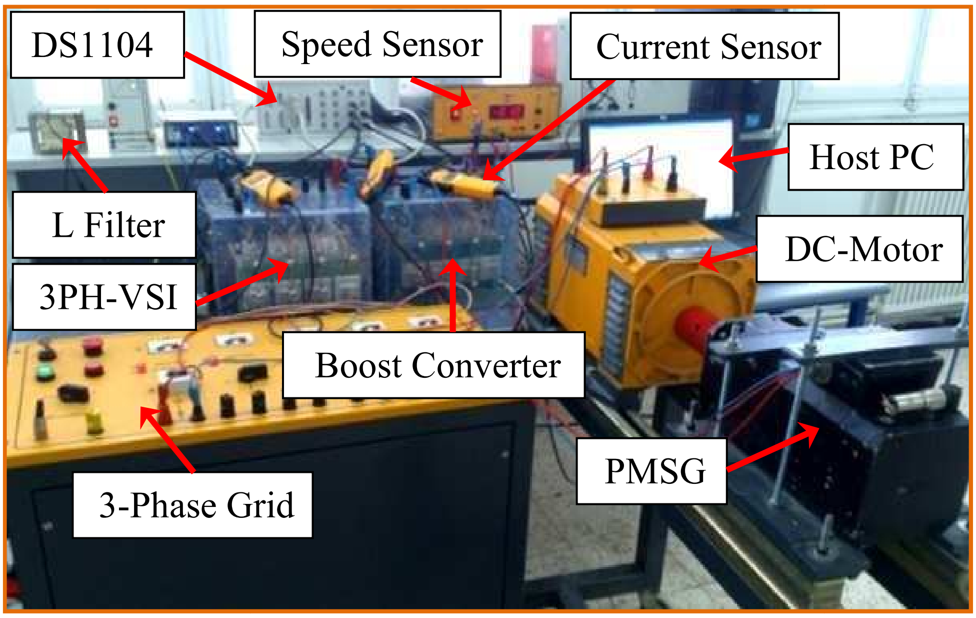

Figure 2.25. Prototype of direct-driven wind energy system.

Figure 2.26 shows the global schema of the studied system connected to the grid, examined, and evaluated in real-time when the generator speeds up and the speed of the PMSG is governed by the control device of the machine-side converter. The real-time implementation of the developed FS-MPC techniques requires dSPACE 1104 cards and a complex programmable logic device. The DS1104 controller must guarantee the three main tasks, namely, (i) provide the torque reference from the wind turbine emulator, (ii) extract and exploit the maximum power from the wind (iii), and feed the grid with good quality of electric energy. The controller performance is evaluated in both the machine- and grid-side converter. The obtained results are presented in dynamic conditions for the variations in wind speed and steady state for reference active and reactive power.

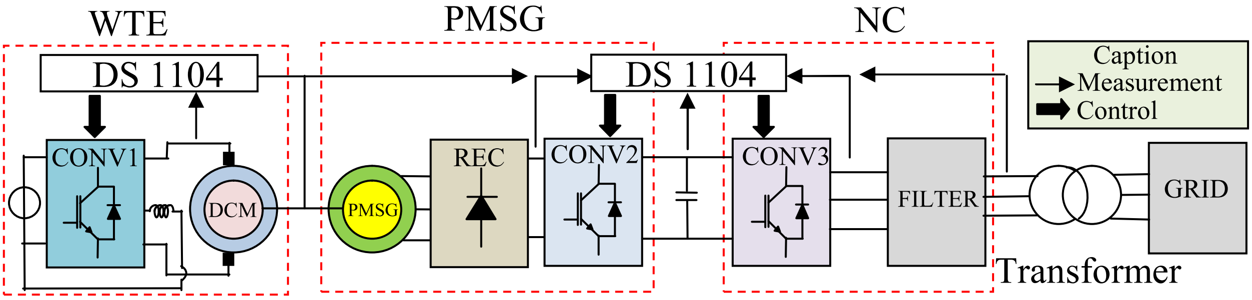

Figure 2.26. Schematic diagram of the experimental platform.

2.6.1. Test Results under Transient State

Figures 2.27(a)-(j) show several experimental results presented using the Control Desk software. The wind speed is shown in Figure 2.27(a). Figure 2.27(b) shows that the rotor speed of the PMSG can track the tendency of the optimal reference speed very well and regulate the turbine torque to extract maximum power from the wind generator. The power coefficient C_p is usually near to the optimal value of C_{p_max}= 0.48 despite the high rotational turbulence as shown in Figure 2.27(c). Figure 2.27(d) presents the control performance of the rectified (inductor) current. As depicted, the control performance of the proposed FS-MPC algorithm is very good under wind variations. Figure 2.27(e) shows the change in electromagnetic torque, we can remark that its value increases as the wind speed increases. The turbine mechanical input power is illustrated in Figure 2.27(f). Typically, the mechanical power is oscillated due to wind speed variations. The DC-link voltage is controlled at its reference with good precision during the wind variations, as shown in Figure 2.27(g). The grid current controlled by the proposed FS-MPC algorithm is displayed in Figure 2.27(h). The grid current can reach the steady state within one cycle, which illustrates that the proposed method has good dynamic performance. The grid current is in phase with the main voltage, as depicted in Figure 2.27(i). Figure 2.27(j) indicates that good tracking performances are achieved in terms of grid active and reactive power with respect to wind speed variations.

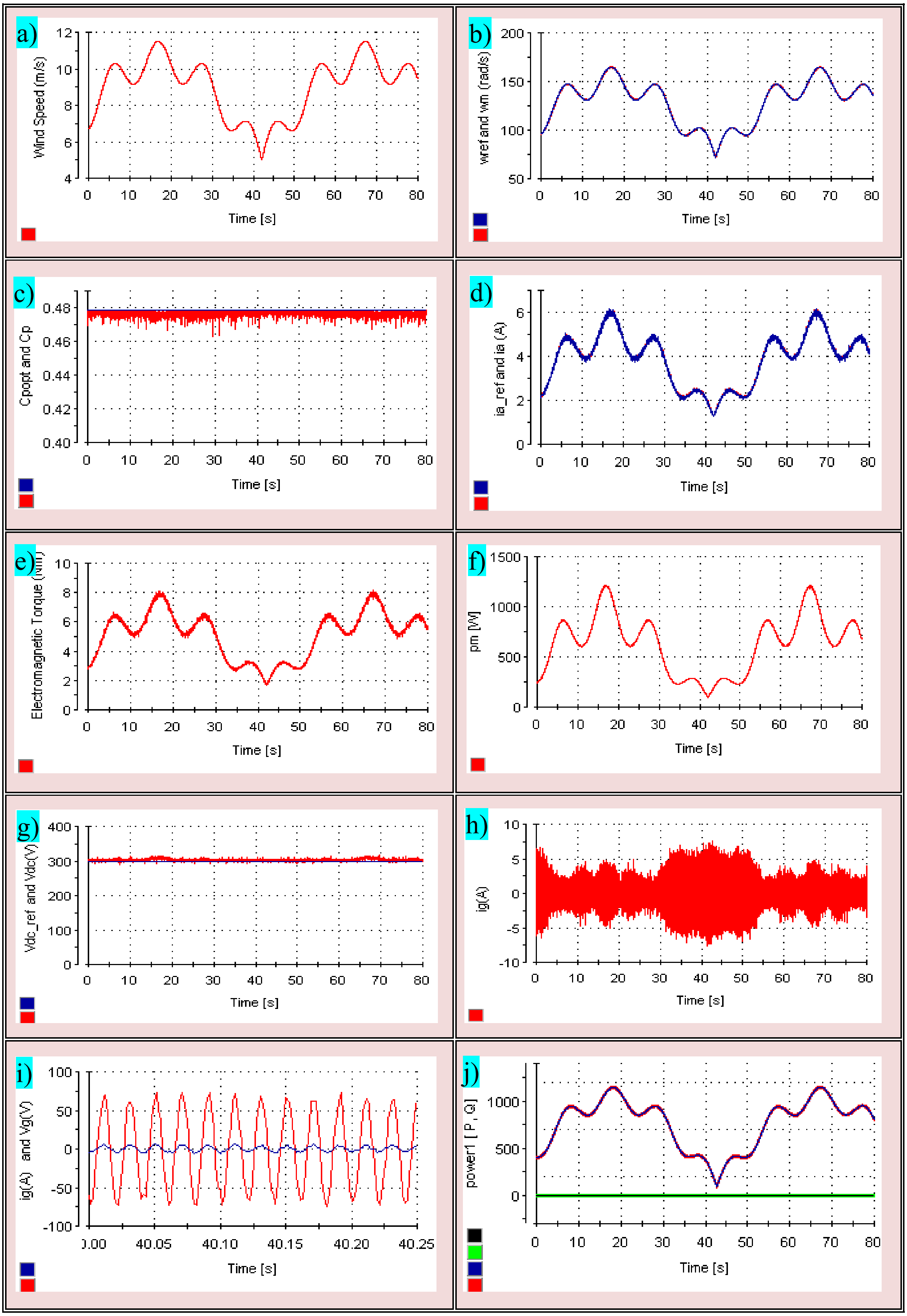

Figure 2.27. Experimental results of system for wind speed variation.

2.6.2. Test Results under Steady-State Condition

The characteristic waveforms of the grid-interfaced wind energy system under steady-state condition, where the wind speed is assumed to be constant, are shown in Figures 2.28(a) to 2.28(d). It is clearly seen from Figure 2.28(a) that the total harmonic distortion (THD_i) of the injected current is less than 5% in the entire three-phase, limit imposed by the IEEE-519 norm. Figure 2.28(b) shows the measured results of the power factor (PF) of the system versus grid connected power. It is obvious that the power factor (PF) is very close to the unity where it presents a value of 0.974, and can satisfy the PF demand in industrial applications. Figure 2.28(c) illustrates the three-phase grid currents of sinusoidal waveforms. Also, it can be clearly remarked that the three-phase currents are symmetric and strictly follow their corresponding phase voltages. The DC link voltage (V_o) is maintained close to its references with good precision and stability. The injected current is in phase with the main voltage, as depicted in Figure 2.28(d).

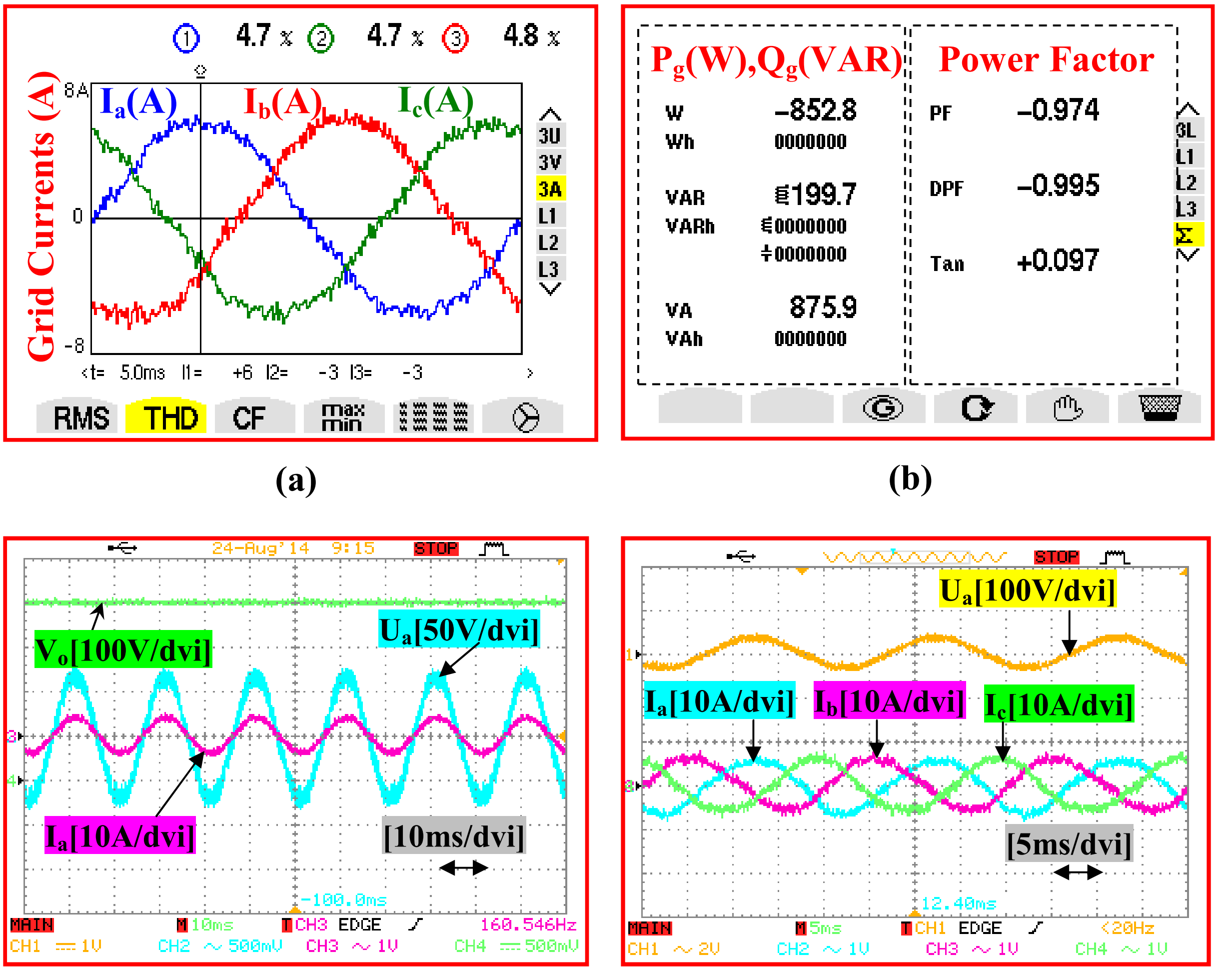

(a) (b)

(c) (d)

Figure 2.27. Experimental steady-state waveforms of proposed FS-MPC direct power control (DPC): (a) THDi of grid currents. (b) Measured power factor. (c) Grid phase voltage and current. (d) Grid phase voltage, grid currents and DC-link voltage.

The experimental results in steady state for unity, lagging, and leading power factor operation with corresponding grid reactive power are illustrated in Figures 2.29(a) to 2.29(c), respectively.

It is clearly seen in this representation that the grid voltage and current for the two cases of the system function.

The first operating with a unity power factor (Figure 2.29(a)) and the second one with a lagging and leading PF (Figures 2.29(b) and 2.29(c)) are in phase for the first case and phase shifted for the second case. In addition, the reactive power reacts correctly in both tests.

In order to test and evaluate the ability of the proposed system to control the reactive power that is governed for unity, lagging, and leading PF functions at the grid-side is tested and evaluated with the conservation of active power constant, as presented in Figure 2.29(d), it shows the capability of controlling the reactive power of the proposed wind energy system. The steady-state (SS) analysis has been carried out and summarized in Table. 2.4.

Table 2.4
Steady-state analysis with experimental results.

Case	P*(W)	Q*(VAR)	eP %	eQ %	eVdc %	THDi %	fsw(Hz)
SS1	1200	0	3.85	1.73	0.63	4.93	885
SS2	850	0	3.36	1.26	0.75	4.70	926
SS3	1200	700	5.56	1.07	0.35	5.30	753
SS4	1200	-700	5.85	1.15	0.47	4.88	992

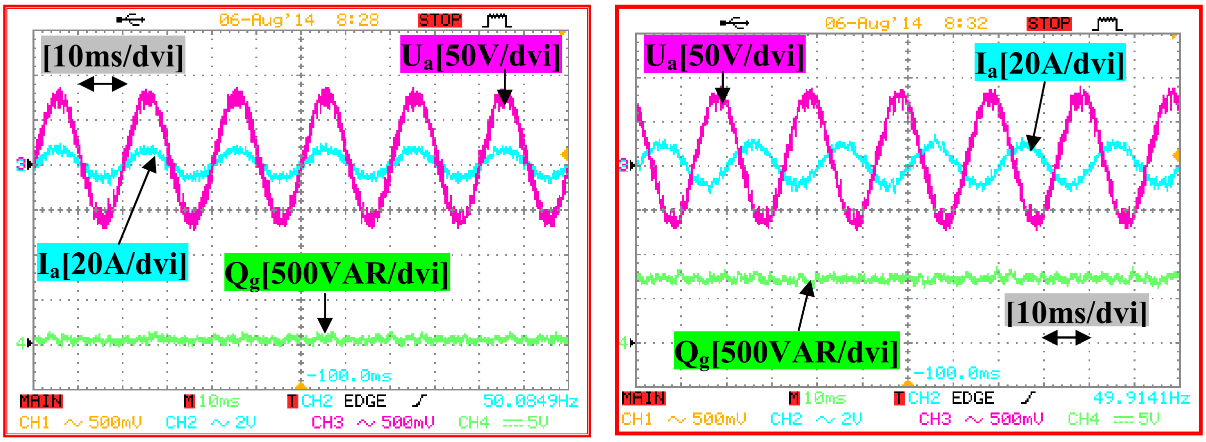

(a) (b)

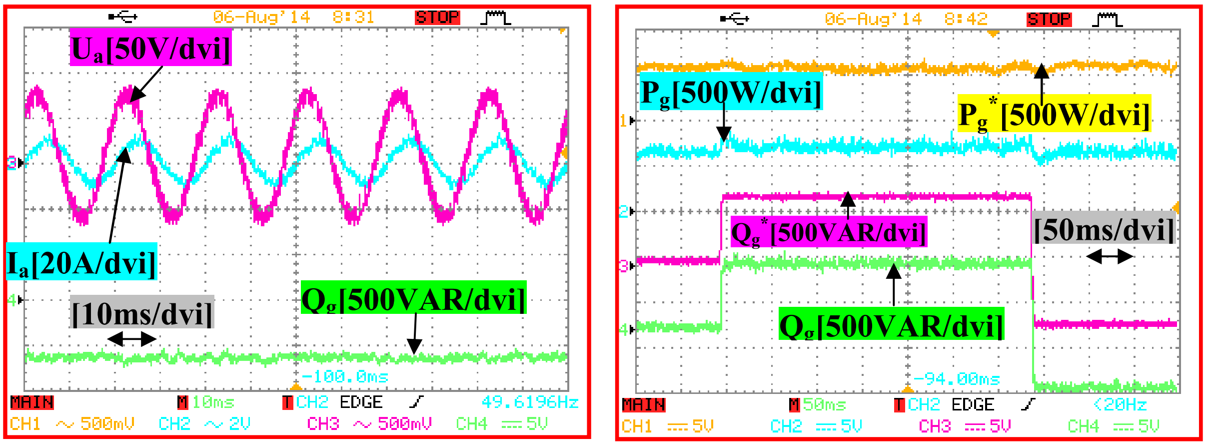

(c) **(d)**

Figure 2.29. Experimental steady-state waveforms of proposed FS-MPC direct power control (DPC): (a) Grid phase voltage, grid current and reactive power for unity power factor case (b) Grid phase voltage, grid current and reactive power for leg power factor case. (c) Grid phase voltage, grid current and reactive power for lead power factor case (d) Step change in Q_g while P_g=Constant.

2.7. Conclusions

In this Chapter, a simple and intuitive approach that uses the FS-MPC strategy was developed for a grid connected PMSG-based wind energy system. For full use of wind energy, the developed control method ensures the decoupling of active and reactive power for the grid-side converter and guarantees maximum power point tracking (MPPT) for the machine-side converter. The operating principle of FS-MPC strategy is presented for ideal and implementation cases. The cost function flexibility and potentiality in achieving different control and technical requirements is discussed. The issues and challenges related to the FS-MPC strategy, such as the computational burden, development of control algorithm, delay compensation, and extrapolation of reference variables is discussed in detail. After literature studies, two FS-MPC strategies were chosen: FS-MPC with MPPT control algorithm for the machine-side DC/DC boost converter, and FS-MPC with direct power control for the grid-side inverter. The wind turbine requirements, such as MPPT and active and reactive power generation, are modeled as the reference control variables. The machine- and grid-side cost functions are defined to deal with these control objectives. During each sampling interval, the control goals are achieved based on minimization of cost functions. The efficiency of the system has been evaluated through simulation and experimental tests. The results showed fast, accurate, and effective responses in dynamic and steady-state operating conditions, and the analysis presented in this Chapter favors the FS-MPC strategy as the next generation control tool to achieve high performance operation for the wind energy systems.

References

[1] **Liserre M, Cardenas R, Molinas M, and Rodriguez J:** “Overview of multi-MW wind turbines and wind parks,” *IEEE Trans. Ind. Electron 2011; 58(4): pp. 1081–1095.*

[2] **Blaabjerg F and K. Ma:** “Future on power electronics for wind turbine systems,” *IEEE J. Emerging and Selected Topics in Power Electron.2013 ; 1(3); pp. 139–152.*

[3] **Blaabjerg F, Liserre M, and K. Ma:** “Power electronics converters for wind turbine systems,” *IEEE Trans. Ind. Appl. 2012; 48(2): pp. 708–719.*

[4] **Kouro S, Cortes P, Vargas R, Ammann U, and Rodriguez J:** “Model predictive control-A simple and powerful method to control power converters,” *IEEE Trans. Ind. Electron.2009; 56(6): pp. 1826–1838.*

[5] **Rodriguez J and Cortes P:** “Predictive Control of Power Converters and Electrical Drives”, *1sted. Chichester,UK: IEEE Wiley press 2012.*

[6] **Cortes P, Kazmierkowski M, Kennel R, Quevedo D, and Rodriguez J:** “Predictive control in power electronics and drives,” *IEEE Trans. Ind. Electron.2008; 55(12): pp. 4312–4324.*

[7] **Rodriguez J, Kazmierkowski M.P, Espinoza J.R, Zanchetta P, Abu-Rub H, Young H.A, and Rojas C.A:** “State of the art of finite control set model predictive control in power electronics,” *IEEE Trans. Ind. Informat.2013; 9(2): pp.1003–1016.*

[8] **Rodriguez J and Cortes P:** “Predictive Control of Power Converters and Electrical Drives”, *Chichester: Wiley 2012.*

[9] **Cortes P, Kouro S, La Rocca B, Vargas R, Rodriguez J, Leon J.I, Vasquez S, and Franquelo L.G:** “Guidelines for Weighting Factors Design in Model Predictive Control of Power Converters and Drives,” *International Conference on Industrial Technology 2009; ICIT Churchill, Australia.*

[10] **Camacho E.F and Bordons C:** “Model Predictive Control”, *2nd ed. London: Springer-Verlag 2007.*

[11] **Wang L:** “Model Predictive Control System Design and Implementation Using MATLAB”, *London: Springer-Verlag, 2009.*

[12] **Linder A, Kanchan R, Stolze P, and Kennel R:** “Model-based Predictive Control of Electric Drives”, *Göttingen: Cuvillier Verlag, 2010.*

[13] **Mohan N, Undeland T.M, and Robbins W.P:** “Power Electronics: Converters, Applications and Design”, *2nd ed. New York: Wiley, 1995.*

[14] **Batarseh I:** “The power MOSFET,” in Power Electronics Handbook: Devices, Circuits, and Applications”, *3rd ed., M. H. Rashid, Ed. Oxford, UK: Elsevier 2011: pp. 43-71.*

[15] **Espinoza J.R:** “Inverters in Power Electronics Handbook: Devices, Circuits, and Applications”, *3rd ed., M. H. Rashid, Ed. Oxford, UK: Elsevier 2011: pp. 357-408.*

[16] **Bouafassa A, Rahmani L, Kessal A, Babes B:** “Unity power factor Converter based on a Fuzzy controller and Predictive Input Current”, *ISA Transactions 2014; 53: pp.1817–1821.*

[17] **Yang S, Lei Q, Peng F.Z, and Qian Z:** "A robust control scheme for grid connected voltage source inverters," *IEEE Trans. Ind. Electron. 2011; 58(1): pp. 202-212.*

[18] **Song Z, Chen W, and Xia C:** "Predictive direct power control for three phase grid connected converters without sector information and voltage vector selection," *IEEE Trans. Power Electron. 2014; 29(10): pp.5518-5531.*

[19] **Laks J.H, Pao L.Y, and Wright A.D:** "Control of wind turbines: Past, present, and future," *in 2009 American Control Conference 2009: pp. 2096-2103.*

[20] **Li S, Haskew TA, and Xu L:** "Conventional and novel control designs for direct driven PMSG wind turbines," *Electric Power Systems Research 2010; 80(3): pp. 328-338.*

[21] **Yaramasu V, Wu B, Rivera M, Rodriguez J, and Wilson A:** "Cost-function based predictive voltage control of two-level four-leg inverters using two step prediction horizon for standalone power systems," *In IEEE Appl. Power Electron. Conf. Expo. (APEC), Orlando, FL, USA 2012; pp. 128–135.*

[22] **Davari S, Khaburi D, and Kennel R:** "Using a weighting factor table for FCS-MPC of induction motors with extended prediction horizon," *In IEEE Ind. Electron. Conf. (IECON) 2012, pp. 2086–2091.*

Chapter 3

A Novel Predictive Controller Designs and High Efficiency Power Conditioning Topology for Maximum Power Extraction in Grid Connected Wind Energy Systems

Abstract

This Chapter suggests a high gain and high efficiency power conditioning topology for grid connected wind energy systems based on permanent magnet synchronous generator (PMSG). The proposed configuration combines the advantages of proven wind turbine technologies, such as efficient machine-side converter, and low cost grid-side inverter. Two fixed frequency model predictive controllers (MPCs) are introduced to control the complete wind generation system. The first one, is a hill climb searching (HCS) algorithm utilizes MPC for controlling the DC/DC switched inductor boost converter (SIBC) and maximize the energy harvest. The second one, is a robust predictive current controller (PCC) is designed for controlling the single-phase full bridge inverter, improve the power quality, and achieves a sinusoidal current into the grid with low distortion.

The major tasks being carried out in this Chapter are summarized as follows:

- Continuous- and discrete-time modeling of the complete wind energy system including a DC/DC switched inductor boost converter (SIBC) and single-phase full bridge inverter are presented;
- Independent predictive control loops are presented for the SIBC and single-phase full bridge inverter;
- The average semiconductor device switching frequencies are fixed at 10 kHz for the SIBC and single-phase full bridge inverter.
- Feasibility of the proposed converters and control scheme is verified through MATLAB simulations and dSPACE DS1104-based experiments on a 3 kW wind energy conversion system prototype.

3.1. Introduction

The low conversion efficiency of wind turbines is an obstacle to the growth of wind energy systems. MPPT ensures that the maximum available wind energy is harnessed from the wind turbines. Many MPPT methods have been suggested over the past few decades; the relative merits of these various approaches are discussed in [1, 2]. The critical operating regime in wind energy systems is low wind velocity. Capturing all of the available wind power during low wind speed periods can substantially improve the system performance. An effective MPPT controller and converter can use available energy to significantly reduce the amount of installed wind energy systems. Considering the MPPT techniques listed in [1], candidate techniques include P&O [3, 4] and hill climb searching (HCS) algorithms [5]. Each approach has certain advantages and disadvantages for the present application. Hill climb searching (HCS) algorithm is a well-known technique with relatively good performance [6]; however, HCS algorithm cannot always converge to the true maximum power point (MPP). Also, HCS algorithm is relatively slow, which limits its ability to track transient environmental conditions.

The main contribution of this Chapter is to improve the HCS algorithm performance by predicting the error two-steps ahead in horizon of time through the MPC technique. The proposed method consists of two-stage. The first stage is a HCS algorithm used to generate the necessary reference current that achieves the maximum power point (MPP). The model predictive control (MPC) constructs the second stage. It is based on the optimization of the cost function that determines the switching action for the SBIC switch. Adding MPC improves the performance of the MPPT control and gives faster response and better operation in case of fast environmental changes without requiring expensive sensing and communications equipment. The SIBC is chosen as a DC/DC boosting stage converter. It is controlled using two-steps MPC-MPPT algorithm. The main advantages of the SIBC are high boosting gain, lower switching losses. With this topology, the 50 V DC-input voltage can be boosted to 600 V with 12 DC/DC conversion gain ratio and efficiency reaches approximately to 92.5%. These surveys show that SIBC topologies are more efficient, lighter, less bulky and less costly than the conventional DC/DC boost converters.

In the wind energy systems grid-connected inverters are required to help convert the DC power to AC power in a single conversion stage [7, 8]. Numerous inverter circuits can be used for wind power conditioning system (PCS) [9]. For small scale distributed renewable energy generation systems, single-phase utility interactive inverters are of particular interest [10]. This type of application normally requires a power level lower than 5 kW [11]. The Single-phase full bridge inverter is widely used in the conventional low power applications. It is simple to control, easily integrated and reliable. These inverters commutate at high frequencies and thus eliminate the low frequencies harmonics, smaller filters are used and the cost and the physical size are reduced. Moreover, the power factor created by these types of inverters could be controlled and the losses on the grid-side are thus reduced. Based on that, the single-phase full bridge inverter has been identified as the best topology for transformerless single-phase grid connected wind energy systems. Consequently, the performance of the inverters connected to the grid depends largely on the control strategy applied. A suitable control of these inverters is needed to get an efficient energy transfer and to ensure the corresponding AC level in the utility grid. So, many methods for the current control of grid connected single-phase inverters have been developed. These methods include the use of the proportional integral (PI) controller [12], proportional resonant (PR) controller [13], repetitive based controller [14], deadbeat controller [15], hysteresis controller [16], and predictive controller [17]. Although, the latter has the advantage of outstanding current regulation, higher power factor, lower current harmonic distortions and fast dynamic response during the transient conditions, but demands more computing resources and requires a good knowledge of system parameters. Thanks to the availability of powerful, low cost digital signal processors (DSP), the implementation of predictive strategies as digital controllers has been of particular interests in recent studies. In [18, 19], the digital predictive current controllers for single-phase and three-phase voltage source inverters (VSI) are proposed. The laboratory test studies have shown that the inverter controlled by this traditional predictive current algorithm has a poor performance under inverter component parameter variations. Aiming at overcoming these disadvantages of traditional predictive controller, an improved predictive current controller (IPCC) has been developed by the authors for single-phase full bridge grid connected inverters and has been verified through simulation studies and experimental tests.

The organization of this Chapter is as follows: the system structure is described in Section 2. Then, the analyses of the switched inductor boost converter (SIBC) are presented in Section 3, Followed by, the control scheme development in Section 4. Comprehensive simulation and real-time implementation have been investigated in detail in Section 5 and 6, respectively. In section 7, some conclusions are drawn.

3.2. System Topology Structure

The circuit configuration of the proposed wind energy system is depicted in Figure 3.1. The system consists of two stages.

The first stage is a high-gain switched inductor with voltage multiplication boost converter to provide high-gain, high-efficiency and also the DC source required by the single-phase voltage source inverter.

The second stage is a single-phase full bridge inverter is used to inject a sinusoidal current into the grid with low harmonic distortion as possible.

The switched inductor consists of two inductors and three diodes with the shown arrangement in Figure 3.1. This arrangement enables the two inductors to be charged in parallel during the On-state, and discharged in series manners during the Off-state.

The boost converter switch S1 is designed to operate at high frequency to decrease the inductor values and the overall system size.

The single-phase full bridge inverter is composed of switches S2–S5. It has the advantage of operating at high frequency.

This reduces the volume and cost, and thus the system overall efficiency can be improved too.

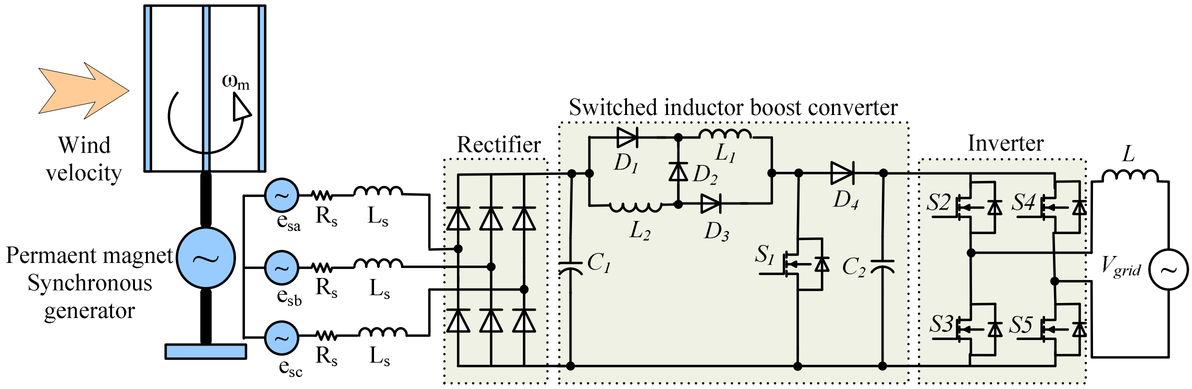

Figure 3.1. Configuration of proposed wind energy system.

3.3. Analyses of the Switched Inductor Boost Converter (SIBC)

The SIBC topology [20] and its operational modes are shown in Figures 3.2(a–c). It is very similar to the conventional DC/DC boost converter.

It has also two modes of operations based on the inductor current operation: store or release energy.

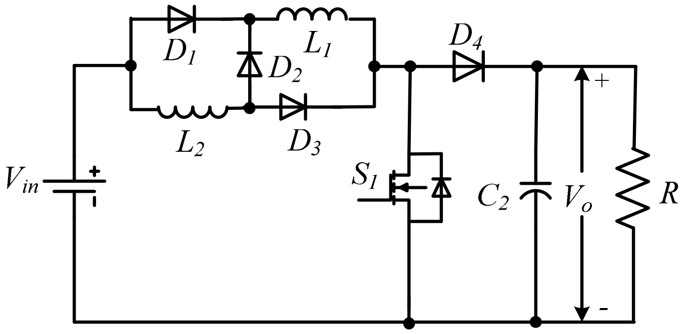

(a)

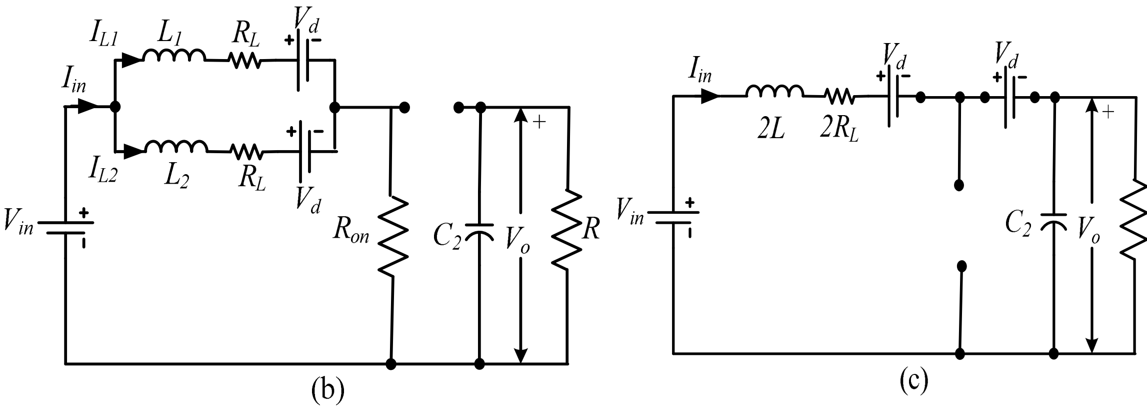

Figure 3.2. SIBC circuit and its operational modes; a) SIBC circuit, b) Circuit during mode 1 operation, c) Circuit during mode 2 operation.

The arrangement of diodes and inductors of the switched inductor enables the two inductors to store energy in parallel, whereas the two branches of the inductor release energy in a series manner. Thus the instantaneous values of the two branches of the inductor currents I_{L1} and I_{L2} are equal; $I_{L1}(t) = I_{L2}(t) = I_L(t)$. Also, to simplify this analysis, the SIBC will be discussed assuming a simple resistive load R is connected across its terminal instead. SIBC modes of operations are explained as:

Mode 1: Occurs when the switch S1 is “ON”, this causes diodes D_1 and D_3 to be turned “ON” and diodes D_2 and D_4 to be turned “OFF”. Thus the two branches of inductors are charging in parallel. Figure 3.2(b) shows the proposed converter circuit of mode 1. Let the inductor internal resistance to be R_L, diode voltage drop V_d and switch internal MOSFET on-resistance to be Ron. The inductor voltage $V_L(t)$, capacitor current $I_{c2}(t)$, and the input current $I_{in}(t)$, in this mode are given by the following equations:

$$V_L(t)=V_{in}(t)-2I_L(t)R_{on}-V_d-I_L(t)R_L \tag{3.1}$$

$$I_{c2}(t)=-\frac{V_o(t)}{R} \tag{3.2}$$

$$I_{in}(t)=2I_L(t) \tag{3.3}$$

where $V_{in}(t)$, $V_o(t)$ and R are the input voltage, output voltage of the SIBC and the resistor that represents the load connected across the SIBC, respectively.

Mode 2: Occurs when the switch S_1 is “OFF”, this causes diodes D_1 and D_3 to be turned “OFF” and diodes D_2 and D_4 to be turned “ON” and thus the two branches of the inductor discharge in series. Figure 3.2(c) shows the proposed converter circuit of mode 2. Similarly, the inductor voltage, the capacitor current and the input current in this mode are given by the following equations:

$$V_L(t)=0.5(V_{in}(t)-2V_d-2I_L(t)R_L-V_o(\mathrm{t})) \tag{3.4}$$

$$I_{c2}(t)=I_L(t)-\frac{V_o(t)}{R} \tag{3.5}$$

$$I_{in}(t)=I_L(t) \tag{3.6}$$

Then, applying inductor volt second balance and capacitor charge balance [21], equations (3.1)–(3.6) yield the following equations for the proposed converter model:

$$\langle V_L(t)\rangle_T=d(t)\left[V_{in}(t)-2I_L(t)R_{on}-V_d-I_L(t)R_L\right]+\left[1-d(t)\right]\left[0.5(V_{in}(t)-2V_d-2I_L(t)R_L-V_o(\mathrm{t}))\right] \tag{3.7}$$

$$\langle I_c(t)\rangle_T=d(t)\left(-\frac{V_o(t)}{R}\right)+\left(1-d(t)\right)\left(I_L(t)-\frac{V_o(t)}{R}\right) \tag{3.8}$$

$$\langle I_{in}(t)\rangle_T=\left(1+d(t)\right)I_L(t) \tag{3.9}$$

From the DC analyses, the DC operating point of the proposed converter with a constant duty ratio $d= D$ can be determined by equating the right-hand sides of equations (3.7) and (3.8) to zero and solving the two resulting algebraic equations for I_L and Vo, resulting in:

$$I_L(t)=\frac{V_o}{R(1-D)} \tag{3.10}$$

$$V_o=\frac{R(1-D)\left[0.5(1+D)V_{in}-V_d\right]}{R_L+2R_{on}D+0.5R(1-D)^2} \tag{3.11}$$

Then, the voltage boosting gain of the proposed converter is found as:

$$G=\frac{V_o}{V_{in}}=\frac{R(1-D)\left[(1+D)-2V_d/V_{in}\right]}{2R_L+4R_{on}D+R(1-D)^2} \tag{3.12}$$

The DC component of the input current is obtained from equations (3.9) to (3.11) as:

$$I_{in}=(1+D)\frac{V_o}{R}=\frac{(1+D)\left[(1+D)V_{in}-V_d\right]}{R_L+2R_{on}D+0.5R(1-D)^2} \tag{3.13}$$

Also, the input power of the system P_{in} which represents the wind extracted power P_{wind} is derived as:

$$P_{in} = P_{wind} = V_{in} \frac{(1+D)\left[0.5(1+D)V_{in} - V_d\right]}{R_L + 2R_{on}D + 0.5R(1-D)^2} \tag{3.14}$$

From equations (3.10) to (3.14), the efficiency of the DC–DC SIBC is calculated as follows:

$$\eta_{SIBC} = \frac{V_o^2 / R}{V_{in} I_{in}} = G\frac{V_o}{RI_{in}} = G\frac{(1-D)}{(1+D)} \tag{3.15}$$

To study the performances of the SIBC, the aforementioned derived analysis has been used advantageously. The effect of the SIBC circuit parameters has been considered for the converter boosting gain and its efficiency. The used parameters in this test are $V_{in} = 30V$, $R_L = 0.01\Omega$, $R_{on} = 0.01\Omega$, $R = 200\Omega$, and $V_d = 1.5V$.

Figure 3.3 shows a comparison between the gain of the SIBC and conventional DC/DC boost converter in ideal case. This figure shows that, the gain of the SIBC is theoretically higher than the conventional DC/DC boost converter by a factor of (1+D).

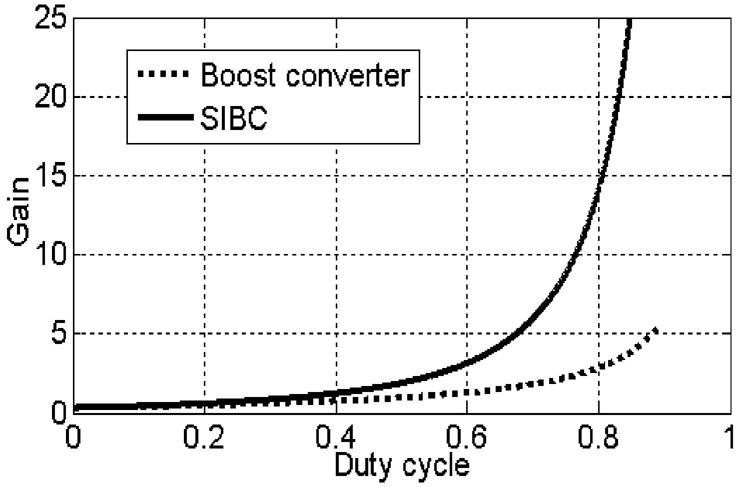

Figure 3.3. Comparison between the proposed SIBC and the conventional DC/DC boost converter boosting gain ratio.

Applying the practical conditions of the circuit parameters, Figures 3.4(a) and 3.4(b) gives the gain and the efficiency of the SIBC against duty cycle for various values of input voltages, respectively. The first observation yield from these two curves is that, the converter enters the unstable region beyond duty cycle 0.9. Therefore it should keep the duty cycle below 0.9. The effect of changing the input voltage on the gain is small because as the input voltage increases results in slight increase on the gain for the same duty cycle as shown in Figure 3.4(a). On the other hand, the effect of changing the input voltage on the SIBC efficiency is very noticeably. As the input voltage decreases, it results in deterioration of the converter efficiency as shown in Figure 3.4(b). It can be concluded that, the used input voltage for this converter should not be less than 20V to obtain an acceptable efficiency.

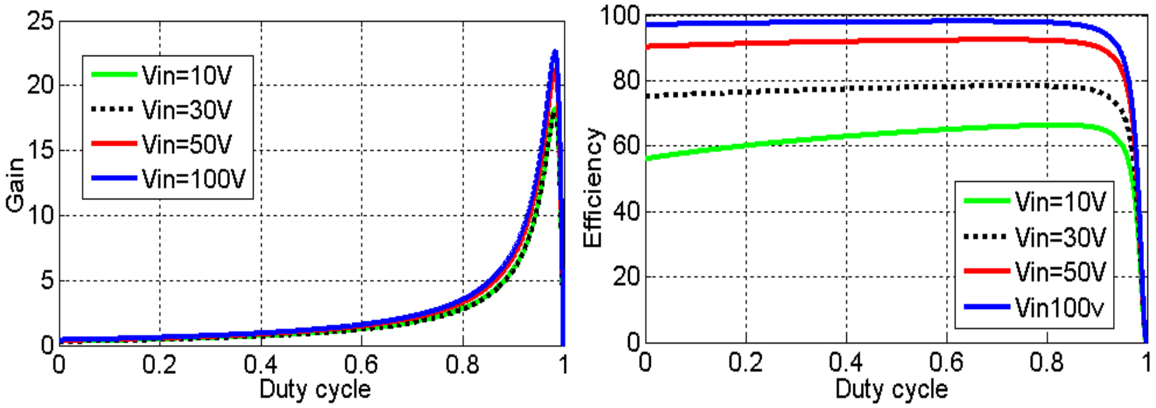

(a) **(b)**

Figure 3.4. Performances of the SIBC gain and efficiency, **a)** Effect of the input voltage on the SIBC gain, **b)** Efficiency of the SIBC for various values of input voltage.

Figures 3.5(a) and 3.5(b) illustrate the gain and the efficiency of the SIBC against duty cycle for various values of switch on-resistance, respectively. Figures 3.5(a) and 3.5(b) reveal that, the effect of the switch on-resistance on both the converter gain and also the efficiency is very trivial especially for low values of duty cycle (below 0.6). However, the converter efficiency starts to deteriorate as the duty cycle becomes closer to 0.8. Therefore it limits the upper limit for the duty cycle operation.

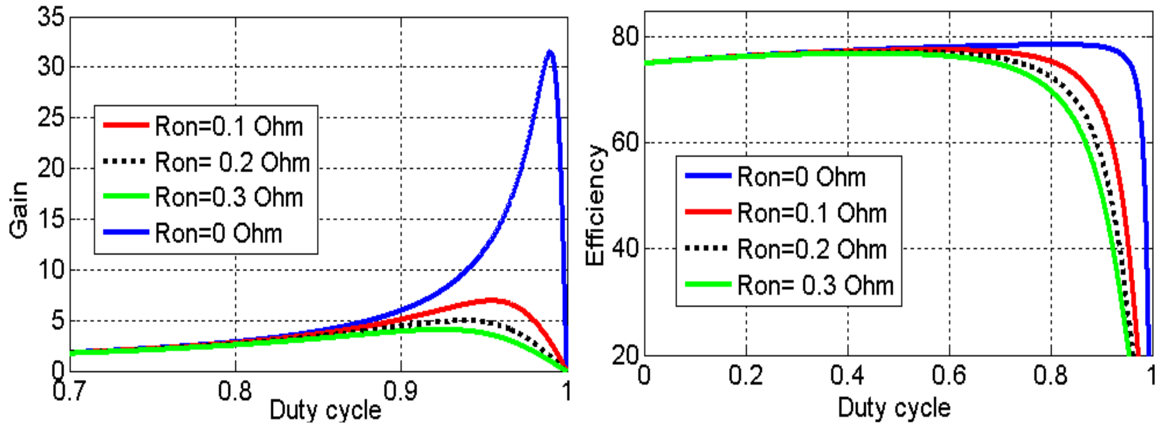

(a) **(b)**

Figure 3.5. Performances of the SIBC gain and efficiency, **a)** Gain of the SIBC for various values of switch on-resistance, **b)** Efficiency of the SIBC for various values of switch on-resistance

The calculated efficiency of equation (3.15) has been plotted against the output power for various values of input voltage as shown in Figure 3.6. The main observation is that, as the input voltage increases, the converter efficiency is improved for the same output power. It is worth to note that for input voltage less than 50V, the converter efficiency decreases vary rapidly lower than 90% which means the converter is economically failed.

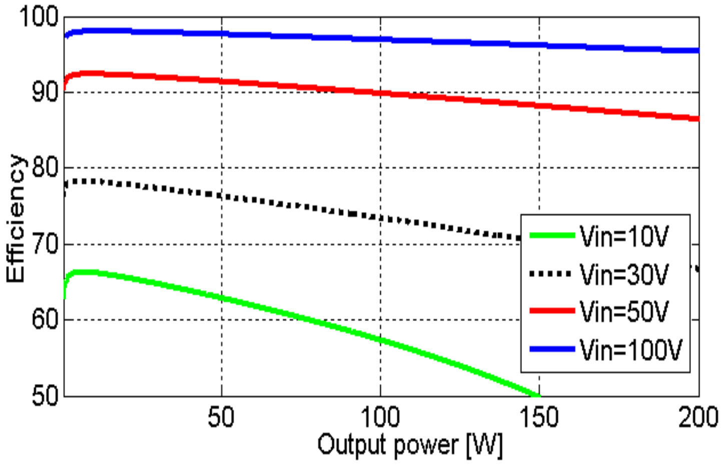

Figure 3.6. Efficiency of the SIBC against input power for various values of input voltage.

3.3.1. Design details

The SIBC is performed by controlling the amplitude of the inductor current and this in turns is done through the modulation function of switching pulses as shown in Figure 3.7.

When the switch S1 is turned “ON”, V_{in} is the voltage across the inductor, and when the switch is turned “Off”, $(V_o-V_{in})/2$ is the voltage across the inductor.

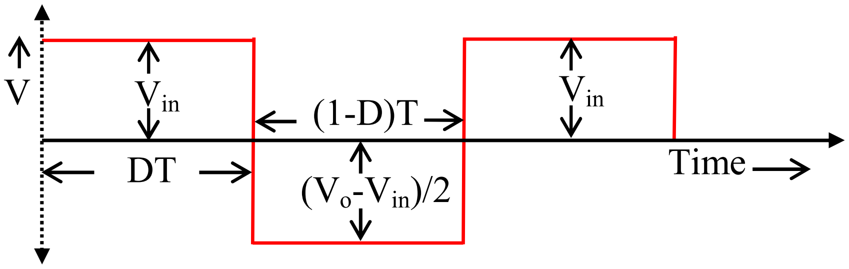

Figure 3.7. Voltage across inductor.

Applying volt-sec balance theorem:

$$V_{in}DT+\left(\frac{V_o-V_{in}}{2}\right)(1-D)=0 \tag{3.16}$$

Voltage induced in an inductor is given by:

$$L\frac{dI_L}{dt}=V_L \tag{3.17}$$

By considering Figure 3.7 and equation (3.17), voltage across the inductor during On-state can be written as:

$$L\frac{(\Delta I_L)_{On}}{t_{on}}=V_{in} \tag{3.18}$$

From equation (3.18), t_{on} can be written as:

$$t_{on}=\frac{L(\Delta I_L)_{On}}{V_{in}} \tag{3.19}$$

Similarly, voltage across the inductor during Off-state can be written as:

$$L\frac{(\Delta I_L)_{Off}}{t_{Off}}=\frac{V_0-V_{in}}{2} \tag{3.20}$$

From equation (3.20), t_{off} can be written as:

$$t_{Off}=\frac{2L(\Delta I_L)_{Off}}{V_0-V_{in}} \tag{3.21}$$

The total time period (T) can be written as:

$$T=t_{On}+t_{Off} \tag{3.22}$$

From equations (319), (3.21) and equation (3.22):

$$T=\frac{L(\Delta I_L)_{On}}{V_{in}}+\frac{2L(\Delta I_L)_{Off}}{V_0-V_{in}} \tag{3.23}$$

$$(\Delta I_L)_{On} = (\Delta I_L)_{Off} = \Delta I_L \tag{3.24}$$

From equations (3.23) and (3.24):

$$T = \frac{L(\Delta I_L)(V_0 + V_{in})}{V_{in}(V_0 - V_{in})} \tag{3.25}$$

From equations (3.16) and (3.25):

$$\Delta I_L = \frac{2V_{in}D}{Lf_s} \tag{3.26}$$

where $f_s=1/T$ is the switching frequency of the SIBC circuit. The inductor current I_L can be written as:

$$I_L = \frac{\Delta I_L}{2} \tag{3.27}$$

From equations (3.26) and (3.27):

$$I_L = \frac{V_{in}D}{Lf_s} \tag{3.28}$$

Considering converter to be ideal:

$$V_{in}I_L = \frac{V_o^2}{R} \tag{3.29}$$

From equations (3.28) and (3.29):

$$\frac{V_{in}^2 D}{Lf_s} = \frac{V_o^2}{R} \tag{3.30}$$

From equations (3.30) and (3.16) critical inductance of converter can be obtained as:

$$L = \frac{RD}{f_s} = \left(\frac{1-D}{1+D}\right)^2 \tag{3.31}$$

The decoupling capacitance C_2 controls the double line frequency over the wind power conditioning stage.

Therefore to assure a low voltage ripple, a designed decoupling capacitor is selected as:

$$C_2 = \frac{P}{2\pi f_r V_0 \Delta V} \tag{3.32}$$

where f_r is the double line frequency, P is the system power (equals P_{wind} with ignoring losses), and ΔV is the allowed voltage ripple.

3.4. Control System

3.4.1. Improved MPPT Control Scheme

In this section a maximum power tracker controller by using model predictive control (MPC) will be presented for the SIBC in order to operate the wind turbine at the optimal power point until wind changes.

In general hill climb searching (HCS) control method has a simple feedback structure and fewer measured parameters like voltage and current sensor.

It operates on the principle that the slope of the power curve is zero at the MPP, positive to the left of the MPP, and negative to the right.

Therefore individual signs of the input current and input voltage increments are determined to get information about power change and the last search direction, respectively.

In this manner, the peak power tracker continuously seeks the peak power condition and hence the corresponding current can be calculated. The Possible conditions and the flowchart for HCS-MPPT algorithm is shown in Figures 3.8 and 3.9, respectively.

When the steady state is reached, the HCS algorithm oscillates around the peak power point. In order to keep the power variation to be small, the perturbation size is kept very small amount, which limits its ability to track transient conditions during changes in wind velocity and decreasing the efficiency of the system.

Based on the above, the main goal to using the MPC technique in HCS-MPPT algorithm is to increase the response of the control of MPPT on the wind energy systems when there is abrupt change in the environmental conditions such as wind speed and direction, because predictions of the future values of the system variables gives the advantages of fast reference tracking.

The proposed algorithm is developed in such a manner that it sets a reference current corresponding to the peak power of the wind turbine by predicting the error at next sampling time before applying the switching signal to the SIBC.

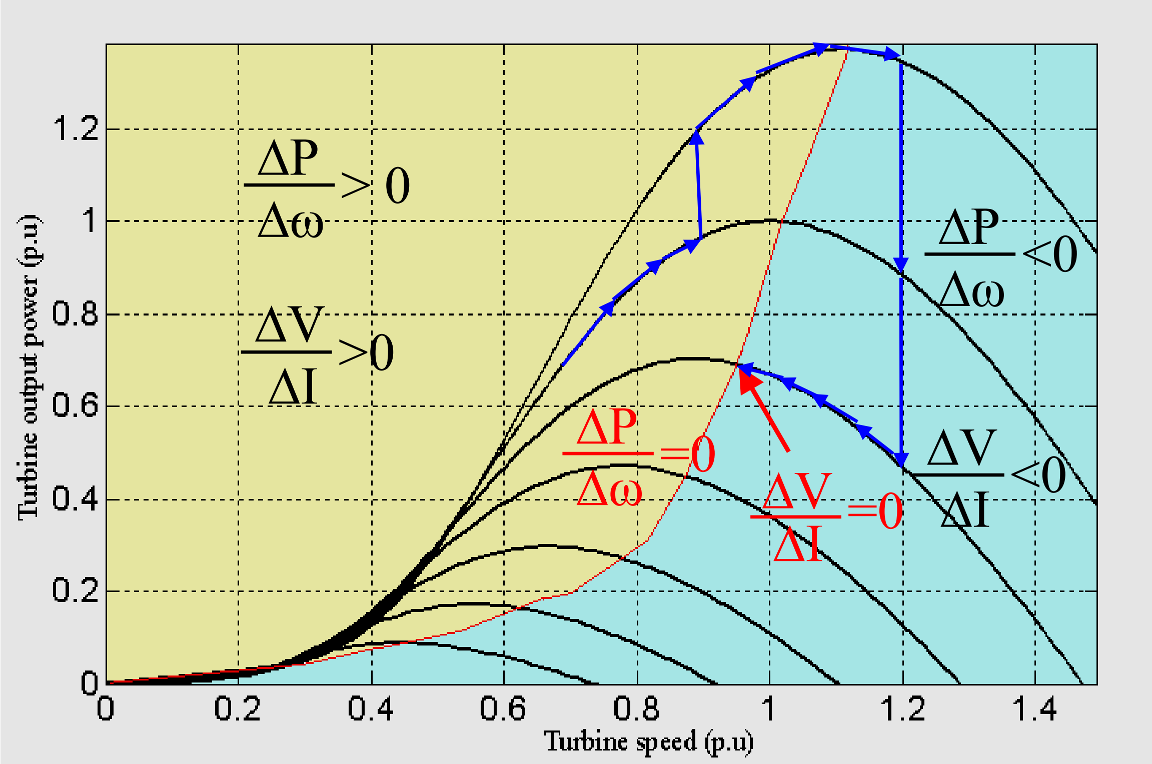

Figure 3.8. Possible conditions for HCS-MPPT algorithm.

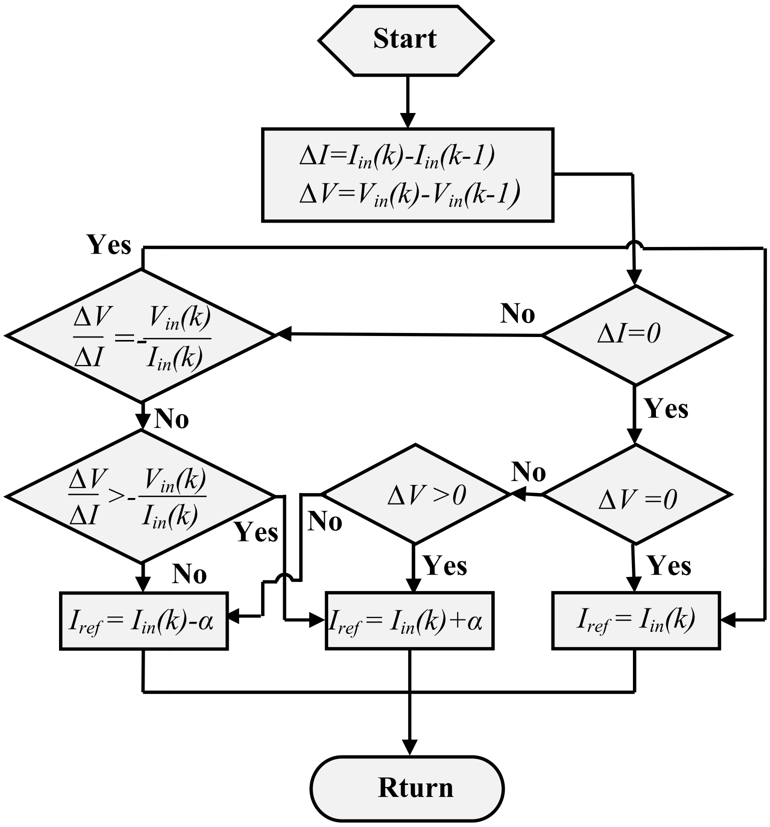

Figure 3.9. HCS procedure to determine reference current using.

3.4.2. Principle of Fixed Frequency Model Predictive Control

The main characteristic of MPC is predicting the future behavior of the desired control variables [22] until a specific time in horizon.

The predicted control variables will be used to obtain the optimal switching state by minimizing a cost function. The discrete-time model of the control variables will be used for prediction which can be presented as state-space model as follow [23]:

$$\begin{aligned} x(k+1) &= Ax(k)+Bu(k) \\ y(k) &= Cx(k)+Du(k) \end{aligned} \tag{3.33}$$

Then a cost function that takes into consideration the future states, references and future actuations can be defined as [23]:

$$g = f(x(k), u(k), \ldots, u(k+n)) \tag{3.34}$$

The defined cost function "*g*" should be minimized for a predefined horizon in time "*N*"; the result is a sequence of "*N*" optimal actuations will be determined where the controller only applies the first element of sequence:

$$u(k) = \begin{bmatrix} 1 & 0 & \ldots & 0 \end{bmatrix} \arg\min_{u} g \tag{3.35}$$

At each sampling time the optimization problem is solved again by using new set of measured data to obtain a new sequence of optimal actuation. The MPC principle of working is illustrated graphically in Figure 3.10. As it is shown that by using the measured information and system model until time (t_k), the future value of the system state is predicted until time (t_k+n) in horizon. Then, the optimal actuation is calculated by optimizing the cost function (g).

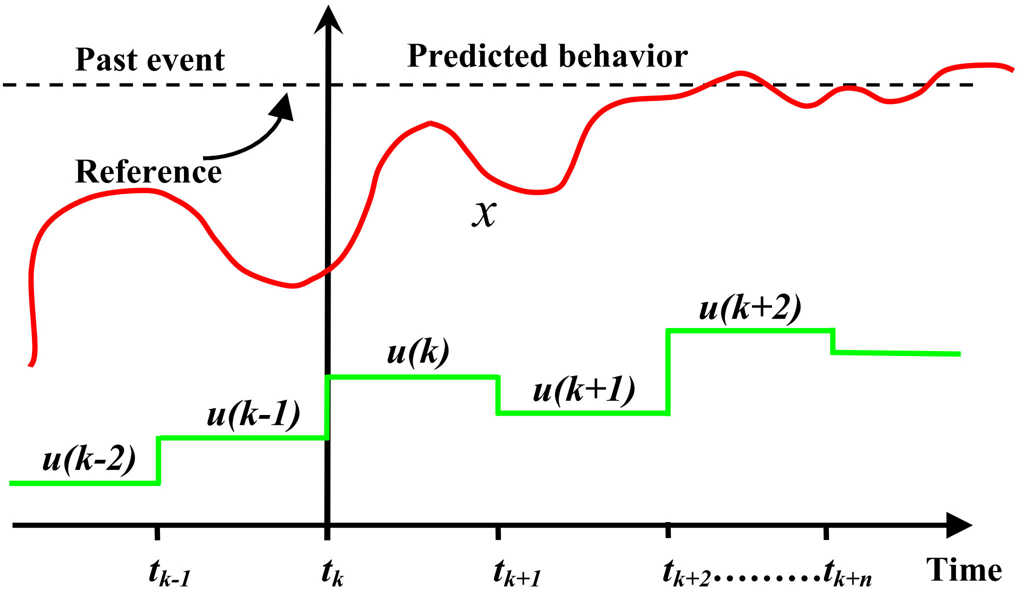

Figure 3.10. MPC principle of working.

The MPC for power electronics converters can be designed using the following steps [22]:

- Determination of power converter model which specify the input-output relation of the voltages and currents.
- Determination of discrete-time model of the control variables for predicting their future behavior.
- Designing the cost function, subject to minimization, which demonstrates the preferred behavior of the power converter.

The general scheme of MPC for power electronics converters is illustrated in Figure 3.11. In this scheme, measured variables, $x(k)$, are used in the model to calculate predictions, $\tilde{x}(k+1)$, of the controlled variables for each one of the n possible actuations, that is, switching states, voltages, or currents. Then these predictions are evaluated using a cost function, which considers the reference values, $x^*(k+1)$, design constraints, and the optimal actuation, S, is selected and applied to the converter. The general form of the cost function, g, subject to minimization can be formulated as:

$$g=[\tilde{x}_1(k+1)-x_1^*(k+1)]+\lambda_1[\tilde{x}_2(k+1)-x_2^*(k+1)]+...+\lambda_n[\tilde{x}_n(k+1)-x_n^*(k+1)] \qquad (3.36)$$

where λ is the weighting factor for each objective. To select the switching state, which minimizes the cost function g, all possible states are evaluated and the optimal value is stored to be applied next. The power converter can be from any topology and number of phases, while the generic load shown in Figure 3.11 can represent an electrical machine, the grid, or any other active or passive load. In this chapter, the SIBC has been selected as power conversion stage for MPPT control.

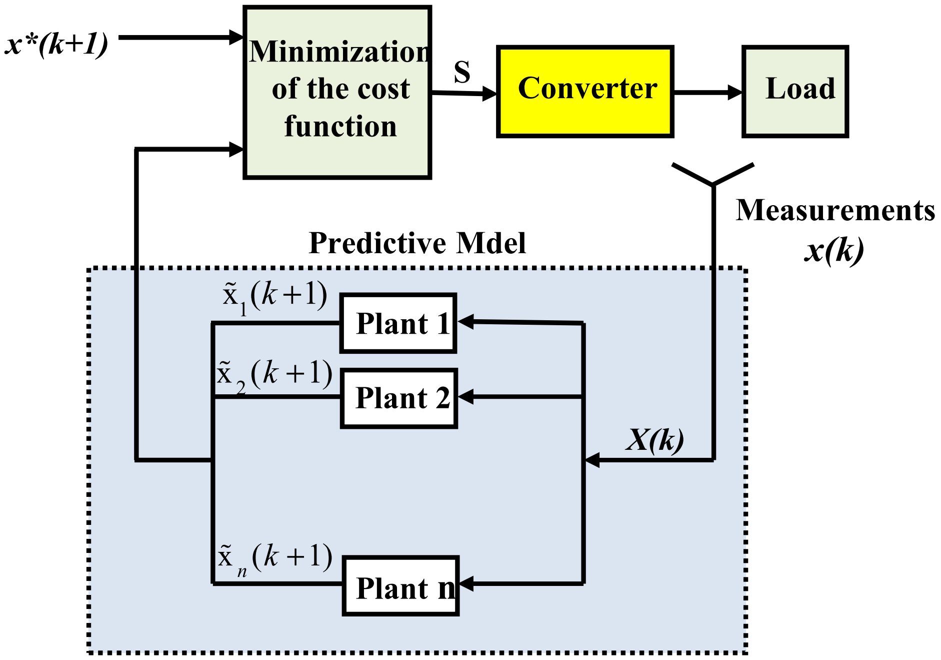

Figure 3.11. MPC general schematic for power electronics converters [24].

To allow the MPC to operate at a fixed frequency, choose the desired switching frequency with a time period, T_{sw} where the switching period is divided into a number of N steps and each step represents the sampling period, T_s. The relationship between T_{sw}, N and, T_s is as follows:

$$\frac{T_{sw}}{Ts} = N \text{ where } N \in \{2,4,6\dots\dots\}$$

Figures 3.12 and 3.13 illustrate how the MPC designed to operate at fixed frequency. The operation of fixing the switching frequency of the MPC can be simplified as follows: while $n<N/2$, the algorithm assumes starting in the "ON" state and predicts whether to stay "ON" or to turn "Off". The algorithm then generates active states until the optimization process indicates that zero states are required. As a result, zero states remain until $n=N/2$. For $n>=N/2$, the algorithm assumes that the system now starts in the "OFF" state, and a prediction is made to determine whether the system should stay "OFF" or turn "ON". Once the system is switched "ON", it will remain on until the end of the switching period. After it has been resettled, the prediction process is restarted for the next switching period. This approach ensures that the system is switched at a fixed switching frequency.

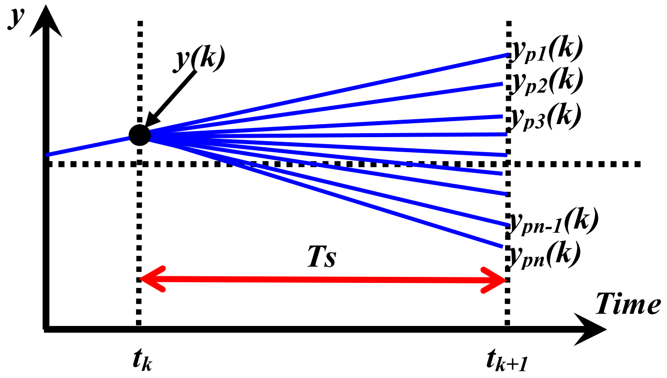

Figure 3.12. MPC principle of working.

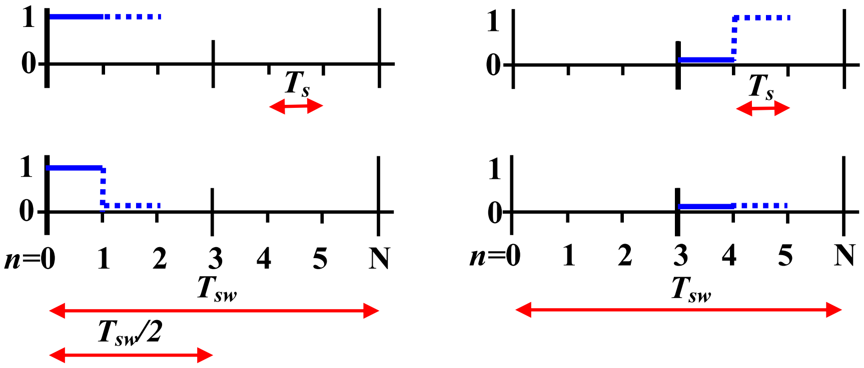

Figure 3.13. Depiction of the MPC switching period and prediction possibilities. **(a)** redictions when $n<N/2$. **(b)** Predictions when $n>N/2$.

3.4.3. Proposed MPPT Using Fixed Frequency MPC

3.4.4. Discretization

The main descriptive equations of the SIBC in continuous form when the switch is turned "ON" and "OFF" can be determined using the following expressions, respectively.

$$L\frac{dI_{in}}{dt}=V_{in}-V_d-\left(\frac{R_L}{2}+R_{on}\right)I_{in} \tag{3.37}$$

$$C_1\frac{dV_{in}}{dt}=I_{dc}-I_{in} \tag{3.38}$$

When switch is "OFF":

$$L\frac{dI_{in}}{dt}=\frac{1}{2}\left(V_{in}-2V_d-V_o-2I_{in}R_L\right) \tag{3.39}$$

$$C_1\frac{dV_{in}}{dt}=I_{dc}-I_{in} \tag{3.40}$$

where C_1 is the SIBC input capacitor value and I_{dc} is the DC-side current.

A discretization of the proposed SIBC model is required for the implementation of the predicted MPPT. By using the Euler forward approximation technique, the derivative of the input current and input voltage can be approximately discretized as follows:

$$\frac{dI_{in}}{dt}=\frac{I_{in}(k+1)-I_{in}(k)}{T_s} \tag{3.41}$$

$$\frac{dV_{in}}{dt}=\frac{V_{in}(k+1)-V_{in}(k)}{T_s} \tag{3.42}$$

Consider the sampling time is T_s. As a result, the discretization of the SIBC equations can derive from equations (3.43) and (3.44) discrete equations when the switch is "ON":

$$I_{in}(k+1)=\frac{T_s}{L}\left(V_{in}(k)-V_d\right)+\left(1-\frac{T_s}{L}\left(\frac{R_L}{2}+R_{on}\right)\right)I_{in}(k) \tag{3.43}$$

$$V_{in}(k+1)=V_{in}(k)+\frac{T_s}{C_1}\left(I_{dc}(k)-I_{in}(k)\right) \tag{3.44}$$

The discrete equations when the switch is "OFF" are given by equations (3.45) and (3.46) as follow:

$$I_{in}(k+1)=\frac{T_s}{2L}\left(V_{in}(k)-2V_d-V_o(k)\right)+\left(1-\frac{T_s}{L}R_L\right)I_{in}(k) \tag{3.45}$$

$$V_{in}(k+1)=V_{in}(k)+\frac{T_s}{C_1}\left(I_{dc}(k)-I_{in}(k)\right) \tag{3.46}$$

By using the discrete-time set of equations (3.43), (3.35), (3.36) and (3.37), the behavior of SIBC can be predicted at the next sampling time (t_k+*1*). As a good approximation for number of sensors reduction, the predicted value for $V_{in}(k+1)$ could be expressed as follow:

$$V_{in}(k+1)\cong 2V_{in}(k)-V_{in}(k-1) \tag{3.47}$$

The model used for prediction is a discrete-time model which can be presented as State-space model. The above equations when a switch is turned "ON" can be expressed in the matrix form as in equation (3.48), and when a switch is turned "OFF" can be expressed in the matrix form as in equation (3.49):

$$\begin{bmatrix}I_{in}(k+1)\\V_{in}(k+1)\end{bmatrix}=\begin{bmatrix}1-\frac{T_s}{L}\left(\frac{R_L}{2}+R_{on}\right) & \frac{T_s}{L}\\ 0 & 2\end{bmatrix}\begin{bmatrix}I_{in}(k)\\V_{in}(k)\end{bmatrix}+\begin{bmatrix}0\\-1\end{bmatrix}\begin{bmatrix}V_{in}(k-1) & V_d\end{bmatrix} \tag{3.48}$$

$$\begin{bmatrix}I_{in}(k+1)\\V_{in}(k+1)\end{bmatrix}=\begin{bmatrix}1-\frac{T_s}{L}R_L & \frac{T_s}{2L}\\ 0 & 2\end{bmatrix}\begin{bmatrix}I_{in}(k)\\V_{in}(k)\end{bmatrix}+\begin{bmatrix}0 & -\frac{T_s}{L} & -\frac{T_s}{2L}\\ -1 & 0 & 0\end{bmatrix}\begin{bmatrix}V_{in}(k-1)\\V_d\\V_0\end{bmatrix} \tag{3.49}$$

Previous work has suggested the addition of a second stage of MPC for even better system performance and model accuracy [25]. In order to predict the control variables at time (t_k+2), the estimated value of the input current and input voltage at time (t_k+1) are used. Thus at sampling time (t_k+2), four values for control variables are predicted, and the optimum value is selected as illustrated graphically in Figure 3.14. Equations (3.48) and (3.49) are adjusted to get equations (3.50) and (3.51) for two-stage MPC:

$$\begin{bmatrix}I_{in}(k+2)\\V_{in}(k+2)\end{bmatrix}=\begin{bmatrix}1-\frac{T_s}{L}\left(\frac{R_L}{2}+R_{on}\right) & \frac{T_s}{L}\\ 0 & 2\end{bmatrix}\begin{bmatrix}I_{in}(k+1)\\V_{in}(k+1)\end{bmatrix}+\begin{bmatrix}0\\-1\end{bmatrix}\begin{bmatrix}V_{in}(k) & V_d\end{bmatrix} \tag{3.50}$$

$$\begin{bmatrix}I_{in}(k+2)\\V_{in}(k+2)\end{bmatrix}=\begin{bmatrix}1-\frac{T_s}{L}R_L & \frac{T_s}{2L}\\ 0 & 2\end{bmatrix}\begin{bmatrix}I_{in}(k+1)\\V_{in}(k+1)\end{bmatrix}+\begin{bmatrix}0 & -\frac{T_s}{L} & -\frac{T_s}{2L}\\ -1 & 0 & 0\end{bmatrix}\begin{bmatrix}V_{in}(k)\\V_d\\V_0\end{bmatrix} \tag{3.51}$$

This model can then be generalized to m-stage MPC as:

$$\begin{bmatrix} I_{in}(k+m+1) \\ V_{in}(k+m+1) \end{bmatrix} = \begin{bmatrix} 1-\frac{T_s}{L}\left(\frac{R_L}{2}+R_{on}\right) & \frac{T_s}{L} \\ 0 & 2 \end{bmatrix} \begin{bmatrix} I_{in}(k+m) \\ V_{in}(k+m) \end{bmatrix} + \begin{bmatrix} 0 \\ -1 \end{bmatrix} \begin{bmatrix} V_{in}(k) \\ V_d \end{bmatrix} \tag{3.52}$$

$$\begin{bmatrix} I_{in}(k+m+1) \\ V_{in}(k+m+1) \end{bmatrix} = \begin{bmatrix} 1-\frac{T_s}{L}R_L & \frac{T_s}{2L} \\ 0 & 2 \end{bmatrix} \begin{bmatrix} I_{in}(k+m+1) \\ V_{in}(k+m+1) \end{bmatrix} + \begin{bmatrix} 0 & -\frac{T_s}{L} & -\frac{T_s}{2L} \\ -1 & 0 & 0 \end{bmatrix} \begin{bmatrix} V_{in}(k) \\ V_d \\ V_0 \end{bmatrix} \tag{3.53}$$

Where: $m \in 0,1,2,\ldots N.$

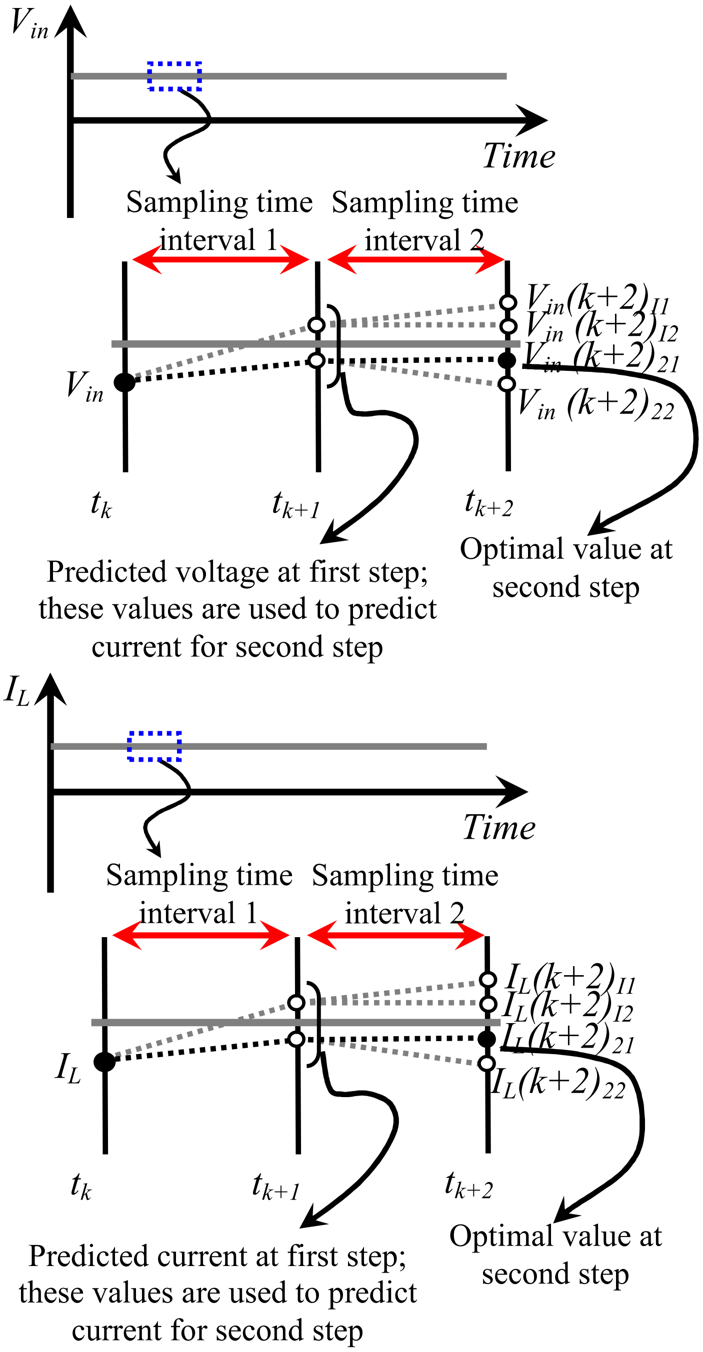

Figure 3.14. Prediction of SIBC inductor current and input voltage observation.

The input current $I_{in}(k+2)$ is determined from equations (3.50) and (3518), and the reference current, I_{ref}, found using the procedure illustrated in Figure 3.9.

The cost function for the MPC algorithm is calculated with the consideration that the switch of the SIBC is turned "ON" and "OFF" it is given as:

$$g_{s=1,0} = \left| I_{in}(k+2) - I_{ref} \right| \tag{3.54}$$

So now after using equations (3.50) and (3.51) for the predictive input current and input voltage for both two states, and equation (3.54) for a cost function, a flowchart in Figure 3.15 will show all the main steps of the modified MPPT control by using the MPC.

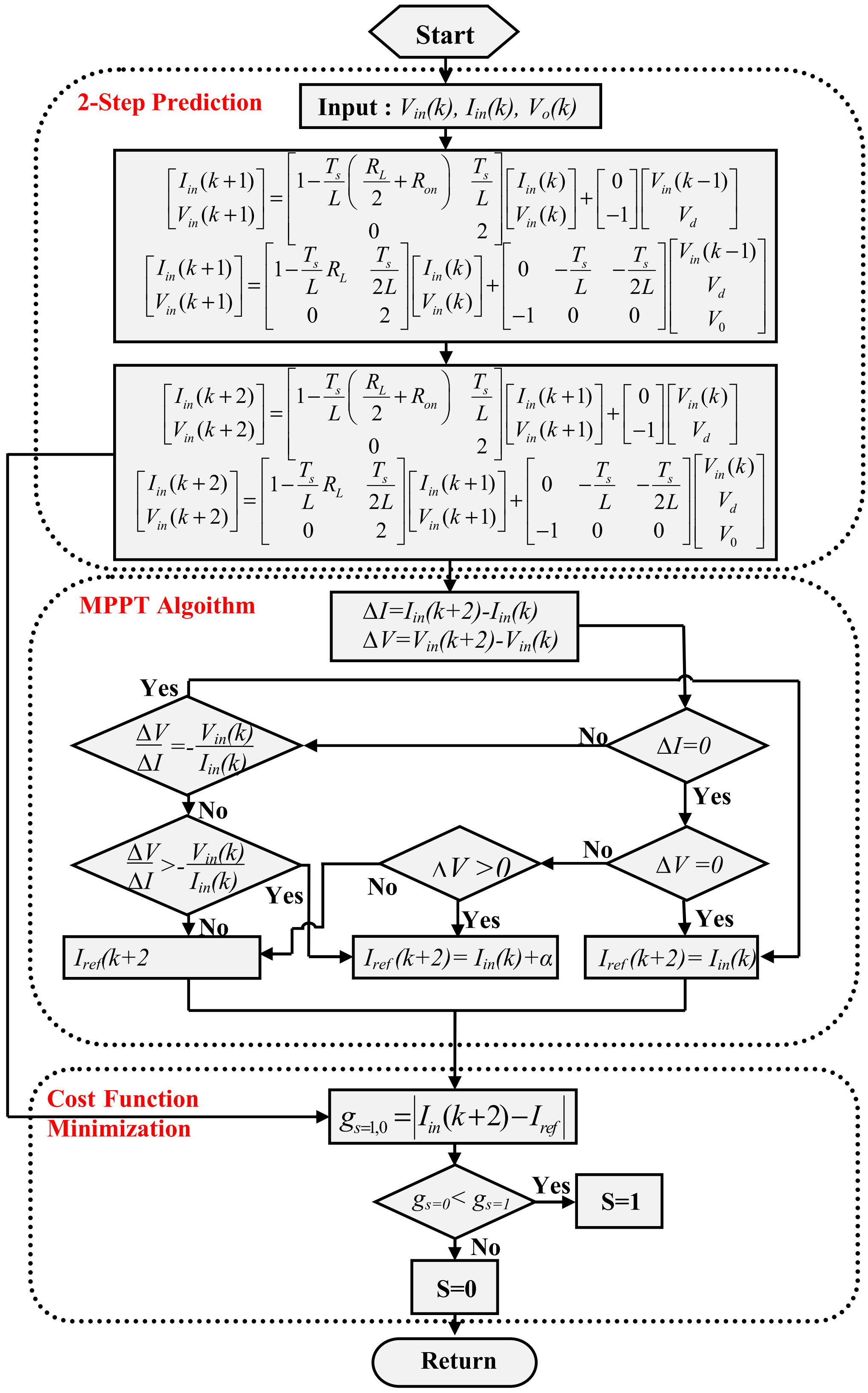

Figure 3.15. MPC-MPPT procedure to determine reference current and determination of switching state using cost function minimization.

The cost function assures the tracking of predicted input current from the reference provided by the MPPT algorithm. Comparison of cost function for different switching states determines the control actions for the following time instant. Figure 3.16 shows the implemented of modified MPPT control scheme to the proposed SIBC.

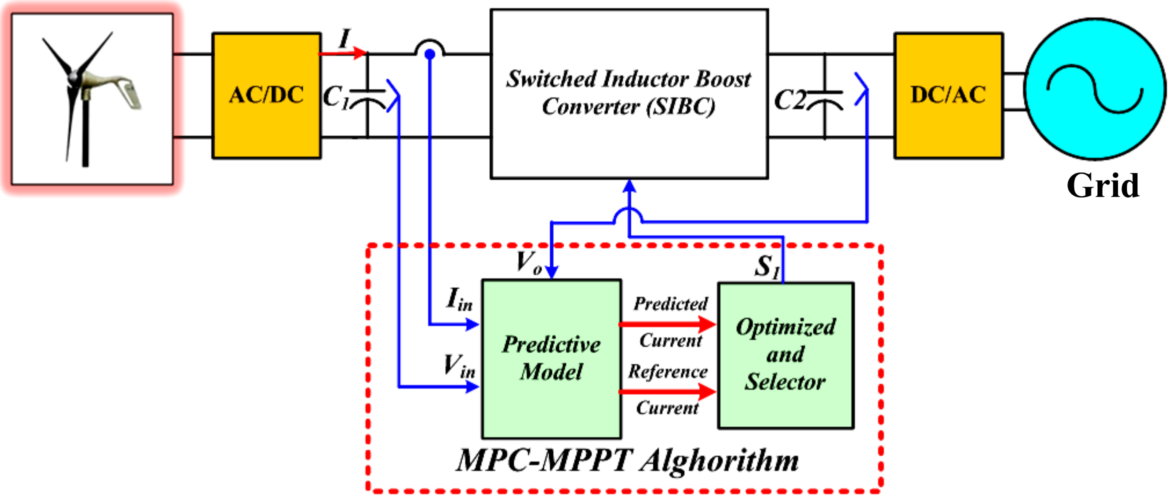

Figure 3.16. Simplified schematic of the overall grid connected wind energy system configuration implementing MPPT through MPC technique.

As shown in Figure 3.16 the SIBC boosts a small voltage of diode rectifier to be valid for feeding the single-phase full bridge inverter, and in the same time to extract the maximum power from the wind turbine.

The proposed controller senses the input current, and the input and output voltage of the SIBC. Then the MPC generates the predicted input current and input voltage signals. Moreover, the optimized and selector take these signals and then give the pulses to the SIBC. This width of this signal is dependent on the MPPT control.

3.4.5. Grid connected system

3.4.6. Traditional predictive current controller for the single-phase full bridge inverter

Figure 3.17 shows the general structure of a single phase full bridge inverter. It is composed of a DC-voltage source, four power switches and a filter inductor. The full bridge inverter’s operation can be divided into four modes: two modes in positive grid current period and two modes in negative grid current period. Table 3.1 illustrates the different operating modes.

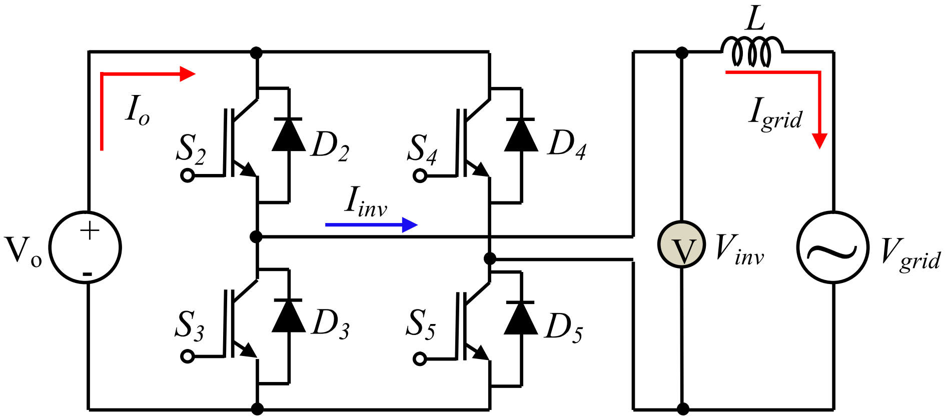

Figure 3.17. Single-phase grid connected full bridge voltage source inverter.

Table 3.1
Single phase grid connected inverter's operational modes.

Mode	**S2**	**S3**	**S4**	**S5**	**D2**	**D5**	**V_{inv}**	**I_{grid}**
1	ON	OFF	OFF	ON	OFF	OFF	Vo	+
2	ON	OFF	OFF	OFF	ON	OFF	0	+
3	OFF	ON	ON	OFF	OFF	OFF	-Vo	-
4	OFF	ON	OFF	OFF	OFF	ON	0	-

Referring to Figure 3.17, the mathematical form of the required inverter output voltage can be written as the following differential equation:

$$V_{inv} = V_{grid} + L\frac{dI_{grid}}{dt} \tag{3.55}$$

where V_{inv} is the inverter terminal output voltage, V_{grid} is the grid voltage, and L is the series filter inductance with negligible internal resistance.

Assuming that the inverter operates with fixed switching frequency, the grid voltage and the grid current are known (measured); a simple and direct predictive current control algorithm is proposed in [19] and [26]. With constant switching period T_s, equation (3.55) can be written in discrete-time form as:

$$V_{inv-av}[k] = V_{grid-av}[k] + L\frac{I_{grid}[k+1] - I_{grid}[k]}{T_s} \tag{3.56}$$

where $V_{inv\text{-}av}[k]$ is the average required inverter output voltage during the switching interval $[t_k, t_{k+1}]$, $V_{grid\text{-}av}[k]$ is the average grid voltage during the switching interval $[t_k, t_{k+1}]$, Ts is the constant switching period, $I_{grid}[k]$ and I_{gr-}

$_{id}[k+1]$ are the measured grid currents at the sampling time $[t_k]$ and $[t_k+1]$, respectively.

The predictive current controller (PCC) goal is to force the grid current $I_{grid}[k+1]$ to be equal the reference current $I_{ref}[k+1]$ at the sampling time $[t_k+1]$, so that $I_{gid}[k+1]$ can be replaced with $I_{ref}[k+1]$ and equation (3.56) can be written as:

$$V_{inv-av}[k]=V_{grid-av}[k]+L\frac{I_{ref}[k+1]-I_{grid}[k]}{T_s} \tag{3.57}$$

In practical implementation, the controller needs a certain computational time to do the required digital sampling and computations before the control command proceeds to the inverter switches. This means that, the digital controller cannot solve for $V_{inv-av}[k]$ because $V_{grid-av}[k]$ and $I_{grid}[k]$ are not available for the controller in the switching interval $[t_k, t_{k+1}]$.

To overcome these problems, a certain adjustment to the control equation (3.57) is required.

In [19] D.G Holmes and D.A Martin suggested using the previous switching period results in order to estimate a proper average grid voltage and grid current values. Figure 3.18 shows the traditional PCC timing schematic for the proposed algorithm.

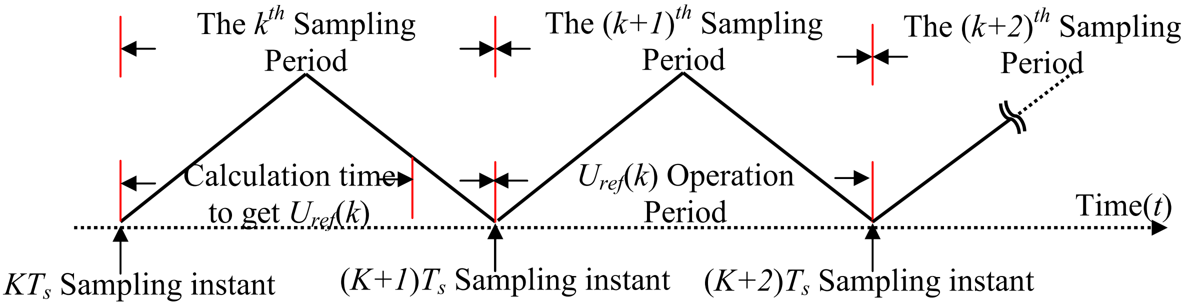

Figure 3.18. Traditional PCC Timing Schematic [27].

Referring to Figure 3.18, it is obvious that the traditional predictive controller should use the measured values of the grid current Igrid[k-1] and grid voltage Vgrid[k-1] which are available when the calculations start at the beginning of switching interval [tk-1, tk].

Then, the required average inverter output voltage will be applied in the interval [tk, tk+1]. This average inverter voltage can be used in any proper pulse width modulation (PWM) circuit to generate the required inverter gating signals.

Figure 3.19 shows the traditional predictive current control system block diagram.

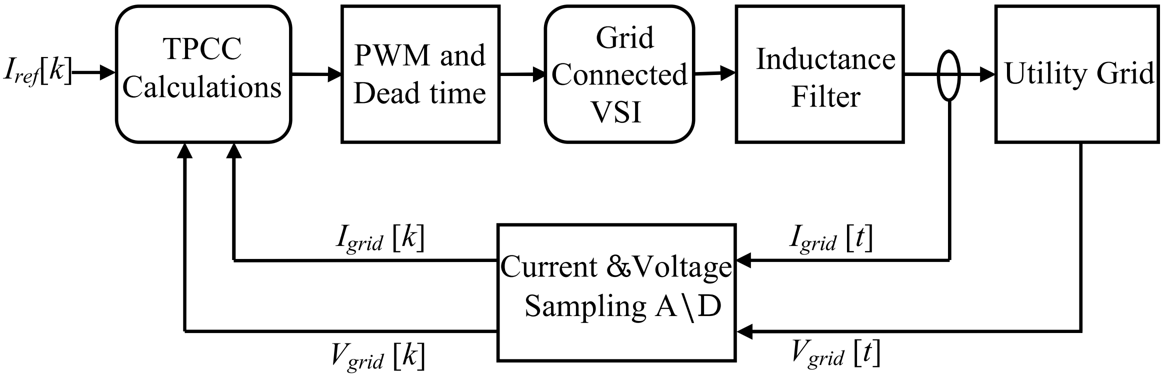

Figure 3.19. Traditional PCC system block diagram.

3.4.7. Average grid voltage linear extrapolation

With the known previous grid voltage average value, the average grid voltage over the switching interval [t_k, t_k+1] can be estimated by using the simple linear extrapolation. Figure 3.20 illustrates the switching intervals with the average grid voltage values.

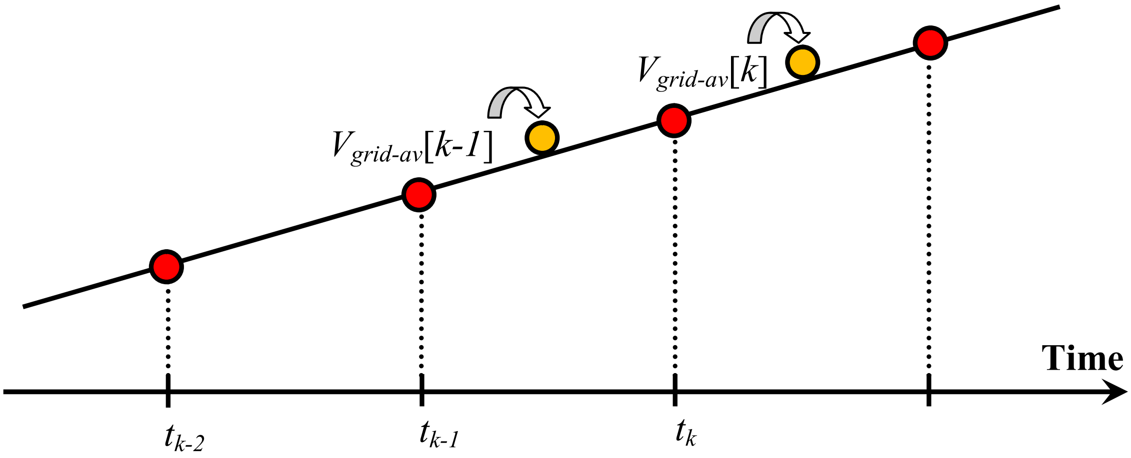

Figure 3.20. Switching intervals with the average grid voltage values.

In Figure 3.20, we assume that the grid voltage change during the intervals is linear and this change is equal from one interval to the other. Then the average grid voltage over the interval [t_k, t_k+1] can be written as:

$$V_{grid-av}[k]=\frac{V_{grid}[k+1]-V_{grid}[k]}{2} \tag{3.58}$$

The grid voltage value at the sampling point [t_k+1] can be predicted as:

$$V_{grid}[k+1]=V_{grid}[k]+\Delta V_{grid}[k] \tag{3.59}$$

Where ΔV_{grid} is the grid voltage change during the switching interval, since the inverter operates with fixed switching frequency we can assume that ΔV_{grid} is constant in any interval. Taking the interval $[t_{k-1}, t_k]$, then ΔV_{grid} can be written as:

$$\Delta V_{grid}[k] = V_{grid}[k] - V_{grid}[k-1] \tag{3.60}$$

Substituting equation (3.60) into equation (3.59) lead to:

$$V_{grid}[k+1] = V_{grid}[k] + \left(V_{grid}[k] - V_{grid}[k-1]\right) \tag{3.61}$$

Then for the interval $[t_{k-2}, t_{k-1}]$, $V_{grid}[k]$ can be written as:

$$V_{grid}[k] = V_{grid}[k-1] + \left(V_{grid}[k-1] - V_{grid}[k-2]\right) \tag{3.62}$$

Substituting equation (3.61) and equation (3.62) into equation (3.58) leads to:

$$V_{grid-av}[k] = \frac{5}{2}V_{grid}[k-1] - \frac{3}{2}V_{grid}[k-2] \tag{3.63}$$

Notice that $V_{grid-av}[k]$ can be calculated by substituting equation (3.61) into (3.58). We have:

$$V_{grid-av}[k] = \frac{3}{2}V_{grid}[k] - \frac{1}{2}V_{grid}[k-1] \tag{3.64}$$

3.4.8. Grid Current Estimation

Under the same assumption that the inverter operates with constant switching frequency and linear grid voltage change, we can assume that the grid current is linearly changed with the inverter voltage change.

We can rewrite equation (3.56) for the sampling time $[t_k\text{-}1]$ as:

$$V_{inv-av}[k-1] = V_{grid-av}[k-1] + L\frac{I_{grid}[k] - I_{grid}[k-1]}{T_s} \tag{3.65}$$

Solving equation (3.65) for $I_{grid}[k]$ lead to:

$$I_{grid}[k] = I_{grid}[k-1] + \frac{T_s}{L}\left(V_{inv-av}[k-1] - V_{grid-av}[k-1]\right) \tag{3.66}$$

We can rewrite equation (3.64) for the sampling time $[t_k\text{-}1]$ as:

$$V_{grid-av}[k-1]=\frac{3}{2}V_{grid}[k-1]-\frac{1}{2}V_{grid}[k-2] \tag{3.67}$$

Substituting equation (3.67) into (3.66) leads to:

$$I_{grid}[k]=I_{grid}[k-1]+\frac{T_s}{L}\left(V_{inv-av}[k-1]-\frac{3V_{grid}[k-1]-V_{grid}[k-2]}{2}\right) \tag{3.68}$$

From equation (3.68), it is clear that the grid current at time [t_k] is estimated by adding the mustered grid current $I_{grid}[k\text{-}1]$ at time [$t_k\text{-}1$] to the predicted current change in the switching period [t_{k-1},t_k]. Figure 3.21 illustrates the switching periods with the grid current values.

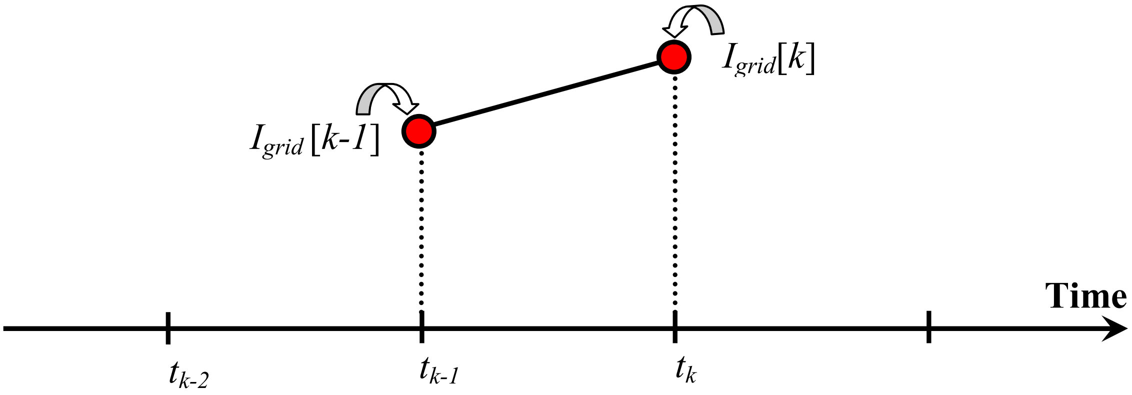

Figure 3.21. Switching periods with the grid current values.

The estimated average grid voltage and grid currant given by equations (3.63) and (3.68), respectively, can be substituted in equation (3.57) to give the traditional predictive current control (TPCC) equation as:

$$V_{inv-av}[k]=4V_{grid}[k-1]-2V_{grid}[k-2]-V_{inv-av}[k-1]+L_m\frac{i_{ref}[k+1]-i_{grid}[k-1]}{T_s} \tag{3.69}$$

where L_m is the modeled inductance of filter inductor. The block diagram of inverter system with the TPCC is shown as Figure 3.22.

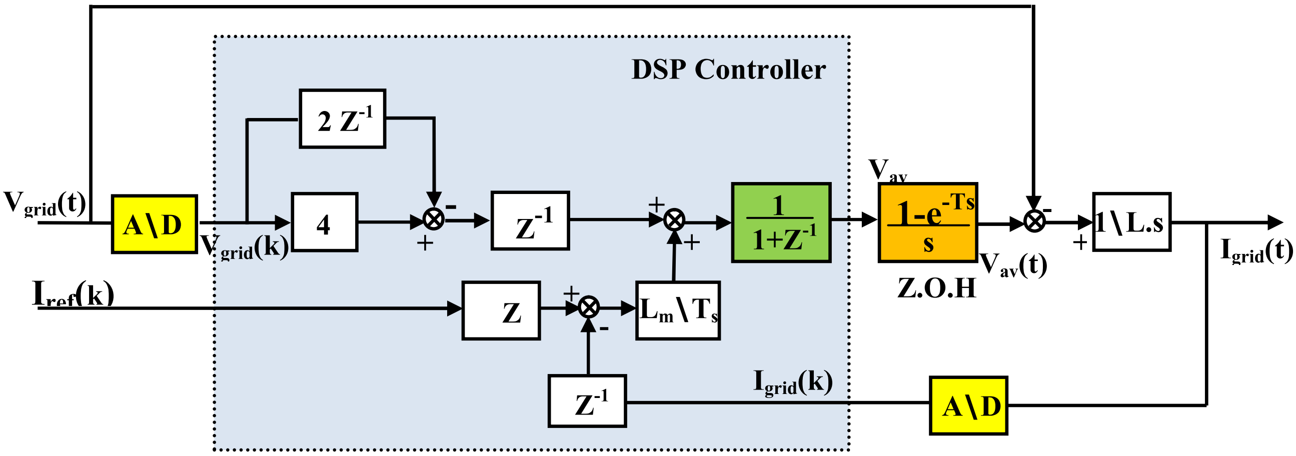

Figure 3.22. Block diagram of inverter system with the TPCC.

From equation (3.69) we notice that, all values are available to the controller when the calculation proceeds at the instant time [t_k-1] and the result will be applied during the switching period [t_k, t_k+1].

The state-space equation of inverter system with the TPCC is derived from equations (3.68) and (3.69). The target of the controller $I_{grid}[k]$, $I_{grid}[k-1]$ and the output of the controller $V_{inv\text{-}av}[k-1]$ are set as state variables. The closed loop system equations are given as:

$$\begin{bmatrix} I_{grid}[k+1] \\ V_{inv-av}[k] \end{bmatrix} = \begin{bmatrix} -\dfrac{L_m}{T_s} & 1 & -\dfrac{T_s}{L} \\ -\dfrac{L_m}{T_s} & 0 & -1 \end{bmatrix} \begin{bmatrix} I_{grid}[k-1] \\ I_{grid}[k] \\ V_{inv-av}[k-1] \end{bmatrix} + \begin{bmatrix} \dfrac{L_m}{L} & \dfrac{4T_s}{L} & -\dfrac{2T_s}{L} & -\dfrac{T_s}{L} \\ \dfrac{L_m}{T_s} & 4 & -2 & 0 \end{bmatrix} \begin{bmatrix} I_{ref}[k+1] \\ V_{grid}[k-1] \\ V_{grid}[k-2] \\ V_{grid-av}[k] \end{bmatrix} \tag{3.70}$$

The characteristic equation of the TPCC closed-loop system is:

$$z^3 + \left(\frac{L_m}{L} - 1 \right) z = 0 \tag{3.71}$$

From equation (3.71) the TPCC closed-loop poles of system are derived:

$$p_1 = 0,\ p_{2,3} = \pm\sqrt{\Delta L} \tag{3.72}$$

where: $\Delta L = 1 - \dfrac{L_m}{L}$ is the relative error between the actual inductance L and modeled inductance L_m of filter inductor.

3.4.9. Improved Predictive Current Control for Single-Phase Grid Inverter

In TPCC, the controller starts the calculation at the beginning of the previous switching interval and the result will be applied to the next interval. This means, the controller has full switching interval time to do the algorithm computations. Low switching frequencies are used for high power applications. So as a result, with the availability of high speed controllers we can conclude that this given time is more than enough and it can be reduced further more.

An improved predictive current control (IPCC) algorithm with better robustness to parameters mismatch is developed by setting the sampling time just ahead the controlling point by the total sampling and computation delay (T_d). Figure 3.23 shows the improved predictive current control (IPCC) timing schematic for the proposed algorithm.

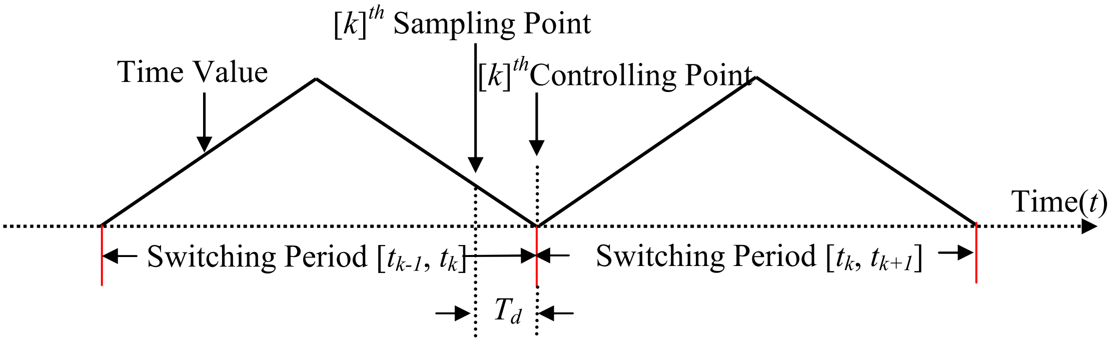

Figure 3.23. Improved PCC timing diagram [27].

As mentioned in Figure 3.23, the sampling period is set at time $[kT_s\text{-}T_d]$.

T_d is very small compared to T_s, with fast controllers and low switching frequencies for power applications, we can assume that this delay time is negligible.

With the above assumption, we can write the grid current $I_{grid}[k]$ and the grid voltage $V_{grid}[k]$ as:

$$I_{grid}[k] \cong I_{grid}[kT_s - T_d] \tag{3.73}$$

$$V_{grid}[k] \cong V_{grid}[kT_s - T_d] \tag{3.74}$$

From above, the values of $I_{grid}[k]$ and $V_{grid}[k]$ are available to the controller at time $[kT_s\text{-}T_d]$, so the calculations can proceed and the result will be applied in the switching period $[t_k, t_k+1]$. The actual grid current at time $[t_k+1]$ given as:

By substituting equation (3.64) into equation (3.57) the control equation for IPCC can be written as:

$$V_{inv-av}[k] = \frac{3}{2}V_{grid}[k] - \frac{1}{2}V_{grid}[k-1] + L_m\left(\frac{i_{ref}[k+1] - i_{grid}[k]}{T_s}\right) \tag{3.75}$$

Comparing equation (3.75) to equation (3.69) it is clear that the improved algorithm has simple computation process and gives more enhanced performance for the injected power to the grid. The block diagram of inverter system with the IPCC is shown as Figure 3.24.

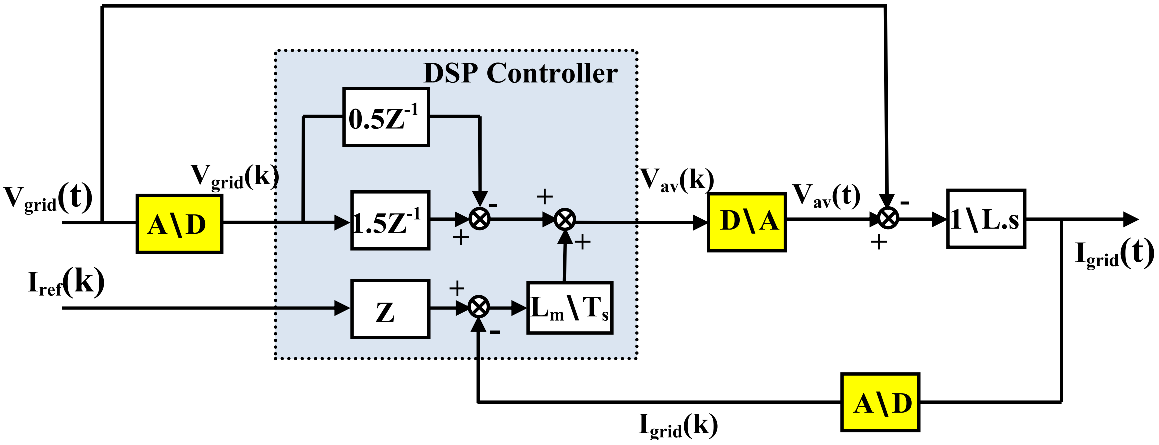

Figure 3.24. Block diagram of inverter system with the IPCC.

Based on equation (3.66) and equation (3.75), the state-space equation of inverter system with the IPCC is derived. Again, the controller target $I_{grid}[k]$ and controller output $V_{inv-av}[k-1]$ are set as state variables [17]. The closed loop system is derived as:

$$\begin{bmatrix} I_{grid}[k+1] \\ V_{inv-av}[k] \end{bmatrix} = \begin{bmatrix} \Delta L & 0 \\ -\frac{L_m}{T_s} & 0 \end{bmatrix} \begin{bmatrix} I_{grid}[k] \\ V_{inv-av}[k-1] \end{bmatrix} + \begin{bmatrix} 0 & 0 & 1-\Delta L \\ -0.5 & 1.5 & \frac{L_m}{T_s} \end{bmatrix} \begin{bmatrix} V_{grid}[k-1] \\ V_{grid}[k] \\ I_{ref}[k+1] \end{bmatrix} \tag{3.76}$$

The characteristic equation of the IPCC closed-loop system is:

$$z^2 - z + \frac{L_m}{L}z = 0 \tag{3.77}$$

From equation (3.77) the IPCC closed-loop poles of system are derived:

$$p_1 = 0 \quad , \quad p_2 = \Delta L \tag{3.78}$$

3.4.10. Influence of Model Mismatch on the System Stability

From the controller equations, we notice that the average inverter voltage depends on the filter inductance value. The relative error of inductance between the actual and modeled inductance, ΔL, will influence the locations of closed-loop poles. This model mismatch will influence the transient response characteristics and the stability of the two systems.

The relative error of inductance, ΔL, could be positive ($\Delta L \geq 0$) or negative ($\Delta L < 0$). The positive relative error implies that the modeled inductance value is smaller than actual inductance value ($L_m < L$). The negative relative error implies that the modeled inductance value is bigger than actual inductance value ($L_m \geq L$).

For traditional predictive current controller, the poles of closed-loop system in z-plane are $p_1 = 0, p_{2,3} = \pm\sqrt{\Delta L}$. When the relative inductance error is positive, one pole is on the positive half real axis and another one is on the negative half real axis and the third pole is located at the origin. When the relative inductance error is negative, one pole is on the positive half imaginary axis and another one is on the negative half imaginary axis and the third pole is located at the origin. Figure 3.25 illustrates the closed-loop poles of traditional predictive system.

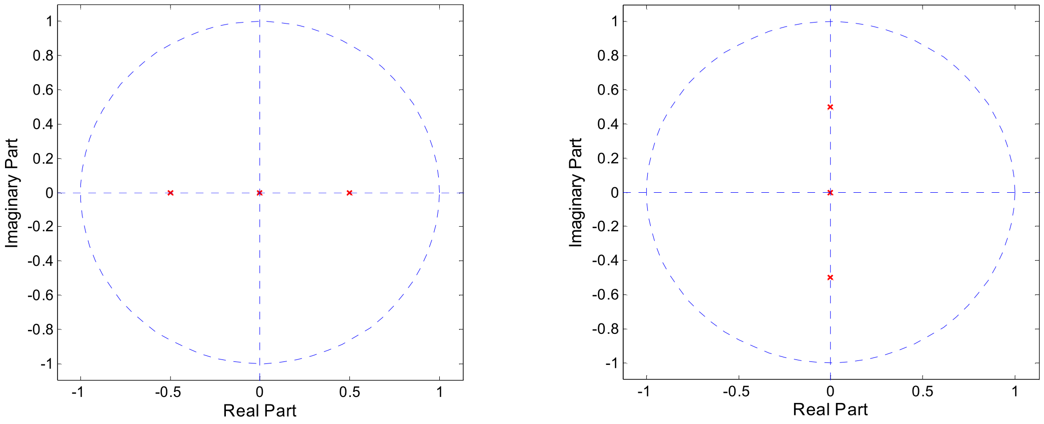

(a) **(b)**

Figure 3.25. Closed-loop poles of traditional predictive system, **(a)** with positive $\Delta L \geq 0$, **(b)** with negative $L < 0$.

On the other hand, for improved predictive current controller, the poles of closed-loop system are $p_1 = 0$ and $p_2 = \Delta L$. When the relative inductance error is positive, one pole is on the positive half real axis and another pole is at origin point. When the relative inductance error is negative, one pole is on the negative half real axis and another pole is at the origin point. Figure 3.26 illustrates the closed-loop poles of improved predictive system.

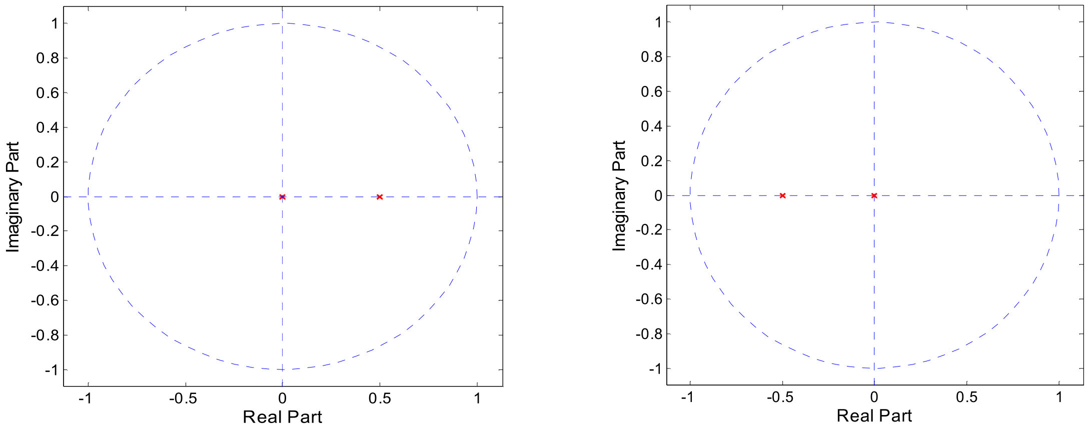

(a) **(b)**

Figure 3.26. Closed-loop poles of improved predictive system, (a) with positive $\Delta L \geq 0$, **(b)** with negative $\Delta L < 0$.

Next, the stable range of two systems is discussed with respect to the relative error between the actual and modeled inductance. The stable criterion of a controlled system in z-plane is that the poles of closed-loop system are located within the unit circle.

For traditional predictive system, the poles of closed-loop system are $p_1 = 0, p_{2,3} = \pm\sqrt{\Delta L}$. So the stable range of relative error of inductance is:

$$-1 \leq \Delta L \leq 1 \tag{3.79}$$

The stable range of the modeled filter inductance for traditional predictive system is then:

$$0 \leq L_m \leq 2L \tag{3.80}$$

For improved predictive system, the poles of closed-loop system are $p_1 = 0$ and $p_2 = \Delta L$. The stable range of the relative error of inductance is:

$$-1 \leq \Delta L \leq 1 \tag{3.81}$$

The stable range of the modeled filter inductance for improved predictive system is:

$$0 \leq L_m \leq 2L \tag{3.82}$$

Then, traditional and improved predictive systems have the same stable range of the modeled filter inductance.

3.4.11. DC-Link Voltage Compensator

To regulate the DC-link capacitor voltage (V_o), the voltage controller needs to be designed properly. For such design, a simple PI controller is used as the DC voltage loop compensator, which has the form of:

$$G_v(s) = K_p^v + \frac{K_i^v}{s} \tag{3.83}$$

Unlike reactive power control, there is no easy way to find a linearized transfer function for DC-link voltage control.Therefore, the process reaction curve method, developed by Ziegler and Nichols, was used to find a starting point for tuning the PI controller [28]. Based on the process reaction curve (step response), the initial PI gains were determined as [29]:

$$K_p^v = \frac{-0.9}{\gamma T} \tag{3.84}$$

and

$$K_i^v = \frac{0.3K_p^v}{T} \tag{3.85}$$

where γ is the slope of the tangent line of the curve, and T is the time between when the step command was issued and the process, the DC-link voltage in this case, began to change. The process reaction curve for the DC-link voltage is shown in Figure 3.27. The initial gains were found with equations (3.84) and (3.85) and tuned until a satisfactory response was obtained. The final gains were $K_p^v = -0.56$ and $K_i^v = -0.32$. The gains are negative because this process exhibits reverse action, meaning an increase in the controller output produces a decrease in the process variable [30].

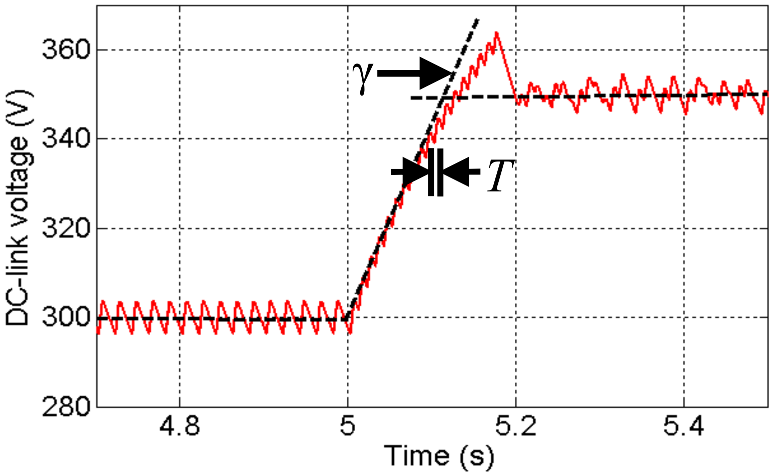

Figure 3.27. DC-link voltage process reaction curve.

3.5. Simulation Results

The proposed predictive current controllers for the single-phase grid connected inverter are verified by simulation using MATLAB/SIMULINK with a sampling period of 10 µsec. For all of the simulations, the DC-link voltage and grid voltage are 400V and 220V, respectively.

The filter inductor is 5mH, the output power is 1 kW, and the switching frequency of IGBTs is set at 10 kHz. For positive relative inductance error ($\Delta L>0$) the TPCC and IPCC approaches are simulated with three different modeled filter inductance values ($L_m=0.9L$, $L_m=0.6L$, $L_m=0.2L$).

The predictive average output voltage, and grid current waveforms with TPCC and IPCC are monitored in Figure 3.28 and Figure 3.29 respectively for comparison.

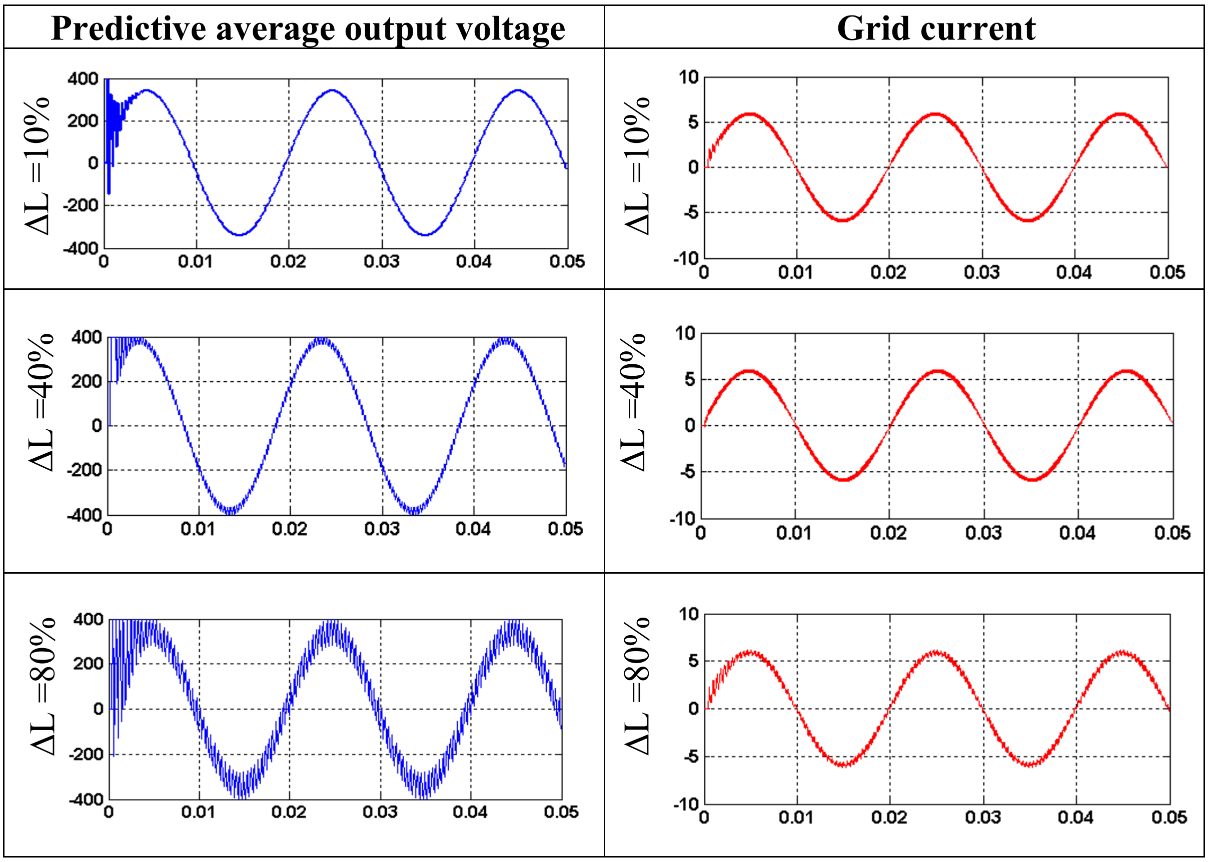

Figure 3.28. Model mismatch ($\Delta L>0$) influence with the TPCC.

Figure 3.28 illustrates the simulation results of proposed system with the traditional predictive current algorithm, where the modeled inductance is smaller than the actual inductance.

It is noted that the predictive output voltage and grid current begin to oscillate when $\Delta L>0=10$ %. The oscillations become more obvious when ΔL turns bigger ($\Delta L>0=40$ % and *80* %).

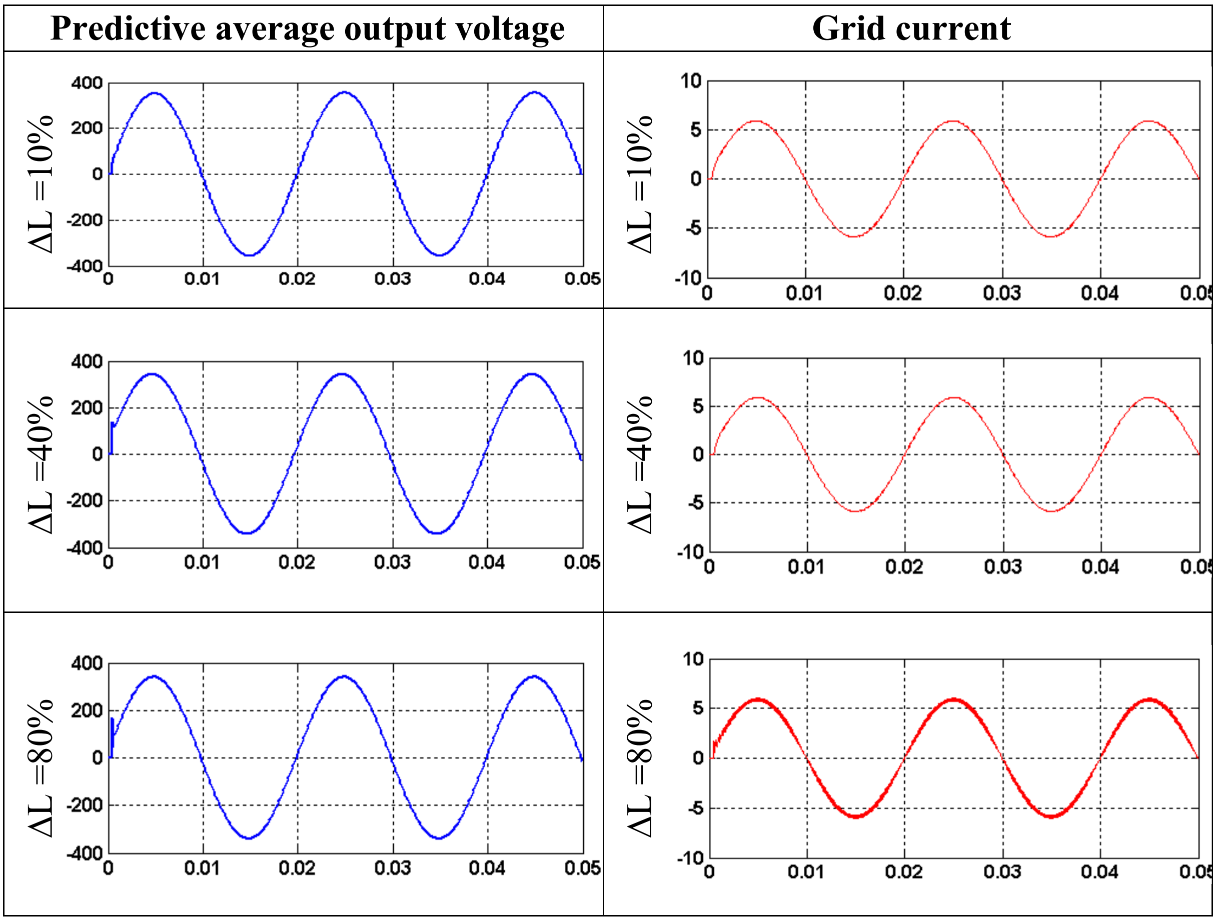

Figure 3.29. Model mismatch (Δ*L*>*0*) influence with IPCC.

Figure 3.29 illustrates the simulation results of proposed system with the improved predictive algorithm, where the modeled inductance is smaller than the actual inductance. It is seen that there is no oscillation in predictive output voltage and grid current. So the conclusion in Section 4.4.1 has been confirmed by simulation results.

Figure 3.30 illustrates the simulation results of proposed system whose controller implements the traditional predictive algorithm, where modeled inductance is bigger than the actual inductance. It is found that that the predictive output voltage and grid current begin to oscillate when Δ*L* = -10 %. The oscillation turns more obviously when Δ*L* = -40 %. When Δ*L* = -80 %, the predictive output voltage and grid current oscillate continuously. This confirms the analysis previous Section 4.4.1 that a traditional system turns unstable when model inductance is two times bigger than actual inductance.

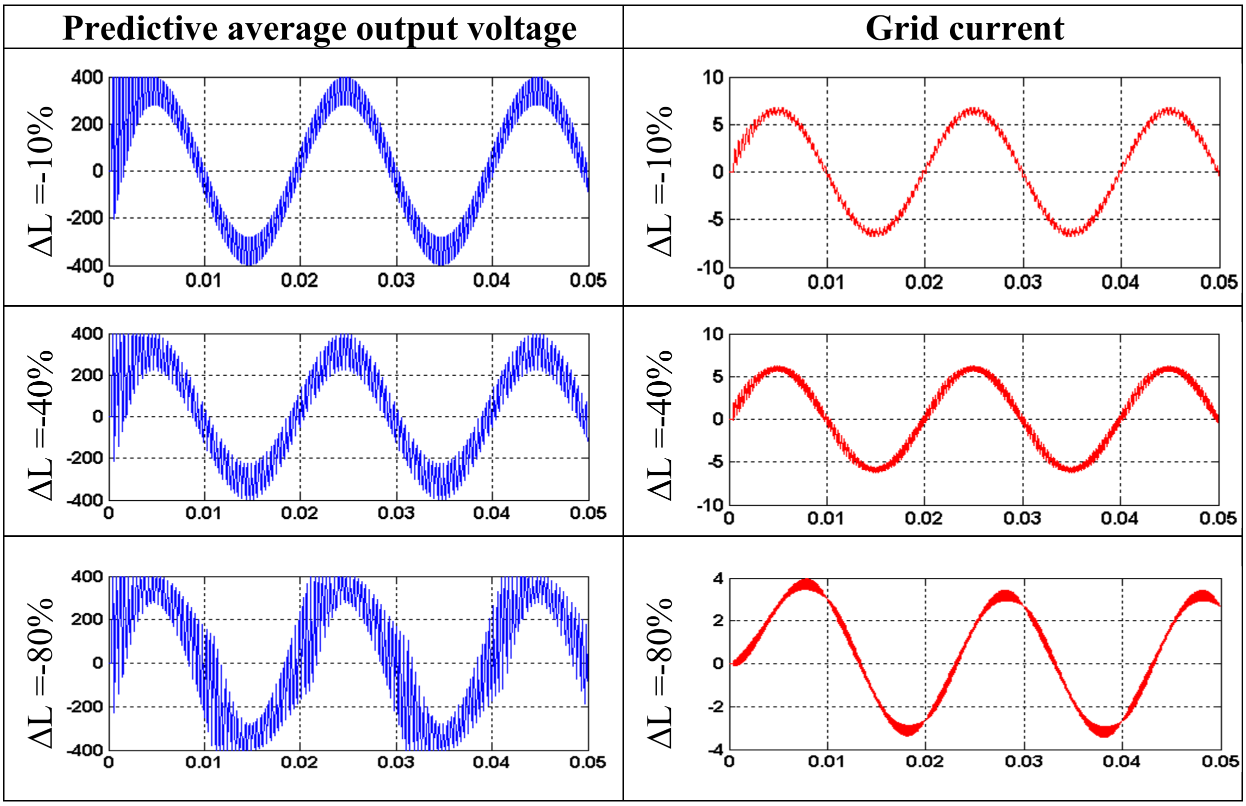

Figure 3.30. Model mismatch (Δ*L*<0) influence on System I with TPCC.

Comparing Figure 3.28 and Figure 3.30, one can also notice that the oscillations are similar at Δ*L* = 80 % and Δ*L* =-10%. This proves that the proposed system with the traditional predictive current algorithm is more sensitive to the relative inductance error when relative inductance error is negative (-1<Δ*L*<0) than when relative inductance error is positive (0<Δ*L*<1).

Figure 3.31 illustrates the simulation results of proposed system whose controller implements the improved predictive algorithm, where the modeled inductance is bigger than the actual inductance. It is shown that the predictive output voltage and grid current begin to oscillate when Δ*L* = -10 %. The oscillation becomes more obvious at Δ*L* = -40 %. When Δ*L* = -80 %, the predictive output voltage and grid current oscillate continuously. This confirms the analysis in Section 4.4.1 that the proposed system with the improved predictive algorithm becomes unstable when model inductance is two times bigger than actual inductance.

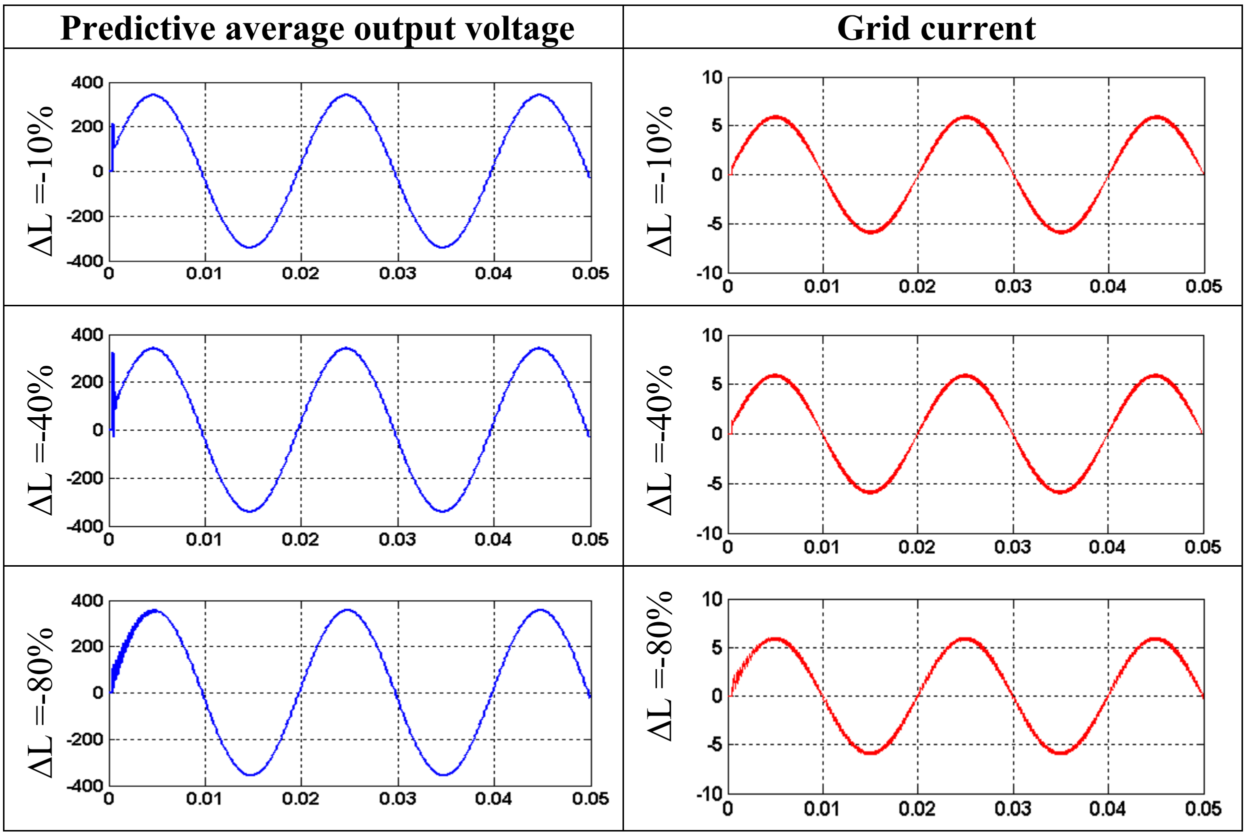

Figure 3.31. Model mismatch (ΔL <0) influence on System II with IPCC.

By comparing both Figure 3.30 and 3.31, it is worth noting that both systems start to oscillate continuously when modeling inductance is two times bigger than the actual one, but the magnitude of perturbations in the traditional method is much bigger than the proposed one.

In addition, for $|\Delta L| \leq 40\%$, the proposed method has an acceptable output current waveform with small THDi. However, the traditional method has an unacceptable THDi for $|\Delta L| \geq 10\%$.

The simulation results have proven that the model mismatch of the filter inductor influences the system stability and transient response characteristics. For predictive controllers, the accuracy of the model will affect the controller performance dramatically.

The system with the improved predictive control algorithm is more robust than the system with the traditional predictive algorithm.

The closed loop system poles for TPCC and IPCC are shown in Figure 3.32.

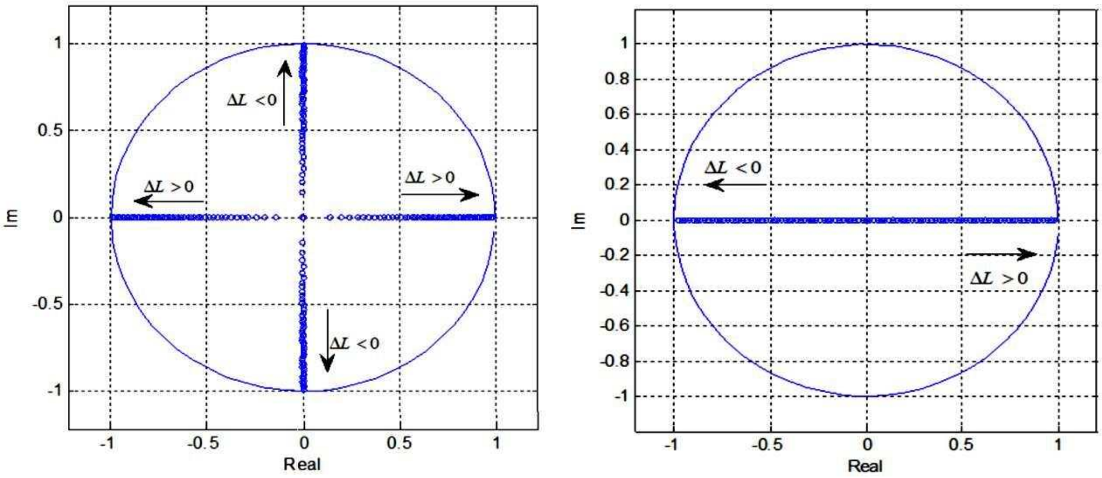

(a) **(b)**

Figure 3.32. Closed loop poles plot for ($0<L_m<2L$). **(a)** TPCC poles, **(b)** IPCC poles.

3.6. Experimental Implementation and Validation

3.6.1. Experimental Setup

To verify the performance of proposed MPC-MPPT algorithm for the SIBC and the IPCC algorithm for the single-phase full bridge inverter, a prototype of grid connected wind energy system based on a small PMSG is developed as shown in Figure 3.33.

The prototype has been built by Semikron SKM75GB123D dual-pack IGBT modules, SKKD75F12 dual-pack diode modules and SKHI22B dual core gate drivers.

The experimental system is set up by coupling a DC-Motor to drive the PMSG as depicted in Figure 3.34. The DC-Motor is most frequently used for wind turbine emulators, which is able to simulate the turbine power curves without using a closed loop control system.

The flow chart of the proposed MPC-MPPT algorithm and IPCC algorithm are implemented by using the dSPACE-DS1104 controller board.

The Real-Time Workshop and dSPACE Control Desk are used together to handle the control algorithm.

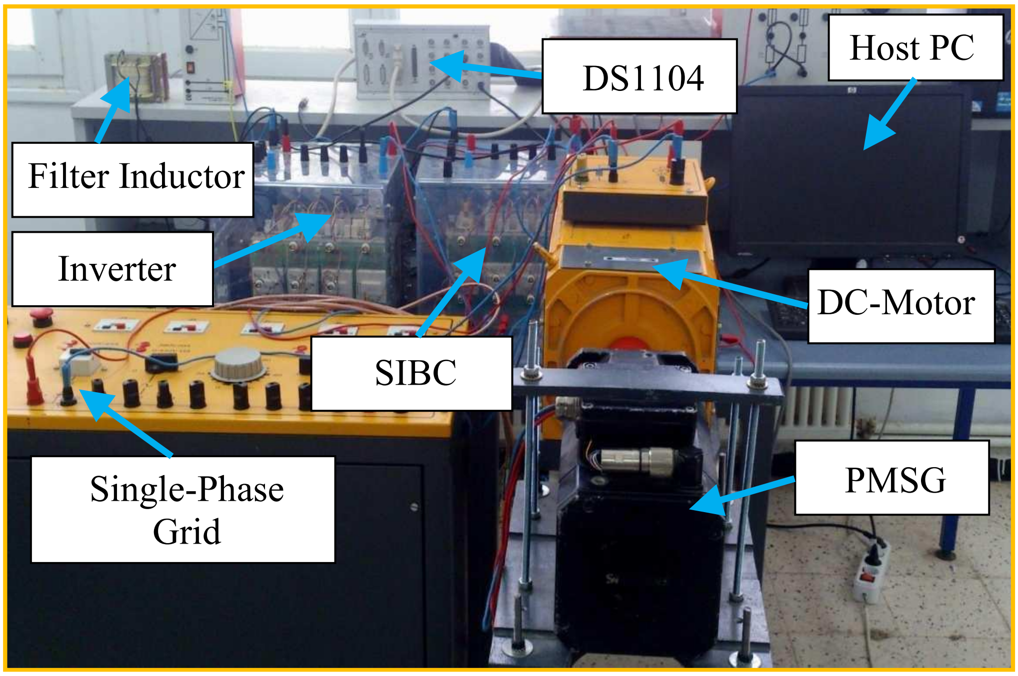

Figure 3.33. Photograph of the experimental setup.

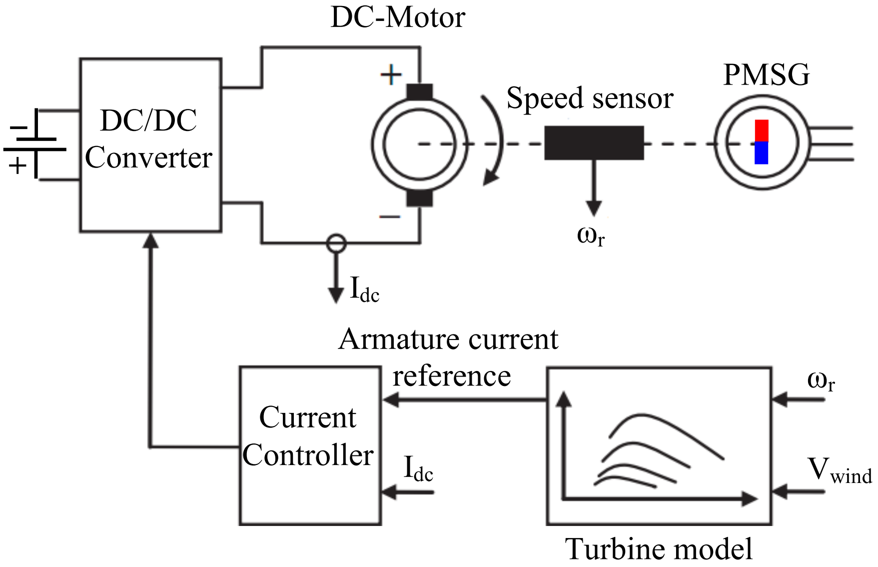

Figure 3.34. Control scheme of the turbine emulator that uses a DC-Motor.

Figure 3.35 shows the experimental results of the output power of wind generator (mechanical power) versus rotational speed curves of the PMSG under the DC-Motor driver setting as: 100V, 120V, 140V, 160V, 180V, 200V, and 220V. The above armature voltages can equivalently represent the wind speed as: 6 m/sec, 7 m/sec, 8 m/sec, 9 m/sec, 10 m/sec, 11 m/sec, and 12 m/sec, respectively.

The curves of Figure 3.34 are the base of the wind turbine emulator, they have been obtained for a 3 kW DC-motor.

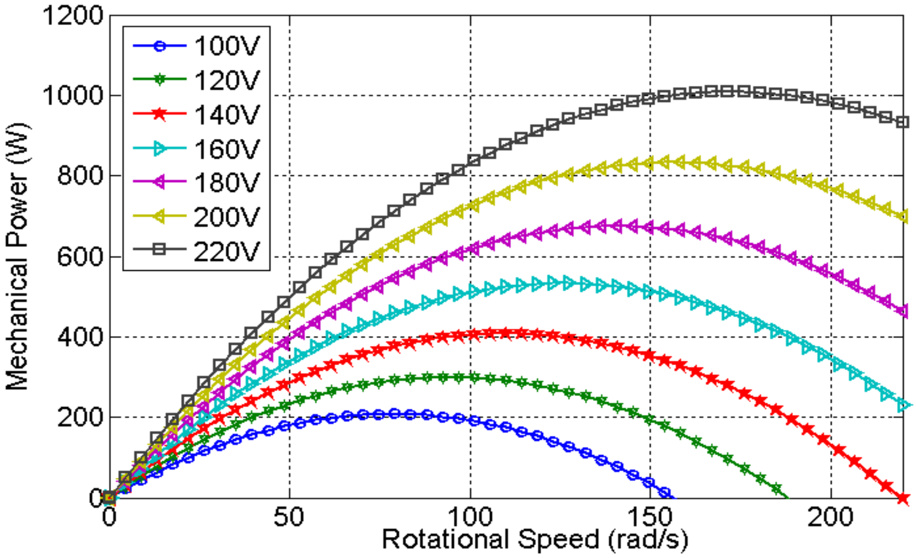

Figure 3.34. DC-Motor mechanical power curves for various values of the DC-voltage source

As seen in Figure 3.34, it can be found that each different wind speed has different maximum power points (MPPs). This means that the proposed MPC-MPPT algorithm must be incorporated in the control of the SIBC to operate the wind energy system effectively.

Figure 3.35 shows the experimental result of the system using the proposed MPC-MPPT algorithm. In this test, the algorithm goal is to track the maximum power operating point of the system and the wind speed has changed in several steps.

The graphs shown the correspond respectively to: the wind speed, the turbine shaft speed, the input current of the SIBC and its optimal reference, the power conversion coefficient C_p, the mechanical torque, the power captured from wind (mechanical power) and the power provided to the grid (electrical power), the DC-link capacitor voltage (V_o) and the armature current of the DC-Motor (I_{dc}).

As can be seen from the plots the turbine shaft speed is continuously matched to the wind speed in such a way that it is extracted maximum power out of the wind. The DC-input current of SIBC is controlled according to the MPPT strategy and can be better regulated to achieve the optimum reference current during wind speed step changes.

Also, the power conversion coefficient C_p is kept constant, and varies in a relatively small range around its optimal value of 0.47, which means the wind turbine tracks maximum power from the wind. The mechanical torque changes accordingly to accommodate the variations in the wind speed.

The mechanical power had small fluctuations phenomenon, but the value of the wind turbine power would back to the best value soon.

It is noticed that the mechanical input power is slightly greater than the electrical power production due to the system losses. The DC-link voltage response is completely robust with perfect rejection of wind speed disturbances and is maintained within the variation of 2%.

Note also that only active power is delivered to the grid when the PI controller reaches its steady state value. The armature current (I_{dc}) is variable and depends on the mechanical power variations, thus the armature current is changed as the wind speed changes.

The obtained results confirm that the proposed MPC-MPPT algorithm of the SIBC works properly and quite able to track the maximum wind power of the wind generation system effectively according to an increase/decrease in the wind speed. This verifies that the tracking performance of the proposed MPC-MPPT algorithm is very good.

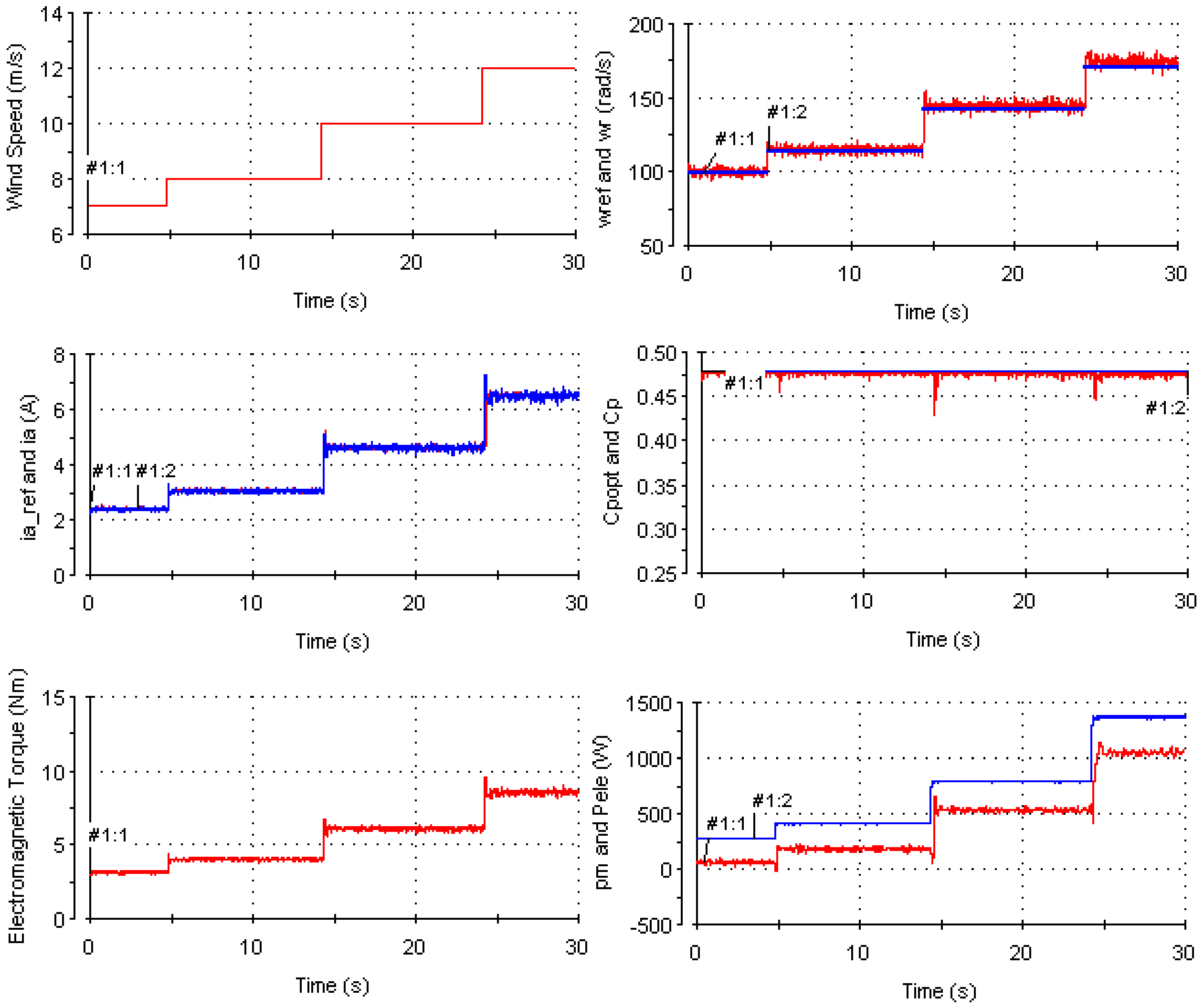

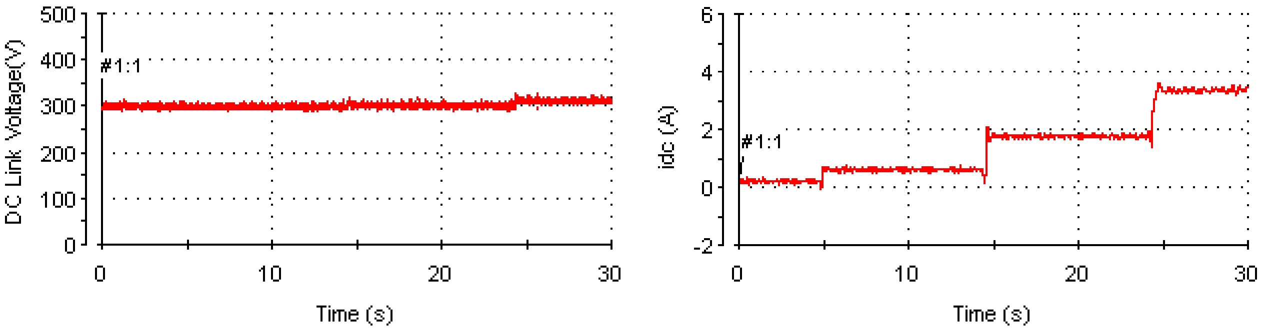

Figure 3.35. Practical dynamic response of the proposed wind energy system.

Figure 3.36 shows the tracking performance comparison between three typical MPPT algorithms: the Tip-Speed Ratio (TSR) algorithm, the P&O algorithm, and the proposed MPC-MPPT algorithm. It can be seen from Figure 3.36 that every MPPT algorithm works properly, i.e. successfully tracks the maximum power point (MPP). The proposed MPC-MPPT algorithm was found to be the fastest in achieving the MPP. The recovery time upon wind speed change was also faster for the proposed MPC-MPPT algorithm. The dynamic response for algorithms based on proposed MPC-MPPT and TSR is relatively similar. In comparison, the P&O algorithm was found to be the slowest algorithm. Therefore it can be concluded that the robust tracking performance is achieved using the proposed MPC-MPPT algorithm under the wind speed variation.

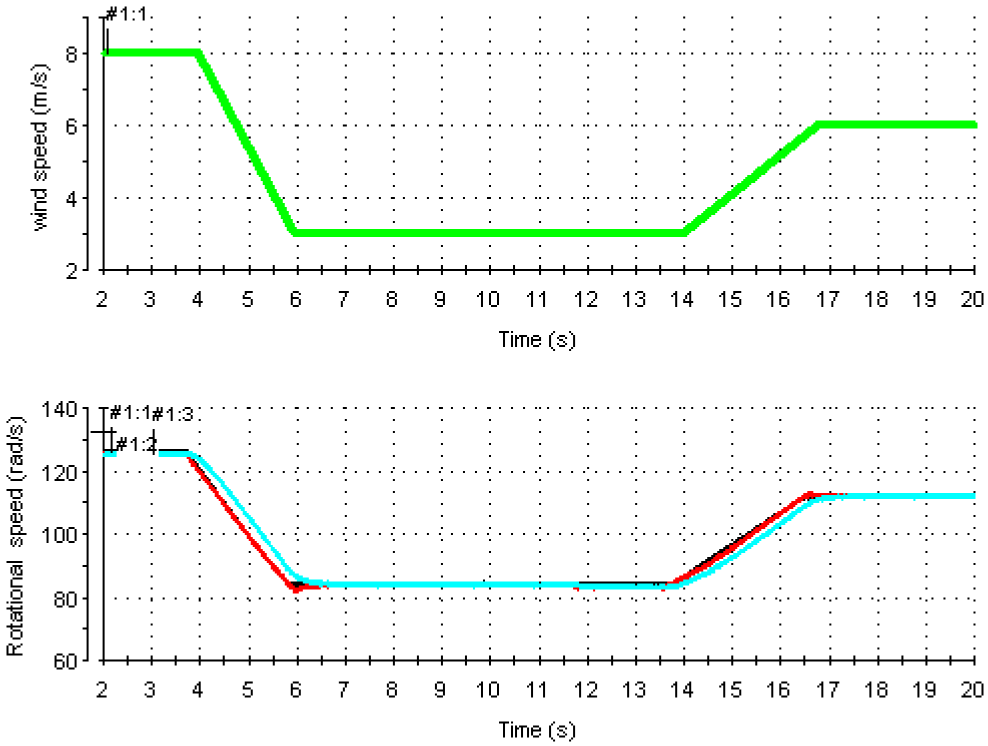

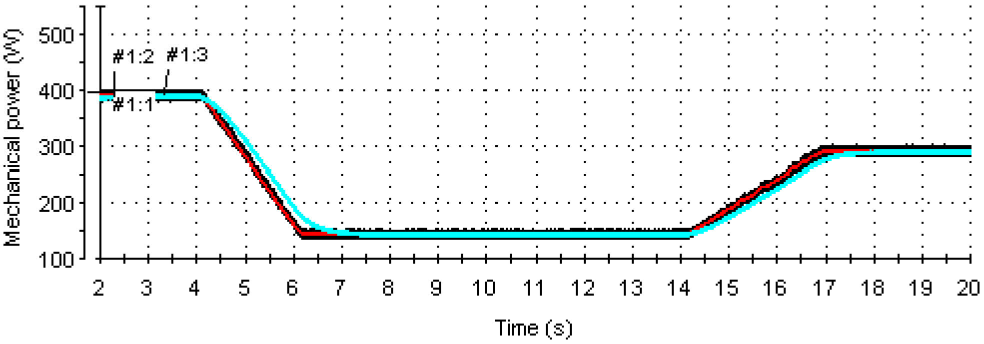

Figure 3.36. Comparison of MPPT tracking performance: based on the proposed MPC-MPPT (Black), based on the P&O (Cyan), based on the TSR (Red); from the top: reference wind speed (m/s), turbine rotational speed (rad/s), turbine mechanical power (W).

The comparisons of the three typical algorithms considering the efficiency and energy yield are summarized in Table 3.2 Based on results and analysis, the proposed MPC-MPPT algorithm reached the highest value of power conversion coefficient (C_p). It was followed by the Tip-Speed Ratio (TSR) algorithm, with the average value of C_p being 0.4627. The P&O algorithm was found to be the least efficient method.

Table 3.2

Summary of performance of three MPPT algorithms.

Method	**C_p**	**Response time (s**	**Recovery time (s)**	**Energy (W)**	**Efficiency (%)**
MPC-MPPT(Proposed)	0.4785	0.0247	0.0007	734.5	96.48
Tip-speed ratio (TSR)	0.4627	0.0885	0.0024	665.9	90.42
P&O	0.4123	0.2478	0.0371	597.4	80.44

The improved predictive current control (IPCC) has been applied in a single-phase full bridge inverter. After having synchronized and connected the wind energy inverter system to the grid. The test is conducted on a chosen wind profile varying as step functions from 7 to 12 m/sec and 12 to 7 m/sec, respectively.

For these operating conditions, the waveforms of the voltage and current on the utility grid are recorded by using the digital oscilloscope. Figure 3.37 shows the experimental waveforms of the inverter output current and utility voltage during a step transient in wind speed.

As can be seen the output current waveform of the inverter is highly sinusoidal, and is in opposite phase with the fundamental component of the grid voltage. The change of current peak value is created by varying wind speed.

It is obvious that the system has an excellent dynamic performance, whose controller implements the improved predictive current control (IPCC) algorithm.

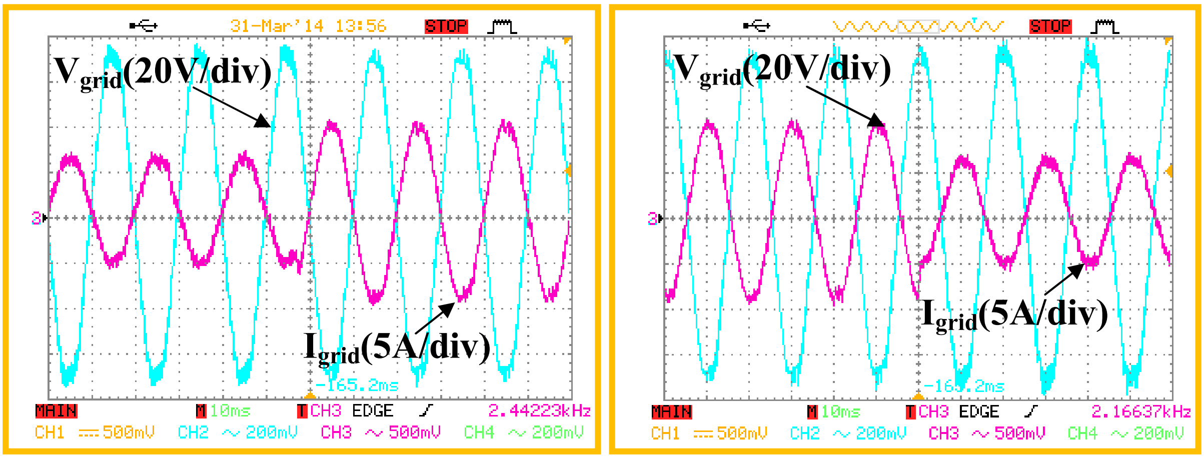

(a) **(b)**

Figure 3.37. Experimental dynamic response of the grid-side inverter during the wind change. **(a)** Grid current and grid voltage when wind speed up. **(b)** Grid current and voltage when wind speed down.

The characteristics waveforms of grid interfaced wind energy system under steady state condition where the wind speed is assumed to be constant are shown in Figure 3.38(a-d).

It is clearly seen that the total harmonic distortion (THDi) of grid current is approximately 2.7%, whish respect the standards imposed by IEEE-519 as shown in Figure 3.38(a). Figure 3.38(b) gives the measured results of power factor (PF) of the system versus the active power (Pg) injected into the grid.

It is obvious that a unity power factor is achieved (PF=0.999), which can satisfies the power factor demand in industrial applications. Figure 3.38(c) illustrates Fresnel diagram of grid phase current and voltage using the proposed IPCC scheme of the single-phase full bridge inverter.

As shown in Figure 3.38(c), the grid current leads the grid voltage by approximately 180°. Finally, Figure 3.38(d) shows the experimental waveforms of grid phase voltage and current, in this figure it can be observed that the grid current and voltage are well regulated sinusoidal with almost unity power factor, i.e. grid current and voltage are in a 180° phase shift.

These tests results confirms that the proposed wind energy system can convert the wind power generated from the PMSG to a high quality AC power, and this AC power injects into the utility grid.

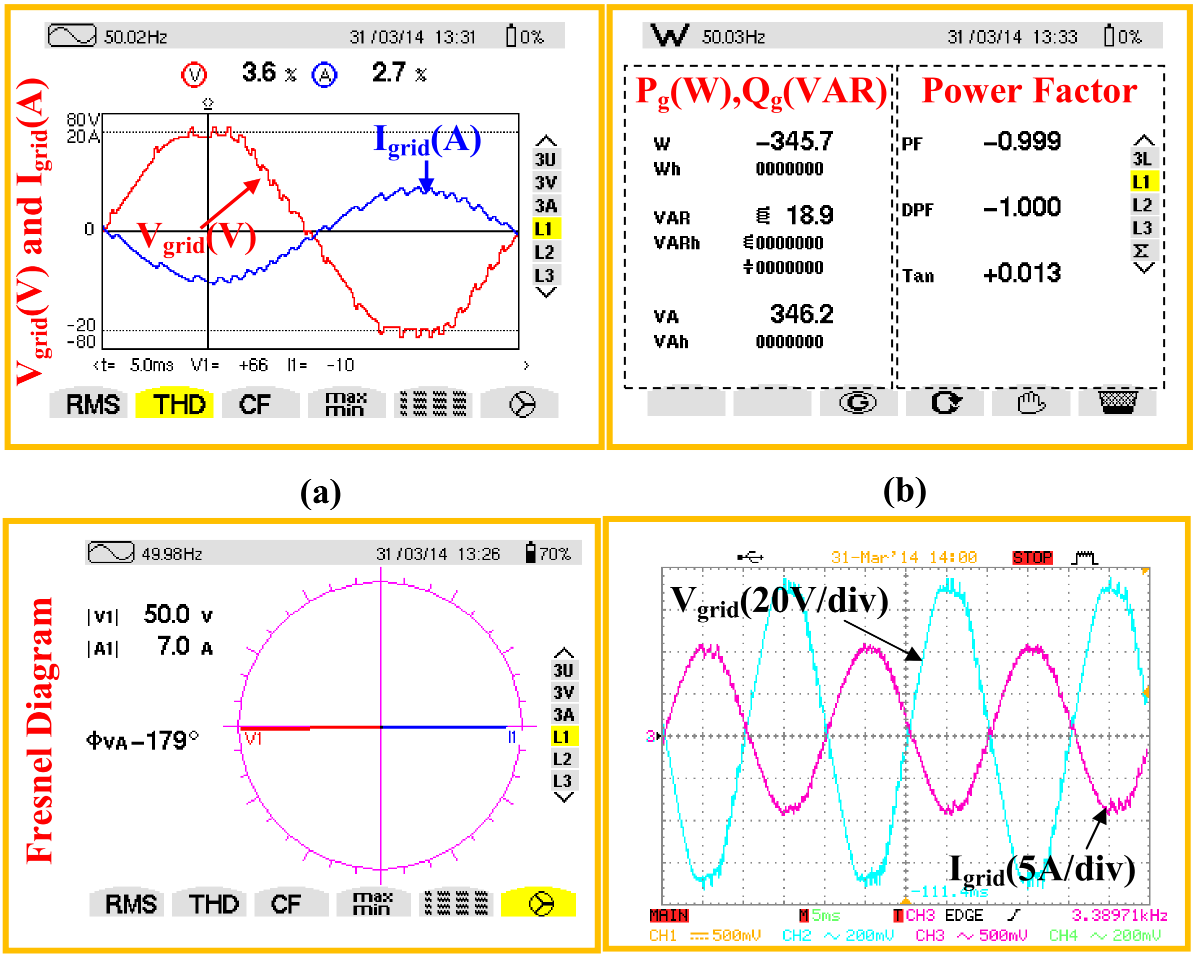

(a) (b)

(c) (d)

Figure 3.38. Experimental steady-state waveforms. (a) THDi of grid current and voltage. **(b)** Measured power factor (PF). **(c)** Fresnel diagram. **(d)** Grid phase voltage and current.

3.7. Conclusion

In this chapter, an efficient power conditioning system for grid connected wind energy applications was introduced. The proposed system can potentially reduce the cost and size of wind turbine generator systems. A switched inductor boost converter (SIBC) is a totally novel technology, it has been used as DC/DC boosting stage converter due to its inherent features such as high DC/DC conversion ratio and better efficiency. Hence, MPPT techniques based on HCS algorithm employing a MPC method is proposed to extract maximum power from the wind generator through the SIBC. Modifications applied to the traditional HCS algorithm enabled the proposed MPC-MPPT algorithm to interact quickly for rapidly varying wind conditions. Moreover, it has been shown that the proposed

MPC-MPPT algorithm can be easily implemented with reduced hardware setup because only current and voltage sensors have been used. So, neither the measurement of the wind speed nor the knowledge of the wind turbine characteristics is required. Then, three of the typical MPPT algorithms (tip-speed ratio (TSR) algorithm, P&O algorithm, and proposed MPC-MPPT algorithm) have been implemented practically. A comparison between the MPPT algorithms has been carried out to demonstrate the advantages of the proposed MPC-MPPT algorithm, the results have shown that the proposed MPC-MPPT algorithm is the most favorable featuring fast dynamic response, and accuracy under almost any conditions. Finally, an additional improved predictive current controller (IPCC) is proposed in order to achieve the synchronization to the grid and to perform the power management between the wind generation system and the electrical grid. Theoretical analysis of such IPCC and traditional predictive current controller (TPCC) is presented in this Chapter. Effect of model parameter mismatch on the performance of the IPCC and TPCC is presented. The simulation results indicate that the sensitivity of IPCC is reduced to disturbances and uncertainty in filter inductor. The developed IPCC has been successfully implemented in a single-phase grid connected wind energy system. The practical results confirm that the application of IPCC in grid connected inverters provide better THDi value based on IEEE standards. In addition the power factor can approach to unity (PF=0.999) and meets IEC commercial standard.

References

[1] **Shukla R.D, and Tripathi R.K:** "Maximum power extraction schemes and power control in wind energy conversion system," *International Journal of Scientific and Engineering Research 2015; 3(6): pp.1–7.*

[2] **Musunuri S, Ginn H.L:** "Comprehensive review of wind energy maximum power extraction algorithms," *In IEEE Power and Energy Society General Meeting 2011, Detroit, Michigan, USA, pp.1-8.*

[3] **Kesraoui M, Korichi N, Belkadi A**: "Maximum power point tracker of wind energy conversion system", *Renewable Energy 2010; 36(10): pp.2655-2662.*

[4] **Koutroulis E, Kalaitzakis K:** "Design of a maximum power tracking system for wind-energy-conversion applications", *IEEE Transactions on Industrial Electronics 2006; 53(2): pp.486-494.*

[5] **Hui J:** "An adaptive control algorithm for maximum power point tracking for wind energy conversion systems," *Master's thesis, Queen's University, Kingston, Ontario, Canada, 2008.*

[6] **R. Kazmi S.M, Goto H, Guo H.J, and Ichinokura O:** "A novel algorithm for fast and efficient speed-sensorless maximum power point tracking in wind energy conversion systems," *IEEE Trans. on Indust. Elec. 2011; 58(1): pp.29–36.*

[7] **Baroudi JA, Dinavahi V, Knight AM:** "A review of power converter topologies for wind generators", *Renewable Energy 2007; 32(14): pp.2369-2385.*

[8] **Chen Z, Guerrero J.M, and Blaabjerg F:** "A review of the state of the art of power electronics for wind turbines," *IEEE Trans. Power Electron. 2009; 24(8): pp. 1859–1875.*

[9] **Wang H, Nayar C, Su J, Ding M:** "Control and interfacing of a grid-connected small-scale wind turbine generator", *IEEE Transactions on Energy Conversion 2011; 26(2): pp.428-434.*

[10] **Kjaer S, Pedersen J, and Blaabjerg F:** "A review of single-phase grid-connected inverters for photovoltaic modules," *IEEE Transactions on Industry Applications 2005;41(5): pp.1292–1306.*

[11] **Wu T.F, Sun K.H, Kuo C.L, and Chang C.H:** "Predictive current controlled 5-kW single-phase bidirectional inverter with wide inductance variation for DC-micro grid applications," *IEEE Trans. Power Electron. 2010; 25(12): pp.3076-3084.*

[12] **Dannehl J, Fuchs F.W, and Hansen S:** "PI state space current control of grid-connected PWM converters with LCL filters," *IEEE Trans. Power Electron. 2010; 25(9):pp. 2320-2330.*

[13] **Shen G, Zhu X, Zhang J, and Xu D:** "A new feedback method for PR current control of LCL-filter-based grid-connected inverter," *IEEE Trans. Ind. Electron. 2010; 57(6): pp. 2033–2041.*

[14] **Costa-Costello R, et. Al:** "Odd-harmonic digital repetitive control of a single-phase current active filter," *IEEE Transactions on Power Electronics 2004; 19(4):pp.1060-1068.*

[15] **Kukrer O, Komurcugil H:** "Deadbeat control method for single-phase UPS inverters with compensation of computation delay," *Electric Power Applications, IEE Proceedings 1999; 146(1): pp.123-128.*

[16] **Komurcugil H:** "Double-band hysteresis current-controlled single-phase shunt active filter for switching frequency mitigation", *Int. J. Electr. Power Energy Syst 2015; 69: pp.131–140.*

[17] **Yu B:** “Predictive Current Controlled PWM Strategy for Grid-connected Single-Phase Inverter,” *M.Sc. thesis, Univ. New Brunswick, Fredericton, NB, Canada, 2004.*

[18] **Holtz J and Stadtfeld S:** “A predictive controller for the stator current vector of AC machines fed from a switched voltage source,” *In Proc. Annul. Meeting Int. Power Electron. Conf.1983; pp.1665–1675.*

[19] **Holmes D.G and Martin D.A:** “Implementation of a direct digital predictive current controller for single and three phase voltage source inverter,” *IEEE Annul Meeting on Industry Applications, vol. 2, San Diego 1996, pp.906–913.*

[20] **Abdel-Rahim O, Orabi M, Ahmed M:** “Development of high-gain high-efficiency grid-connected inverter for PV module”, *IEEE Symp. On Int. Power Electronics for Distributed Generation Systems 2010; pp. 368–373.*

[21] **Erickson RW, Maksimovic D:** “Fundamental of power electronics”, *Kluwer Academic Publishers, New York, 2004; pp.187–204.*

[22] **Rodriguez J, Kazmierkowski M.P, Espinoza J.R, Zanchetta P, Abu-Rub H, Young H.A, Rojas C.A:** “State of the art of finite control set model predictive control in power electronics,” *IEEE Trans. Ind. Informat. 2013; 9(2): pp.1003–1016.*

[23] **Rodriguez J and Cortes P:** “Predictive Control of Power Converters and Electrical Drives”, *Hoboken, NJ, USA: Wiley 2012, vol. 37.*

[24] **Shamad M.B,. Balog R.S, and Abu-Rub H:** “Model Predictive Control of PV Sources in a Smart DC Distribution System: Maximum Power Point Tracking and Droop Control”, *IEEE Transaction on Energy Conversion 2014; 29: pp.913-921.*

[25] **Shadmand M.B, Mosa M, Balog R.S, and Abu-Rub H:** "Maximum Power Point Tracking of Grid Connected Photovoltaic System Employing Model Predictive Control”, *IEEE Applied Power Electronics Conference & Exposition (APEC) 2015.*

[26] **Kojabadi, Hossein Madadi, Bin Yu, Idris A. Gadoura, Liuchen Chang, & Mohsen Ghribi:** “A novel DSP-based current-controlled PWM strategy for single phase grid connected inverters”, *IEEE Transactions on Power Electronics 2006; 21(4): pp.985-993.*

[27] **Timothy L. Skvarenina:** “The Power Electronics Handbook Industrial Electronics Series”, *2nd ed. CRC Press, 2002.*

[28] **Ziegler J and Nichols N:** “Optimum settings for automatic controllers,” *Trans. ASME 1942; 64: pp.759–768.*

[29] **Franklin G, Powell J, and Emami-Naeini A:** “Feedback Control of Dynamic Systems”, *Upper Saddle River, NJ, USA: Pearson Prentice-Hall, 2006; pp.198–199.*

[30] **Johnson C.D:** “Process Control Instrumentation Technology”, *Engle-wood Cliffs, NJ, USA: Prentice-Hall1993.*

Chapter 4

Fuzzy MPPT and Fuzzy Model Based-Multivariable Predictive Controller Design for Fast and Efficient Speed Sensorless Maximum Power Extraction of Renewable Wind Generators

Abstract

In the Chapter 1, the finite set model predictive control (FS-MPC) of the DC/DC boost converter was presented. In this chapter, another approach based on fuzzy logic and fuzzy model based-multivariable predictive control is proposed to get the maximum power for a direct driven small-scale wind energy systems connected to the grid, assuming that the grid-side converter regulates the active power delivered to the grid.

The concept of the proposed fuzzy MPPT strategy is simple and does neither require to measure the wind speed nor to know the turbine parameters. A fuzzy logic generator is particularly employed to derive the optimum rectified current corresponding to the best power point based on the variations of measured DC power and rectified voltage, while a robust fuzzy model based multivariable predictive controller (FMMPC) is presented to track the derived optimum current with minimum steady-state error.

The major issues of the proposed control strategy such as detailed design process and stability conditions analysis of the two controllers have been thoroughly investigated and presented in this Chapter. The feasibility of the proposed control method has been applied to a wind turbine generator driving a PMSG in variable speed mode through the MATLAB/Simulink tests.

In order to confirm the simulation results, a practical implementation have been performed on a 3kW test bench consisting of a dSPACE 1104 controller board, PMSG and DC-motor drive. Comparative experimental results have demonstrated the achievable significant performance improvements on the maximum wind power extraction and overall system response by using the proposed control strategy as compared with a conventional PI controller.

4.1. Introduction

Many MPPT approaches are proposed in literature for the maximum power extraction enhancement of PMSG wind turbines such as: duty cycle control [1], look-up table for optimum rotor speed control [2], and optimum tip-speed ratio (TSR) control [3]. Generally, these schemes require a correct knowledge of the wind power system parameters either before or during execution. Moreover, the wind turbine components tend to modify their characteristics over the time. Therefore, a control strategy independent of the wind turbine parameters and does not require prior knowledge of wind speed, such as perturbation and observation (P&O) method is very flexible and accurate [4, 5]. This control method is relatively simple and is appropriate for wind turbines with small inertia. Recently, considerable investigations of this method mainly include simplified and advanced perturbation and observation algorithm [6], adaptive MPPT compensation algorithm [7], two-stage control method [8], hill-climb searching control method [9], and variable step size-based perturbation and observation algorithm [10]. Although relatively simple and flexible. However, this control method suffers from the problems of high steady state errors and large frequency oscillations. Other MPPT control algorithms, such as fuzzy reasoning based MPPT control [11], neural network control [12], and advanced vector control [13], have also been proposed in the literature. However, such control strategies necessitate time consuming computations, and have relatively low efficiency. Furthermore, such control methods need additional control efforts and expensive sensors [14]. This Chapter presents a new hybrid MPPT control “Fuzzy MPPT controller + robust fuzzy model based multivariable predictive controller (FMMPC)” for grid connected wind energy systems. The developed control strategy mainly consists of a novel fuzzy logic MPPT controller for deriving the reference current and an innovative fuzzy model based multivariable predictive controller (FMMPC) that is designed to exactly track the reference current and hence to realize the MPPT control. The main reason of the use of FMMPC in wind energy systems is the ability of the FMMPC to optimally control multivariable nonlinear systems under constraints. The presence of constraints in the predictive control strategy is important. Input constraints give more realism to the control actions by modeling the saturation and the slew rate constraints in the actuator. Output constraints are used to ensure a safety operation of the plant [15]. Fuzzy logic is widely used in model predictive control (MPC). Its use can be classified into two general classes of approaches [16]. In the first class, a fuzzy model is used as a predictor. The second class of methods depends on the multistage fuzzy decision making [17]. The cost function and the constraints are fuzzy, while the system model may be fuzzy or no fuzzy [18, 19].

The design of stabilizing fuzzy model based multivariable predictive controllers (FMMPCs) is the main aim of most researchers. In [20], Keerthi and Gilbert used the cost value function as a Lyapunov function for establishing stability of

FMMPC, techniques based on end point constraints are used to stabilize the FMMPC systems in [21, 22]. The main disadvantage of these techniques is that there is no guarantee that the FMMPC drives the states to the terminal region. In [23], constraints on the control signal and its increment are given to guarantee robust asymptotic stability of the FMMPC. This method can be used only for open loop bounded-input bounded-output (BIBO) stable processes.

In this Chapter, a robust fuzzy multivariable model predictive controller (FMMPC) using Linear Matrix Inequalities (LMIs) formulation is suggested to ensure exponential stability of the closed-loop systems. The main idea is to solve at each time instant, an LMI optimization problem that incorporates input, output and constrained receding horizon predictive control (CRHPC) constraints. The proposed FMMPC is easily designed by solving a convex optimization problem subject to LMI conditions, and adds more flexibility by selecting control actions that minimizes a general cost function in the predicted errors through a prediction horizon, the applied control actions through a control horizon, and the increments of control actions through a control horizon. Furthermore, the proposed FMMPC ensures robust asymptotic stability, does not need an auxiliary controller, and can be used with any feasible controller parameters. In addition, this Chapter demonstrates how major issues in the design and implementation of the two controllers (Fuzzy MPPT controller + robust FMMPC) can be handled effectively. Comparative experimental results are presented to demonstrate the achievable significant performance improvements in maximum power extraction, and overall wind energy system response by using the proposed control strategy.

The Chapter is arranged as follows. In Section 2, the wind energy studied system is presented. In Section 3, the fuzzy MPPT control design to attain the maximum wind energy is introduced. In Section 4, the integrated T-S fuzzy model based-multivariable predictive controller (FMMPC) is totally reviewed, and the optimization problem with LMI constraints is also discussed. In Section 5, the discrete T-S fuzzy model based-multivariable predictive controller (FMMPC) for the DC/DC boost converter is developed. In Section 6, the fuzzy MPPT control and the performance of the proposed control strategy under large wind speed variation are verified by simulation results. In Section 6, the experiment validation and a comparison with traditional PID controller are given. In Section 9, the conclusions of this chapter are summarized.

4.2. Configuration of proposed wind energy system

The synoptic schematic of the studied wind energy system is shown in Figure 4.1. The conversion chain is composed of a three-bladed horizontal axis wind turbine, a multi-pole three-phase permanent magnet synchronous generator (PMSG), a three-phase bridge rectifier, a DC/DC boost converter and a three-phase voltage source inverter (3PH-VSI) which is connected to the grid through a LC_I filter . The extracted wind power is directly transmitted to the PMSG, and is converted into electrical power by this generator. The generated electrical power can then be rectified by the simple diode rectifier bridge, boosted by the DC/DC boost converter, and consequently fed to the utility grid via a 3PH-VSI. Due to the uncontrollability of the diode bridge rectifier, a DC/DC boost converter is used to guarantee the maximum power capture of electrical energy from the wind generator. The grid-side inverter regulates the power transfer between the DC-link capacitor and the utility grid. Hence, independent regulations for the active and reactive powers at the generator and the grid-sides can be achieved effectively.

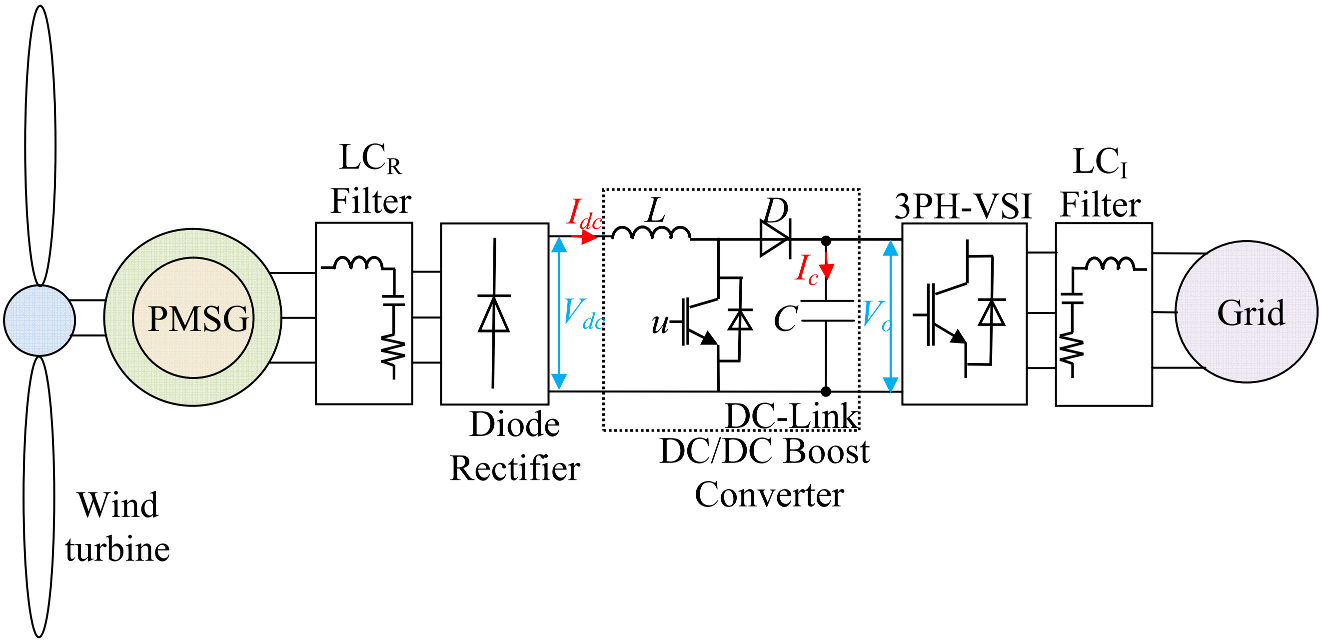

Figure 4.1. Configuration of wind energy system.

4.2.1. Generator and Input Rectifier Characteristics

The PMSG, which is driven by a wind turbine, converts mechanical power into electrical power. The mechanical power produced by the wind energy system, is given by:

$$P_m = \frac{1}{2}\rho A C_p(\lambda,\beta)\vartheta_w^3 \tag{4.1}$$

where ρ is the mass density of air, C_p is the performance coefficient of the turbine, A is the swept area of the turbine blade , ϑ_w is the wind velocity , λ is the tip-speed ratio (TSR) and β is the blade pitch angle, in this study set to zero.

For a PMSG with a constant flux, the phase back electromotive force (EMF) is proportional to the generator speed and can be expressed as:

$$E = k_e\omega_m \tag{4.2}$$

where E is the back EMF of the generator, k_e denotes the back-EMF constant (positive) of the PMSG, and ωm is the rotational angular velocity of the PMSG.

Assuming that the inner resistance of the PMSG is zero, the phase terminal voltage V_{ac} in Root-Mean Square (RMS) for a non-salient PMSG is written as:

$$V_{ac} = E - j\omega_e L_s I_{ac} \tag{4.3}$$

$$\omega_e = p\omega_m \tag{4.4}$$

where I_{ac}, L_s are the phase current in RMS and the phase inductance of the PMSG, ω_e is the electrical angular frequency, and p is the number of pole pairs. Figures 4.2(a) and 4.2(b) show the equivalent circuit per phase and the phasor diagram of the PMSG connected to the diode rectifier obtained at certain operating conditions.

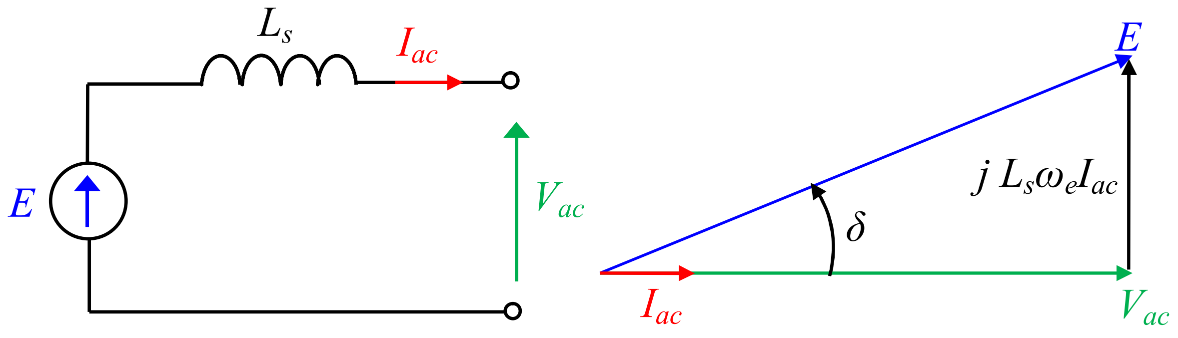

Figure 4.2. PMSG run with the diode rectifier wind energy system. **(a)** Equivalent circuit per phase, **(b)** Phasor diagram.

We assume that there is no energy loss, the electrical AC power generated by the PMSG (P_{ac}) is converted into electrical DC power (P_{dc}) can be denoted ideally as follows:

$$P_{ac} = P_{dc} = 3V_{ac}I_{ac} = V_{dc}I_{dc} \tag{4.5}$$

where P_{ac} is the generator power, and V_{dc} and I_{dc} are the average rectified voltage and current, respectively, of the three-phase bridge diode rectifier. The rectified voltage (V_{dc}) at the rectifier output shown in Figure 4.3 is proportional to the generator phase voltage, and can be expressed as:

$$V_{dc} = \frac{3\sqrt{2}}{\pi}V_{LL} = \frac{3\sqrt{6}}{\pi}V_{ac} \tag{4.6}$$

where V_{LL} is the line-to-line voltage of the PMSG.

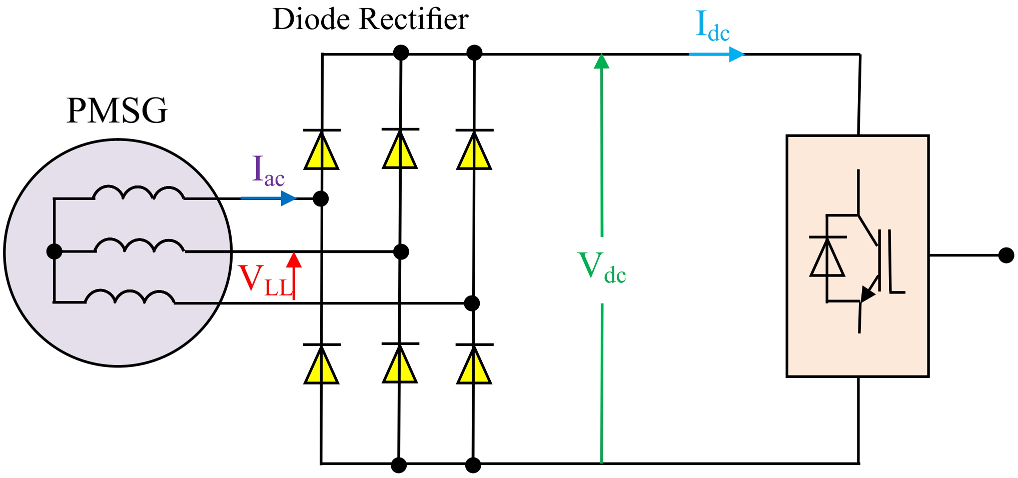

Figure 4.3. Topology of the PMSG with the diode rectifier supplying DC/DC boost converter

The rectified current I_{dc} can be obtained by substituting equation (4.6) into equation (4.5) as:

$$I_{dc} = \frac{\pi}{\sqrt{6}} I_{ac} \tag{4.7}$$

The rectified voltage V_{dc} is proportional to rotational speed ω_m as is shown in Figure 4.4. The speed varies from ω_{m-min} to ω_{m-max} and then at the minimum speed the rectified voltage has to be V_{dc-min}, where the V_{dc-max} the maximum of rectified voltage.

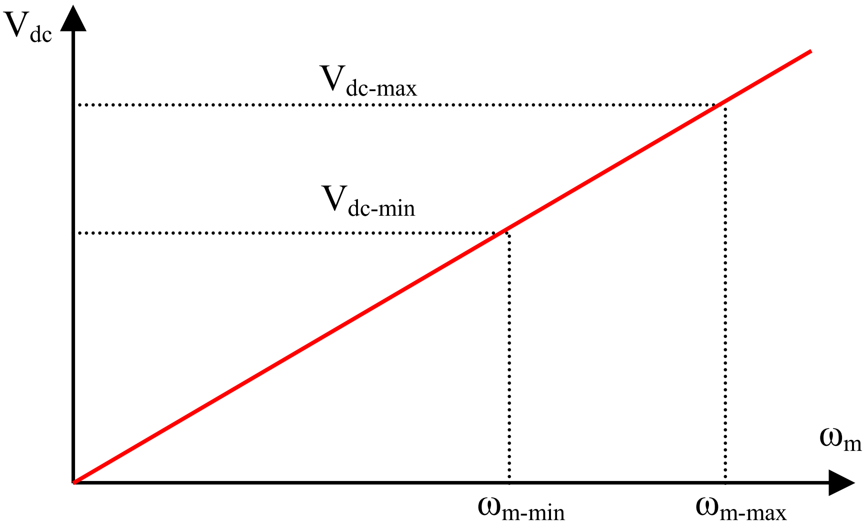

Figure 4.4. Rectifier output voltage supplying DC/DC boost converter.

The relationship between the rotational angular velocity of the PMSG and the rectifier output-voltage can be obtained from equations (4.2), (4.3) and (4.7) is expressed as follows:

$$V_{dc} = \frac{3\sqrt{6}}{\pi}\left(k_e - \frac{\sqrt{6}}{6} p\, L_s I_{dc}\right)\omega_m \tag{4.8}$$

The TSR is defined as the ratio between the linear blade tip-speed and the wind speed, is expressed as:

$$\lambda = \frac{\omega_m R}{\vartheta_w} \tag{4.9}$$

where ϑ_w and R are the wind velocity and radius of the turbine blade respectively.

It is considerable to notice that there is a unique optimum value of the λ_{opt} at which the power coefficient is maximum C_{p_max} [24]. If the system operates at the optimal point, the maximum mechanical power expression can be established as follows:

$$P_{max} = K_p \omega_{m\_opt}^3 \tag{4.10}$$

where P_{max} is the maximum mechanical power, ω_{m_opt} is the optimum wind rotor angular velocity corresponding to a specific wind speed, k_p is a power control gain given by:

$$k_p = \frac{\rho \pi R^5 C_{p\_max}}{2\lambda_{opt}^3} \tag{4.11}$$

From equations (4.1) and (4.10), there is the approximate relationship:

$$P_{max} \propto \vartheta_w^3 \propto \omega_{m\_opt}^3 \tag{4.12}$$

The relationship between the optimum rectified voltage and the optimum angular velocity near the maximum power point (MPP) is expressed as:

$$V_{dc\_opt} = \frac{3\sqrt{6}}{\pi}\left(k_e - \frac{\sqrt{6}}{6} p\, L_s I_{dc}\right)\omega_{m\_opt} \tag{4.13}$$

where V_{dc_opt} is the optimum rectified voltage at the MPP.

Substituting equation (4.10) into equation (4.13) yields:

$$V_{dc} \propto \omega_m \text{ and } V_{dc\_opt} \propto \omega_{m\_opt} \tag{4.14}$$

From equations (4.10) and (4.13), at the MPP, the following relationship is valid:

$$P_{max} \propto V_{dc\_opt}^{3} \tag{4.15}$$

Meanwhile, the optimum rectified DC power can be described as:

$$P_{dc\_opt} = \eta\, P_{max} = V_{dc\_opt}\, I_{dc\_opt} \tag{4.16}$$

where $\eta<1$ is the transmission efficiency is assumed to be a constant to take into account mechanical and electrical power leakages., $I_{dc\text{-}opt}$ denote the optimum rectified current.

Combining equations (4.15) and (4.16) yields:

$$I_{dc\_opt} \propto V_{dc\_opt}^{2} \tag{4.17}$$

Substituting equation (4.17) into equation (4.16) yields:

$$I_{dc\_opt} \propto \left(P_{dc\_opt}\right)^{\frac{2}{3}} \tag{4.18}$$

As indicated in equations (4.17) and (4.18), the optimum rectified rent I_{dc_opt} is proportional to the square of the rectified voltage V_{dc_opt}, and is directly related to the optimum rectified DC power P_{dc_opt}. Therefore, the maximum electrical power can be captured by the wind generator when the rectified current I_{dc} is well kept around its optimum value I_{dc_opt}.

The stator current (Iac) of the PMSG is described as:

$$I_{ac} = \frac{E}{j\omega_e L_s} sin\delta \tag{4.19}$$

where δ is called the phase angle.

From equations (4.5) and (4.20), the generator active power is expressed as:

$$P_{ac} = 3\frac{V_{ac}E}{j\omega_e L_s} sin\delta \tag{4.20}$$

By assuming that the inductance of the PMSG and the DC-link output voltage of the boost converter are almost constant, the back EMF and the terminal voltage of the PMSG are changed by the duty-ratio control of the boost converter. If the back EMF (E) and the terminal voltage (V_{ac}) are changed to the E' and V'_{ac} by the control of the boost converter, the stator current (I_{ac}) of the generator is also changed to I'_{ac}. Thus, power of the generator can be controlled by the duty-ratio control of the boost converter. Consequently, the generator can be operated at the optimal operating point using the proposed MPPT control under the given wind speed condition. A phasor diagram of the proposed system is shown in Figure 4.5.

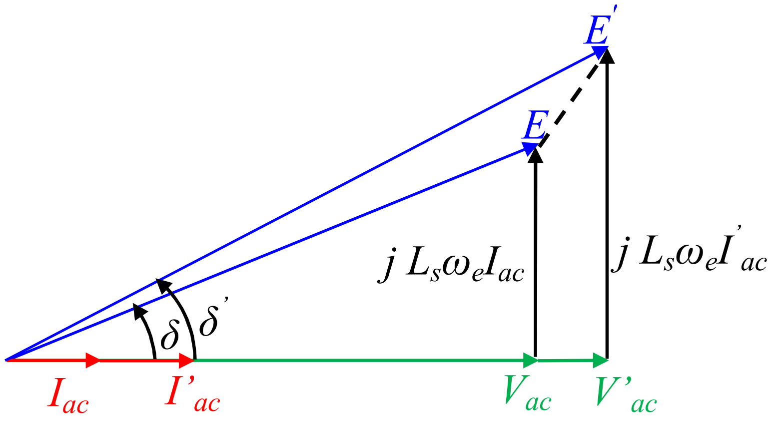

Figure 4.5. Phasor diagram of the PMSG run with the diode rectifier wind energy system.

4.3. Fuzzy-Based MPPT Control

The main objective of this section is to construct an MPP current-reference generator by using a Fuzzy Logic Controller (FLC) that meets the actual MPP. In particular, this generator is designed in order to compute on-line the optimal rectified current value ($I_{dc_{opt}}$).

So that, if the rectified current (I_{dc}) is being equal to I_{dc_opt} then, the maximal power is captured. The main advantage of this method is that it does not require either wind velocity sensors or rotor speed sensors.

Generally, there are three stages in this control algorithm, namely fuzzification, fuzzy reasoning method and defuzzification.

As shown in Figure 4.6, the electrical DC power (P_{dc}) and rectified voltage (V_{dc}) variations are selected as the two input variables for the FLC.

At the k^th sampling period, both variables are normalized by the scaling factors K_1, K_2 and updated using the following equations:

$$\Delta P_{dc}[k] = K_1(P_{dc}[k] - P_{dc}[k-1]) \tag{4.21}$$

$$\Delta V_{dc}[k] = K_2(V_{dc}[k] - V_{dc}[k-1]) \tag{4.22}$$

where $\Delta P_{dc}[k]$ and $\Delta V_{dc}[k]$ denote the electrical DC power and rectified voltage variations, respectively, $P_{dc}[k]$, $V_{dc}[k]$, $P_{dc}[k-1]$ and $V_{dc}[k-1]$ indicate the electrical DC power and rectified voltage at the sampling instants (t_k) and (t_{k-1}), respectively.

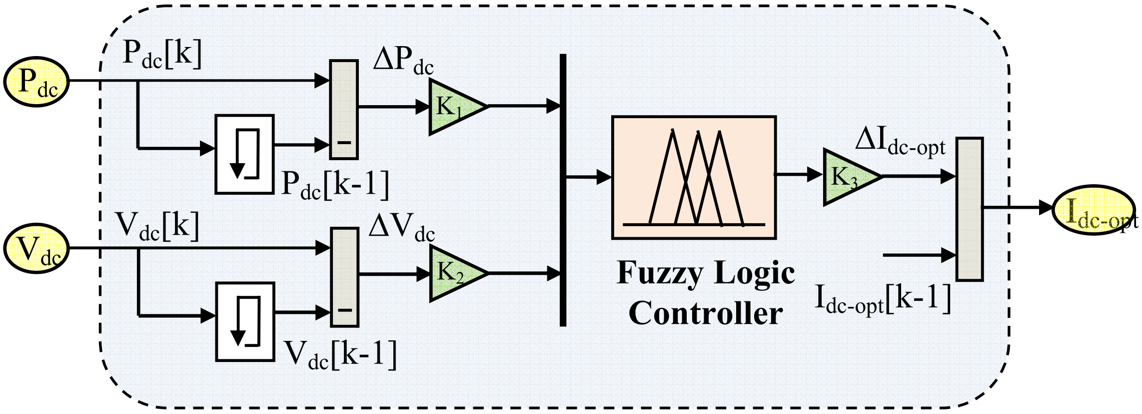

Figure 4.6. Block diagram of the proposed FLC-MPPT controller.

The DC power can be defined as:

$$P_{dc}[k] = V_{dc}[k].I_{dc}[k] \qquad (4.23)$$

Where $I_{dc}[k]$ and $V_{dc}[k]$ denote the rectified current and voltage at the sampling instant (t_k), respectively.

The change in the optimum rectified current ($\Delta I_{dc\_opt}[k]$) is used as an output of the proposed FLC. To design the fuzzy sets of the inputs and output variables, the triangular symmetrical membership functions with the overlap are used to yield more sensitivity to small signals, which are illustrated in Figure 4.7.

The input and output variables, i.e. $\Delta P_{dc}[k]$, $\Delta V_{dc}[k]$ and $\Delta I_{dc\_opt}[k]$ are represented by linguistic variables or labels such as **PB** (Positive Big), **PM** (Positive Medium), **PS** (Positive Small), **Z0** (Zero), **NB** (Negative Big), **NM** (Negative Medium), and **NS** (Negative Small) using basic fuzzy subsets.

The control rules are derived from the experience and knowledge on the control system. The fuzzy mapping of the input variables to the output is expressed by the following rules:

R_i:**IF** $\Delta P_{dc}[k]$ is A_i **and** $\Delta V_{dc}[k]$ is B_j, **THEN** $\Delta I_{dc\_op}[k]$ is C_k,
where $i,j=1,2,..,7;\ k=1,2,3,...,49$

where A_i and B_j denote the antecedents, and C_k denotes the consequent part, respectively. The fuzzy rules are given in Table 4.1.

Table 4.1 Fuzzy Control Rules.

$\Delta I_{dc\_opt}(k)$		**$\Delta V_{dc}(k)$**						
		NB	NM	NS	ZO	PS	PM	PB
$\Delta Pdc(k)$	NB	PB	PB	PB	ZO	NM	NB	NB
	NM	PM	PM	PM	ZO	NS	NM	NM
	NS	PM	PS	PS	ZO	NS	NS	NM
	ZO	NM	NM	NS	ZO	PS	PM	PB
	PS	NM	NS	NS	ZO	PS	PS	PM
	PM	NM	NM	NM	ZO	PS	PM	PM
	PB	NB	NB	NB	ZO	PM	PB	PB

The fuzzy with the Mamdani type is applied for the inference mechanism [25]. The output level $\Delta I_{dc\_opt}[k]$ of each rule is weighted by the firing strength W_i of the rule, which is obtained from the minimum operation as:

$$W_i = min\{\mu_{\Delta p_{dc}}(\Delta P_{dc}[k]), \mu_{\Delta V_{dc}}(\Delta V_{dc}[k])\} \tag{4.24}$$

The defuzzification is performed using the centroid of area (COA) of final combined fuzzy set.

The final combined fuzzy set is defined by the union of all rule output fuzzy sets using the maximum aggregation method [26].

Thus, the change of the optimum rectified current $\Delta I_{dc_{opt}}[k]$ is determined by the COA method as follows:

$$\Delta I_{dc_{opt}}[k] = \frac{\sum_{j=1}^{n} \mu\left(\Delta I_{dc\_opt_j}\right) \times \Delta I_{dc\_opt_j}}{\sum_{j=1}^{n} \mu\left(\Delta I_{dc\_opt_j}\right)} \tag{4.25}$$

The output of fuzzy logic controller is the change of the optimum rectified current $\Delta I_{dc_{opt}}[k]$, which is converted to the optimum rectified current $I_{dc_{opt}}[k]$ by:

$$I_{dc\_opt}[k] = I_{dc\_opt}[k-1] + \Delta I_{dc\_opt}[k] \tag{4.26}$$

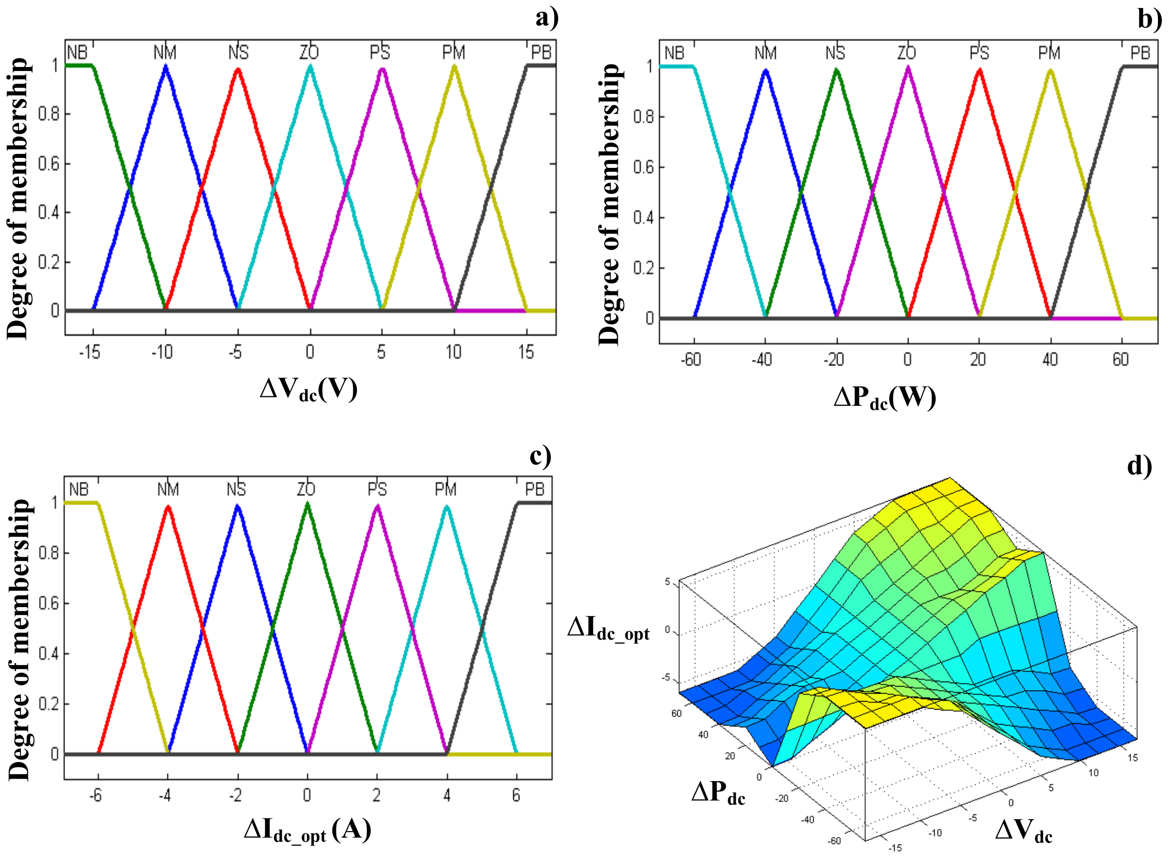

Figure 4.7. Normalized membership functions (MFs) and corresponding surface viewer. **a).** Input variable MF–ΔV_{dc}, **b).** Input variable MF–ΔP_{dc}, **c).** Output variable MF–ΔI_{dc_opt}, **d).** Surface-graph viewer between input and output of fuzzy rules.

4.4. Design of Constrained Fuzzy Multivariable Model Predictive Controller (FMMPC)

In the next section, the discrete T-S fuzzy dynamic model is used to describe the original nonlinear system for the control design aim via the sector nonlinearity approach.

4.4.1. Fuzzy Discrete Time T-S Model

T–S fuzzy models are suitable for modeling a large class of nonlinear systems [27-29]. They consist of fuzzy IF–THEN rules which represent local linear input–output relations of a nonlinear system. The overall fuzzy model of the system is achieved by fuzzy blending of the linear system models [30]. In a discrete fuzzy system (DFS), the rules of the T–S fuzzy model take the form [30].

$$\mathrm{R}_i : IF \quad z_1(\mathrm{k}) \ is \ M_{i1} \ and...and \ z_p(\mathrm{k}) \ is \ M_{ip} \tag{4.27}$$

$$\begin{aligned} THEN \quad & x(\mathrm{k}+1) = A_i x(\mathrm{k}) + B_i u(\mathrm{k}) \\ & y(\mathrm{k}) = C_i x(\mathrm{k}) \qquad\qquad i = 1, 2, ..., r \end{aligned} \tag{4.28}$$

In the above equations $z_p(k)$ are the decision variables (fuzzy scheduling variables) assumed measurable, M_{ij} are the corresponding fuzzy set ($j = 1, ..., p$) of $z_j(k)$ in rule R_i, k is the time index, r is the number of model rules: $x(k) \in R^n$ is the state vector, $u(k) \in R^m$ is the input vector, $y(k) \in R^q$ is the output vector, $A_i \in R^{n\times n}$, $B_i \in R^{n\times m}$, $C_i \in R^{q\times n}$,and $D_i \in R^{q\times m}$ are the state space matrices of the local systems, $z_1(k),\dots, z_p(k)$ are known premise variables that may be functions of the state variables, external disturbances and time.

Given a pair of ($x(k)$, $u(k)$) , and by fuzzy blending, the final outputs of the discrete T–S fuzzy system is inferred as follows [30]:

$$\begin{aligned} \mathrm{x}(\mathrm{k}+1) &= \frac{\sum_{i=1}^{r} w_i(z(\mathrm{k}))\{A_i x(\mathrm{k}) + B_i u(\mathrm{k})\}}{\sum_{i=1}^{r} w_i(z(\mathrm{k}))} \\ &= \sum_{i=1}^{r} h_i(z(\mathrm{k}))\{A_i x(\mathrm{k}) + B_i u(\mathrm{k})\} \end{aligned} \tag{4.29}$$

$$\begin{aligned} \mathrm{y}(\mathrm{k}+1) &= \frac{\sum_{i=1}^{r} w_i(z(\mathrm{k}))\{C_i u(\mathrm{k})\}}{\sum_{i=1}^{r} w_i(z(\mathrm{k}))} \\ &= \sum_{i=1}^{r} h_i(z(\mathrm{k}))\{C_i u(\mathrm{k})\} \end{aligned} \tag{4.30}$$

where $h_i(z(k))$ is the weight function defined as:

$$h_i(z(\mathrm{k})) = \frac{w_i(z(\mathrm{k}))}{\sum_{i=1}^{r} w_i(z(\mathrm{k}))} \tag{4.31}$$

$$w_i(z(\mathrm{k})) = \prod_{j=1}^{p} M_{ij}(z_j(\mathrm{k})) \tag{4.32}$$

It is also true, for all k, the weight activation function with the i$^{\mathrm{th}}$ sub model is such that:

$$\begin{cases} \sum_{i=1}^{r} h_i(z(\mathrm{k})) \rangle 0, \quad h_i(z(\mathrm{k})) \in [0,1], \ i = 1, 2, ..., r \\ z(\mathrm{k}) = \left(z_1(\mathrm{k}), ..., z_p(\mathrm{k})\right) \end{cases} \tag{4.33}$$

The term $M_{ij}(z_j(k))$ is the grade of membership of $z_j(k)$ in M_{ij}.

The following two approaches can be used to obtain the discrete T-S fuzzy model:

1. Identification using input-output data [31, 32].
2. Derivation from the nonlinear system equations [33, 34].

In this Chapter, the second approach is used to construct the discrete T-S fuzzy model of the DC/DC boost converter. Sector nonlinearity is a method used to obtain the T-S fuzzy model from the nonlinear system equations. Its idea first appeared in [33].

Consider a nonlinear system $x(k) = f(x(k))$, where $f(0)= 0$. The following Lemma will be used in the sequel of the chapter.

Lemma: Let $f(x(k)): R \to R$ is a bounded function ($\alpha \leq f(x(k)) \leq \beta$).

It always exist tow functions, $\eta_1(x(k)$ and $\eta_2(x(k))$ and two scalars α and β such that:

$$f(x(k)) = \alpha \times \eta_1(\mathrm{x(k)}) + \beta \eta_2(\mathrm{x(k)}) \tag{4.34}$$

With:

$$\eta_1(\mathrm{x(k)}) + \eta_2(\mathrm{x(k)}) = 1 \tag{4.35}$$

$$\eta_1(\mathrm{x(k)}) \geq 0,\ \eta_2(\mathrm{x(k)}) \geq 0 \tag{4.36}$$

And:

$$\alpha = \max\,(f(x(k)),\ \beta = \min\,(f(x(k)), \tag{4.37}$$

$$\eta_1(\mathrm{x(k)}) = \frac{f(x(k) - \beta}{\alpha - \beta},\ \eta_2(\mathrm{x(k)}) = \frac{\alpha - f(x(k))}{\alpha - \beta} \tag{4.38}$$

4.4.2. Constraints Model Predictive Control

4.4.3. Model Predictive Control (MPC)

The basic function of the model predictive control (MPC) scheme is to calculate a sequence of future actuation signals in such a way that it minimizes a cost function defined over a prediction horizon [35].

Consider the nonlinear discrete system:

$$x(\mathrm{k}+1) = f(x(\mathrm{k}), u(\mathrm{k})) \tag{4.39}$$

where k is the discrete time index, $x(k) \in R^n$ and $u(k) \in R^m$ is a continous mapping,

$$\boldsymbol{f}\text{:}\ \mathrm{R}^{\mathrm{n}} \times \mathrm{R}^{\mathrm{m}} \to \mathrm{R}^{\mathrm{n}} \tag{4.40}$$

It is required to find an optimal control sequence for this system with respect to the following quadratic cost function [36]:

$$\mathrm{J} = \sum_{j=H_w}^{H_p} \big(Y_{ref}(k+j) - \hat{Y}(k+j|k)^T\, Q\big(Y_{ref}(k+j) - \hat{Y}(k+j|k) + \sum_{j=1}^{H_u} (U(k+j-1)^T R\, U(k+j-1) + \Delta U(k+j-1)^T S\, \Delta U(k+-1)) \quad (4.41)$$

where k is the current sampling instant, J is the cost function, H_u is the control cost horizon, H_w is first point of the prediction horizon, H_p is last point of the prediction horizon, $H_u < H_p$, and $\Delta U(k+j-1)$ is a vector of control increments, $Y_{ref}(k+j)$ is a future reference trajectory is driven by the desired output reference, $\hat{Y}(k+j|k)$ is a j steps ahead prediction of the system, Q is the weighting matrix of the tracking error, R and S are weighting matrices of the control effort.

The predicted output may be written as:

$$\hat{\mathrm{Y}}(k+j|k) = \Gamma + \Lambda\Delta U \quad (4.42)$$

where Γ is called the free output response as it does not depend on the control sequence, and $\Lambda\Delta U$ is the called the force output response as it depends on the selected control sequence.

The following constraints are taken into account:

$$X_{min} \leq \hat{X}(k+j|k) \leq X_{max} \quad (4.43)$$

$$Y_{min} \leq \hat{Y}(k+j|k) \leq Y_{max} \qquad \forall t = k+1, \dots k+N_p \quad (4.44)$$

$$U_{min} \leq \hat{U}(k+j|k) \leq U_{max} \qquad \forall t = k+1, \dots k+N_c \quad (4.45)$$

$$\Delta U_{min} \leq \Delta U(k+j|k) \leq \Delta U_{max} \quad (4.46)$$

The cost function (4.41) depends on two terms: the first term concerns the minimization of the error between the desired trajectory and the predicted output. The second term represents a penalty on the control effort. Further, the above cost function can be rewritten to more general matrix form [37]:

$$J(\Delta U) = J_{\min} + 2\big[(\Gamma - \mathrm{Y}_{\mathrm{ref}})^{\mathrm{T}}\mathrm{Q}\Lambda - \bar{\mathrm{U}}_{\mathrm{k-1}}^{\mathrm{T}}\mathrm{S}\Delta\big]\Delta U + \Delta U^T[\Lambda^T Q\Lambda + \mathrm{R} + \Delta^T \mathrm{S}\Delta]\Delta U \quad (4.47)$$

where:

$$J_{\min} = \mathrm{Y}_{\mathrm{ref}}^{\mathrm{T}}\, QY_{ref} + \Gamma^T Q\Gamma - 2\mathrm{Y}_{\mathrm{ref}}^{\mathrm{T}}\mathrm{Q}\Gamma + \bar{\mathrm{U}}_{\mathrm{k-1}}^{\mathrm{T}}\mathrm{S}\bar{\mathrm{U}}_{\mathrm{k-1}}^{\mathrm{T}} + \bar{\mathrm{U}}_{\mathrm{k-1}}^{\mathrm{T}}\mathrm{R}\bar{\mathrm{U}}_{\mathrm{k-1}}^{\mathrm{T}} \quad (4.48)$$

$J_{\min}$ is the minimum cost due to the reference and the free output response.

The discrete T-S fuzzy model equation (4.29) is used to predict the process output, subject to level and rate constraints on the control inputs and outputs.

The constraints can be written as follows [38]:

$$\begin{bmatrix} I_{H_u+1} \\ -I_{H_u+1} \\ L_{H_u+1} \\ -L_{H_u+1} \\ \Lambda \\ -\Lambda \end{bmatrix} \Delta U < \begin{bmatrix} U_{max} + U_{k-1} \\ -U_{min} - U_{k-1} \\ U_{max} \\ -U_{min} \\ Y_{max} - \Gamma \\ -Y_{max} + \Gamma \end{bmatrix} \tag{4.49}$$

And:

$$I_{H_u+1} = \begin{bmatrix} 1 & 0 & \dots & 0 \\ 0 & 1 & \dots & 0 \\ \vdots & \vdots & \ddots & \vdots \\ 0 & 0 & \dots & 1 \end{bmatrix} \in R^{H_u+1\times H_u+1}, L_{H_u+1} = \begin{bmatrix} I_{H_u+1} & 0 & \dots & 0 & 0 \\ -I_{H_u+1} & I_{H_u+1} & 0 & 0 & 0 \\ 0 & -I_{H_u+1} & I_{H_u+1} & 0 & 0 \\ \vdots & \vdots & \ddots & \vdots & \vdots \\ 0 & 0 & \dots & -I_{H_u+1} & I_{H_u+1} \end{bmatrix}$$

$$\in R^{H_u+1\times H_u+1}$$

4.4.4. Model Constrained Receding Horizon Predictive Control (CRHPC)

The constrained receding horizon predictive control (CRHPC) [39, 40] is a variant of the MPC which guarantees the closed-loop stability under certain conditions by imposing constraints on the output, so that the desired output reference $Y_{ref}(k+j)$ and the predicted value $\hat{Y}(k+j|k)$ coincide on a horizon beyond the prediction horizon.

$$\hat{Y}(k+j|\mathrm{k}) = Y_{ref}(\mathrm{k+j}), \ \mathrm{j}=1,\dots,\mathrm{m} \tag{4.50}$$

where *m* is instants beyond the prediction horizon represents the terminal constraints.

The prediction that is extended for *m* instants beyond the prediction horizon results in c index signifies the terminal constraints:

$$\hat{\mathrm{Y}}_{\mathrm{c}} = \Gamma_{\mathrm{c}} + \Lambda_{\mathrm{c}}\Delta U \tag{4.51}$$

where $\hat{\mathrm{Y}}_c \in \mathrm{R}^{\mathrm{H_p n_o}}, \Gamma_{\mathrm{c}} \in \mathrm{R}^{\mathrm{H_p n_o}}$, $\Lambda_{\mathrm{c}} \in \mathrm{R}^{\mathrm{H_p n_o \times H_p n_i}}$, and $\Delta\mathrm{U} \in \mathrm{R}^{\mathrm{H_p n_i}}$, $\mathrm{n_0}$ and $\mathrm{n_i}$ are the number of system outputs and system inputs, respectively.

Γ_{c} Is the free output response for *m* instants beyond the prediction horizon, as it does not depend on the control sequence, and $\Lambda_{\mathrm{c}}\Delta U$ is the forced output response as it depends on the selected control sequence, based on the future control actions.

$$\Lambda_{\mathrm{c}} \Delta U-(\mathrm{Y}_{ref}(\mathrm{k+j})-\Gamma_{c})-\alpha\gamma I_{H_u} \langle 0 \tag{4.52}$$

$$-\Lambda_{\mathrm{c}} \Delta U+(\mathrm{Y}_{ref}(\mathrm{k+j})-\Gamma_{c})-\alpha\gamma I_{H_u} \langle 0 \tag{4.53}$$

Then, the new optimization problem consists of minimizing a cost function (4.47), on a convex domain (4.54) and terminal constraints (4.52) and (4.53).

$$\begin{bmatrix} I_{H_u+1} \\ -I_{H_u+1} \\ L_{H_u+1} \\ -L_{H_u+1} \\ \Lambda \\ -\Lambda \\ \Lambda_{\mathrm{c}} \\ -\Lambda_{\mathrm{c}} \end{bmatrix} \Delta U < \begin{bmatrix} U_{max}+U_{k-1} \\ -U_{min}-U_{k-1} \\ U_{max} \\ -U_{min} \\ Y_{max}-\Gamma \\ -Y_{max}+\Gamma \\ Y_{ref}-\Gamma_c+\alpha\gamma I_{H_u} \\ -Y_{ref}+\Gamma_c+\alpha\gamma I_{H_u} \end{bmatrix} \tag{4.54}$$

This convex minimization has a global minimum only if the Hessian of the function objective is positive definite [41]. In this sense, the matrix equation (4.47) can be transformed into the form:

$$min\, \Delta U(k)^T H \Delta U(k) - P^T \Delta U(k) \tag{4.55}$$

Subject to the inequality constraints (4.54). Where the Hessien matrix H, is positive definite if the matrix Λ satisfies:

$$rank\ (\Lambda) = H_u \tag{4.56}$$

Therefore, the constraints (4.54) may be structured as a single formalism easily exploitable later by the optimization algorithms.

$$\Lambda U(k) \leq B \tag{4.57}$$

To transform the nonlinear criterion (4.55) in LMI form, the Schur complement lemma is used.

4.4.5. Robust Model Predictive Control (MPC)

This section illustrates the problem formulations, i.e, modification of the cost function by deriving an upper bound, and the motivation of the Linear Matrix Inequalities (LMIs) approach [42].

4.4.6. LMI form transformation

An optimization LMI problem requires that the initial problem is restructured so as to involve a linear cost function and strict inequality constraints. In general, the minimization of a convex quadratic function $J(\Delta U)$ can be obtained by the following equivalent minimization strategy:
Minimize γ and find an ΔU admissible that satisfied:

$$J(\Delta U) < \gamma \tag{4.58}$$

The equation (4.47) can be transformed into LMI problem using the Schur complements [42].

Given: $\mathrm{L(x)} = \mathrm{L(x)}^{\mathrm{T}}, \mathrm{M(x)} = \mathrm{M(x)}^{\mathrm{T}}$, and $\mathrm{W(x)}$ depend affinely on *X*. Then the following LMIs are equivalent:

$$i) \begin{bmatrix} \mathrm{L(x)} & \mathrm{W(x)} \\ \mathrm{W(x)}^{\mathrm{T}} & \mathrm{M(x)} \end{bmatrix} < 0 \tag{4.59}$$

$$ii) \begin{cases} \mathrm{M(x)} < 0 \\ \mathrm{L(x)} - \mathrm{W(x)}\mathrm{M(x)}^{-1}\mathrm{W(x)}^{\mathrm{T}} < 0 \end{cases} \tag{4.60}$$

From Schur complement, LMI based optimization can be formulated as [42]:

$$\text{minimize}\, c^T x$$

$$\text{subject to: } \mathrm{F(x)} > 0 \tag{4.61}$$

Here $\mathrm{F(x)}$ is a symmetric matrix that depends affinely on the optimization variable x, and c is a real vector of appropriate size. The solution then minimizes the linear term $c^T x$ [43].

4.4.7. LMI conditions for MPC

The LMI formulation consists on solving conditions that incorporates input and output constraints. However inequality (4.58) is in nonlinear form. In order to get LMI conditions, LMI-based optimization can be formulated using Schur complement:

$$\begin{gathered} \min \gamma \in R^+ \\ Subject\ to: \\ \begin{bmatrix} 2[(\Gamma - \mathrm{Y}_{\mathrm{ref}}^{\mathrm{n}})^{\mathrm{T}} \mathrm{Q}\Lambda - \bar{\mathrm{U}}_{\mathrm{k-1}} \mathrm{S}\Delta]\Delta U + J_{\min} - \gamma & \Delta U^T \\ \Delta U & -[\Lambda^T Q\Lambda + \mathrm{R} + \Delta^T \mathrm{S}\Delta]^{-1} \end{bmatrix} < 0 \end{gathered} \tag{4.62}$$

Finally, the second inequality of equation (4.62) is always verified by the Hessian structure in the MPC case.

The previous constraints equations (4.52), (4.53) and (4.54) must be presented in a diagonal form defining thus a matrix convex space and symmetric. Therefore, the final form of the original optimization problem can be formulated as LMI terms. The cost function is transferred as below:

$$\begin{gathered}\min \gamma \in R^{+} \\ Subject\ toLMI\ constraints: \\ \begin{bmatrix} 2\left[\left(\mathit{\Gamma}-Y_{ref}^{n}\right)^{T}Q\mathit{\Lambda}-\bar{U}_{k-1}S\Delta\right]\Delta U+J_{min}-\gamma & \Delta U^{T} \\ \Delta U & -[\mathit{\Lambda}^{T}Q\mathit{\Lambda}+R+\Delta^{T}S\Delta]^{-1} \end{bmatrix}<0\end{gathered} \tag{4.63}$$

$$\begin{bmatrix} I_{H_u+1} \\ -I_{H_u+1} \\ L_{H_u+1} \\ -L_{H_u+1} \\ \Lambda \\ -\Lambda \\ \Lambda_{\mathrm{c}} \\ -\Lambda_{\mathrm{c}} \end{bmatrix}\Delta U<\begin{bmatrix} U_{max}+U_{k-1} \\ -U_{min}-U_{k-1} \\ U_{max} \\ -U_{min} \\ Y_{max}-\Gamma \\ -Y_{max}+\Gamma \\ Y_{ref}-\mathit{\Gamma}_{c}+\alpha\gamma I_{H_u} \\ -Y_{ref}+\mathit{\Gamma}_{c}+\alpha\gamma I_{H_u} \end{bmatrix} \tag{4.64}$$

$$diag\left(L_{H_u+1}\Delta U-(U_{max}-U_{k-1})\right)\leq 0 \tag{4.65}$$

$$diag\left(-L_{H_u+1}\mathit{\Delta}U-(U_{min}+U_{k-1})\right)\leq 0 \tag{4.66}$$

$$diag\left(I_{H_u+1}\Delta U-U_{max}\right)\leq 0 \tag{4.67}$$

$$diag\left(-I_{H_u+1}\mathit{\Delta}U+U_{min}\right)\leq 0 \tag{4.68}$$

$$diag(\Lambda\Delta U-Y_{max}+\Gamma)\leq 0 \tag{4.69}$$

$$diag(-\Lambda\Delta \mathrm{U}+Y_{min}-\Gamma)\leq 0 \tag{4.70}$$

$$diag\left(\Lambda_{\mathrm{c}}\Delta U-(Y_{ref}-\mathit{\Gamma}_{c})-\alpha\gamma I_{H_u}\right)\leq 0 \tag{4.71}$$

$$diag\left(-\Lambda_{\mathrm{c}}\Delta U+(Y_{ref}-\mathit{\Gamma}_{c})-\alpha\gamma I_{H_u}\right)\leq 0 \tag{4.72}$$

4.5. Design of Robust Fuzzy Model Based-Multivariable Predictive Controller (FMMPC) for DC/DC Boost Converter

In this part, robust fuzzy model based multivariable predictive controller (FMMPC) is designed for DC/DC boost converter to track the derived optimum current I_{dc_opt}, and hence achieve the fuzzy MPPT control through PWM (pulse-width modulation).

The FMMPC controller is suitable for the DC/DC boost converter since the control strategy is a type of control methods introduced initially as a means for the regulation of constrained linear or nonlinear systems. Furthermore, the FMMPC offers the fast dynamic response, high stability and robustness against parameter uncertainties over a wide range of operating conditions. Due to the fact that the PMSG can be viewed as a current source to the DC/DC boost converter, and provide the rectified current (I_{dc}), only the dynamics of the DC/DC boost converter is considered and expressed. In the next section, the T-S fuzzy model of the DC/DC boost converter is used to describe the original nonlinear behavior for the control design aim via the sector nonlinearity approach.

4.5.1. T-S Fuzzy Representation of the DC/DC Boost Converter

The global nonlinear dynamical behavior of the DC/DC boost converter in standard state variable form is as follows:

$$\begin{bmatrix} \frac{dI_{dc}}{dt} \\ \frac{dV_o}{dt} \end{bmatrix} = \begin{bmatrix} 0 & \frac{-(1-u)}{L} \\ \frac{(1-u)}{C} & \frac{-1}{R_L C} \end{bmatrix} \begin{bmatrix} I_{dc} \\ V_o \end{bmatrix} + \begin{bmatrix} \frac{1}{L} \\ 0 \end{bmatrix} V_{dc} \tag{4.73}$$

where I_{dc} is the input inductor current or rectified current, u is an equivalent control function taking values in the set $\{0, 1\}$, while $R_L = V_o/I_o$ present the total equivalent resistance, V_o is the output DC-link voltage, I_o is the output DC-link current, C and L present the capacitance and inductance values of the DC/DC boost converter, respectively.

The discrete-time state space model of the DC/DC boost converter is used to derive equation (4.73), considering the sampling period T_s, and replacing the binary signal u by its respective duty cycle $d(k)$. The result of this discretization process can be written as:

$$\begin{bmatrix} I_{dc}(k+1) \\ V_o(k+1) \end{bmatrix} = \begin{bmatrix} 1 & -\frac{T_s}{L} \\ \frac{T_s}{C} & 1-\left(\frac{T_s}{R_L C}\right) \end{bmatrix} \begin{bmatrix} I_{dc}(k) \\ V_o(k) \end{bmatrix} + \begin{bmatrix} \frac{(V_{dc}-V_o(k))T_s}{L} \\ -\frac{I_{dc}(k)T_s}{C} \end{bmatrix} d(k) \tag{4.74}$$

According to the expressions (4.73) and (4.74) and the discrete T-S fuzzy modeling approach, the DC/DC boost converter can be described by a second order r_c- rule discrete T-S fuzzy model. The i^{th} rule of the discrete T-S fuzzy model is of the following form:

Fuzzy ruls

if $w_1(k)\ is\ F_{i1} and \ldots and\ w_g(k)\ is\ F_{g1}$, **then** $x(k+1) = A_i x(k) + B_i u(k)$ (4.75)

Where, i=1,2,…,r, $A_i \in R^{n\times n}, B_i \in R^{n\times m}$, r values denote the number of fuzzy rules, $w_1, w_2, \dots, w_g$ are the premise variables, $F_{ij}(j = 1,2,\dots,g)$ are the fuzzy sets, , $x(k) \in R^n$ are the system variables, $u(k)$ are the control input signal, A_i, B_i are the state matrices of the local sub-system with appropriate dimensions. By using the singleton fuzzifier, product inference rule, and weighted average defuzzifier, the above fuzzy rules base is inferred as follows:

$$x(k+1) = \sum_{i=1}^{k} \mu_i\,(w(k))\{A_i x(k) + B_i u(k)\} \tag{4.76}$$

where:

$$\mu_i\big(w(k)\big) = \frac{\prod_{j=1}^{g} F_{ij}(w_j(k))}{\sum_{i=1}^{k}\prod_{j=1}^{g} F_{ij}(w_j(k))} \tag{4.77}$$

The term $F_{ij}(w_j(k))$ is the grad of membership of $w_j(t)$ in F_{ij} .
Note that: $\sum_{i=1}^{k} \mu_i\big(w(k)\big) = 1$, where $0 \le \mu_i\big(w(k)\big) \le 1$, for i=1,2,…,k.

For deriving the discrete T-S system of the DC/DC boost converter, let the fuzzy premises variable vector $w(k)$ be selected as:

$$w_1(k) = I_{dc}(k), \quad w_2(k) = V_o(k)$$

Since, the system states of the DC/DC boost converter are bounded; the premise variables will also be bounded. In this paper the fuzzy premise variables vary in the range defined as:

$$\max\ (I_{dc}(k)) = D_1,\ \min\ (I_{dc}(k)) = d_1,\ \max\ (V_o(k)) = D_2, \min\ (V_o(k)) = d_2,$$

From the above, the corresponding membership functions of the discrete T-S fuzzy model can be written as:

$$F_{11} = \frac{I_{dc}(k) - d_1}{D_1 - d_1},\ F_{12} = 1 - F_{11},\ F_{21} = \frac{V_o(k) - d_2}{D_2 - d_2}, \qquad F_{22} = 1 - F_{22},$$

These membership functions are considered triangular shape as demonstrated in Figure 4.8.

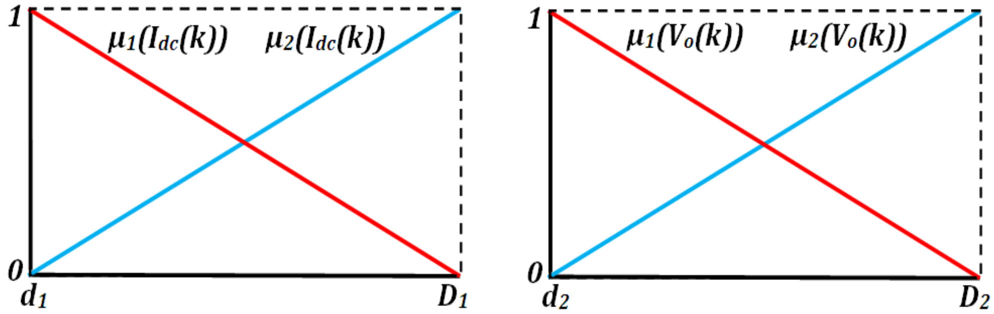

Figure 4.8. Membership functions (MFs) of the T-S fuzzy model.

Based on the sector nonlinearity concept, we have the following relationships:

$$I_{dc}(k) = F_{11}\mathrm{D}_1 + F_{12}d_1, \quad V_o(k) = F_{21}D_2 + F_{22}d_2$$

Therefore, the exact discrete T-S fuzzy model based dynamic system of the DC/DC boost converter can be obtained as following:

$$x(k+1) = \sum_{i=1}^{4} \mu_i \left(I_{dc}(k), V_o(k)\right)\{A_i x(k) + B_i d(k)\} \tag{4.78}$$

Where A_i and B_i are the local sub-models matrices given by (for i=1,2,...,4):

$$A_1 = A_2 = A_3 = A_4 = A = \begin{bmatrix} 1 & -\frac{T_s}{L} \\ \frac{T_s}{C} & 1 - \left(\frac{T_s}{R_L C}\right) \end{bmatrix} \tag{4.79}$$

And:

$$B_1 = \begin{bmatrix} \dfrac{(V_{dc} - d_2)T_s}{L} \\ -\dfrac{d_1 T_s}{C} \end{bmatrix}; \; B_2 = \begin{bmatrix} \dfrac{(V_{dc} - d_2)T_s}{L} \\ -\dfrac{D_1 T_s}{C} \end{bmatrix};$$

$$B_3 = \begin{bmatrix} \dfrac{(V_{dc} - D_2)T_s}{L} \\ -\dfrac{d_1 T_s}{C} \end{bmatrix}; \; B_2 = \begin{bmatrix} \dfrac{(V_{dc} - d_2)T_s}{L} \\ -\dfrac{d_1 T_s}{C} \end{bmatrix}.$$

Since:

$$\sum_{i=1}^{k} \mu_i\left(\left(I_{dc}(k), V_o(k)\right)\right) = 1 \text{, and } A_i = A. \tag{4.80}$$

Therefore the entire discrete T-S fuzzy DC/DC boost converter model corresponds to:

$$x(k+1) = Ax(k) + \left(\sum_{i=1}^{4} \mu_i \left(I_{dc}(k), V_o(k)\right) B_i\right) d(k) \tag{4.81}$$

It is worth to observe that equation (4.81) corresponds with the system (4.74) inside the polytope region [d_1, D_1] × [d_2, D_2]. This operating space is shown in Figure 4.9.

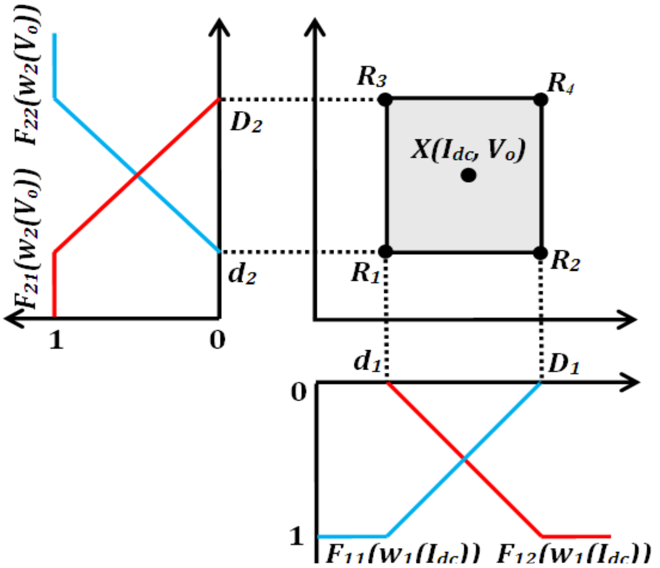

Figure 4.9. Discrete T-S Fuzzy representation of the DC/DC boost converter.

The control strategy, which takes into account constraints such as control effort and state variables of the DC/DC boost converter, is presented in the next section.

4.5.2. Constraints Model Predictive Control of DC/DC Boost Converter

In order to achieve accurate tracking control of the optimum current for the DC/DC boost converter, a robust multivariable predictive current control strategy based on the discrete T-S fuzzy model is used to replace the traditional PI controller. In this section during the system operation, the range of state variables and control inputs of the DC/DC boost converter is limited by physical constraints imposed by the turbine actuators due to hardware specifications of the power converter. Hence, constraints should be considered in the design of the DC/DC boost converter controller.
The constraints are chosen as:

$$0 \leq I_{dc}(k) \leq 10\,A, and\ \ 0 \leq V_o(k) \leq 600\,V$$

Also, an added constraint on the DC/DC boost duty cycle is imposed to ensure the asymptotic stability of the closed loop system:

$$0 \leq d(k) \leq 0.98$$

The value of the weighting matrices in the cost function (4.41) are:
$Q = eye(H_p),\qquad S = 0.5 * eye\big((H_u + 1) * n_i\big),\qquad R = 0.1 * eye\big((H_u + 1) * n_i\big)$

The discrete-time local models of fuzzy system (4.78) for the DC/DC boost converter can be easily obtained using a sampling time of 0.001ms, the FMMPC scheme is developed with the following conditions: The control horizon is $H_u= 2$, and the prediction horizon is $H_p=20$, it is required to design a stabilizing FMMPC for the DC/DC boost converter.

The FMMPC based LMI seen in Section 4.3, shows that when calculating the objective function (J), the variation between the model and the real plant is represented in the predicted output by the forced response. This allows the control of the DC/DC boost converter to maintain the wind energy system tracking of maximum power while regulating the rectified current (I_{dc}) without fluctuation.

4.6. Current Control of Three-Phase Grid Connected Inverter

An overview of the total control scheme of a three-phase grid connected wind energy system is shown in Figure 4.10 Again, it must be remarked that the three-phase voltage source inverter (3PH-VSI) control is not the focus of this Chapter. For this reason, a simple control scheme for injecting current satisfying unity power factor condition is used. As can be seen in Figure 4.10, the instantaneous voltage and current of the grid and inverter in the *abc* three-phase AC system are measured and transformed to two-phase AC system by using the Clarke's transformation $\alpha\beta$. The grid voltage, in this new reference frame (v_{Rab}), is transformed into polar coordinates and is represented by its magnitude $|v_R|$ and its rotating angle θ_R.

Where:

$$\vec{v}_R = |v_R|\, e^{j\theta_R} \tag{4.82}$$

And :

$$\begin{cases} |v_R| = \sqrt{(v_{R\alpha})^2 + \left(v_{R\beta}\right)^2} \\ \theta_R = tan^{-1}\left(\frac{v_{R\beta}}{v_{R\alpha}}\right) \end{cases} \tag{4.83}$$

For a given DC-Link voltage V_o, the inverter output voltage is proportional to modulation index m_R. The SVM generator uses the modulation index m_R can be approximately expressed as:

$$m_R = \frac{\sqrt{3}\ |v_R|}{V_o} \tag{4.84}$$

From which the modulation index for the SVM scheme is in the range of:

$$0 \leq m_R \leq 1 \tag{4.85}$$

It must be noted that the grid and inverter output currents are not in phase, because the LC_I filter introduces a phase shift. In order to correct this deviation, 3PH-VSI reference angle θ_R is calculated adding grid voltage angle θ_{vR} and a PI controller output, whose input is the cross product between current and voltage vectors ($i_{\alpha\beta} \times v_{\alpha\beta}$). This product is equal to zero when the current and voltage are in phase. A saturation block limits the PI output to $-\pi/2 < \theta < \pi/2$. The SVM module provides voltage at the AC terminals of the 3PH-VSI, whose fundamental component depends on modulation index m_R and DC-Link voltage V_o. When the SVM generator, based on symmetrical triangle wave as the carrier and sinusoidal reference is applied, then output voltage contains components:

- Fundamental frequency f_{ac1}.
- High frequency harmonic, that results from the switching carrier frequency f_{sc}.
- Side band harmonics f_{sb},
- Very high frequency harmonics at MHz range.

The side band harmonics with frequency f_{sb} are function of switching carrier frequency f_{sc}

$$f_{sb} = n \times f_{sc} = m \times f_{ac1} \tag{4.86}$$

Where: $m = 0, 2, 4\ldots$ and $n = 1, 3, 5\ldots$

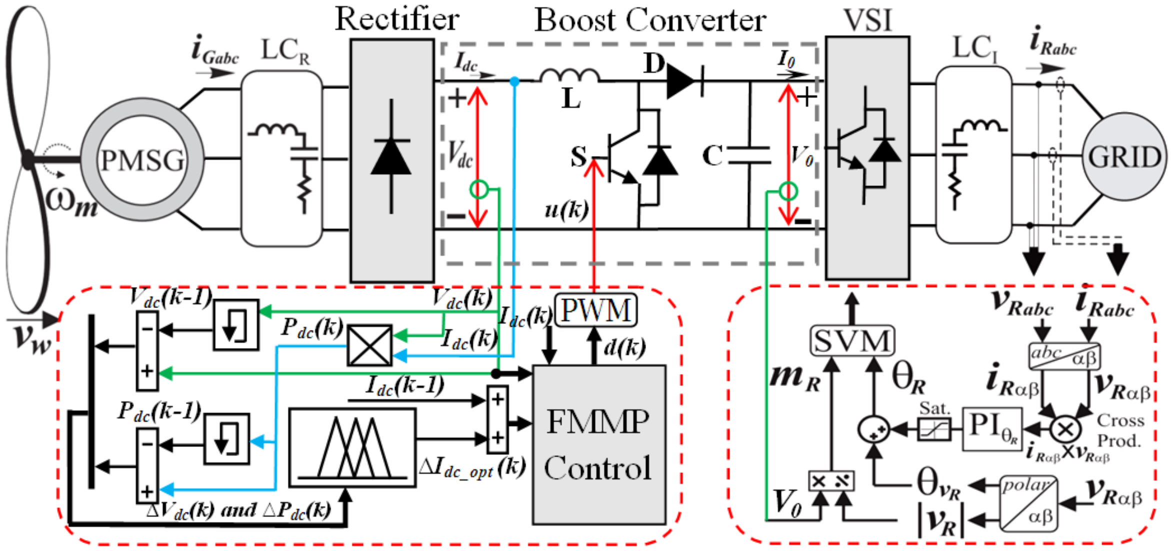

Figure 4.10. Proposed fuzzy MPPT control scheme for DC/DC boost converter and FMMPC control for 3PH-VSI based PMSG wind energy system.

4.7. Numerical Simulation

To evaluate the performance of the proposed fuzzy MPPT control strategy, numerical simulations were carried out by using Matlab/Simulink. The main parameters for computer simulations are listed in Table 4.2. The test scenario is as follows: Within the interval [0, 20] s, the wind speed is kept constant at 9 m/s, which leads to a maximum output power of 600 W and an optimum rectified current of approximately 5 A. At 20 s the wind speed decreases to 8 m/s and is kept constant until 40 s, then it starts to change to 6 m/s at 40 s. From 63 s, the wind speed increases again to 9.5 m/s and is kept at this speed until 90s.

Table 4.2. System parameters.

Parameters of the PMSG used in simulation	Values
Rated power	3 kW
Rated phase voltage	380 V
Pole pairs	4
Rated torque	9.5 N.m
Rated speed	3000 rpm
Rated phase current	8 A
Back-EMF constant	150 V/rpm
Stator resistance	0.245 Ω
d-axis inductance	5 mH
q-axis inductance	5 mH
Inertia	5 Kg.m2

The simulation plots of each state variable are shown in Figure 4.11(a-h). Figure 4.11(a) shows the wind input used for the simulation results shown in this subsection. Figure 4.11(b) shows the simulated waveform of the power conversion coefficient C_p, which is kept at the maximum value of 0.478, and it is not affected by the variations of the generators speed, which shows good performances of the developed fuzzy based MPPT scheme. The resulting tip-speed ratio λ is shown in Figure 4.11(c). It shows that the tip-speed ratio of the blade is kept constant and varies in a relatively small range around the optimal tip-speed ratio of 8.01. It is seen from Figure 4.11(d) that the measured rectified current follows the optimum current quite well, and regulate the turbine torque to extract maximum power from the wind turbine with faster response by using the proposed control strategy. As illustrated in Figure 4.11(e), the turbine shaft speed is continuously adapted to the wind speed, in such a way that it is extracted maximum power out of wind. Figure 4.11(f) displays the generator output power which is related to the wind speed change i.e. from this figure, it can be observed that by means of the proposed control method the generator output power recovers to its maximum value rapidly according to an increase/decrease in the wind speed. As can be seen from Figure 4.11(g) the rectified voltage is directly related to the optimum rectified current, their relationship agrees well with equation (4.8) and can be better regulated to achieve the optimum voltage by using the proposed fuzzy MPPT control strategy. The simulation results indicate that the proposed control system is quite able to generate the maximum wind power under varying wind conditions by regulating the rectified current of the DC/DC boost converter, thus evaluating and exploring the disturbance rejection capability.

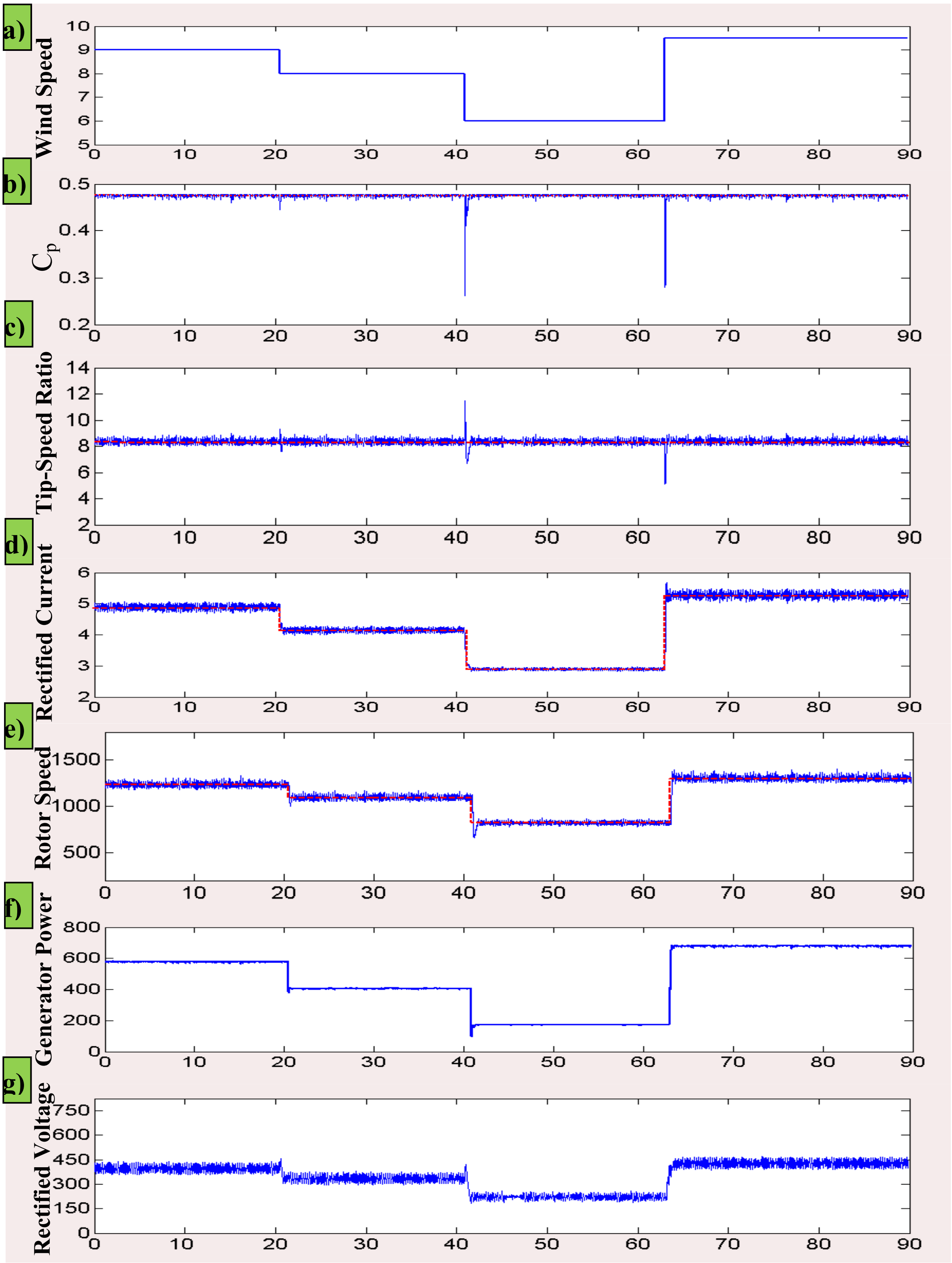

Figure 4.11. Simulation results of the proposed Fuzzy-MPPT technique.

4.7. Experimental Verification of Control System

The 5 *kW* controlled wind energy system scheme is built in laboratory to verify the validity of the proposed control methods.

In the experimental system, the PMSG is driven by a 3 *kW* DC-shunt motor to simulate the wind turbine characteristics, and a general DC/DC boost converter is adopted to drive the DC-motor. The parameters of the experimental wind generation system are shown in Table 4.3. The power converters are built with SEMIKRON SKM75GB124DE insulated gate bipolar transistors (IGBTs), and the driver circuit for the IGBTs is SEMIKRON SKHI61.

Voltage sensors and Hall Effect current sensors are used to sense the rectified voltage, rectified current, DC-bus voltage and the grid voltages and currents, respectively. The proposed controller is implemented in real-time using a dSPACE DS1104 controller board installed in a host PC computer, the sampling frequency is set as 20 kHz, and the switching frequency of the IGBTs is also kept at 10 kHz.

For the purpose of recording the experimental data, a power quality analyzer and a four channel digital storage oscilloscope (DSO) are used. The block diagram of the entire experimental setup is shown in Figure 4.12, and the experimental components of the wind energy system are shown in Figure 4.13.

Table 4.3. Wind energy system parameters.

Parameters of the PMSG for Experiments	**Values**
Rated power	5 kW
Rated phase voltage	380 V
Pole pairs	4
Rated torque	22.5 N.m
Rated speed	2000 rpm
Rated phase current	12 A
Permanent magnet flux	0.39 Wb
Stator resistance	0.65 Ω
d-axis inductance	8 mH
q-axis inductance	8 mH
Torque constant	2.39 Nm/A
Mechanical time constant	2.30 ms

Parameters DC-motor	Values
Rated current	15 A
Rated voltage	220 V
Grid-connected converter parameters	**Values**
DC-link capacitor	2200 μF
Filter inductance	10 mH
Filter resistance	0.20 Ω
Rated grid phase voltage	220 V

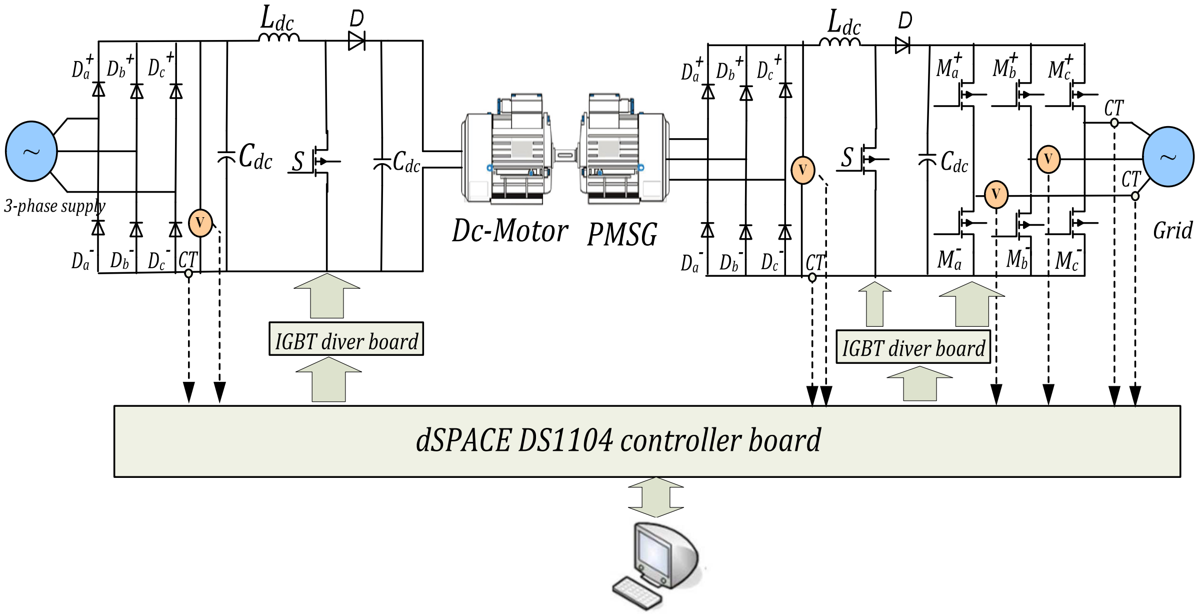

Figure 4.12. Arrangement of laboratory system.

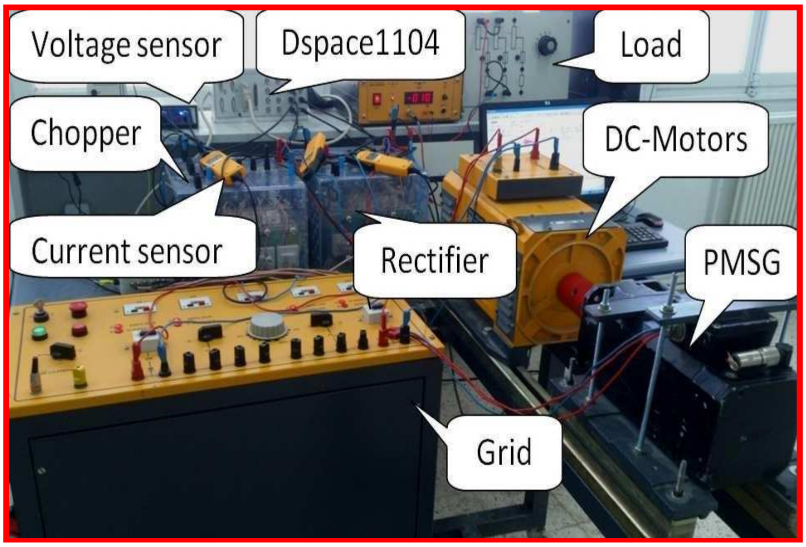

Figure 4.13. Laboratory test rig.

4.8.1. Experimental Results

The proposed fuzzy MPPT algorithm is first experimentally tested under a variable wind speed profile.

In this test, the wind speed is step-changed or ramp-changed randomly between 6 m/s and 8 m/s as illustrated in Figure 4.14(a).

The power coefficient C_p of the emulated wind turbine as well as the rectified voltage, the output electrical power of the PMSG (DC power), and the boost duty cycle are shown in Figure 4.14(b).

The results show that a fast MPP is achieved by using the proposed control algorithm. During the wind variation, the actual value of C_p tracks the maximum value $C_{p\text{-max}}$=0.47 well. Compared with the fast variation of the wind velocity, the rectified voltage and the DC power are smoothed because of the system DC-link capacitor and inertia.

Experiments have also been carried out with time-varying wind speeds. All the waveforms are given in Figures 4.15(a) and 4.15(b).

It can be seen that the proposed fuzzy MPPT controller of the wind energy system is always searching for the MPP. Although the actual value of power coefficient C_p tracks the maximum value $C_{p\text{-max}}$=0.47 well with only a small deviation.

Therefore, the proposed control algorithm enables the MPPT control to be adaptive to the aging process of the wind turbine such that it can always generate the maximum wind power.

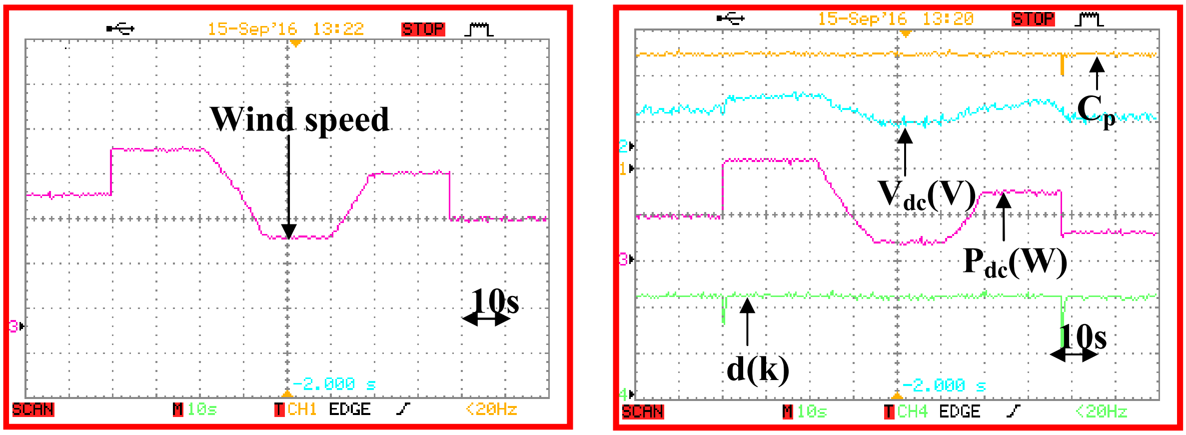

(a) (b)

Figure 4.14. Experimental results with step changes in wind velocity. **a).** wind speed (CH3-2m/s/div). **b).** Power coefficient (CH1-0.2/div), Rectified voltage (CH2-500V/div), DC-power (CH3-200W/div), Duty cycle (CH4-0.5/div).

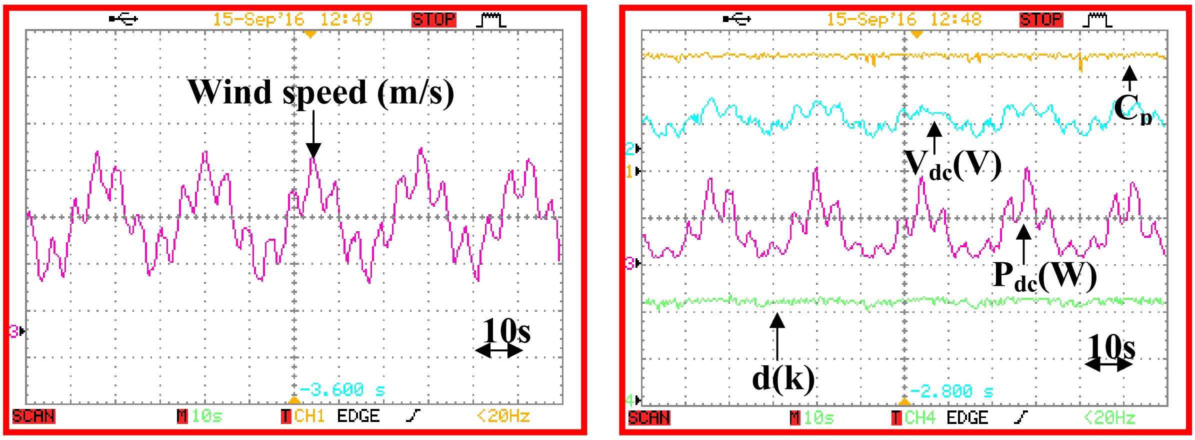

(a) **(b)**

Figure 4.15. Experimental results with turbulent wind changes. **a).** wind speed (CH3-2m/s/div). **b).** Power coefficient (CH1-0.2/div), Rectified voltage (CH2-500V/div), DC-power (CH3-200W/div), Duty cycle (CH4-0.5/div).

The functionality of the proposed FMMP current controller was of DC/DC boost converter also experimentally verified and compared with the conventional PI control method using a 2-minute field measured varying wind speed profile.

The comparison has been accomplished by observing the power coefficient C_p, the rectified voltage, the DC power and the boost duty ratio waveforms.

The test result in Figure 4.16 illustrates the automatic transitioning between the proposed FMMP and PI current control modes. During the testing scenario, the C_p and output electrical power track their optimal values well by using the proposed FMMP current control algorithm.

The largest deviation of the C_p from its optimal value is 0.02 and no obvious deviation between the actual and optimal output electrical powers is found. However, when using the conventional PI control method, the C_p form vacillates in a larger range, and deviations of the actual electrical power from its optimal value are observed from time to time.

Obviously, by the proposed FMMP current control method, the total electrical energy output of the generator is higher than that by the conventional PI current control method, as shown in Figure 4.17.

This affirms the improved efficiency of the proposed FMMP current control method of DC/DC boost converter.

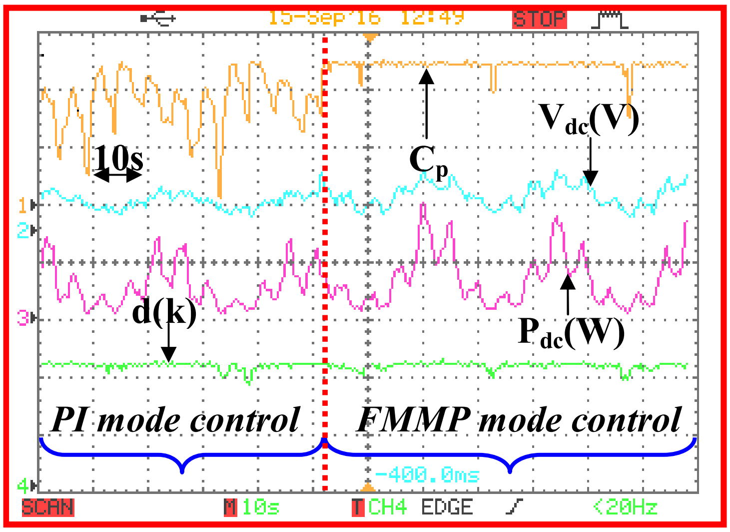

Figure 4.16. Comparison of proposed FMMP current controller to conventional PI control method. Power coefficient (CH1-0.2/div), Rectified voltage (CH2-500V/div), DC-power (CH3-200W/div), Duty cycle (CH4-0.5/div).

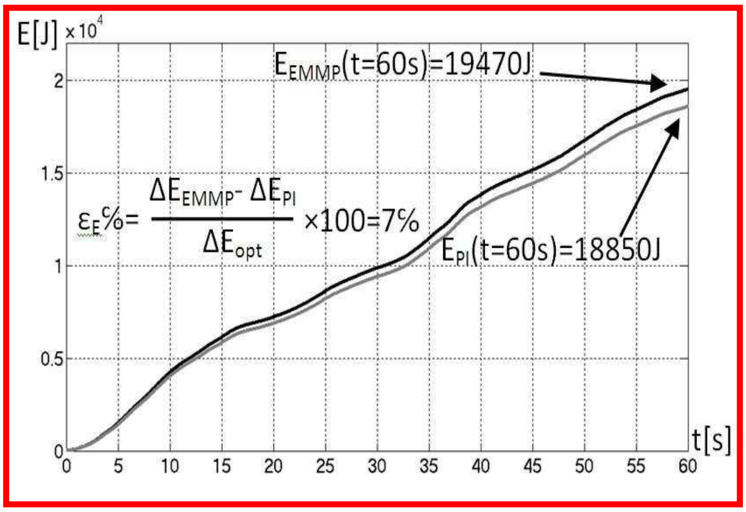

Figure 4.17. Experimental results of total generated electrical energy.

Finally, Figures 4.18(a) and 4.18(b) shows the PMSG phase voltages and currents at 10 m/sec. The PMSG stator voltage and current waveforms are distorted due to the natural commutation of the diode-bridge rectifier and the control of the DC/DC boost converter. The fundamental components of the PMSG stator voltage and current are not in-phase (not shown in figure) due to the higher harmonics in the PMSG three-phase currents. This is the only disadvantage of using diode-rectifiers for the PMSG turbines. Also, due to the decoupled nature of the power converters, these harmonics are not reflected to the grid and thus they do not cause any conflict to the grid codes. Figures 4.19(a) and 4.19(b) shows the system performances on the grid-side inverter. We can see in Figure 4.19(a) that the injected grid currents and voltages have a 50 Hz sinusoidal form. It is important to note that the grid voltage and current are in-phase. Figure 4.19(b) illustrates the Fresnel diagram of grid current and voltage using the proposed control scheme of the grid-side inverter. As indicted in this figure, the phase shift between grid current and voltage is 0°, which ensure that the system acts as a reactive power compensator. Figure 4.20(a) illustrate that the THD (Total Harmonic Distortion) measured for injected grid current and voltage is 2.5%, which is quite low per Standard IEEE-519. Also, it satisfies the power factor demand with a 0.996 power factor, as illustrated in Figure 4.20(b).

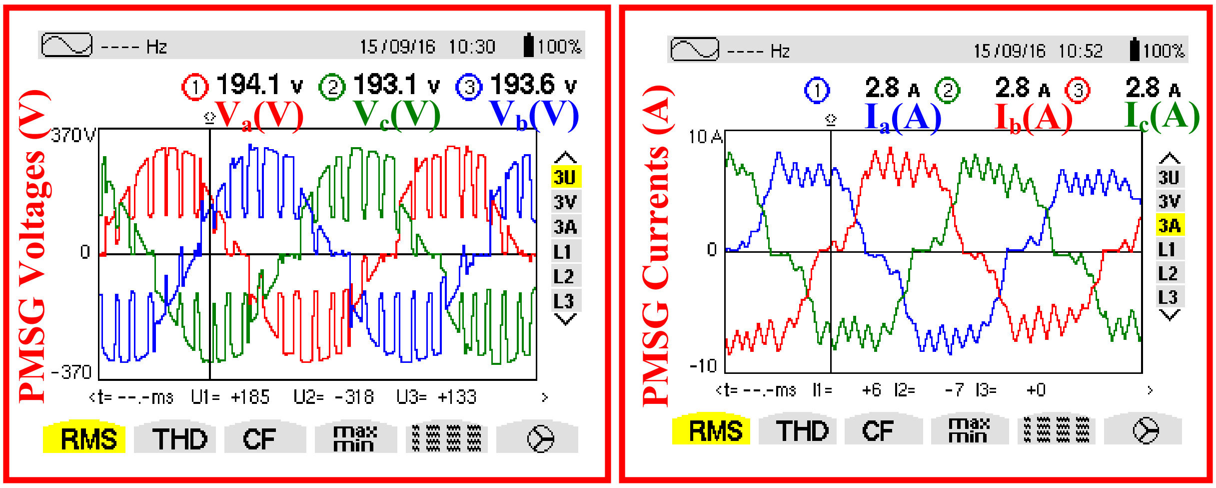

(a) **(b)**

Figure 4.18. Experimental results of the wind power system with the proposed fuzzy-MPPT control method. **(a)** Generator voltage. **(b)** Generator phase current.

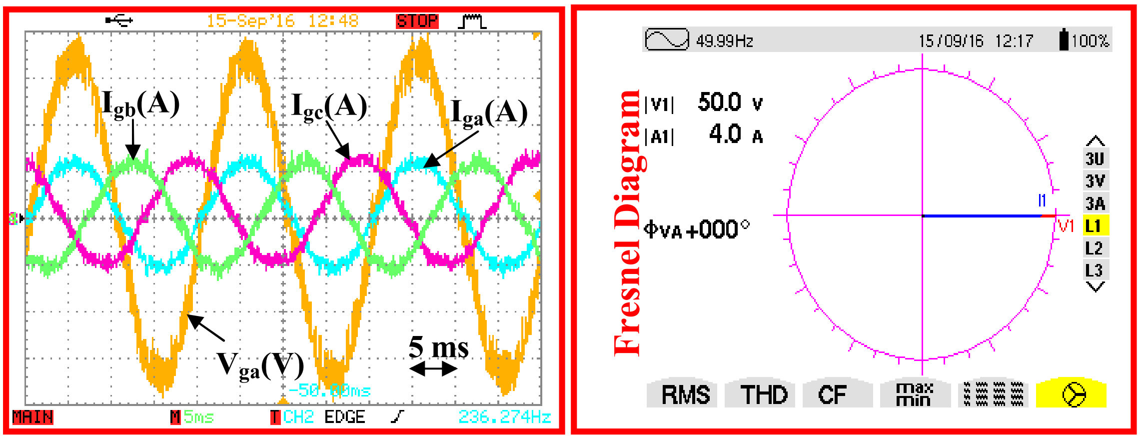

(a) **(b)**

Figure 4.19. Experimental results of the wind power system with the proposed grid-side control method. **(a).** grid currents and voltage. **(b)** Fresnel diagram.

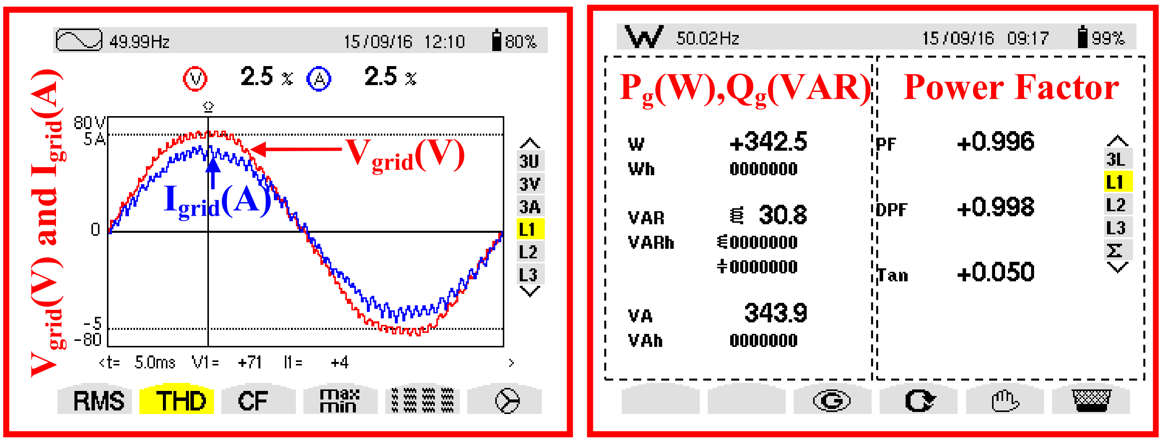

W +342.5
Wh 0000000
VAR 30.8
VARh 0000000
0000000
VA 343.9
VAh 0000000
PF +0.996
DPF +0.998
Tan +0.050

(a) **(b)**

Figure 4.20. Experimental results of the wind power system with the proposed grid-side control method. **(a).** THD of grid current and voltage. **(b)** Measured Power factor (PF).

4.9. Conclusion

In this Chapter, an extension of a robust fuzzy multivariable based model predictive control (FMMPC) strategy has been applied to the DC/DC boost converter in order to enhance the capability of capture the maximum wind power of the wind turbine. In the considered control strategy the FMMPC synthesis is based on the discrete T-S fuzzy model, optimization technique and linear matrix inequalities (LMIs) formulation. In this approach, at every sampling period a quadratic cost function with a specific prediction horizon and control horizon is minimized such that constraints on the control input and output are satisfied. The fuzzy logic MPPT controller has been also employed in this Chapter to derive the optimum rectified current corresponding to the best power point of wind turbine based on the variations of measured electrical DC power and rectified voltage. While the FMMPC controller has been designed to track the derived optimum current with minimum steady-state tracking error and hence to achieve the maximum electrical energy from wind generator. Simulation and experimental results have confirmed significant enhancements in electrical power harvest, mechanical stresses reduction, and capability of optimizing the reference rectified current tracking performances can be achieved via the suggested control strategy. The proposed control strategy also has higher overall control efficiency and can be excellent used to more effectively extract the maximum wind energy as compared with the conventional PI control method.

References

[1] **Yatim M, Tan C, Saidur R:** "A review of maximum power point tracking algorithms for wind energy systems", *Renew Sustain Energy Rev 2012; 16: pp.3220-7.*

[2] **Bekka H, Taraft S, Rekioua D, Bacha S:** "Power control of a wind generator connected to the grid in front of strong winds", *J Electr Syst 2013: pp.267-278.*

[3] **Datta R and Ranganathan V.T:** "A Method of Tracking the Peak Power Points for a Variable Speed Wind Energy Conversion System," *IEEE Trans. On Energy Conversion, Mar. 2003: 18: pp. 163–168.*

[4] **Kesraoui M, Korichi N, and Belkadi A**: "Maximum power point tracker of wind energy conversion system", *Renew Energy 2011; 36(10): pp.2655–2662.*

[5] **Zhu Y, Cheng M, Hua W, Wang W:** "A novel maximum power point tracking control for permanent magnet direct drive wind energy conversion systems", *Energies 2012;5: pp.1398–1412.*

[6] **Xia Y, Ahmed K, and W. Williams B:** "A new maximum power point tracking technique for permanent magnet synchronous generator based wind energy conversion system", *IEEE Trans Power Electron 2011; 26(12): pp.3609–3620.*

[7] **Pan CT, Juan YL:** "A novel sensorless MPPT controller for a high efficiency micro-scale wind power generation system", *IEEE Trans Energy Convers 2010; 25(1): pp.207–216.*

[8] **Agarwal V, Rakesh K, Pravin A, Patki PC**: "A novel scheme for rapid tracking of maximum power point in wind energy generation systems", *IEEE Trans Energy Convers 2010; 25(1): pp.228–236.*

[9] **Lin WM, Hong CM:** "Intelligent approach to maximum power point tracking control strategy for variable speed wind turbine generation system", *Energy 2010; 35(6): pp.2440–2447.*

[10] **Kazmi SMR, Goto H, Guo HJ, Ichinokura O:** "A novel algorithm for fast and efficient speed-sensorless maximum power point tracking in wind energy conversion systems", *IEEE Trans Ind Electron 2011; 58:pp.29–36.*

[11] **Piccolo GA, Sia P:** "Designing an adaptive fuzzy controller for maximum wind energy extraction", *IEEE Trans Energy Convers 2008; 23(2): pp.559–569.*

[12] **Pucci M, Cirrincione M:** "Neural MPPT control of wind generators with induction machines without speed sensors", *IEEE Trans Ind Electron 2011; 58(1): pp.37–47.*

[13] **Cardenas R, Pena R:** "Sensorless vector control of induction machines for variable speed wind energy applications", *IEEE Trans Convers Energy 2004; 19(1): pp.196–205.*

[14] **Chedid R, Mrad F, Basma M:** "Intelligent control of a class of wind energy conversion systems", *IEEE Trans Energy Convers 1999; 14(4): pp.1597–1604.*

[15] **Espinosa J, Vandewalle J, Wertz V:** "Fuzzy Logic, identification and Predictive Control", **Springer, Berlin, 2005.**

[16] **Belarbi K, Megri F:** "A stable model-based fuzzy predictive control based on fuzzy dynamic programming", *IEEE Trans. Fuzzy systems 2007;15 (4): pp.746–754.*

[17] **Bellman R.E, Zadeh L:** "Decision-making in a fuzzy environment", *Manage. Sci 1970; 17: pp.141–164.*

[18] **Li SY, Hu W, Yang YP:** "Receding horizon fuzzy optimization under local information environment with case study", *Int. J. Inf. Technol. Decision Making 2004; 3: pp.109–127.*

[19] **Li SY, Zou T, Yang YP:** "Finding the fuzzy satisfying solutions to constrained optimal control systems and application to robot path planning", *Int. J. Gen. Syst. 2004; 33: pp. 321–337.*

[20] **Keerthi SS, Gilbert EG:** "Optimal infinite horizon feed-back laws for a general class of constrained discrete time systems: stability and moving-horizon approximations", *J. Optim. Theory Appl. 1988; 57: pp. 265–293.*

[21] **Michalska H, Mayne DQ:** "Robust receding horizon control of constrained nonlinear systems", *IEEE Trans. Autom. Control 1993; 38: pp.1623–1632.*

[22] **Scokaert POM, Mayne DQ, Rawlings JB:** "Suboptimal model predictive control (feasibility implies stability)", *IEEE Trans. Autom. Control 1999; 44(3): pp.648–654.*

[23] **Mollov S, Van den Boom T, Cuesta F, Ollero A, Babuska R:** "Robust stability constraints for fuzzy model predictive control", *IEEE Trans. Fuzzy Syst. 2002;10(1): pp.50–64.*

[24] **Kim KH, Jeung YC, Lee DC, Kim HG:** "LVRT Scheme of PMSG Wind Power Systems Based on Feedback Linearization", *IEEE Trans Power Electron 2012; 27(5): pp. 2376–2384.*

[25] **Bose Bimal K:** "Expert system fuzzy logic and neural network applications in power electronics and motion control", *Proc IEEE August 1994; 82(8):pp.1303–1321.*

[26] **Mamdani EH, Assilian S:** "An experiment in linguistic synthesis with a fuzzy logic controller", *Int J Hum Comput Stud 1999; 51(2): pp.135–147.*

[27] **Tanaka K, Ikeda T, Wang HO:** "Design of fuzzy control systems based on relaxed LMI stability conditions", *In: 35th IEEE Conf. on Decision and Control, Kobe 1996;1: pp. 598–603.*

[28] **Wang HO, Tanaka K, Griffin MF:** "An analytical framework of fuzzy modeling and control of nonlinear systems: stability and design issues". *In: Proc. 1995, Amer. Control Conf., Seattle: pp. 2272–2276.*

[29] **Yen J, Wang L, Gillespie CW:** "Improving the interpretability of TSK fuzzy models by combining global learning and local learning", *IEEE Trans. Fuzzy Syst. 1998; 6(4): pp.530–537.*

[30] **Tanaka K, Wang HO:** "Fuzzy Control Systems Design and Analysis: A Linear Matrix Inequality Approach", *Wiley, New York, 2001.*

[31] **Sugeno M, Kang GT:** "Structure identification of fuzzy model", *Fuzzy Sets and Systems 1986; 28: pp.329–346.*

[32] **Sugeno M:** "Fuzzy Control", *Nikkan Kougyou Shinbunsha Publisher, Tokyo, 1988.*

[33] **Kawamoto S, et al:** "An approach to stability analysis of second order fuzzy systems", *In: Proc. First IEEE Internat. Conf. on Fuzzy Systems 1992; 1:pp.1427–1434.*

[34] **Teixeira MCM, Zak SH:** "Stabilizing controller design for uncertain nonlinear systems using fuzzy models", *IEEE Trans. Fuzzy Syst. 1999; 7(2): pp.133–142.*

[35] **Wang L:** "Model Predictive Control System Design and Implementation Using MATLAB", *Springer 2009; Melbonrne, Australia.*

[36] **Maciejowski J:** "Predictive control with constraints", *Prentice Hall; 2002.*

[37] **Kothare MV, Balakrishnan V, Morari M:** "Robust constrained model predictive control using linear matrix inequalities", *Automatica 1996; 32(10): pp.1361–1379.*

[38] **Bououden, B, Chadli M, Filali S, and El Hajjaji A:** "Fuzzy model based multivariable predictive control of a variable speed wind turbine: LMI approach", *Renew. Energy 2012; 37(1): pp.434–439.*

[39] **Takagi T, Sugeno M:** “Fuzzy identification of systems and its application to modeling and control”, IEEE Trans on systems. Man and Cybernetics 1985; 15(1): pp.116-132.

[40] **Thomsen SC, Poulsen NK:** “A disturbance decoupling nonlinear control law for variable speed wind turbines”, *The 15th IEEE Mediterranean Conference on control and Automation MED'7, Athens, Greece 2007; pp. 27-29.*

[41] **Gill PE, Murray W:** “Linearly constrained problems including linear and quadratic programming, the state of the art in numerical analysis”, *Academic Press; 1977; pp. 313–363.*

[42] **Boyd S, Ghaoui LE, Feron E, and Balakrishnan V:** “Linear Matrix Inequalities In Systems and Control Theory”, *SIAM, Philadelphia, 1994.*

[43] **Boyd S, Balakrishnan V, Feron E, El Ghaoui L:** “Control system analysis and design via linear matrix inequalities”, *Proc of the Amer Con Conf, San Francisco, CA 1993; pp. 2147–2154.*

Chapter 5 Generalized Approach for Predictive Control in High-Performance Back-to-Back Converters with PMSG Wind Energy Systems

Abstract

Back-to-back power converter driven systems permit instant power reverse and allows for true four-quadrant operations, which is an important property for high performance drives, grid-tied distributed wind energy systems, etc. For such topology, model predictive control becomes a nice alternative [1]. The Generalized Predictive Control (GPC) strategy is a popular method of process control. It has been successfully implemented in many industrial applications for over two decades, showing good performance and certain degree of robustness [2]. This Chapter presents a development of simple GPC as both the machine-side and the grid-side control algorithm of a grid integrated wind energy system, which allows eliminating electromagnetic torque oscillations for the PMSG and exchanging sinusoidal currents with the AC grid. In addition to the GPC definition, this Chapter includes a conceptual study of the DC-link voltage control. Compared with the classical DC-link PI controller based control scheme, the Uncertainty and Disturbance Estimator (UDE) technique shows nice characters such as: easy to tune, fast and controllable DC-link dynamics, no extra PI DC-link controller, etc. To deal with this, a reliable DC-link voltage based on the Uncertainty and Disturbance Estimator (UDE) control scheme for back-to-back variable speed PMSG wind energy system is further proposed in this Chapter.

The main contributions of this Chapter are highlighted as follows:

- Generalized predictive-based vector control is developed for both the machine-side converter with PMSG control, and the grid-side converter with grid current control to achieve reliable current decoupling control with fast response in varying wind speed conditions.
- Reliable DC-link voltage regulation control is developed based on the Uncertainty and Disturbance Estimator (UDE) algorithm to deal with model uncertainty, such as power losses, equivalent series resistance, equivalent series inductance and here active power on the capacitor, and external disturbances with varying wind speed conditions.

- As a natural requirement, the implemented controller was aimed to be tested at a real plant, or on reasonable wind turbine emulator.

5.1. Introduction

In PMSG-based variable speed wind energy systems, full scale back-to-back converters are often adopted for achieving maximum capture of wind power, providing low harmonic distortion of current, and operating the wind energy systems for provision of supplementary services [3]. The full scale back-to-back converters include a machine-side converter (MSC) connected with the generator, grid-side converter (GSC) connected to the AC grid, and a DC-link capacitor placed between the MSC and the GSC. The vector control strategy based on the d–q reference frame is still applied in both the MSC for PMSG control, and the GSC for power output control [4]. However, the conventional vector control with PI regulators faces some difficulties, for example, it is sensitive to parameters tuning and uncertainty in the d–q reference frame for current decoupling control [5]. Model Based Predictive Control (MBPC) has enjoyed great popularity for more than a decade since the introduction of Richalet's IDCOM algorithm [6] and the Dynamic Matrix Control (DMC) approach developed in the Shell Laboratories [7]. Several algorithms pertain to the same category, namely Long Range Predictive Control (LRPC), the most popular of which is the Generalized Predictive Control (GPC) algorithm [8]. GPC's real power lies in several factors:

1. The process model it is built upon, a CARIMA model;
2. Its ease of implementation and great flexibility by allowing for various difficult multivariable control problems that include inequality constraints.
3. Its inclusion of key control objectives by means of a cost function that encompasses the variance of the output as well as the control effort.

However, GPC applications to electrical power generations are largely unexplored and they involve only few research laboratories. For example in [9] an experimental evaluation of GPC is done for the control of a single phase PWM inverter. [10] Introduces the GPC for field oriented control of induction machines, and [11] simulates the GPC as a power flow controller on a UPFC. Therefore, in order on the control solutions for PMSG wind energy system, simple GPC techniques will be employed in this Chapter and the easy back-to-back voltage source converter will be used as both machine-side and grid-side converters. The proposed GPC is based on the same control principles as the conventional vector control technique. Based on this GPC method, the PMSG wind energy system is able to operate at considerably low electromagnetic torque oscillations and sinusoidal currents, in both machine-side converter currents and AC grid-side currents. Furthermore, the DC-link control issues of the back-to-back power converter systems have been discussed in this Chapter. The DC-link voltage control represents a key part of a back-to-back power converter based wind energy system. The DC-link voltage is influenced by many factors, such as fluctuating power captured from wind, non-sinusoidal currents and reactive power delivered to the AC grid, and equivalent series resistance and inductance in the DC-link capacitor [12]. Therefore, a great amount of investigations have been made in this direction. In [13], a feedback linearization scheme was proposed for controlling the DC-link voltage of a back-to-back system with an extremely small DC-link capacitor. In [14] a similar feedback linearization idea is used for controlling a grid-tied AFE. In [15], a nonlinear controller that uses a new complex state-space modeling method was proposed and verified against a grid-tied AFE. In [16], the DC-link control was fulfilled by using a proportional integration (PI) controller, which generates the reference for grid-side inner predictive power controller. For steady state, the DC-link voltage and grid-side active power are controlled nicely. However, a typical second-order fluctuation of sizable magnitude is observed during system transient phases. In [17], by using a dynamic reference generation concept the DC-link voltage control was directly included into the grid-side predictive controller for a grid-tied AFE with a DC-link R-Load. The uncertainty and disturbance estimator (UDE) algorithm, which was proposed in [18], is based on the assumption that the uncertainty and disturbance can be estimated by using a filter with the appropriate bandwidth. In recent years, the UDE algorithm demonstrated excellent performance in handling uncertainties and disturbances in different systems, and was employed to robustify an input–output linearization controller [19] and input–output delay systems [20], and applied to robust trajectory tracking [21], a class of non-affine nonlinear systems [22], three-DOF experimental helicopters [23], piezoelectric actuator [24], and quadrotor vehicles [25]. In this Chapter, in the grid-side controller, the UDE-based DC-link voltage regulation control is proposed to generate a real power output reference, then the GPC is developed for the GSC with grid current control to facilitate the achievement of reliable DC-link voltage regulation.

This Chapter presents an implementation of GPC as both the machine-side and the grid-side control algorithm of a grid integrated wind energy systems, and is organized in the following manner. The system configuration and working principle of wind energy conversion system are elaborately described in Section 2. A detailed explanation of control scheme and algorithm are mentioned in Section 3. The formulation of GPC algorithm, with CARIMA model and its cost quality function are given and discussed in Section 4. Two robust GPC schemes applied to the current control loop for a back-to-back power converter PMSG wind turbine systems are proposed in Sections 5 and 6, respectively. To conquer its DC-link tracking bias problem, Section 7 presents a UAE controller and its application to the DC-link voltage regulation. The efficiency and performance of the proposed GPC controlled back-to-back power converter driven PMSG system is verified with a 3 Kw experimental set-up and the experimental results are analyzed in Section 8. Finally the conclusions are drawn in Section 9.

5.2. Overview of Full Scale Back-to-Back Converters with PMSG Wind Energy System

The block diagram shown in Figure 5.1 describes a detailed back-back voltage source converter switching model of the variable speed PMSG wind turbine. As a configuration suitable for small-scale grid connected wind energy systems, the variable speed multiple pole PMSG is directly driven by a fixed-pitch low power wind turbine and connected to an AC grid through a two level three-phase back-back voltage source converter (VSC). The back-back VSC consists of the three-phase AC/DC voltage source converter (VSC) at the machine-side and the same configuration of three-phase DC/AC voltage source inverter (VSI) at the AC grid-side. The machine-side is connected to the AC grid-side through a capacitor which serves as a storage device, filters voltage ripple and a point of isolation between the generator frequency and the grid-side frequency. This configuration can be modified to include a transformer at the AC grid-side when higher voltage is needed to integrate to AC grid.

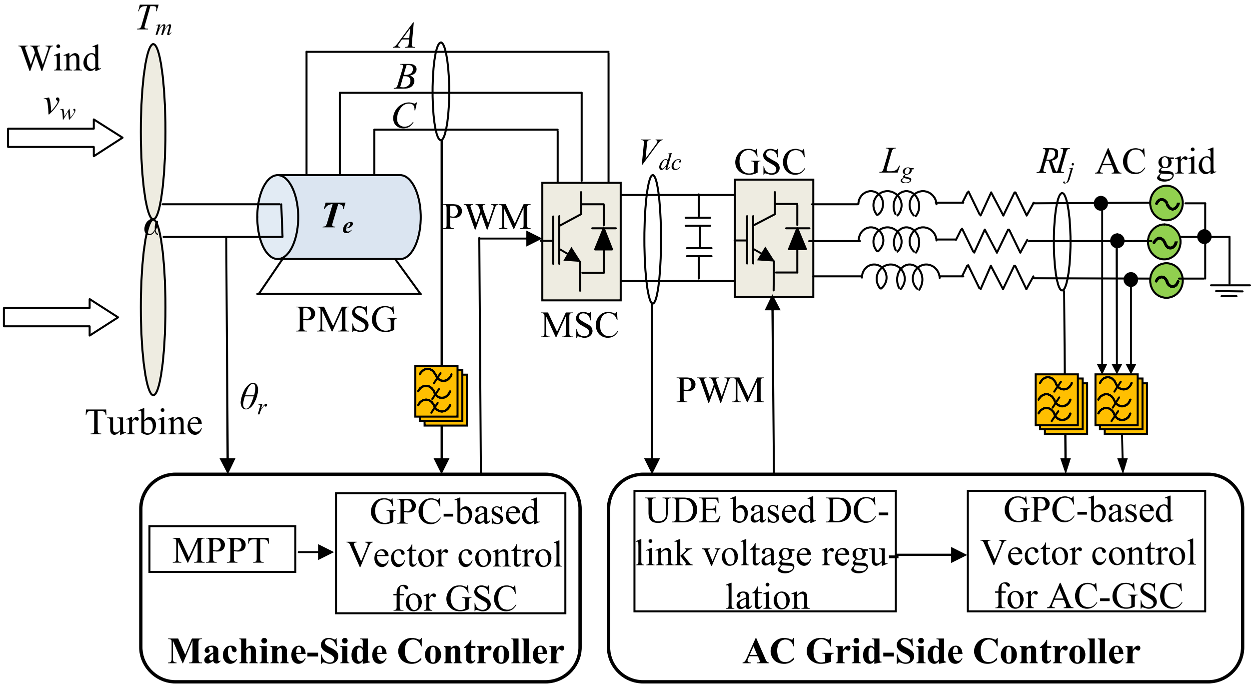

Figure 5.1. Block diagram of two level three-phase back-to-back PWM voltage source converters switching with variable speed PMSG wind energy system.

Compared with the configuration shown in Figure 2.10 (Chapter 2), the number of power electronic devices is now increased to a total of 12 power electronic converter switches and 12 anti-parallel diodes (6 at the generator-side and 6 at the AC grid-side). Under the action of the proposed generalized predictive control (GPC) strategy, the generator-side converter and processes variable frequency AC-voltage to DC-voltage, while the grid-side converter and processes DC-voltage to fixed frequency AC-voltage. The controller at the generator-side and the gird-side depends on the choice of control parameters. In a wind energy system, the aim of the control is to track as much power from the wind and delivered a constant frequency power to the AC grid. In order to achieve MPPT and DC-link voltage regulation as the wind speed changes, the generator-side converter is designed to control the wind turbine and generator speed to track maximum power at various wind speeds, while the grid-side converter matches the output power from the generator to the AC grid by maintaining a constant DC-link voltage. This enables a fixed frequency and fixed voltage to be supplied to the utility grid.

5.3. Control Strategy

In order to implement the detailed switching of back-back voltage source converters with variable speed PMSG wind turbine, a control strategy must be selected, developed and applied. It is obviously very important for any control strategy to take into account the variability of wind speed. The control techniques considered in this Chapter is based on generalized predictive control (GPC) algorithm. The GPC method was proposed by Clarke et al. [2, 8] is a well-established independent control technique in which each d- and q-axis current is controlled independent of the other. It is implemented with GPC regulators. There are four GPCs, the generator-side controller and the grid-side controller. The generator-side controller is designed to control the speed and the torque of the PMSG to track maximum power from the wind by controlling the stator currents, and the grid-side controller controls the AC grid currents, in order to control the power flow to the utility grid.

5.4. Formulation of Generalized Predictive Control (GPC)

The design process of GPC algorithm includes system model description and cost function configuration steps. The model is used to predict the controlled variable trajectory over the chosen horizon and the cost function is used to determine the optimal control input in accordance with the chosen optimality terms. In the following sections both design steps are described and control law transfer function coefficients can be obtained in this way.

5.4.1. Process Model

In predictive controllers, different process models can be applied. In the following the most common ones are presented.

5.4.2. Transfer Function Model

In order to design a GPC control loop, the model must be expressed as a transfer function formulation described by controlled auto-regressive integrated moving average (CARIMA) model [26]:

$$A(z^{-1})\,\mathrm{y(t)} = B(z^{-1})\,z^{-d}u(t-1) + C(z^{-1})\frac{e(t)}{\Delta} \tag{5.1}$$

Where the expressions of the polynomials *A*, *B* and *C* in the backward shift operator z-1 are given as follow [26]:

$$A(z^{-1}) = 1 + a_1 z^{-1} + a_2 z^{-2} + \ldots + a_{na} z^{-na} \tag{5.2}$$

$$B(z^{-1}) = b_0 + b_1 z^{-1} + b_2 z^{-2} + \ldots + a_{nb} z^{-nb} \tag{5.3}$$

$$C(z^{-1}) = 1 + c_1 z^{-1} + c_2 z^{-2} + \ldots + c_{nc} z^{-nc} \tag{5.4}$$

where $u(t)$ and $y(t)$ are the control and output variables of the plant and $e(t)$ is a zero mean white noise. $\Delta = 1 - z^{-1}$ is the discrete differentiation operator.

For simplicity, in the following the delay *d* is considered to be equal to 0, and the noise polynomial $C(z^{-1})$ is chosen to be 1.

5.4.3. State Space Model

The model for SISO process is the following:

$$x(\mathrm{t}+1) = Ax(t) + Bu(t) \tag{5.4}$$

$$y(\mathrm{t}) = Cx(t) \tag{5.5}$$

where *x* is the state vector, *A*, *B*, *C* are the matrices of the system, input and output respectively. The prediction is given by:

$$\hat{y}(t+j\,|\,t) = C\hat{x}(t+j\,|\,t) = C\left[A^k x(t) + \sum_{i=1}^{k} A^{i-1}Bu(t+k-j\,|\,t)\right] \tag{5.6}$$

This predictor requires the state vector. If the state variables are not measured, then state observer is required to implement a state space model based predictive controller. The state space model is the most convenient for multivariable processes.

Other**:** Non-linear models can also be used to represent the process but the problem of their use springs from the fact that they cause the optimization problem to be more complicated. Neural nets as well as fuzzy logic are other forms of representation used in some applications.

5.4.4. Cost function

The various GPC algorithms propose different cost functions for obtaining the control law. The general aim is that the future plant output *y(t+j)* on the considered horizon should follow a determined reference signal *r(t+j)* and, at the same time, the control effort $\Delta u(t)$ necessary for doing so should be penalized. This is accomplished by minimizing a multistage cost function *J*. The general expression for such an objective function can be written as [27]:

$$J(N_1,N_2,N_u) = E\left\{ \sum_{j=N_1}^{N_2} \delta(j)\left[\hat{y}(t+j|t) - r(t+j)\right]^2 + \sum_{j=1}^{N_u} \lambda(j)\left[\Delta u(t+j-1)\right]^2 \right\} \quad (5.7)$$

where *E{.}* is the expectation operator, $\hat{y}(t+j|t)$ is an optimum j-step ahead prediction of the system output on data up to time *t*, and $r(t+j)$ is the future reference trajectory. The tuning parameters of the GPC can be properly seen in the cost function:

N_1 is the minimum costing horizon, specifying the beginning of the horizon in the cost function, from which point the output error is taken into account. Since the control action affects the process output only after the process delay, the minimum horizon is suggested to be equal or higher than the process delay.

N_2 is the prediction horizon, specifying the end of the horizon in the cost function, in other words the last output error that is taken into account.

N_u is the control horizon, the number of consecutive changes in the control signals.

$\Delta(j)$, $\lambda(j)$ are the weighting sequences, enabling the weighting of the terms in the cost function also with respect to their appearance in time.

In order to optimize the cost function the optimal prediction of $y(t+j)$ for $j>N_1$ and $j\leq N_2$ will be obtained. To get the prediction, the following Diophantine equation is considered:

$$1 = E_j(z^{-1})\Delta A(z^{-1}) + z^{-j}F_j(z^{-1}) \quad (5.8)$$

$$1 = E_j(z^{-1})\tilde{A}(z^{-1}) + z^{-j}F_j(z^{-1}) \quad (5.9)$$

The polynomials $E_j(z^{-1})$ and $F_j(z^{-1})$ are uniquely defined with degrees $j-1$ and *na* respectively. They can be obtained dividing 1 by $\tilde{A}(z^{-1})$ until the remainder can be factorized as $z^{-j}F_j(z^{-1})$. The quotient of the division is the polynomial $E_j(z^{-1})$.
If equation (5.1) is multiplied by $\Delta E_j(z^{-1})z^j$

$$\tilde{A}(z^{-1})E_j(z^{-1})y(t+j) = E_j(z^{-1})B(z^{-1})\Delta u(\mathrm{t+j-d-1}) + E_j(z^{-1})\mathrm{e}(\mathrm{t}+j) \quad (5.10)$$

Considering equations (5.8) and (5.9), equation (5.10) can be written as:

$$(1 - z^{-j}F_j(z^{-1}))y(t+j) = E_j(z^{-1})B(z^{-1})\Delta u(\mathrm{t+j-d-1}) + E_j(z^{-1})\mathrm{e}(\mathrm{t}+j) \quad (5.11)$$

This can be rewritten as:

$$y(t+j) = F_j(z^{-1})\,\mathrm{y(t)} + E_j(z^{-1})B(z^{-1})\Delta u(\mathrm{t+j-d-1}) + E_j(z^{-1})\mathrm{e}(\mathrm{t}+j) \quad (5.12)$$

As the degree of polynomial $E_j(z^{-1})=j-1$ the noise terms in equation (5.12) are all in the future. The prediction of $y(t+j)$ is therefore:

$$\hat{y}(t+j|t)=G_j(z^{-1})\Delta u(\mathrm{t+j-d-1})+F_j(z^{-1})y(\mathrm{t}) \tag{5.13}$$

where:

$$G_j(z^{-1})=E_j(z^{-1})B(z^{-1}) \tag{5.14}$$

It is very simple to show that the polynomials $E_j(z^{-1})$ and $F_j(z^{-1})$ can be obtained recursively. The recursion of the Diophantine equation has been demonstrated in [2]. A simpler demonstration is given in the following. There are other formulations of GPC not based on the recursion of the Diophantine equation [28].

Consider that polynomials $E_j(z^{-1})$ and $F_j(z^{-1})$ have been obtained by dividing 1 by $\tilde{A}(z^{-1})$ until the remainder of the division can be factorized as $z^{-j}F_j(z^{-1})$.

With:

$$F_j(z^{-1})=f_{j,0}+f_{j,1}z^{-1}+...+f_{j,na}z^{-na} \tag{5.15}$$

$$E_j(z^{-1})=e_{j,0}+e_{j,1}z^{-1}+...+e_{j,j-1}z^{-(j-1)} \tag{5.16}$$

Suppose that the same procedure is used to obtain $E_{j+1}(z^{-1})$ and $F_{j+1}(z^{-1})$, that is, dividing 1 by $\tilde{A}(z^{-1})$ until the remainder of the division can be factorized as $z^{-(j+1)}F_{j+1}(z^{-1})$

With:

$$F_{j+1}(z^{-1})=f_{j+1,0}+f_{j+1,1}z^{-1}+...+f_{j+1,na}z^{-na} \tag{5.17}$$

It is clear that only another step of the division performed to obtain the polynomials $E_j(z^{-1})$ and $F_j(z^{-1})$ has to be taken in order to obtain the polynomials $E_{j+1}(z^{-1})$ and $F_{j+1}(z^{-1})$.

The polynomial $F_{j+1}(z^{-1})$ will be given by:

$$E_{j+1}(z^{-1})=E_j(z^{-1})+e_{j+1,j}z^{-j} \tag{5.18}$$

With:

$$e_{j+1,j}=f_{j,0} \tag{5.19}$$

The coefficients of polynomial $F_{j+1}(z^{-1})$ can then be expressed as:

$$f_{j+1,i}=f_{j+i,1}-f_{j,0}\tilde{a}_{i+1} \quad i=0...na-1 \tag{5.20}$$

The polynomial $G_{j+1}(z^{-1})$ can be obtained recursively as follows:

$$G_{j+1} = E_{j+1}B = (E_j + f_{j,0}z^{-j})B \tag{5.21}$$

$$G_{j+1} = G_j + f_{j,0}\, z^{-j} B \tag{5.22}$$

That is, the first *j* coefficient of $G_{j+1}(z^{-1})$ will be identical to those of $G_j(z^{-1})$ and the remaining coefficients will be given by:

$$g_{j+1,j+i} = g_{j,j+i} + f_{j,0}\, b_i \quad i = 0 \ldots nb \tag{5.23}$$

To solve the GPC problem the set of control signals *u(t)*, *u(t + 1)*, …, *u(t + N)* has to be obtained in order to optimize equation (5.7). As the system considered has a dead time of *d* sampling periods, the output of the system will be influenced by signal *u(t)* after sampling period *d+1*. The values N_1, N_2 and N_u defining the horizon can be defined by $N_1=d+1$, $N_2=d+N$ and $N_u=N$. Notice that there is no point in making $N_1<d+1$ as terms added to expression (5.7) will only depend on the past control signals. On the other hand, if $N_1>d+1$ the first points in the reference sequence, being the ones guessed with most certainty, will not be taken into account. Now consider the following set of *j* ahead optimal predictions:

$$\hat{y}(t+d+1|t) = G_{d+1}\, \Delta u(t) + F_{d+1}\, y(t) \tag{5.24}$$

$$\hat{y}(t+d+2|t) = G_{d+2}\, \Delta u(t+1) + F_{d+2}\, y(t) \tag{5.25}$$

$$\vdots$$

$$\hat{y}(t+d+N|t) = G_{d+N}\, \Delta u(t+N-1) + F_{d+N}\, y(t) \tag{5.26}$$

Which can be written as:

$$y = Gu + F(z^{-1})\, y(t) + G'(z^{-1})\Delta u(t-1) \quad \ldots\ldots\ldots\ldots (5.27)$$

where:

$$y = \begin{bmatrix} \hat{y}(t+d+1|t) \\ \hat{y}(t+d+2|t) \\ \vdots \\ \hat{y}(t+d+N|t) \end{bmatrix} \qquad u = \begin{bmatrix} \Delta u(t) \\ \Delta u(t+1) \\ \vdots \\ \Delta u(t+N-1) \end{bmatrix}$$

$$G=\begin{bmatrix} g_0 & 0 & \cdots & 0 \\ g_1 & g_0 & \cdots & 0 \\ \vdots & \vdots & \vdots & \vdots \\ g_{N-1} & g_{N-2} & \cdots & g_0 \end{bmatrix} \quad G'(z^{-1})=\begin{bmatrix} (G_{d+1}(z^{-1})-g_0)z \\ (G_{d+2}(z^{-1})-g_0-g_1z^{-1})z^2 \\ \vdots \\ (G_{d+N}(z^{-1})-g_0-g_1z^{-1}-\cdots-g_{N-1}z^{-(N-1)})z^N \end{bmatrix}$$

$$F(z^{-1})=\begin{bmatrix} F_{d+1}(z^{-1}) \\ F_{d+2}(z^{-1}) \\ \vdots \\ F_{d+N}(z^{-1}) \end{bmatrix}$$

Notice that the last two terms in equation (5.27) only depend on the past and can be grouped into “f” leading to:

$$\mathrm{y}=\mathrm{Gu}+\mathrm{f} \tag{5.28}$$

Notice that if all initial conditions are zero, the free response “f” is also zero. If a unit step is applied to the input at time *t*, that is:

$$\Delta u(t)=1,\ \Delta u(t+1)=0,\cdots,\Delta u(t+N-1)=0 \tag{5.29}$$

The expected output sequence $[\,\hat{y}(t+1),\hat{y}(t+2),\ldots,\hat{y}(t+N)\,]^T$ is equal to the first row of matrix “*G*”. That is the first row of matrix “*G*” can be calculated as the step response of the plant when a unit step is applied to the manipulated variable. The free response term can be calculated recursively by:

$$\mathrm{f}_{\mathrm{j+1}}=\mathrm{z}(1-\tilde{\mathrm{A}}(\mathrm{z}^{-1}))\mathrm{f}_{\mathrm{j}}+\mathrm{B}(\mathrm{z}^{-1})\Delta\mathrm{u}(\mathrm{t}-\mathrm{d}+\mathrm{j}) \tag{5.30}$$

With: $\mathrm{f}_0=\mathrm{y(t)}$ and $\Delta\mathrm{u(t+j)}=0$ for $\mathrm{j}\geq 0$.

Equation (5.7) can be written as:

$$\mathrm{J}=(\mathrm{Gu}+\mathrm{f}-\mathrm{w})^{\mathrm{T}}(\mathrm{Gu}+\mathrm{f}-\mathrm{w})+\lambda\mathrm{u}^{\mathrm{T}}\mathrm{u} \tag{5.31}$$

Where:

$$w=\left[w(t+d+1)\ \ w(t+d+2)\cdots w(t+d+N)\right]^T \tag{5.32}$$

Equation (5.31) can be written as:

$$J = \frac{1}{2}u^{T}Hu + b^{T}u + f_{0} \tag{5.33}$$

where:

$$H = 2(G^{T}G + \lambda I) \tag{5.34}$$

$$b^{T} = 2(f - w)^{T}G \tag{5.35}$$

$$f_{0} = (f - w)^{T}(f - w) \tag{5.36}$$

The minimum of J, assuming there are no constraints on the control signals, can be found by making the gradient of J equal to zero, which leads to:

$$u = -H^{-1}b \tag{5.37}$$

Notice that only the first element of “u” is applied and the procedure is repeated at the next sampling time. The solution to the GPC given involves the inversion (or triangularization) of a $N \times N$ matrix which requires a substantial amount of computation. In [2] the concept of control horizon is used to reduce the amount of computation needed, assuming that the projected control signals are going to be constant after $N_u < N$. This leads to the inversion of a $N_u \times N_u$ matrix which reduces the amount of computation (in particular, if $N_u=1$ it is reduced to a scalar computation), but restricts the optimality of the GPC. It is worth noting that future plans are to apply the proposed GPCs technique to other control strategies such as vector control.

5.5. Design of GPC for the Machine-Side Converter

The machine-side converter control technique shown in Figure 5.2 consists of two main parts which are the outer speed control loop, and the inner current (torque) control loop. The outer speed control loop controls the PMSG speed by controlling the generator stator current in a manner to track maximum power of the wind turbine at various wind speeds.

The basic principle is that the machine-side converter controller indirectly controls the electromagnetic torque by controlling the generator rotational speed to its optimum rotational speed and in so doing maintains the tip-speed ratio TSR at the optimum value at various wind speeds.

The machine-side converter uses the MPPT control to generate the optimum rotational speed ω_r^* (speed reference) which the outer speed control loop compares with the measured speed to generate a speed error signal.

The speed error is fed into and processed by the PI regulator to generate the reference current for the inner GPC control loop. In the internal loop, the GPC is applied to the *d-q* axis stator currents of the PMSG in order to provide the components of the stator reference voltages ($V_{d\text{-}ref}$, $V_{q\text{-}ref}$).

For this aim, both discrete transfer functions of the PMSG first have to be established.

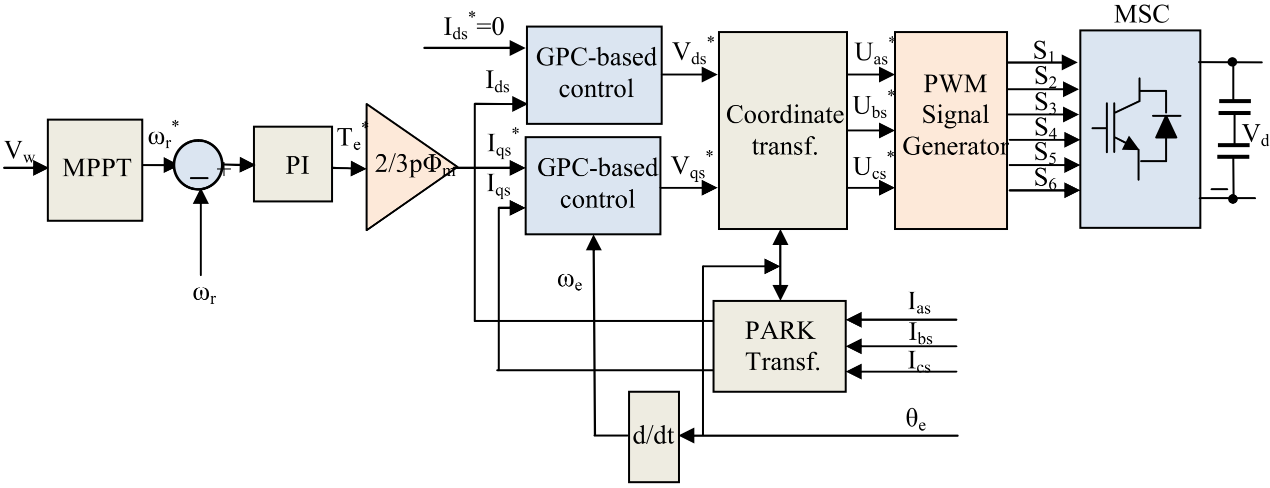

Figure 5.2. Machine-side control technique structure.

5.5.1. Stator Current Loop Model for Machine-Side Converter

To derive the necessary discrete transfer functions for the both GPC stator current controllers, the electrical part of the PMSG equations considering rotating reference frame is required:

$$V_{ds} = R_s I_{ds} + L_d \dot{I}_{ds} - L_q I_{qs} \omega_e \tag{5.38}$$

$$V_{qs} = R_s I_{qs} + L_q \dot{I}_{qs} - (L_d I_{ds} + \Phi_m) \omega_e \tag{5.39}$$

where V_{ds}, V_{qs} represent stator voltages in the *d*- and *q*-axis, I_{ds} and I_{qs} represent stator currents in the *d*- and *q*-axis, and L_d, L_q are *d*- and *q*-axis inductances.

The stator phase resistance is represented by R_s, and electrical angular velocity by ω_e, and $\omega_e = p^*\omega_r$.

Because I_{ds}, I_{qs} and ω_e will be measured, both PMSG equations can be decoupled and a disturbance feed-forward can be implemented as shown in Figure 5.3.

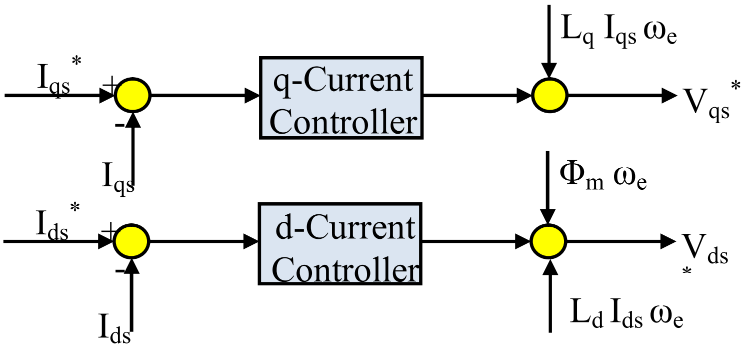

Figure 5.3. Decoupling and disturbance feed forward for PMSG current control.

Therefore the PMSG equations (5.38) and (5.39) reduce as follows:

$$V_{ds} = R_s I_{ds} + L_d \dot{I}_{ds} \tag{5.40}$$

$$V_{qs} = R_s I_{qs} + L_q \dot{I}_{qs} \tag{5.41}$$

Next, the equations (5.40) and (5.41) will be transformed into *S*-domain and rewritten into the following form:

$$\frac{I_{ds}}{V_{ds}} = \frac{1}{R_s + s.L_d} \tag{5.42}$$

$$\frac{I_{qs}}{V_{qs}} = \frac{1}{R_s + s.L_q} \tag{5.43}$$

To get the desired discrete transfer functions, the equations (5.42) and (5.43) will be transformed by means of a zero-order-hold (ZOH) method into *Z*-domain with a sampling interval T_s, and given in equations (5.44) and (5.45):

$$G_d(z^{-1}) = \frac{I_{ds}(z^{-1})}{V_{ds}(z^{-1})} = \frac{\frac{1}{R_S}\left(1-e^{-R_sT_s/L_d}\right)z^{-1}}{1-e^{-R_sT_s/L_d}z^{-1}} = \frac{B_d(z^{-1})}{A_d(z^{-1})} \tag{5.44}$$

$$G_q(z^{-1}) = \frac{I_{qs}(z^{-1})}{V_{qs}(z^{-1})} = \frac{\frac{1}{R_S}\left(1-e^{-R_sT_s/L_q}\right)z^{-1}}{1-e^{-R_sT_s/L_q}z^{-1}} = \frac{B_q(z^{-1})}{A_q(z^{-1})} \tag{5.45}$$

As the prediction is normally not done with $\mathrm{A}(z^{-1})$, but with $\tilde{A}(z^{-1}) = \Delta\mathrm{A}(z^{-1})$, the individual coefficient of the polynomial $\tilde{A}(z^{-1})$ are calculated. Thus for the polynomials $\tilde{A}(z^{-1})$ and $B(z^{-1})$ the following coefficients can be obtained:

$$\tilde{a}_0 = 1 \qquad b_0 = 0$$

$$\tilde{a}_1 = -\left(1 + e^{-R_s T_s / L_d}\right) \qquad b_1 = \frac{1}{R_s}\left(1 - e^{-R_s T_s / L_d}\right)$$

According to the GPC theory and employing the CARIMA model, and taking the previous transfer functions (5.44) and (5.45), where the outputs I_{ds} and I_{qs} are replaced by y_1 and y_2, and the inputs V_{ds} and V_{qs} are replaced by u_1 and u_2, respectively. Next, if in the t instant $\hat{y}_1(t+j-1|t)$ and $\hat{y}_2(t+j-1|t)$ are known. Thus, it ipossible to obtain the predicted outputs $\hat{y}_1(t+j|t)$ and $\hat{y}_2(t+j|t)$ under the form:

$$\hat{y}_1(t+j|t) = (1+\tilde{a}_0) * \hat{y}_1(t) - \tilde{a}_1 * \hat{y}_1(t+j-1|t) + \mathrm{b}_1\, \Delta u_1(t+j-1) \tag{5.46}$$

$$\hat{y}_2(t+j|t) = (1+\tilde{a}_0) * \hat{y}_2(t) - \tilde{a}_1 * \hat{y}_2(t+j-1|t) + \mathrm{b}_1\, \Delta u_2(t+j-1) \tag{5.47}$$

The cost function of a GPC problem is defined as the sum of quadratic terms:

$$J = \sum_{j=N_1}^{N_2} \delta(j)\left[\hat{y}(t+j|t) - r(t+j)\right]^2 + \sum_{j=1}^{N_u} \lambda(j)\left[\Delta u(t+j-1)\right]^2 \tag{5.48}$$

Subject to: $\Delta u(t+j)$ for $j \geq N_u$

If normalized weighting sequences are used then $\delta(j) = 1$ for all j. Also, if a constant value of λ is chosen, i.e. $\lambda(j) = \lambda$, the entire control sequence is weighed equally at every time instant, simplifying the GPC design process.

The polynomial form of GPC requires adjustment of the set parameters N_1, N_2, N_u and λ to ensure good stability. Some guidelines may be found in the literature [29]:

$$\mathrm{N}_1 = \frac{\text{Dead time of the system}}{\text{Sampling period}} = 1 \tag{5.49}$$

$$\mathrm{N}_2 \leq \frac{\text{Response time of the system}}{\text{Sampling period}} \tag{5.50}$$

Very often, N_u is chosen so that $N_u \ll N_2$ and the case N_u=1 is very interesting. Based on the former theory, a robust controller using GPC method is established in MATLAB to validate the control effect. The main parameters of both GPCs design are shown in Table 5.1.

Table 5.1. Design parameters for GPC.

N_1	N_2	N_u	T_s	λ
1	6	1	0.0000001	0.01

5.6. Design of GPC for Grid-Side Converter

The grid-side converter controller ensures that the DC-link voltage stabilizes at the desired reference value as the wind speed (and therefore power onto the DC-link) varies. Unlike the machine-side controller, the grid-side outer control loop is the DC-link voltage control loop. The uncertainty and disturbance estimator (UDE)-based control approach is applied to the regulation of the DC-link voltage. The output of the UDE-based DC-link voltage regulation is designed to generate a real power output reference P^*_{out}. In the inner loop of the AC grid-side controller, the generalized predictive-based vector control is developed to regulate the gird-side currents to achieve real power output control and convert DC power to grid AC power simultaneously.

5.6.1. Robust GPC Applied to Grid-Side Current Loop

In this subsection, a complete design procedure of current controller using GPC on a grid-tied three phase two level inverter for distributed wind power generation systems is presented. The purpose of this controller is to achieve grid currents with low harmonic content as well as unity power factor. Essentially, to obtain output sinusoidal currents, the control strategy must switch the grid-side converter in order to synthesize a sinusoidal fundamental component at the output. The system can be represented as shown in Figure 5.4.

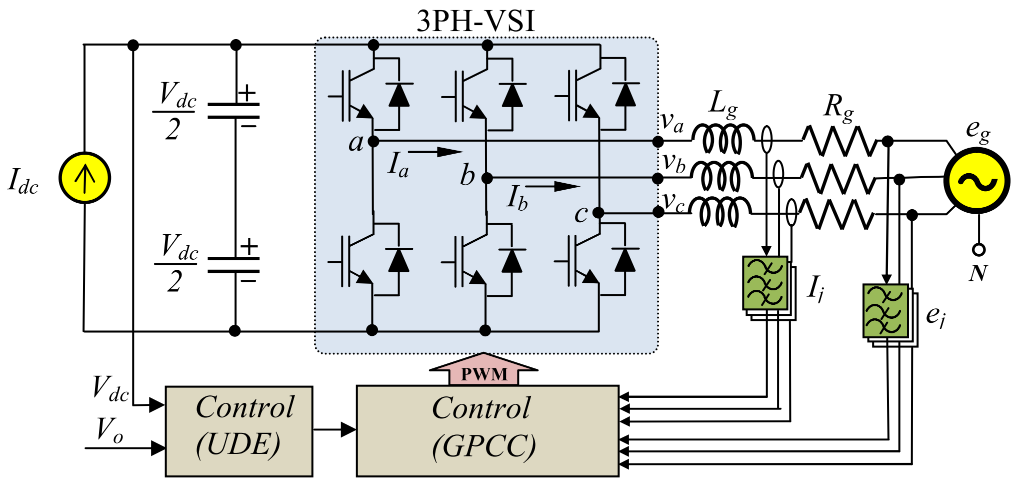

Figure 5.4. Grid-Connected Voltage Source Inverter for wind energy system.

The Power generated from the wind energy system is modeled as current I_{dc} that charges the DC-link capacitor to voltage V_{dc}. Current I_j , with $j = [a,b,c]$ is injected to the grid by means of an inductor filter.

The per-phase model can be described by the following equation:

$$v_j(t) = R_g\, I_j(t) + L_g \frac{dI_j(t)}{dt} + e_j(t) \tag{5.60}$$

where v_j is the voltage applied to the AC grid by the voltage source inverter, e_j represents grid voltage in the *abc* reference frame, R_g and L_g are the equivalent parasitic resistance and filter inductance, respectively, of the 3 wire grid-configuration connection.

Using equation (5.60), a transfer function between applied voltage and output current in the continuous S-domain can be obtained for each phase as:

$$G_j(s) = \frac{1}{R_g + s.L_g} \tag{5.61}$$

By means of a ZOH circuit, the grid current is sampled with a sampling period T_s, chosen in order to guarantee $R_g\ T_s/L_g << 1$. Thus a discrete transfer function is obtained:

$$G_{jd}(z^{-1}) = \frac{m_1.z^{-1}}{1 - n_1.z^{-1}} \tag{5.62}$$

The system model polynomials in the discrete time domain are obtained from the plant transfer function (5.62). As a result $A(z^{-1}) = 1\text{-}n.z^{-1}$ and $B(z^{-1}) = m_1.z^{-1}$.

So, by means of the method explained in previous section, and the chosen values of N_1, N_2, N_u and λ, The GPC controller is implemented as a discrete transfer function in the form of a difference equation which uses the error between the reference and output current samples and gives the control algorithm output sample $w_j(k)$, j= [*a, b*] as a result.

The grid voltages are measured in each phase and also filtered with a first-order low-pass filter (LPF) with f_c = 4 *kHz*, as it is sampled at f_s =10 *kHz*. These measurements are used by the PLL, in order to generate references current relative to the phase of the grid voltage waveform. This type of PLL was chosen to guarantee a unit power factor injection. The reference currents $r_a(k)$ and $r_b(k)$ are built as:

$$r_j(\mathrm{k}) = A(k)\sin(p_i(k) + \phi(k)) \tag{5.63}$$

With: j= [*a, b*]. $A(k)$ is the amplitude of the sinusoidal reference currents, and $\Phi(k)$ is the phase offset of the reference relative to the grid voltage waveform

phase. They are used as control system inputs in order to change active and reactive power injection to the AC grid.
The control algorithm output for the phase *c* is built as:

$$w_c(\mathrm{k}) = -w_a(\mathrm{k}) - w_b(\mathrm{k}) \tag{5.64}$$

To each of these outputs, a grid voltage feed-forward (FF) term is added in order to reject its disturbance effect, and consists of the actual AC grid voltage sample $e_j(k)$, $j= [a,b,c]$. The resulting feed-forward compensated control input U_j (k) is fed into the PWM module, with proper gain correction as shown in Figure 5.5.

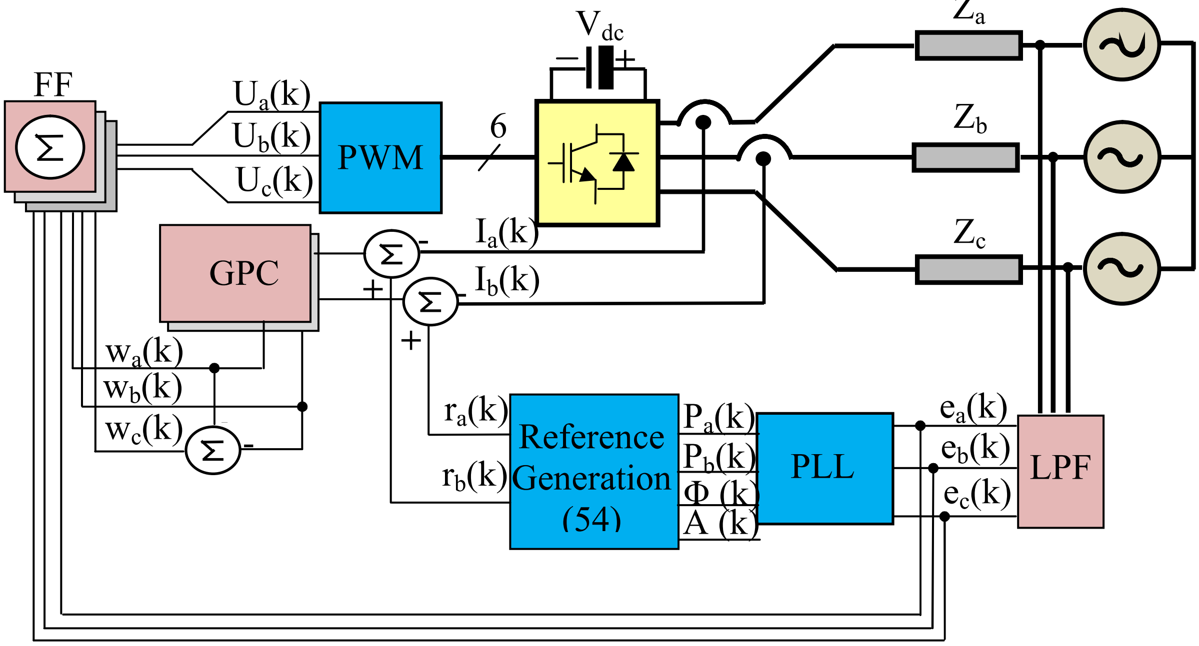

Figure 5.5. Proposed GPC block diagram of grid-side converter.

5.7. UDE-based DC-link voltage Control

A DC-link capacitor between the machine-side converter and the AC grid-side converter is used to balance the DC-link voltage. In order to keep the DC-link voltage stable, the power coming out of the DC-link capacitor should be equal to the power injected into the capacitor. The full DC-link dynamics are very complex and cannot be used for control directly [12]. A DC-link voltage equation simplified from [12] with unknown parameters is shown as:

$$\dot{V}_{dc} = \frac{P_{in}}{CV_{dc}} - \frac{P_{out}}{CV_{dc}} - \frac{P_{loss}}{CV_{dc}} + \Delta v_0 \tag{5.65}$$

where V_{dc} is the DC-link voltage, C is the capacitance value of the DC-link capacitor, P_{in} represents the DC power from the machine-side converter, P_{out} represents the real power output of the AC grid-side converter, P_{loss} denotes the power losses on the DC-link capacitor and the AC grid-side converter, and Δv_0 represents the effects of unknown parameters, such as equivalent series resistance, equivalent series inductance and the reactive power. The DC-link dynamics equation (5.65) show that the DC-link voltage V_{dc} can be controlled through the adjustment of the real power output P_{out} of the grid-side converter. Normally, P_{in} can be measured directly, but P_{loss} and Δv_0 are difficult to be measured directly. Instead of the nominal model (5.65), the following modified model is considered in the presence of the uncertainties and disturbances:

$$\dot{V}_{dc} = \frac{P_{in}}{CV_o} - \frac{P^*_{out}}{CV_o} + \Delta v \tag{5.66}$$

where V_0 is a constant reference value for V_{dc}, and Δv represents the lumped uncertainty and disturbance term $\Delta v = \frac{P_{in}}{CV_{dc}} - \frac{P_{out}}{CV_{dc}} - \frac{P_{loss}}{CV_{dc}} + \Delta v_0 - \frac{P_{in}}{CV_o} + \frac{P^*_{out}}{CV_o}$. In the normal operation condition, the DC-link voltage V_{dc} should be close to V_0.

In particular, the tracking error $e_v = V_o - V_{dc}$ asymptotically converges to zero by following the desired error dynamics:

$$\dot{e}_v = -k_v e_v \tag{5.67}$$

Combining equations (5.65) and (5.66), there is:

$$\dot{V}_o - \frac{P_{in}}{CV_o} + \frac{P^*_{out}}{CV_o} - \Delta v = -k_v e_v \tag{5.68}$$

The real power output reference P^*_{out} needs to satisfy:

$$P^*_{out} = -CV_o\dot{V}_o + P_{in} - CV_o k_v e_v + CV_o \Delta v \tag{5.69}$$

According to the system dynamics in equation (5.66), the uncertainty terms Δv can be represented as:

$$\Delta v = \dot{V}_{dc} - \frac{P_{in}}{CV_o} + \frac{P^*_{out}}{CV_o} \tag{5.70}$$

Following the procedures provided in [18]. It is assumed that $g_{vf}(t)$ is the impulse response of a strictly proper stable filter $G_{vf}(s)$ with the appropriate frequency characteristics over the spectrum of Δv. Then Δv can be accurately approximated by:

$$\hat{\Delta v} = \Delta v * g_{vf} = \left(\dot{V}_{dc} - \frac{P_{in}}{CV_o} + \frac{P^*_{out}}{CV_o} \right) * g_{vf} \tag{5.71}$$

where $\hat{\Delta v}$ is an estimate of Δv.

Replacing Δv with $\hat{\Delta v}$ in equation (5.69) results in:

$$P^*_{out} = -CV_o\dot{V}_o + P_{in} - CV_o k_v e_v + CV_o \left(\dot{V}_{dc} - \frac{P_{in}}{CV_o} + \frac{P^*_{out}}{CV_o} \right) * g_{vf} \tag{5.72}$$

These result in the UDE-based control laws:

$$P^*_{out} = P_{in} + CV_o \left[L^{-1} \left\{ \frac{1}{1 - G_{vf}(s)} \right\} * \left(-k_v e_v \right) + L^{-1} \left\{ \frac{sG_{vf}(s)}{1 - G_{vf}(s)} \right\} * V_{dc} \right] \tag{5.73}$$

The filter design is very important in the UDE algorithm, as the filter should cover the spectrum of disturbances with the unity gain and zero phase shift.

Different choices of filters will result in different forms of UDE controller, which depends on system dynamics and performance requirements.

In this thesis, it is sufficient to choose the filter $G_{vf}(s)$ as the following first-order low-pass filter:

$$G_{vf}(s) = \frac{1}{1 + \tau_v s} \tag{5.74}$$

Then:

$$\frac{s\,G_{vf}(s)}{1 - G_{vf}(s)} = \frac{1}{\tau_v} \tag{5.75}$$

Therefore, the UDE-based control law (5.73) is derived as follows:

$$P^*_{out} = P_{in} - CV_o\dot{V}_o - \frac{CV_o}{\tau_v} \left[\left(k_v \tau_v + 1 \right) e_v + k_v \int_0^t e_v dt \right] \tag{5.76}$$

Considering V_0 as a constant value, $\dot{V}_o = 0$. Then, the UDE-based control law can be reduced to:

$$P^*_{out} = P_{in} - \frac{CV_o}{\tau_v} \left[\left(k_v \tau_v + 1 \right) e_v + k_v \int_0^t e_v dt \right] \qquad (5.76)$$

5.8. Performance Evaluations with Experimental Data

To finally show the effectiveness of the proposed GPC solutions and their Real-Time applicability on a hardware setup, a grid-tied two-level back-to-back power converter PMSG wind turbine system emulator was constructed in the LAS laboratory. An overview of this test-bench is shown in Figure 5.6.

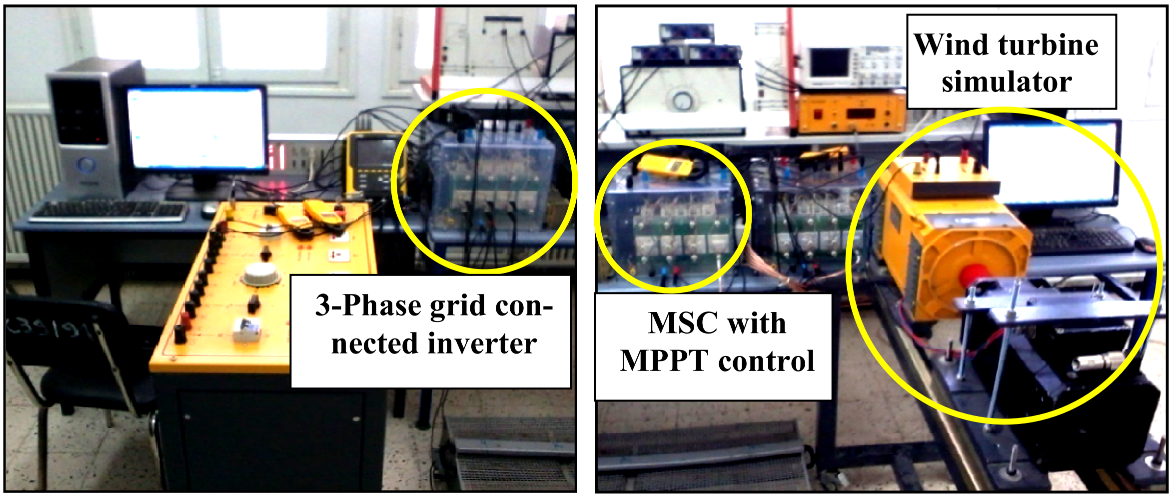

Figure 5.6. Grid-tied two-level back-to-back PMSG wind energy system.

In the following, the transient control performances of both, the machine and grid-side converters are experimentally verified. The testing scenario is maximum power point tracking (MPPT) where the wind speed changes rapidly, while the DC-Link voltage remains at its reference value V_o= 250V to test the most severe condition. The reactive power of both the machine and grid-side are set to *0* Var to achieve a unit power factor. The machine and grid-side transient control performances of GPC algorithm are depicted in Figures 5.7 and 5.8, respectively.

5.8.1. Experimental Results

5.8.2. Transient Analysis of Machine-Side Converter Control

Figures 5.7(a) to 5.7(h) show the dynamic responses of the wind velocity, the rotor speed, the zoom-in view of the rotor position, the electromagnetic torque, the *d*-axis stator current, the *q*-axis stator current, the 3-phase stator currents and the zoom-in view of the steady-state 3-phase stator currents of the PMSG system based on GPC of the machine-side converter, respectively. It has been shown that the proposed system has better transient response. This is clear in Figure 5.7(b) to 5.7(h) where the system with the proposed GPC has attained the steady state value very quickly and the field orientation condition is satisfied. On the other hand, the GPC tracks well the rotor speed reference under large wind variations. The rotor speed overshoot and undershoot is less than 6 rpm at all wind speed conditions as depicted in Figure 5.7(b). Figure 5.7(c) illustrates the rotor position angle response which exactly matches with the stator 'a' phase current. As the PMSG is four pole pair machine, one cycle of rotor position angle corresponds to four cycle of phase ‘a’ stator current. It is seen from Figure 5.7(d) that the electromagnetic torque follows smoothly according to the disturbances in wind velocity. According to the Figures 5.7(e) and 5.7(f), we can find that the *d*- and *q*-axis stator currents of PMSG are perfectly regulated to the desired values. In the proposed GPC strategy the *q*-axis current of the PMSG is maintained at zero and the *q*-axis current is changing corresponding to the wind speed, which achieves maximum wind power point tracking. Figure 5.7(g) shows the 3-phase stator currents response. It is obvious that the stator currents of PMSG have less ripple content. The balanced operation of the PMSG is verified by the zoom-in view of the steady-state three-phase output currents, which are shown in Figure 5.7(h).

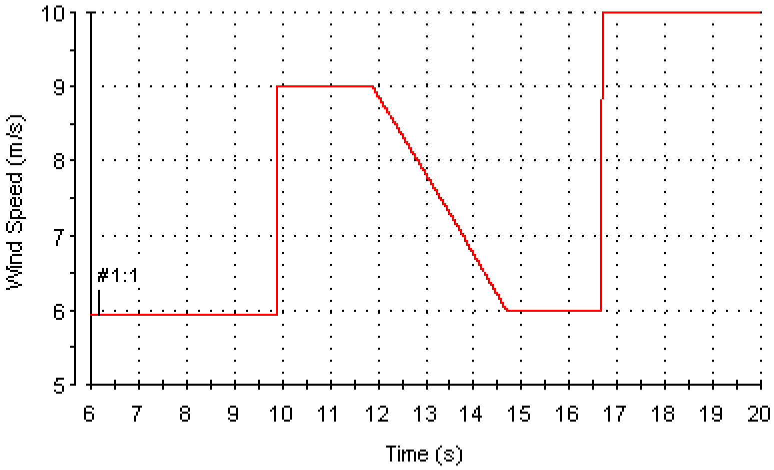

(a). Wind velocity.

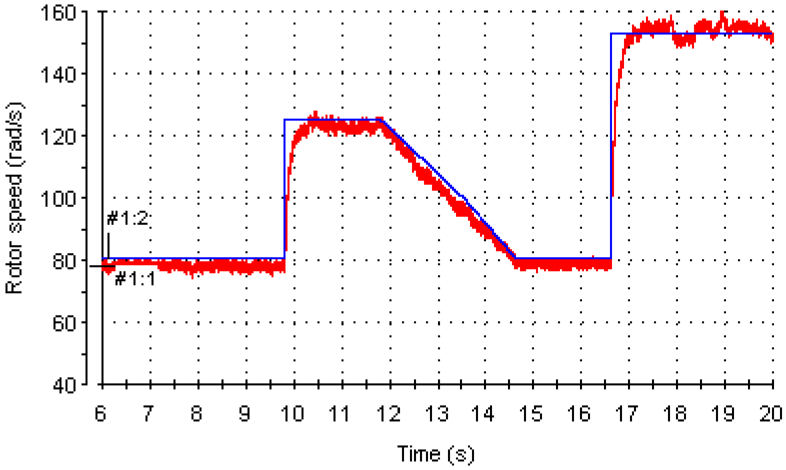

(b). Rotor speed.

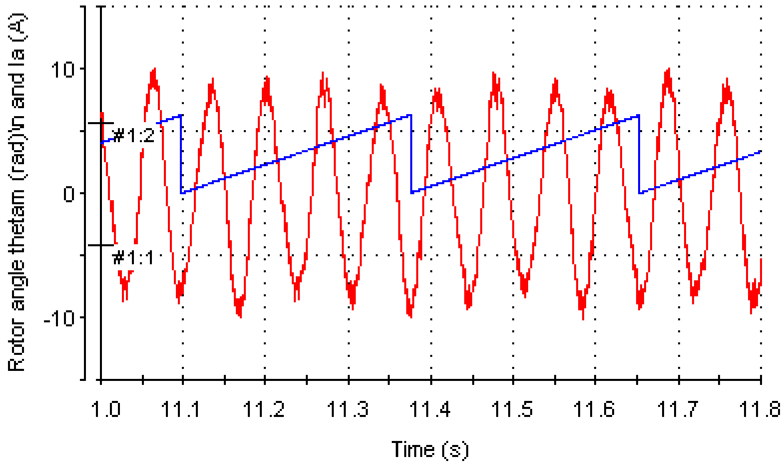

(c). Rotor position and stator 'a' phase current.

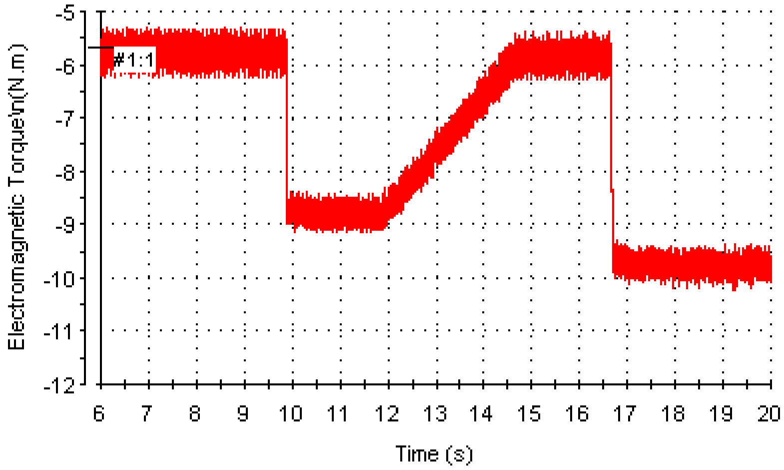

(d). Electromagnetic torque.

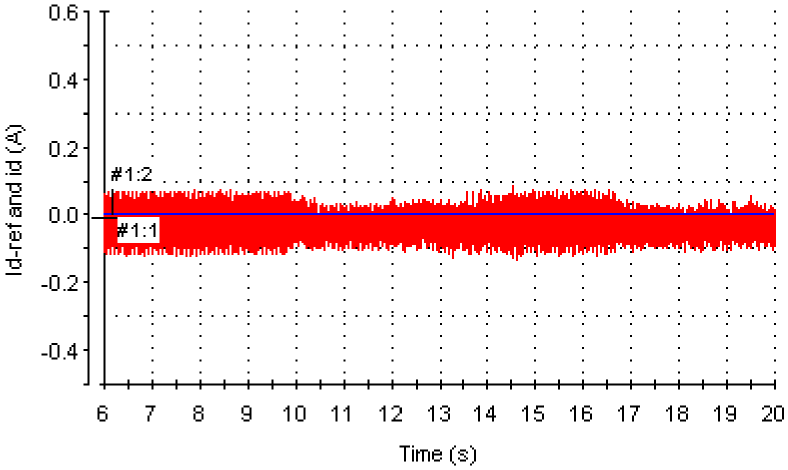

(e). d-axis stator current of PMSG.

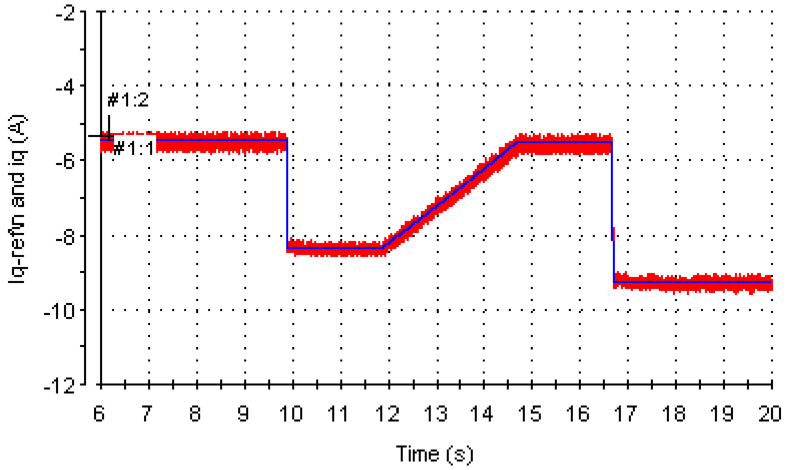

(f). q-axis stator current of PMSG.

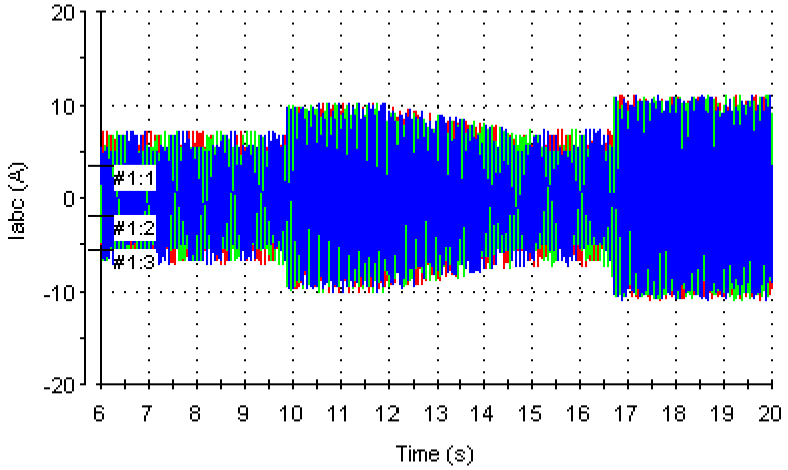

(g). 3-phase stator currents of PMSG.

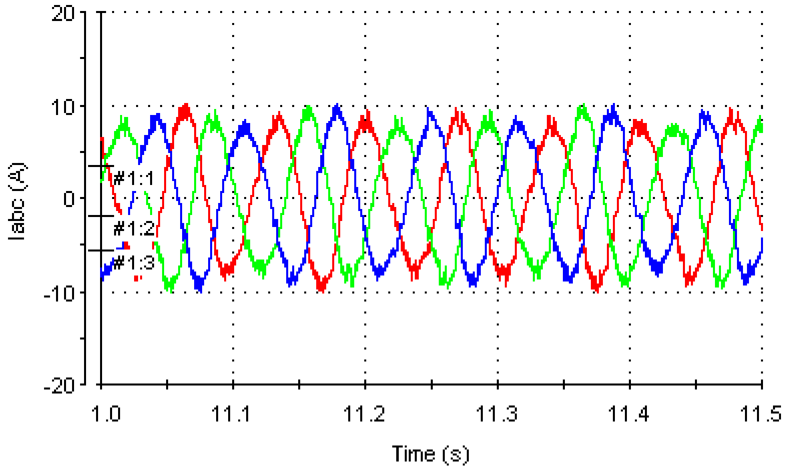

(h). Zoom-in view of steady-state 3-phase stator currents of PMSG.

Figure 5.7. Performance of various parameters of the machine-side converter.

5.8.3. Transient Analysis of Grid-Side Converter Control

Figures 5.8(a) to 5.8(g) show the dynamic responses of the DC-link voltage, the electrical angle of grid voltage, the *d*- and *q*-axis currents of grid-side inverter, the 3-phase currents and the zoom-in view of the three-phase currents of grid-side inverter, the voltage and the current waveforms of one phase in grid-side inverter, respectively.

As can be seen, quite similar overall performances for machine- and AC grid-side control including the DC-link control are obtained. The results in Figures 5.8(a) to 5.8(g) emphasize that the GPC of grid-side converter is less sensitive to wind variation.

Figure 5.8(a) shows that the DC-link voltage is kept steady, no overshoot occurs, and almost not affected during the changing wind velocity. This is due to the dynamic power reference which is immediately generated accordingly and tracked by the inner GPC current control loop. Figure 5.8(b) shows that the electrical angle of grid voltage varies from zero to 2π periodically.

When the electrical angle is equal to zero, the grid voltage reaches its peak value. As displayed in Figures 5.8(c) and 5.8(d), due to the independent control of the *dq*-axis currents and the unity power factor operation, the *q*-axis current of grid-connected inverter is maintained at zero while the *d*-axis current is similar to the wind speed. As shown in Figure 5.8(e) and 5.8(f), the 3-phase currents of grid-connected inverter are sinusoidal and phase “a” grid voltage is phase with phase “a” grid current, which achieves unity power factor.

Figure 5.8(g) displays the voltage and the current waveforms of one phase in grid-side inverter. The phase “a” grid current lags the phase “a” grid voltage by π, which is the power factor angle.

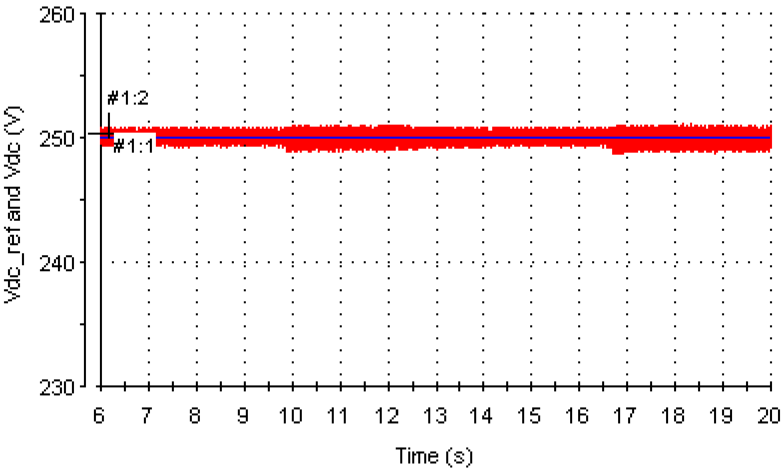

(a). DC-link voltage.

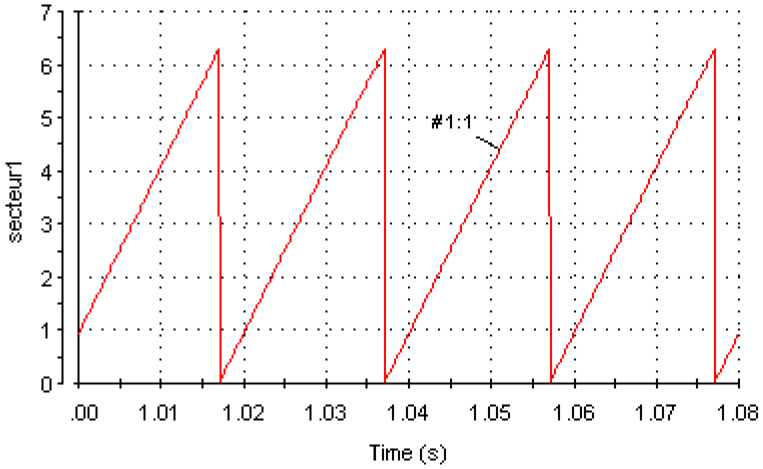

(b). Electrical angle of grid voltage.

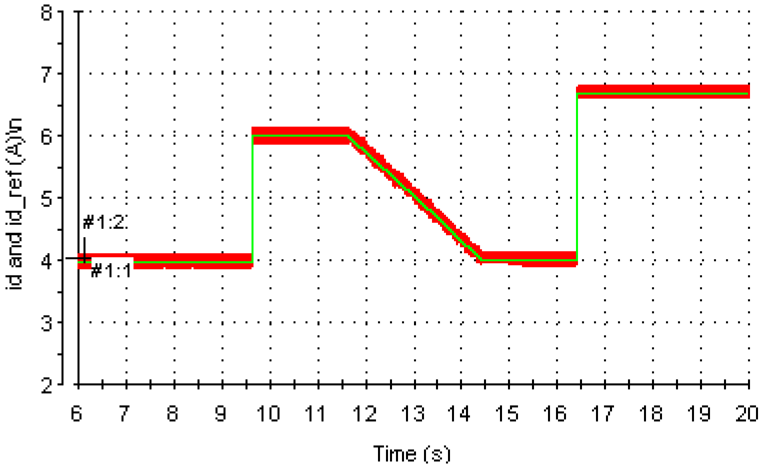

(c). d-axis currents of grid-side inverter.

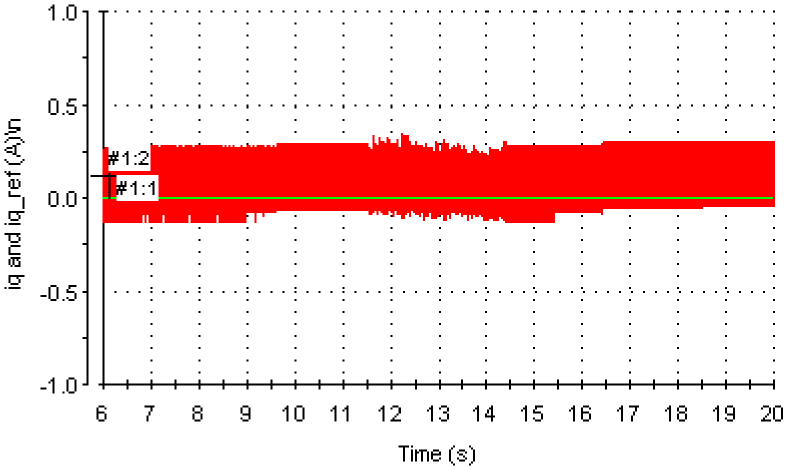

(d). q-axis currents of grid-side inverter.

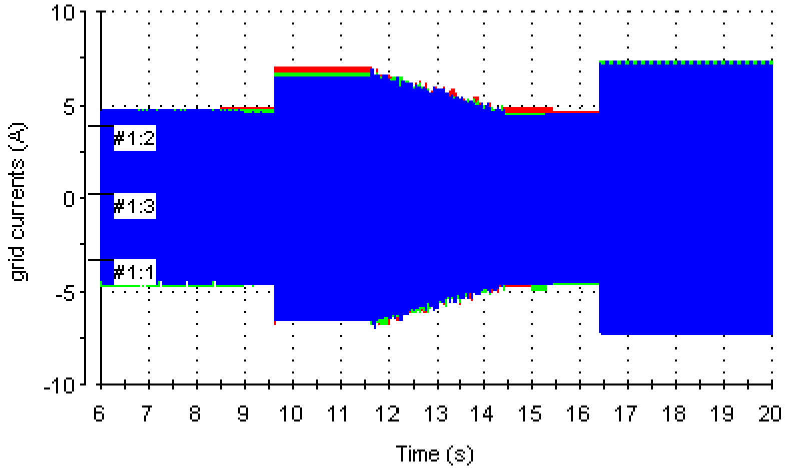

(e). 3-phase grid currents.

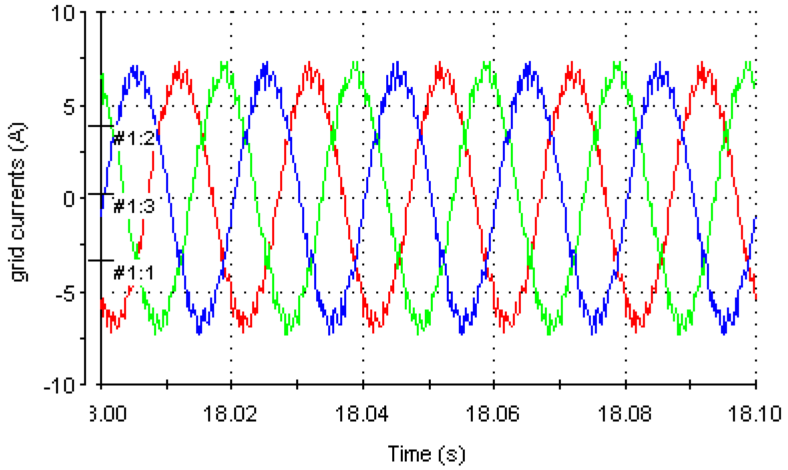

(f). Zoom-in view of the three-phase currents of grid-side inverter.

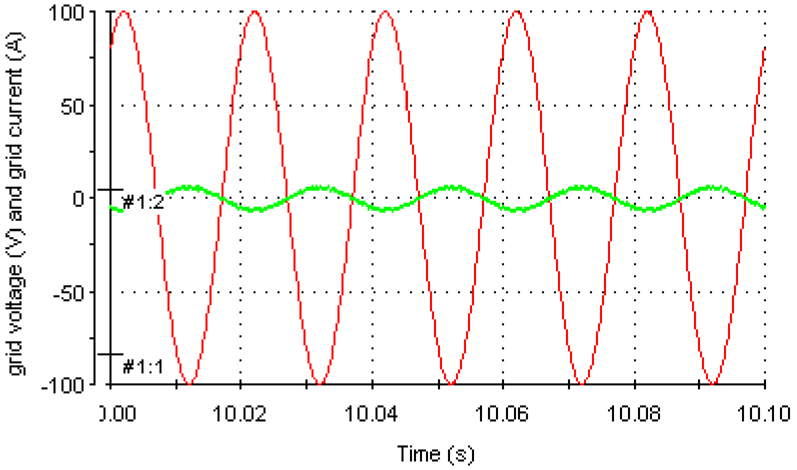

(g). Voltage and the current waveforms of one phase in grid-side inverter.

Figure 5.8. Performance of various parameters of AC gird-side converter.

5.9. Conclusions

Within this Chapter, a robust Generalized Predictive Control (GPC) for two level three-phase back-to-back converters with PMSG wind energy system was introduced, and a novel design procedure for the Uncertainty and Disturbance Estimator (UDE)-based DC-link voltage controller was presented.

The proposed GPC control system is simple, exhibits satisfactory transient response and robustness to wind speed variations. The linearized equations of the system are used to derive transfer functions, in order to select GPC parameters and analyze its stability.

Therefore, the proposed GPC technique can be included as a practical controller in wind energy systems, even without powerful hardware platforms, as opposed to other computationally demanding MPC strategies. For the DC-link voltage regulation, the UDE-based control has been developed to replace the conventional PI controller, to deal with the model uncertainty and external disturbances in the in the DC-link capacitor.

The proposed method is verified for a PMSG wind energy system based on two-level three-phase back-to-back converters. The system has been successfully run and controlled via two dSPACs DS 1104 cards: one controlling the machine-side (wind turbine emulator, PMSG) and the other the grid-side. The experimental results indicate that the proposed GPC strategy performs very well in achieving the control goals for the complete wind energy system.

Also, the proposed UDE approach has shown better robustness to handle extreme varying wind conditions with higher real power generation.

References

[1] **Zhang Z, Wang F, Sun T, Rodriguez J, and Kennel R:** "FPGA Based Experimental Investigation of a Quasi-Centralized Model Predictive Control for Back-to-Back Converters", *IEEE Transactions on Power Electronics 2016; 31(1): pp.662-672.*

[2] **Clarke DW, Mohtadi C, and Tuffs PS:** "Generalized predictive control - part I the basic algorithm", *Automatica 1987; 23(2): pp.137–148.*

[3] **Chen Z, Xiao X, Wang H, and Liu M:** "Analysis of converter topological structure for direct-drive wind power system with PMSG", *In Power System Technology (POWERCON), 2010 International Conference on, 2010, pp.1–5.*

[4] **Laks JH, Pao LY, and.Wright AD:** "Control of wind turbines: Past, present, and future", *In 2009 American Control Conference 2009: pp.2096-2103.*

[5] **Zigmund B, Terlizzi A, Garcia XT, Pavlanin R and Salvatore L:** "Experimental evaluation of PI tuning techniques for field oriented control of permanent magnet synchronous motors," *Advances in Electrical and Electronic Engineering.*

[6] **Richalet J, Rault A, Testud J L, and Papon J:** "Model predictive heuristic control: applications to industrial processes", *Automatica 1978; 14: pp.413 428.*

[7] **Cutler CR, and Ramaker BL: "**Dynamic matrix control a computer control algorithm", *Proceedings of the Joint American Control Conference, San Francisco, California U.S.A. 1980: paper WP5-B.*

[8] **Clarke DW, Mohtadi C, and Tuffs PS:** "Generalized predictive control - part II extensions and interpretations", *Automatica 1987; 23(2): pp.149 –160.*

[9] **Low KS:** "A digital control technique for a single-phase PWM inverter," *IEEE Trans. Ind. Electron. 1998; 45(4): pp.672–674.*

[10] **Kennel R, Linder A, and Linke M:** "Generalized predictive control (GPC)-ready for use in drive applications", *In Proc. PESC Power Electronics Specialists Conference 2001 IEEE 32nd Annual 2001; 4: pp.1839–1844.*

[11] **Allaoui T, Dena M, and Bouhamida M:** "Decoupling multivariable GPC control of UPFC-based power flow compensation," *In 10th International Conference EPE-PEMC 2002.*

[12] **Shariatpanah H, Fadaeinedjad R, and Rashidinejad M:** "A new model for PMSG-based wind turbine with yaw control", *IEEE Transactions on Energy Conversion 2013; 28(4): pp. 929–937.*

[13] **Jung J, Lim S, and Nam K:** "A feedback linearzing control scheme for a PWM converter-inverter having a very small DC-link capacitor", *IEEE Transactions on Industry Applications 1999; 35(5): pp.1124-1131.*

[14] **Lee TS:** "Input-output linearization and zero-dynamics control of three-phase AC/DC voltage-source converters," *IEEE Transactions on Power Electronics 2003;18(1): pp.11-22.*

[15] **Burgos RP, Wiechmann EP, and Holtz J:** "Complex state-space modeling and nonlinear control of active front-end converters", IEEE Transactions on Industrial Electronics 2005; 52(2): pp.363-377.

[16] **Rodriguez J, Pontt J, Cortes P, and Vargas R:** "Predictive Control of a Three-Phase Neutral Point Clamped Inverter", *In Power Electron. Spec. Conf. 2005. PESC'05. IEEE 36th 2005: pp.1364-1369.*

[17] **Quevedo DE, Aguilera RP, Perez MA, Cortes P, and Lizana R:** "Model Predictive Control of an AFE Rectifier With Dynamic References", *IEEE Transactions on Power Electronics 2012; 27(7): pp.3128-3136.*

[18] **Zhong QC, and Rees D:** "Control of uncertain LTI systems based on an uncertainty and disturbance estimator", *Journal of Dynamic System, Measurement, and Control, ASME 2004; 126(4): pp. 905–910.*

[19] **Talole SE, and Phadke SB:** "Robust input–output linearization using uncertainty and disturbance estimation. *International Journal of Control 2009 ; 82(10): pp.1794–1803.*

[20] **Sun L, Zhang Y, Li D, Lee KY, and Zhang X:** "UDE-based 2-DOF control design for input/output delay system", *In Proceedings of American Control Conference Chicago, IL 2015:pp.3974–3979.*

[21] **Kolhe JP, Shaheed M, Chandar TS, and Taloe SE:** "Robust control of robot manipulators based on uncertainty and disturbance estimation", *International Journal of Robust and Nonlinear Control 2013; 23: pp.104–122.*

[22] **Ren B, Zhong QC, and Chen J:** "Robust control for a class of non-affine nonlinear systems based on the uncertainty and disturbance estimator", *IEEE Transactions on Industrial Electronics 2015; 62(9): pp.5881–5888.*

[23] **Zhu B, Liu HHT, and Li Z:** "Robust distributed attitude synchronization of multiple three-DOF experimental helicopters", *Control Engineering Practice 2015; 36: pp.87–99.*

[24] **Chen J, Ren B, and Zhong QC:** "Hysteresis compensation in piezoelectric actuator positioning control based on the uncertainty and disturbance estimator", *In Proceedings of American Control Conference, Chicago IL 2015: pp.2537–2542.*

[25] **Sanz R, Garcia P, Zhong QC, and Albertos P:** "Control of disturbed systems with measurement delays: Application to quadrotor vehicles", *In Proceedings of Control and Automation, Torremolinos 2015: pp.927–932.*

[26] **Rossiter JA:** "Model-Based Predictive Control: A Practical Approach", *Florida: CRC Press, 2013.*

[27] **Camacho EF and Alba CB:** "Model Predictive Control", *Berlin: Springer-Verlag, 2013.*

[28] **Albertos P and Ortega R:** "On Generalized Predictive Control: Two Alternative Formulations", *Automatica 1989; 25(5):pp.753-755.*

[29] **Dumur D, Boucher P, and Röder J:** "Design of an open architecture structure for implementation of predictive controllers for motor drives," *In Pro-*

ceedings of the IEEE International Conference on Control Applications, Trieste 1998: pp.1307-1311.

Conclusion and Future Works

1. Conclusions

In summary, this thesis work has presented several predictive control schemes and various power electronic converters for variable-speed PMSG based wind turbine to improve the power conversion efficiency and transient dynamics of overall wind energy systems. Moreover, it also proves that with the proper predictive control algorithms, and optimum utilization of available power electronic converters (generator- and grid-side converters), the maximum benefits from a wind energy system can be achieved.

The proposed control techniques are modeled, simulated and successfully implemented in laboratory. The extensive simulation results supported by experimental results are provided to validate the proposed control approaches.

Some of the major achievements of the thesis are summarized as follows:

- The proposed configurations are very promising for the future development as they have been designed by combining the best features of the existing commercial wind turbine solutions.
- The research results presented here also endorse the predictive control strategy as a simple, efficient and high performance control tool for power converters which operate at a medium switching frequency.
- Various control objectives such as grid/inductor currents, grid active power and grid reactive power are included in the design and operation of the predictive controller.
- The modeling and analysis presented in this thesis can be used in other power electronics converters and wind energy system applications.

2. Summary of Major Contributions

The major contributions and conclusions of this research work are summarized as follows.

2.1. A review of the wind energy systems, power converters and MPPT control schemes is presented

- An extensive survey on the past, present and future trends of wind energy systems are presented to fill gaps in the existing literature.
- A review of practical and emerging power converters topologies used for PMSG based wind energy systems are presented. Various technical issues, features and drawbacks are analyzed, and important survey results are summarized by tables.
- Various classical and advanced MPPT methods used for PMSG based wind energy systems are discussed and compared.

2.2. Various challenges related to the FCS-MPC strategy are addressed

- A linear extrapolations method is proposed to estimate the future values of the reference variables. The proposed method eliminates the oscillations in the reference active and reactive powers (which are control variables for the case study considered), This method leads to safe and reliable operation for the semiconductor devices during step-changes in the reference control variables.
- A simplified two-step predictive control strategy is proposed to improve the performance and also to reduce the computational burden involved in the real-time implementation. The proposed technique shows a better solution without increasing the converter switching frequency. The proposed solution is promising for high wind power applications where lower switching frequency operation is mandatory.

2.3. Two advanced FCS-MPC techniques are proposed to control the machine-side and the grid-side converters

In this thesis, two advanced control schemes based on FCS-MPC are proposed:

- In the first control strategy, the rectified (inductor) current is controlled, assuming that the grid-side converter regulates the DC-link voltage and grid active and reactive powers.
- In the second control strategy, the grid active and reactive powers are controlled with an assumption that the machine-side converter performs the MPPT control.
- An excellent dynamic response and power quality has been achieved by eliminating the internal current control loops and modulators.
- The proposed solutions can be easily extended to other wind energy conversion system configurations and motor drive applications.

2.4. A continuous-and discrete-time models are presented

- In this thesis, the continuous-time model of the variables to be controlled is presented in terms of power converter switching states. Several variables, such as grid/inductor currents, active power and reactive power, are incorporated in the design of the system model. All the continuous-time models have been converted to discrete-time so as to incorporate the control delay and prediction horizon.

2.5. Two advanced predictive techniques are proposed to control the complete wind energy system

In this thesis, two novel control schemes based on fixed frequency model predictive control (MPC) are proposed:

- In the first strategy, the hill climb searching (HCS) algorithm utilizes the MPC for controlling the switched inductor boost converter (SIBC) and maximize the energy harvest with an assumption that the grid-side converter regulates the DC-link voltage.
- In the second strategy, robust predictive current controllers (PCC) is designed for controlling the single-phase full bridge inverter, improve the power quality, and achieves a sinusoidal current into the grid with low distortion, assuming that the machine-side converter performs MPPT control.
- In both methods, the voltage stress and switching losses of the semiconductor switches are reduced by balancing the DC-link capacitor voltages and by minimizing the switching frequency below 15 kHz, respectively.

2.6. High gain and high efficiency power conditioning topology is proposed

- A new power conversion system based on switched inductor boost converter (SIBC) is explored aimed at the next generation wind energy conversion system. The conversion gain ratio and the efficiency with the SIBC topologies has been increased significantly compared to the traditional DC/DC boost converters.
- A single-phase full bridge inverter is proposed as a grid interfacing inverter. Compared to the commercially available tow level three-phase voltage source inverter, the proposed configuration uses less number of active switches and thus it is less expensive and reliable.

2.7. A new encoderless MPPT control structure for PMSG wind energy conversion system is proposed

- The presented method is a simple method and does not require any knowledge of wind turbine characteristics, which makes it suitable for wind turbine applications.
- Advantages of the proposed scheme include simplicity of controller design, ease of implementation, no need for the aerodynamic control, and avoidance for an anemometer or shaft encoder.
- The proposed control scheme has the potential to reduce the cost and size of the wind turbine generator system.

2.8. A generalized predictive method is proposed to control the full scale back-to-back converters with PMSG based wind energy systems

- In this thesis, similar to those in the classical control methods, a generalized predictive method based on the vector control strategy is presented for both machine-side and grid-side converters of full scale back-back converters with PMSG wind energy conversion system. The proposed method shows a promising solution to controlling the generated power and also to meeting the grid codes requirements.

2.9. A Simulation and experimental studies are conducted to verify the system operations

- All the simulation studies are carried out using MATLAB/SIMULINK software.
- The predictive control algorithms are developed using MATLAB Embedded Function for an easy transfer of code to real-time implementation.
- Several low power prototype converters have been built such as traditional DC/DC boost converter and switched inductor boost converter (SIBC).
- All the theory, control system design and simulation results are validated through the experimental tests.
- A dSPACE DS1104 rapid prototyping controller based test platform has been developed.
- Wind turbine simulator based on a DC motor is developed, which can generate different output power as specified by the wind turbine characteristic curves.

3. Future Works

The following future research works are suggested as an extension to the knowledge presented in this dissertation.

- The stability issues with the FCS-MPC strategy should be studied by employing different discretization methods and prediction horizons.
- Predictive control algorithm can be also applied on pitch control of wind turbine (WT) to reduce the mechanical stress on the drive train and improve the energy conversion efficiency of the WT operating above the rated wind speed. The design will be based on the two-mass model of the WT, while simulation studies will focus on the detailed model provided by the FAST (Fatigue, aerodynamics, structures, and turbulence) software package.
- Investigation of PMSG based wind energy conversion system behavior under unbalanced grid fault conditions and development of new predictive control systems represent a very good research direction to meet the emerging grid code requirements.
- The generalized predictive control approach presented in this thesis can be extended to flying capacitor, active NPC and novel power electronic converters.

- Investigation of multilevel converter configurations can be used to reduce or completely eliminate the grid-side filter.
- For the grid-side converter, the next step should consider how to inject the reactive power into the grid for the purpose of stabilizing the power grid.